GAS-LIQUID FLOWS IN STIRRED REACTOR

A

Thesis

Submitted to the

University of Mumbai

For Ph. D. (Tech.) Degree In

Chemical Engineering

Submitted by

AVINASH RAMCHANDRA KHOPKAR

Under the Guidance of

DR. A. B. PANDIT

INSTITUTE OF CHEMICAL TECHNOLOGY
UNIVERSITY OF MUMBAI
MUMBAI – 400 019

APRIL 2005

STATEMENT TO BE INCORPORATED BY THE CANDIDATE IN THE THESIS AS REQUIRED UNDER ORDINANCES O.770 AND O.771 FOR THE Ph.D. DEGREE

STATEMENT BY THE CANDIDATE

As required by the University Ordinances O.770 and O.771, I wish to state that the work embodied in this thesis titled "**Gas-liquid flows in stirred reactor**", forms my own contribution to the research work carried out under the guidance of **Dr. A. B. Pandit** at the Mumbai University Institute of Chemical Technology (MUICT), University of Mumbai. This work has not been submitted for any other degree of this or other university. Wherever references have been made to the previous work of others, it has been clearly indicated as such and included in the bibliography.

Avinash R. Khopkar
(Research Student)

Certified by

Dr. A. B. Pandit
Research Supervisor,
Chemical Engineering Division, MUICT

Date: April 2005
Place: Matunga, Mumbai – 400 019

CERTIFICATE

The research work described in this thesis has been carried out by **Avinash Ramchandra Khopkar** under my supervision. I certify that this is his bonafide work. The work described is original and has not been submitted for any other degree of this or any other university. Further, that he was a regular student and has worked under my guidance as a full time student at MUICT until the submission of the thesis to the University of Mumbai.

Dr. A. B. Pandit
Research Supervisor,
Chemical Engineering Division,
MUICT

Date: April 2005
Place: Matunga, Mumbai – 400 019

Gas-Liquid Flows In Stirred Reactor [*1]

Thesis submitted by **Avinash R. Khopkar** for the degree of Doctor of Philosophy (Technology) in Chemical Engineering. The following papers on the work presented in this thesis have been published/forwarded/to be forwarded.

1. **Khopkar, A.R.**, Aubin, J., Xureb, C., Le Sauze, N., Bertrand, J and Ranade, V.V. (2003), Gas-liquid flow generated by a Pitched blade turbine: Particle velocimetry measurements and CFD simulations, *Ind. Eng. Chem. Res.*, **42**, 5318-5332.
2. **Khopkar, A.R.**, Mavros, P., Ranade, V.V. and Bertrand, J. (2004), Simulation of flow generated by an axial flow impeller: Batch and continuous operation, *Chem. Eng. Res. Des.*, **82** (A6), 737-751.
3. **Khopkar, A.R.**, Aubin, J., C. Rubio-Atoche, Xuereb, C., Le Sauze, N., Bertrand, J. and Ranade, V. V. (2004), Flow generated by radial flow impellers: PIV measurements and CFD simulations, *I. J.C.R.E.*, Vol.**2**, A18.
4. Dakshinamoorthy, D., **Khopkar, A.R.**, Louvar, J. and Ranade, V.V. (2004), CFD simulations to study early shortstop of runaway reaction in stirred vessel, accepted for presentation, *Journal of Loss Prevention in Proc. Ind.*, **17**, 355-364 [*2].
5. **Khopkar, A.R.**, Rammohan, A., Ranade, V.V. and Dudukovic, M.P. (2005), Gas-liquid flow generated by a Rushton turbine in stirred vessel: CARPT/CT measurements and CFD simulations, *Chem. Eng. Sci.*, **60**, 2215-2229.
6. **Khopkar, A.R.**, Panaskar, S.S., Pandit, A.B. and Ranade, V.V. (2005), Characterization of gas-liquid flows in stirred vessel using pressure and torque fluctuations, *Ind. Eng. Chem. Res.*, in press.
7. **Khopkar, A.R.** and Ranade, V.V. (2005), CFD simulation of gas-liquid flow in stirred vessels: VC, S33 and L33 flow regimes, submitted to *AIChE J*.
8. Jade, A.M., **Khopkar, A.R.**, Jayraman, V.K., Ranade, V.V. and Kulkarni, B.D. (2005), A novel local singularity distribution based method for flow regime identification: Gas-liquid stirred vessel with Rushton turbine, submitted to *Chem. Eng. Sci.*
9. **Khopkar, A.R.**, Mavros, P. and Ranade, V.V. (2002), CFD modelling of the continuous operation of stirred vessel: Influence of inlet/outlet locations on residence time distribution, *Presented at 17th Int. Symp. on Chem. React. Eng.*
10. **Khopkar, A.R.** and Ranade, V.V. (2003), Differences and similarities of gas-liquid flow generated by down-flow, paddle and up-flow turbine, *Presented at 11th Euro. Conf. on Mixing,* held at Bamberg, Germany.
11. **Khopkar, A.R.**, Sardeshpande, M.V., Kasat, G.R., Pandit, A.B. and Ranade, V.V. (2005), CFD simulation of solid suspension in stirred slurry reactor, accepted for oral presentation at CAMURE-5, ISMR-4.

[*1] Received **Professor S.B. Chandaliya award for best research student** (2003-2004) based on the work presented in this thesis.

[*2] Included in **Top 25 hottest articles** of the *Journal of Loss Prevention in Process Industry*.

12. **Khopkar, A.R.**, Kasat, G.R., Pandit, A.B. and Ranade, V.V. (2005), CFD simulation of mixing in tall gas-liquid stirred vessel: Role of local flow patterns, accepted for presentation at FLUID MIXING 8.

13. **Khopkar, A.R.** and Ranade, V.V. (2002), CFD simulation of flow generated by down- pumping axial flow impeller in stirred reactor, presented at CHEMCON 2002, Hyderabad.

14. Sharma, P., Patanaik, M.S., Panaskar, S., **Khopkar, A.R.** and Ranade, V.V. (2003), Power consumption and flow regimes in a gas-liquid stirred vessel equipped with a 6-blade pitched blade turbine, presented at CHEMCON 2003, Bhubaneshwar.

15. Gorasia, A.K., **Khopkar, A.R.** and Ranade, V.V. (2004), CFD simulations of flow and mass transfer in Taylor flow through a narrow channel, presented at INDO-US session, CHEMCON 2004, Mumbai.

Dedicated to
My Parents

“Finish each day and be done with it. You have done what you could; some blunders and absurdities have crept in; forget them as soon as you can. Tomorrow is a new day; you shall begin it serenely and with too high a spirit to be encumbered with your old nonsense”.

Ralph Waldo Emerson

Acknowledgements

There are many people that have been actively present during the tenure of my Ph.D. and I would like to thank all of them for their time, support, efforts, smiles and friendship. There are, however, several peoples that I would like to acknowledge in particular.

I owe great thanks to my Ph.D. supervisors, **Dr. A. B. Pandit,** *MUICT* and **Dr. V. V. Ranade,** *NCL*. I am indeed very lucky to being associated with them, to receive their guidance. I learnt many things from them. They have always promoted me to be self-sufficient and guided me whenever I needed. I hope that this work would partly satisfy their expectations.

During this work, I have worked with few foreign collaborators, in particular Dr. Aubin, *Tolouse, France*; Dr. Rammohan, *St. Louis, USA* and Mr. Durai, *Waynestate, USA*. I really enjoyed while working with them. I also thank Dr. Ashwin Patwardhan, *MUICT*, for the valuable and constructive discussions I had with him. Many post-graduate and under-graduate students were associated with me during my Ph.D. In particular, the association with Mr. Sachin Panaskar and Mr. Gopal Kasat is greatly acknowledged.

Almost one third of this thesis has been dedicated to experimental characterization of gas-liquid flows. I am grateful to Mr. Petkar, *Mechanica systems, Pune*, for his sustained interest in the development of torque sensor and telemetry system. Mr. Wanjale and Mr. Shinde, *NCL workshop*, always came running to help me out when I had problems with my experimental set-up. Without their help, it would have been difficult to complete the work in time.

I am thankful to my colleagues beyond words, namely Dr. Vivek Buwa, Prashant Gunjal, Ranjeet Utikar, Kaustubh Mujumdar, Mohan Rampure, Ajay Gorasia, Yogesh Harshe, Amit Arora, Madhavi Sardeshpande, Harshala Butala, Naren P.R., Saurabh Joshi and several other past and present members of *Industrial Flow Modelling Group, NCL*. They have made their contribution in several ways, through suggestions and discussions. I always have been benefited from their suggestions. I acknowledge many

other friends with whom I lived, enjoyed the social life and had great fun during my stay at *NCL*. No doubt their company has made my stay comfortable and cheerful. In particular, I am thankful to Dr. Vinay Thakur, Vivek Bhagwat, Shishir Sabale and Kapil Rajurkar.

I also sincerely thank *Council of Scientific and Industrial Research*, *New Delhi* for providing the research fellowship. I am grateful to *National Chemical Laboratory, Pune* and *University Institute of Chemical Technology, Mumbai* for making this research work complete.

Last but not least, I have to thank my parents, my sister Rohini, my brother in law Satish and my niece Shravani for their continual lifelong support, encouragement and love. Of course I thank my wife, Aditi and my son, Atharv for their patience, understanding and support.

Avinash R. Khopkar

CONTENTS

Chapter 1

INTRODUCTION

1.1 Gas-Liquid Flows in Stirred Reactors

Stirred reactors are widely used in process industry to carry out large number of gas-liquid catalytic and non-catalytic reactions (such as, hydrogenation, oxidation, alkylation, sulfonation). They offer flexibility in operation to manipulate the performance of the reactor. In a stirred reactor, the overall reaction rate and the reactor performance (selectivity and conversion) are controlled by the fluid dynamics prevailing in the reactor. Despite the wide spread use, the fluid dynamics of these reactors, essentially for the gas-liquid system is not well understood. This lack of understanding and the knowledge of underlying fluid dynamics have caused reliance on empirical information (Oldshue, 1984; Smith, 1985; Tatterson, 1991). Available empirical information is usually described in an overall/ global parametric form. This practice conceals detailed localised information, which may be crucial in the successful design of the process equipment. Reliability of such empirical information and extrapolation beyond the range of parameters studied often remains questionable. It is therefore, essential to develop and apply new tools to enhance our understanding of fluid dynamics prevailing in the stirred reactors. Such understanding will be useful in devising cost effective and reliable scale-up of stirred reactors. Therefore, the present study was undertaken to develop a broad framework for the understanding and modelling of the gas-liquid flows in stirred reactor.

In a stirred reactor, the baffles are positioned along the periphery of the reactor wall to inhibit the formation of free surface vortex due to the rotation of the impeller. The flow around the rotating impeller blades interacts with the stationary baffles and generates a complex, three-dimensional and inherently unsteady flow. The flow approaching from above and below the impeller plane generates three dimensional roll vortices (trailing vortices) behind the blades. In gas-liquid stirred reactor, the sparged gas interacts with these vortices and gets accumulated in the low-pressure region associated with the vortex core. The accumulated gas forms the gas filled pockets *commonly termed as gas cavities* behind the impeller blades. Such gas accumulation significantly alters the power dissipation and the pumping capacity of the impeller. To illustrate the cavity formation behind the impeller blades, close-up of the flow near impeller blades of Rushton turbine for single-phase and for gas-liquid flows is shown in Figure 1.1. The gas cavities behind impeller blades are clearly seen in the close-up of the gas-liquid

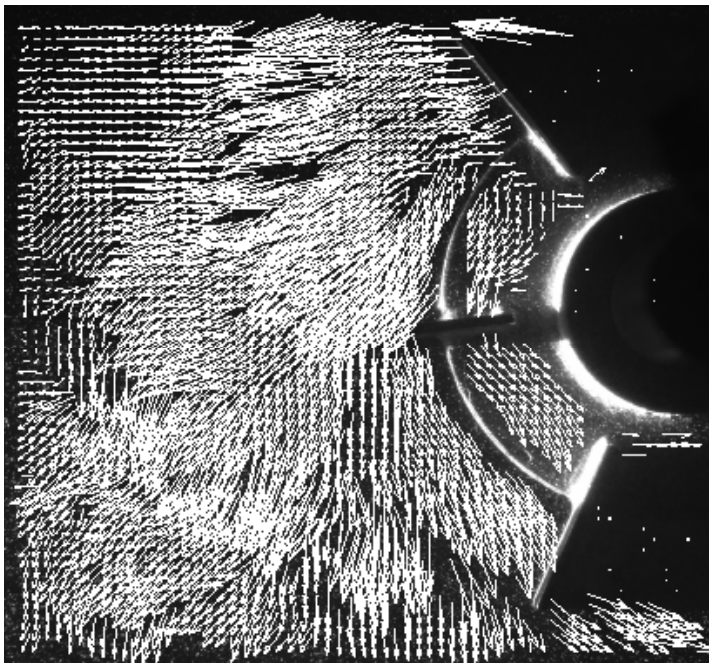

(a) Single-phase flow

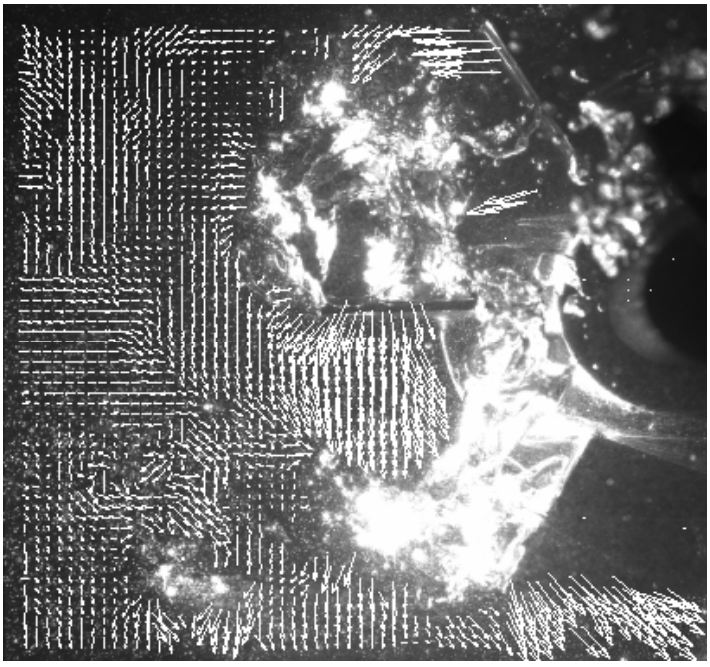

(b) Gas-liquid flow

Figure 1.1 Instantaneous PIV Images of the Flow Field near Impeller Blades of Rushton Turbine (from Deen, 2001)

flows. The comparison of the liquid phase flow pattern of the single-phase system with the gas-liquid flows (Figure 1.1) shows reduction in the liquid velocities generated by an impeller (drop in the pumping efficiency of the impeller) for gas-liquid flows. The relative magnitudes of the impeller pumping capacity and gas flow rates determine the prevailing flow regimes in gas-liquid stirred reactor. The power dissipated by the impeller controls the rates of the transport processes in the stirred reactors.

Various types of impellers, with different shapes and sizes, are used in actual practice. The shape and size of the impeller blades significantly controls the flow around the impeller blades. Therefore, impellers with different blade shapes have been devised and suggested to improve the performance of the impeller in gas-liquid stirred reactor. In recent years, many impeller manufacturers and the researchers have proposed the use of curved blade (especially convex shape because it is expected to minimise the gas accumulation behind the impeller blade) impellers (for example, Smith impeller, Scaba turbine) and the axial flow impellers (for example, pitched blade turbine). Different shapes of blades will obviously lead to different types and characteristics of trailing vortices, which will lead to different gas accumulation behaviour and therefore different performances in the presence of gas. Thus, the understanding of and capability to predict the flow around the impeller blades, trailing vortices and their interaction with gas bubbles and accumulation of gas behind impeller blades is the key for the reliable design and scale-up of gas-liquid stirred reactors.

Different experimental techniques have been used to study the flow characteristics in gas-liquid stirred reactors. However, the experimental measurements were limited to the measurement of overall gas hold-up, power dissipated by an impeller, mixing time and the identification of different flow regimes. Though, these measurements have helped to establish the relationship between reactor performance and operating/design parameters in the form of empirical correlations, the understanding of various flow processes and their interactions is still obscure. In the recent years, advancements in the measurement techniques have provided the wealth of information on the fluid dynamics in the reactors and the flow around the rotating impeller blades. However, most of the available information is limited to the single-phase flow. Very little experimental information is available for gas-liquid flows due to constraints/ limitations associated with the available experimental techniques (see Deen *et al.,* 2001; Khopkar *et al.,* 2003

for more details). The knowledge of flow around impeller blades for higher gas holdup values is necessary to evaluate the performance of new impeller designs for higher gas loading. The constraints of the present experimental techniques proposed a need of other alternative tools to investigate the gas-liquid flows around impeller blades of different shapes.

In last two decades, with the improvement in the knowledge of numerical techniques, turbulence models and the availability of fast computational resources made it possible to develop models based on computational fluid dynamics and use them for 'a priori' prediction of the flow field in chemical process equipments (Ranade, 1995; Kuipers and van Swaaij, 1997; Joshi and Ranade, 2003). However, unlike single-phase flow, which is possible to predict with reasonable confidence (Joshi and Ranade, 2003), the computational models capable of predicting real-life turbulent multiphase flows involving complex geometries and with a wide range of space and time scales are yet to be established. The development of such models will be a significant step towards the prediction of local fluid dynamics. Such models will be useful to explore the possibilities for the performance enhancement of existing reactors and to evolve better reactor configurations. The present study is aimed at developing such models for simulating dispersed gas-liquid flows in stirred reactor. Following section briefly reviews the current status of experimental as well as modelling work and brings out the motivation for undertaking this research.

1.2 Motivation

Gas-liquid flows in stirred reactor exhibits different flow regimes and demonstrate complex interaction of transport and mixing processes with varying spatio-temporal scales. Significant research efforts have been spent on developing flow regime maps and the design correlations (see an excellent review of Nienow, 1998 and the references cited therein). However, the applicability of the developed flow regime maps and the correlations while design, scale-up and for setting up of operating protocols for industrial systems is not yet well established. Therefore, there is a need to develop a new robust experimental methodology based on simple and non-intrusive measurement techniques like wall pressure and torque fluctuations for the characterization of the gas-

liquid flows. The development of such experimental techniques can offer powerful tool to diagnose gas-liquid stirred reactor.

Different flow regimes exhibit different fluid dynamic characteristics (see Figure 1.2) and lead to significantly different rates of transport and mixing processes. Therefore, the knowledge of local flow characteristic distribution, such as liquid velocities, gas holdup and interfacial area distribution over reactor volume becomes essential to control the rates of different transport and mixing processes. The experimental techniques like LDA and PIV have significantly contributed in the measurement of local flow characteristics. However, these techniques are useful for lower value of gas holdup (gas holdup values less than 5%). In gas-liquid stirred reactor, very high values of gas holdup are usually observed behind the impeller blades. In such situations, these techniques do fail to provide the quantitative information of flow characteristics. The limitations associated with the experimental techniques make computational fluid dynamics as a useful tool for providing quantitative information of flow characteristics.

Computational fluid dynamics (CFD) based models were shown to be successful in simulating single-phase flow generated by impeller(s) of any shape in complex reactors (see for example, Ranade, 2002). For multiphase flows, the complexity of modeling increases considerably and this remains an area for further research and development. Despite the complexity, several attempts have been made to simulate the gas-liquid flow in stirred reactors (for example, Gosman *et al.,* 1992; Bakker and van den Akker, 1994; Ranade and van den Akker, 1994; Morud and Hjertager, 1996; Ranade and Deshpande, 1999; Lane *et al.,* 1999 Lane *et al.,* 2000; Ranade *et al.* 2001b; Lane *et al.,* 2004 and Laakkonen *et al.,* 2004). Although some degree of success is reported, a number of limitations are apparent.

Earlier studies were carried out with rather inadequate number of computational cells and were qualitative in nature (see for example, Gosman *et al.,* 1992; Ranade and van den Akker, 1994). Adequate grid resolution is however, essential to correctly simulate flow around impeller blades (Ranade *et al.,* 2001a). Ranade and Deshpande (1999) and Ranade *et al.* (2001b) studied the influence of gas flow rate on trailing vortices of Rushton turbine. The predicted results showed the accumulation of gas behind the

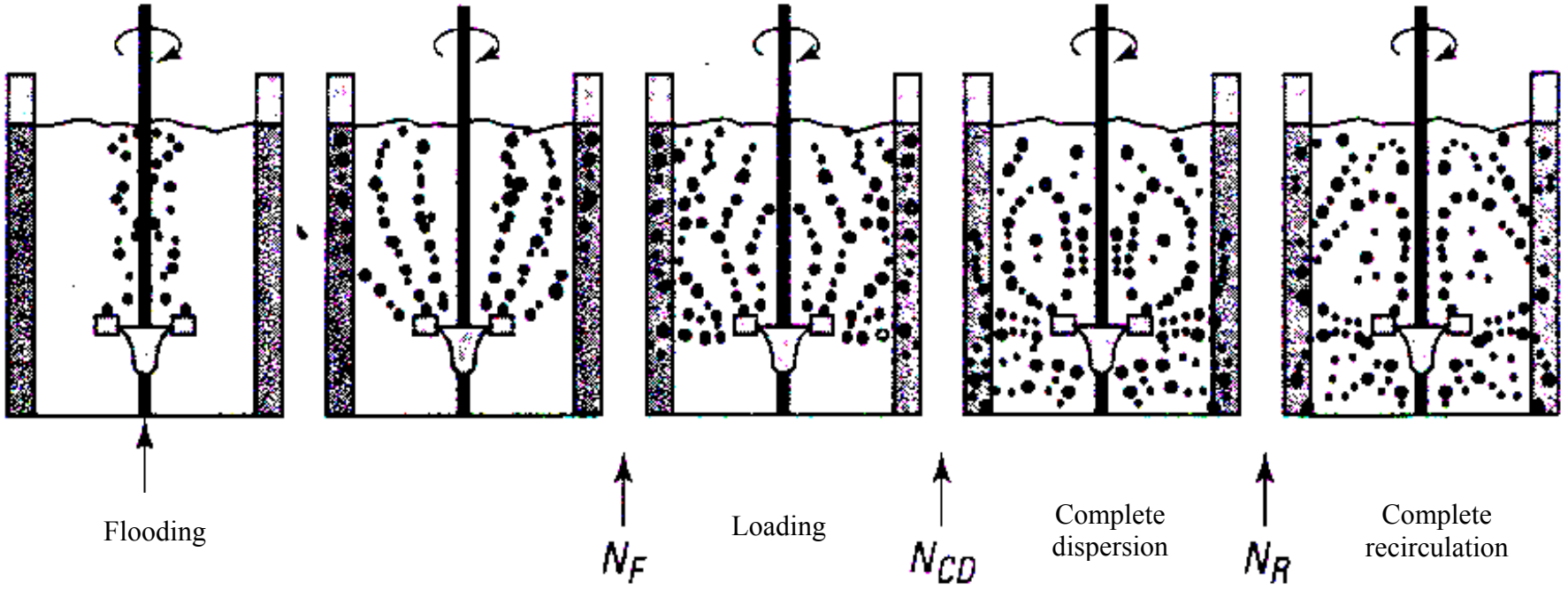

Figure 1.2 Different Flow Regimes in Stirred Reactor Equipped with Rushton Turbine (from Nienow *et al.*, 1985)

impeller blades. However the focus was on near impeller region and whether the models are able to simulate flow characteristics quantitatively or not was not studied.

Most of the published simulations used single bubble diameter for whole reactor. In a gas-liquid stirred vessel, gas bubbles of different sizes co-exist. Very fine bubbles are observed in impeller discharge stream (< 1 mm) where as bubbles of the size of few mm (~5 mm) are observed in the region away from impeller (Barigou and Greaves, 1992). The width of bubble size distribution depends upon the turbulence level and prevailing flow regime. Considering that the importance of right prediction of slip velocity, it might be necessary to use appropriate bubble sizes. The multi-fluid model with appropriate breakage and coalescence rates (see for example, Lane *et al.,* 2000; Laakkonen *et al.,* 2004), which are able to simulate evolution of bubble size distribution within the vessel, may provide a better way to simulate the gas-liquid flow in stirred vessel. Unfortunately available experimental data of bubble size distribution in stirred reactor is not adequate to calculate the parameters appearing in the coalescence and break-up kernels. Also, the multi-fluid models with coalescence-breakup processes increase the demands on computational resources by an order of magnitude and are often forced to use rather smaller number of computational cells and results into not so accurate prediction of flow around impeller blades.

Apart from the uncertainty in the parameters of coalescence and break-up kernels, there is significant uncertainty in the estimation of inter-phase drag force on gas bubbles in the presence of other bubbles and high levels of turbulence prevailing in the reactor. Recently published studies highlighted the importance of appropriate inter-phase drag force formulation (see for example, Brucato *et al.,* 1998; Lane *et al.,* 2002; 2004). Inter-phase drag coefficient was found to affect both, the distribution of gas hold-up and total holdup of gas. Several correlations relating inter-phase drag coefficient to gas hold-up and prevailing turbulence are available. Despite these studies, adequate guidelines to select appropriate model for inter-phase drag force for all the regimes of gas-liquid flows in the stirred reactor are not available. Considering these issues and the present state of the understanding, the option of using multi-fluid computational model for stirred reactors was not thought to be very effective. Therefore, it becomes imperative to provide better understanding of the interphase drag force formulation and incorporate the developed understanding in the computational models to simulate gas-

liquid flows in stirred reactor. The ability of such models to quantitatively simulate different flow regimes needs to be verified by comparing the model predictions with experimental data. In this work, we have collaborated with group of Professor Bertrand (at ENSIGC, Toulouse, France) to get the experimental data measured with PIV. The experimental data measured by our collaborators and the experimental data available in literature were then used to evaluate the CFD models developed in present work.

Finally, the validated CFD models need to be applied to address key reactor engineering issues. In particular, it would be worthwhile to investigate the role of reactor hardware and generated local flow patterns in the liquid phase mixing. With this background, specific objectives of the present work were evolved which are listed in the following.

1.3 Objectives

- Develop robust experimental techniques like wall pressure and torque fluctuations measurement for the identification of the prevailing flow regimes.
- Extract information of the different time scales of fluid dynamics.
- Study the influence of different interphase forces on the prediction of gas-liquid flows and develop necessary sub-models to correctly model the interphase forces.
- Develop computational fluid dynamics based models which are capable of simulating gas-liquid flows in stirred reactor operating in different flow regimes and for different impeller types
- Understand the influence of reactor hardware configuration and local flow patterns on the mixing process

1.4 Methodology

The methodology used to carry the proposed Ph. D. work is summarized in Figure 1.3. The experiments were carried out to understand the fluid dynamics of gas-liquid flows in the reactor with different impeller. An attempt was made towards the on-line characterization of the gas-liquid flows and to setup robust criteria for flow regime

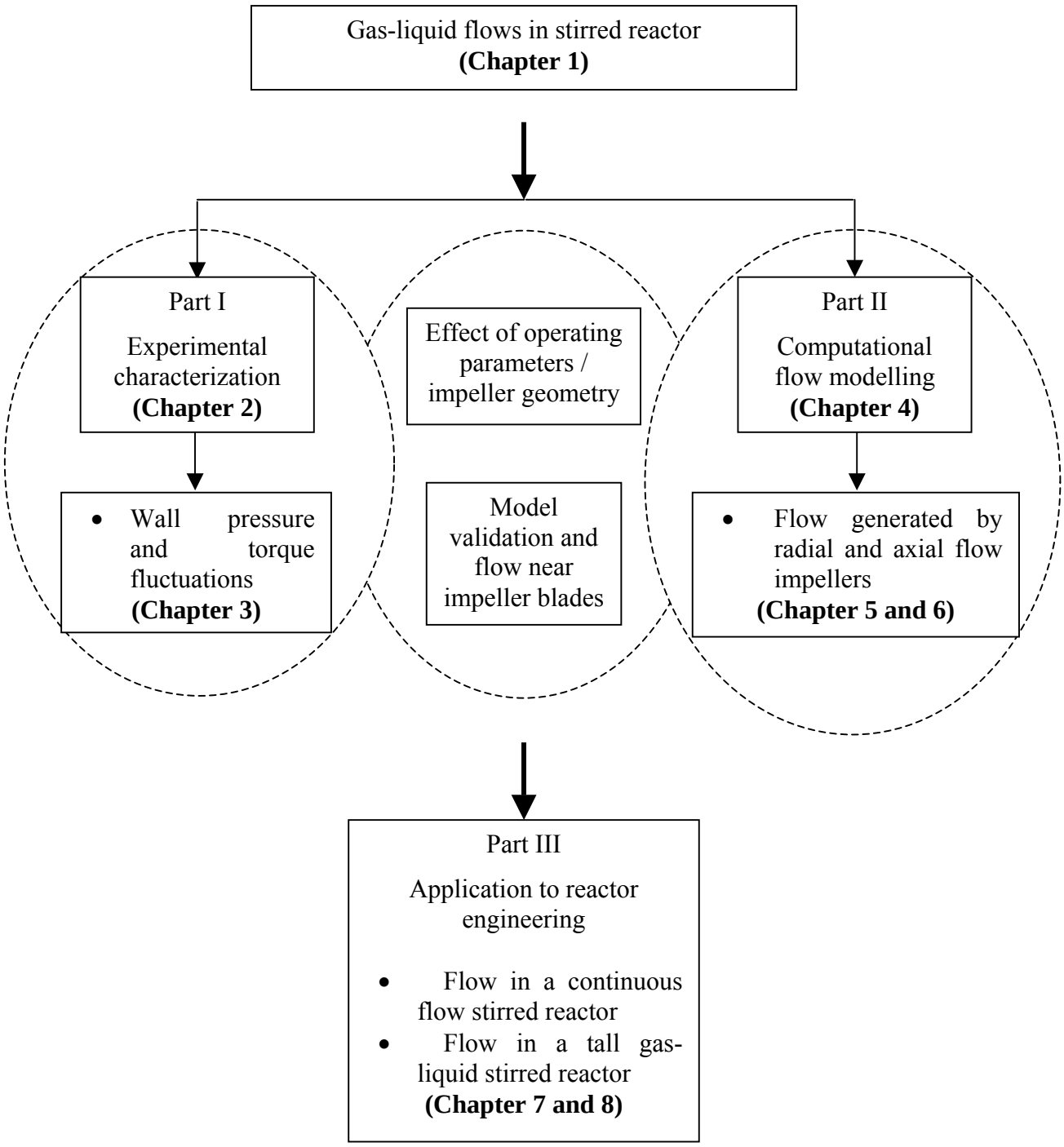

Figure 1.3: Organization of Thesis

identification in the gas-liquid stirred reactors. An important time scale of the fluid dynamics was extracted from the measured data. The developed understanding of the gas-liquid flows was used to carry out Eulerian-Eulerian simulations. Besides the gas holdup distribution pattern, experimental results (measured with PIV by our collaborators) on the velocity and turbulent quantities and flow around impeller blades were used for quantitative validation of the CFD based models. Eulerian-Eulerian models were used to simulate gas-liquid flows in different flow regimes and understand the effect of size and shape of impeller blades on the generated flow. The results of Eulerian-Eulerian simulations for different impeller blades were analyzed together to understand the performance of the different types of impellers in gas-liquid system. Finally, the validated computational models were used to understand the effect of hardware configuration and the local flow structure on the mixing process occurring in the reactor.

In this thesis, gas-liquid flows generated by radial flow impellers (Rushton turbine, Smith turbine and Scaba turbine) and axial flow impellers (6-bladed down- as well as up- pumping pitched blade turbine and Mixel TT) were studied in detail. The selection of these impellers was based on the experimental data available in literature and their wide use in process industry for gas dispersion application. Unfortunately very few data on the fluid dynamics is available in literature for gas-liquid flows. This compelled us to study the gas-liquid flows with different scales of reactors. The selections of those reactors were due to the availability of the experimental data from our research collaborators, literature and the available experimental facility.

1.5 Organization of thesis

The overall thesis is organized as follows. In PART ONE, the experimental characterization of gas-liquid flows using wall pressure fluctuations and torque fluctuations is presented (Chapter 2 and 3). In PART TWO, computational flow modelling using Eulerian-Eulerian approach is presented (Chapter 4, 5 and 6). In PART THREE, the use of computational model as a tool to solve the reactor engineering issues is presented (Chapter 7 and 8).

In **Chapter 1**, general introduction of the thesis is presented. The motivation of undertaking present research, specific research objectives and methodology adopted are discussed. The organization of the thesis is briefly discussed at the end.

PART ONE: Experimental Characterization

In **Chapter 2**, the experimental techniques and the measurements carried out in the literature for characterization of gas-liquid flows in stirred reactor are discussed. The measurement techniques used in this thesis are also discussed and their use is justified.

In **Chapter 3**, the characterization of the gas-liquid flows in a stirred reactor using wall pressure and torque fluctuations are presented. The flow regimes based on the cavity structure developed behind the impeller blades were identified using wall pressure fluctuations. The drop in the impeller pumping efficiency with increase in the gas flow rate for constant impeller speed was estimated using cycle characterization of the wall pressure fluctuations. The torque fluctuations were measured to study the effect of the gas flow rate on the average power dissipation. The different time scales of the fluid dynamics were characterized using torque fluctuations.

PART TWO: Computational Flow Modelling

In **Chapter 4**, hierarchy of impeller modelling options and modelling approaches used for the simulation of dispersed gas-liquid flows are discussed. The computational snapshot approach used to model the impeller rotation is discussed in detail.

In **Chapter 5**, a comprehensive computational model based on the Eulerian-Eulerian approach was developed to simulate gas-liquid flows in a stirred vessel. A separate sub-model was developed to quantitatively understand the influence of turbulence and presence of neighboring bubbles on drag acting on bubbles. This sub-model was used to identify and modify an appropriate correlation for estimating the inter-phase drag force.

The modified correlation was then incorporated in the computational model and then model was used to simulate the gas-liquid flows in a stirred reactor operating in three

distinct flow regimes. The effect of grid size distribution and the virtual mass force on the predicted gas holdup distribution was also studied. Model predictions were verified by comparing the predicted gas holdup distribution with the experimental data of Bombac *et al.* (1997). The model predictions were used to study the gas-liquid flow around the impeller blades. The developed computational model was then extended to simulate the flow generated by modern radial flow impeller, Scaba turbine and an attempt was made to understand the influence of the blade shape on the generated flow.

In **Chapter 6**, the computational model based on the Eulerian-Eulerian approach was used to simulate the flow generated by 6-bladed down pumping pitched blade turbine. The model predictions were verified by comparing the predicted velocity and turbulent quantities with the PIV data of Aubin *et al.* (2003) and the predicted gas holdup distribution with the measured computer tomography data. The computational model was then used to understand the effect of blade angle on the generated gas-liquid flow. An attempt was made to bring out the differences and similarities of the generated gas-liquid flows.

PART THREE: Application to Reactor Engineering

In **Chapter 7**, the computational model was used to understand the effect of hardware configuration on the performance of continuous flow stirred reactor. The effect of inlet/outlet configuration on the performance of a reactor was demonstrated by carrying out simulation of liquid mixing phenomenon. A quasi-steady state approach with 'multiple snapshots', which can adequately account for the interaction of the incoming liquid jet, with the rotating impeller, was used. The model predictions for both batch and continuous mode of operation were verified by comparing the predicted results with the experimental data of Mavros *et al.* (2001). Flow and scalar mixing simulations were carried out to study the influence of different inlet/outlet configurations on the predicted residence time distribution (RTD). An attempt was made for the quantitative estimation of part of the incoming fluid bypassing from the reactor and to suggest possible ways to improve the performance of the reactor.

In **Chapter 8**, the computational model was used to understand the influence of the operating conditions on the flow generated by three down- pumping pitched blade

turbines in tall stirred reactor was studied using CFD simulations. The computational model was then extended to study the implications of local flow patterns developed due to the interaction of impeller-generated flows and the gas driven flow on the liquid phase mixing process. The particle trajectory simulations of neutrally buoyant particle were carried out to extract the information of circulation time distribution. The predicted circulation time distribution along with the predicted flow patterns were then used to explain the mixing time trends observed by Shewale and Pandit (2005). The present work gives useful insights into the mixing process in a multiple-impeller gas-liquid system. Though, we have focused on the simulation of liquid phase mixing in gas-liquid reactor, the developed models can be used to address other reactor engineering issues like gas-liquid mass transfer with chemical reactions or the solid phase suspension and distribution phenomena.

PART I

EXPERIMENTAL CHARACTERIZATION

Chapter 2

EXPERIMENTAL CHARACTERIZATION OF GAS-LIQUID FLOWS

2.1 Introduction

Several experimental measurement techniques are used in practice to characterize the gas-liquid flows in stirred reactors. Most of the earlier work was focused on the measurement of global parameters by measuring the average gas holdup, power dissipated by an impeller, flow regime identification/transition, and so on (for example, Nienow, 1998 and references cited therein). Though these efforts were useful in providing the overall guidelines for the reactor design and operation, but failed to provide the local information of the fluid dynamics. It was observed that the local information is very crucial and controls the local mixing and transport processes occurring in stirred reactor. Also in order to develop and validate the detail computational fluid dynamic models, for simulating the gas-liquid flows in stirred reactor, the systematic experimental study of understanding the local fluid dynamics properties and their dependence on the operating conditions and on design/hardware parameters is needed. In this chapter, we briefly review the key measurement techniques commonly used to characterize the gas-liquid flows in stirred reactors. Due to a vast literature which has been reviewed recently (see excellent review articles, for example, Mavros *et al.*, 2001, Boyer *et al.*, 2002 and references cited there in), the objective of this review is to present a general introduction of the available techniques, their accuracy and limitations.

The commonly used experimental techniques are summarized in Table 2.1. Depending upon the objectives, different measurement techniques with desired adequacy of space and time resolution, the available measurement techniques are broadly classified in two ways. The classification distinguishes between global and the local measurement techniques. Using this classification, the hydrodynamic characteristics measured, are:

- Global characteristics (power consumption, average gas holdup, flow regime, mixing time and so on)
- Local characteristics (velocity and turbulent quantities, gas volume fraction and so on)
- Ensemble characteristics (flow pattern, trailing vortices, cavity structure and so on)

Table 2.1 Measurement techniques (Boyer *et al.*, 2002)

Technique	**Expected results**	**Spatial resolution**	**Time resolution**
Power consumption	Power measurement	Global technique	Hydrodynamic steady state
Level detector	Phase holdup	Global technique	Hydrodynamic steady state
Tracer technique	Mixing characteristics	Global technique	Hydrodynamic steady state
HWA	Liquid velocity field	++	++
LDV	Liquid velocity field	+++	++
UDV	Liquid velocity field, bubble velocity	+	+
Resistivity probe	Gas holdup, bubble velocity, bubble chord distribution	++	+++
Capillary suction tube	Gas holdup, bubble chord distribution	++	++
Photography and image analysis	Bubble size, flow regime, cavity shape	+++	+++
CARPT	Velocity fields and trajectory	+	+
PIV	Velocity field	++	+
γ-Tomography	Phase holdup distribution	+	-
Capacitive or resistive tomography	Phase holdup distribution	+	+++
LIF	Tracer dispersion field	++	+++

Spatial resolutions: +++: << 1 mm; ++: mm; +: cm

Time resolutions: +++: ms; ++: s; +: minute

2.1.1 Global measurement techniques

The global measurement techniques like power consumption, gas and liquid holdup, flow regime, mixing characteristics of liquid phase are discussed. In most of these techniques long time averages are measured.

- Power consumption of an impeller

The power consumption or dissipated by an impeller is a very important hydrodynamic parameter of stirred vessel and it characterizes an impeller in terms of the energy given to the contained fluid. The power consumption not only determines the gas-liquid mass transfer coefficient but is also used to compare the performance of different impellers. The power consumption of an impeller is commonly measured by using either torque table or the strain gauges pasted on impeller shaft (see for example see Rewatkar *et al.*, 1993; Nienow *et al.*, 1985 and the references cited therein). The power consumption can be used to calculate the power number of an impeller as:

$$N_P = \frac{P}{\rho N^3 D^5} \tag{2.1}$$

where, D is the impeller diameter, N is impeller rotational speed and ρ is the density of the liquid. Generally, for aerated conditions the power consumption is presented as the gassed to ungassed power ratio, Pg/P and is a function of the gas flow rate and impeller rotational speed (N). The power reduction curves are also used to identify the flow regimes in an aerated stirred vessel (see for example, Rewatkar *et al.*, 1993; Smith *et al.*, 1987)

- Level detector/taker

In level detector/taker technique, the increase in the liquid height is recorded. The difference between the liquid height before and after the aeration is used to calculate the fractional gas holdup in the vessel (see for example Chapman *et al.*, 1983). The overall gas holdup is calculated as:

$$\alpha_g = \frac{H_g - H}{H} \tag{2.2}$$

where, H_g is the dispersion height and H is the height of the liquid only.

- Tracer techniques

Liquid phase tracer is used to determine the residence time distribution and mixing process as occurring in the reactor. In mixing experiments, a tracer, usually salt solution (electrolyte), is introduced in the reactor and the time evolution of the tracer concentration is monitored at various locations using conductivity probes. Mixing time is then estimated from the time evolution of tracer concentration. Ranade *et al.* (1991) have discussed various definition of mixing time. See Cook *et al.* (1988) for mixing time measurement in gas-liquid stirred reactor.

2.1.2 Single point measurement techniques

- Hot wire / constant temperature anemometry (HWA)

Hot wire anemometry is used in the recent past to measure the liquid velocities in stirred reactors. It is based on the sensing and measurement of the rate of cooling of a fine electrically heated wire. The wire is made up of tungsten, platinum or platinum-iridium. Its diameter is typically of ≈ 5 μm and the length 1-2 mm. All the three components of the velocity vector can be measured by combining several wires on the same probe. Hot wire anemometry is used to measure the characteristics of both steady and unsteady flow fields (see for example, Lu and ju, 1987; Kovacs *et al.*, 2001). Advances in the understanding of the heat transfer of the wire on the velocity, temperature, density and flow angle led to a greater measurement accuracy. However, the hot wire anemometry is an intrusive measurement technique.

- Laser Doppler velocimetry (LDV)

The development of the laser technology resulted in the design of new non-intrusive measurement technique, laser Doppler velocimetry (LDV). The LDV is used extensively to measure the velocities in stirred vessel (see for example, review of Mavros, 2001 and the references cited therein). However most of the measurements were restricted to the single-phase flow. Very few studies have reported the LDV data for gas-liquid stirred vessel (see for example, Mishra and Joshi, 1991; Morud and Hjertager, 1996).

In the LDV technique a laser beam is split and the two resulted coherent beams are made to cross at some point inside the vessel. In the intersection volume, parallel interference fringes are formed. In practice, the frequency of one of the beam is slightly shifted using 'Bragg cell'. This change causes the fringe pattern pulsate at a steady frequency. The presence of the particle in the intersection volume affects this pulsating frequency and registers as Doppler shift frequency. The particle velocity is then estimated from the Doppler shift frequency and the fringe spacing. The velocity component measured by the LDV is the one that lies in the plane of the beams and is normal to the bisector of the two beams. The major limitations of the LDV technique are the need for transparent walls of vessel, transparent fluid and low volume fraction of the dispersed phase (gas or solid). The laser Doppler technique has also been extended – termed as 'phase Doppler anemometry' to measure both liquid velocities and bubble sizes (see for example, Schafer *et al.*, 2000).

- Ultrasonic Doppler velocimetry (UDV)

This is another non-intrusive technique based on the Doppler effect and uses ultrasonic pulse. These transmitted ultrasonic pulses are reflected at the surface s of the minute particles moving with liquids or from the surfaces of the dispersed bubbles. Similar to the LDV measurement the Doppler shift is calculated. This Doppler shift is then used to estimate the velocity component along the beam axis. Ultrasound velocimetry has been used to simultaneously measure the liquid velocity (see for example, Wachter *et al.*, 1996) and gas bubble velocity (see for example, Fischer *et al.*, 1991) in stirred vessel. Fischer *et al.* (1991) has calculated Sauter mean bubble diameter and local gas holdup by using ultrasound Doppler velocimetry.

- Resistivity / conductivity probe

Resistivity or conductivity probes are used to identify the cavity structure present behind the impeller blades and to measure the local gas holdup distribution in gas-liquid stirred vessel (see for example, Bombac *et al.*, 1997). The working of the resistivity probe is based on the difference in the conductivity of the fluids. The local volume fraction of the gas phase, commonly bad conductor of the electricity, is measured by calculating the ratio of the time for which the electrical circuit breaks with the total time of complete time series. However, the resistivity probe is an intrusive technique.

- Capillary suction probe technique

A capillary suction probe (Barigou and Greaves, 1991, 1992; Alves *et al.*, 2002) is used for the measurement of the local bubble size distribution and gas holdup distribution. The basic principle of the technique is to force a representative sample stream from the gas-liquid dispersion through a transparent capillary through a vacuum pump. In the capillary, the bubbles are transformed into cylindrical slugs of equivalent volume. The optical probe that encloses the capillary is designed to measure the velocities and the length of these slugs by the difference of light refraction between two phases. The capillary probes are inexpensive and can be useful for the measurement in opaque dispersion with high gas volume fraction. However, there are certain limitations associated with this technique. The capillary technique is not applicable for small-size vessel, because continuous sampling reduces the dispersion and may disturb the flow.

2.1.3 Ensemble measurement techniques

Ensemble measurement techniques encompass attempts to identify the pseudo two-dimensional flow pattern in stirred vessel. Such patterns are useful for the characterization of the local flow structures, such as trailing vortices and gas accumulation behind impeller blades, present in the reactor.

- High-speed photography

High-speed photography has been used to see the gas cavity structure present behind the impeller blades (see for example, van't Riet and Smith, 1976) and to measure the bubble size distribution in vessel (see for example, Takahashi *et al.*, 1993). For the photographic measurements, the vessel walls and the working fluids are required to be transparent. The photographic studies become difficult for higher values of gas holdup due to the opaqueness of fluid.

- Computer automated radioactive particle tracking (CARPT)

In most of the applications higher values of the fractional gas holdup in the vessel are observed. In those conditions the vessel becomes opaque and limits the use of optical measurement techniques for the measurement of flow. Khopkar *et al.* (2005) has used

CARPT to measure the liquid flow field in the stirred vessel with higher values of the gas holdup. In CARPT measurements, the motion of the neutrally buoyant tracer particle is recorded by an array of scintillated detectors arranged around the vessel. The particle trajectories, measured over a long time, are used to estimate the velocity distribution in the vessel (see for example Rammohan *et al.*, 2001a). Along with the Eulerian information of liquid flow, the CARPT provides the valuable Lagrangian information of the flow. This Lagrangian information was used to infer the different time scales of the liquid fluid dynamics (see for example, Rammohan *et al.*, 2001a; Khopkar *et al.*, 2005). The use of radioactive particle makes this system suitable for the measurement of liquid velocities for high gas loading and in non-transparent vessel. However, this technique cannot provide the information of the flow around the impeller blades.

- Particle image velocimetry (PIV)

PIV is the natural extension of the simple photographic recording of the streaks of particles moving in a stirred vessel. Pictures of the plane cutting through the vessel, illuminated by a powerful light source, are taken at short time intervals. Analyzing the displacement of the each particle in the time between two consecutive frames yields the 2-D velocity. If sufficient seeding particles are present, then the accurate map of the flow in the illuminated plane is obtained. For stirred vessels, image correlation methods are used to determine the individual particle vectors. Because of whole field technique, the PIV can be use to study the trailing vortices and the gas accumulation behind the impeller blades (see for example Deen *et al.*, 2002; Khopkar *et al.*, 2003). One interesting feature of PIV is that each recorded frame represents a 'freeze or snapshot' of the flow for particular time. The time averaging of the consecutive maps generate the flow map, which is characteristic of the impeller and vessel configuration. However, each frame is a transient image of the flow. The accuracy of PIV system is dependant on the overall gas holdup value. Deen *et al.* (2001) concluded that to obtain an accuracy of 90%, one has to keep the total gas holdup value less than 5 %. This limitation of PIV system compels one to carry out measurements with low gas loading.

- Tomography techniques

Tomography techniques are widely used to measure the spatial distribution of phase volume fractions. Measurements are performed at various angular positions and the

average values of the property are obtained over the corresponding diameter. By using the reconstruction algorithms, the acquired signals are then analyzed to provide the phase volume fraction image on a cross-section of the vessel. Different types of tomographic systems have been used, for example γ- or X-ray tomography and electrical resistance tomography. The tomography techniques are widely used to measure the time-averaged holdup profiles and quantitatively measure the liquid phase mixing in process equipment (for example, Wang *et al.*, 2000; Veera *et al.*, 2001).

- Laser induce fluorescence (LIF)

Laser induced fluorescence method is based on the laser sheet visualization of the fluid flows and subsequent image processing. This technique has been developed to understand the mixing process occurring in the stirred reactor. The method consists of the measurement of the fluorescence intensity of a tracer (for example rhodamine B) excited by a thin planer laser sheet and transforming it into an instantaneous concentration field of the tracer. This allows the characterization of the mixing in a plane of the flow illuminated by the laser sheet. This technique provides appreciable information of the mixing by permitting visualization of the coherent mixing structures present in the reactor (see for example Guillard *et al.*, 2000; Distelhoff and Marquis, 2000).

2.2 Present Work

In gas-liquid stirred vessel, different gas flow regimes are present depending upon the impeller dimensions, rotational speed and volumetric gas flow rate. In the past, different experimental techniques have been used to identify the prevailing flow regimes. Though these techniques have identified the flow regimes in gas-liquid stirred vessel, those techniques have been intrusive in nature and therefore cannot be extended to industrial scale reactor. Moreover, the available correlations do not include the physical properties of the working fluids and limits their application. Under such circumstances pressure fluctuations and torque fluctuations offer a simple, cost effective and robust measurement techniques. In the present work, we have therefore used wall pressure and torque fluctuations to characterize the gas-liquid flows in stirred vessel. The mixing time measurements were also carried out to confirm the information of time scale obtained from the wall pressure fluctuations.

Chapter 3

WALL PRESSURE AND TORQUE FLUCTUATION MEASUREMENTS

3.1 Introduction

Gas dispersion in a gas-liquid stirred reactor is a complex process and the fundamental understanding is still underdeveloped. The estimation of the quality of gas dispersion, cavity formation behind the impeller blades and the impeller flooding are of great interest. Significant research efforts have been spent on the understanding of these key issues for gas-liquid flows in stirred reactors. However, the focus of most of the studies has been on developing flow regime maps and design correlations. Applicability of the developed flow regime maps to industrial systems and the question of whether the intended flow regime is realized in the actual operation and whether this can be determined on-line are of great interest but are not well studied. In the present study, an attempt has been made to develop methods for on-line characterization of the various flow regimes and other key fluid dynamic characteristics of gas-liquid stirred reactors.

In a stirred reactor, the flow generated by the rotating impeller blades interacts with the stationary baffles and generates a three-dimensional rotating and complex flow. The liquid flowing over the upper and lower edges of the impeller blades interact with each other and form trailing vortices behind the impeller blades. In a gas-liquid stirred reactor, the sparged gas interacts with these vortices and gets accumulated in the low-pressure region associated with the vortex core. The accumulated gas forms gas pockets "*commonly termed as gas cavities"* behind the impeller blades. The accumulated gas exits from the cavities in the form of bubbles sheared from the cavity tips. The bubbles exiting the cavity are dispersed in the bulk region by convection. A number of experimental studies (see for example, Van't Riet and Smith, 1973; Bruijn *et al.*, 1974; Lu and Ju, 1989; Bombac *et al.*, 1997) has shown that multi-bladed impellers may support ventilated cavities of different shapes on different impeller blade shapes. The different shapes are believed to arise from uneven distribution of gas between blades due to local variations in hydrodynamic conditions and pressure distributions in the flow field. In general, the form and configuration of gas-filled cavity structures are dependent on gas flow rate and impeller details (type, size, number of blades and speed).

The size and shape of these cavities were used to differentiate the fluid dynamic conditions present in an aerated reactor into different gas flow regimes. For example, Nienow *et al.* (1985) and Warmoeskerken and Smith (1985) presented a more detailed flow regime map for Rushton turbine based on cavity structure developed behind impeller blades (see Figure 3.1). These gas-filled cavity structures control impeller pumping, energy dissipation and spatial gas-phase distribution in the reactor. Therefore, the identification of the prevailing flow regime is important for the selection of appropriate operating conditions.

3.1.1 Previous work

Different techniques and some correlations (summarized in Table 3.1 and 3.2) are available to identify the flow regime transitions. All the methods so far suggested, have shown to capture the regime transition successfully in laboratory reactors, but cannot be extended to the industrial scale reactor. For instance, the photographic analysis of cavity structure requires transparent reactor. However, the experimental techniques employed with micro-impeller, constant temperature anemometry or resistivity probe are intrusive and difficult to use with industrial reactors. Sutter *et al.* (1987) used hydrophones to identify the '3-3 structure' for the Rushton turbine. The hydrophone method successfully captured the '3-3' structure and can be used for any size of reactor. The disadvantage associated with the technique was that the hydrophones were pasted on or placed near the impeller blades and hence this makes it difficult to use in industrial reactor. The available correlations are widely used in the actual practice but the uncertainty is apparent. These correlations have been tested with a limited range of working fluids and depend upon the geometric characteristics of the reactor and of the turbine.

To overcome some of these limitations, Pagalianti *et al.* (2000) made an attempt to characterize the gas-liquid flows in a stirred reactor by means of statistical methods such as nonlinear time series analysis from the output signal of the nonintrusive probes. Pagalianti *et al.* (2000) identified the flooding/loading transition by using time series analysis of the measured impedance. The proposed technique was limited only to identify a flooding/loading transition, which is clear and sharp more so than the other

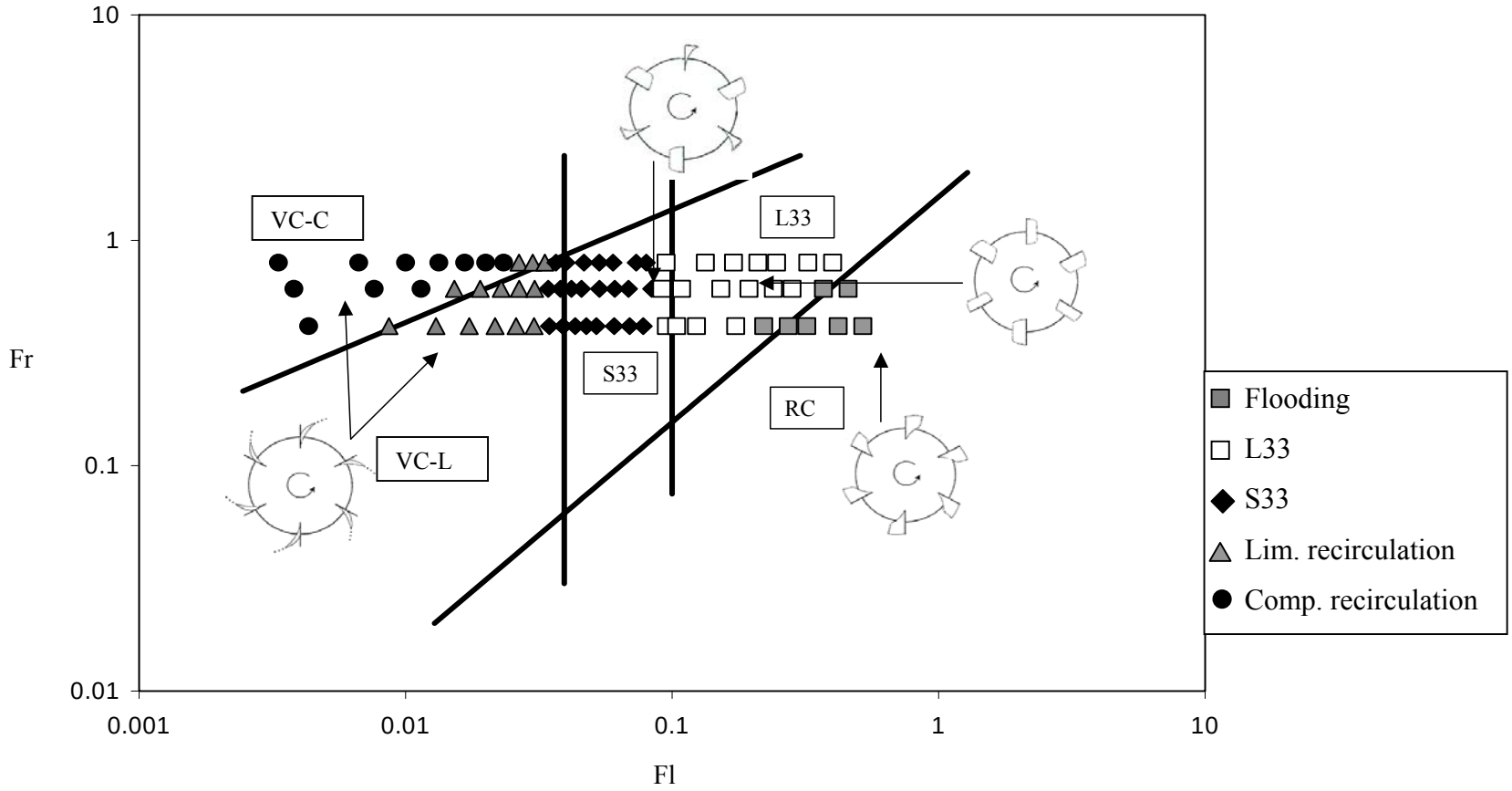

Figure 3.1: Flow Regime Map for Rushton Turbine based on Cavity Structures Developed behind Impeller Blades

(Flow regime map from Warmoeskerken and Smith, 1985)

Table 3.1: Review of Previous Work on Identification of Flow Regime Transition

Authors	**Measurement technique**	Impeller type	Flow regime identification criteria
Van't Riet and Smith (1973)	Photography	Rushton turbine	Cavity shape and structure
Bruijn *et al.* (1974)	Power dissipation	Rushton turbine	Ratio of gassed to ungassed power against the gas flow rate
Nienow *et al.* (1977)	Power dissipation	Rushton turbine	Ratio of gassed to ungassed power against the gas flow rate
Loiseau *et al.* (1977)	Power dissipation and overall gas holdup	Rushton turbine	Ratio of gassed to ungassed power against the gas flow rate and variation of overall gas holdup with impeller rotational speed
Kuboi *et al.* (1983)	Photography	Rushton turbine	Cavity shape and structure
Chapman *et al.* (1983)	Power dissipation, instantaneous torque fluctuations	Rushton turbine, 4-blade pitched turbine (down- as well as up-pumping)	Ratio of gassed to ungassed power against the gas flow rate, variation of overall gas holdup
Ismail *et al.* (1984)	Power dissipation	Disc turbine (with different number of blades)	Ratio of gassed to ungassed power against the gas flow rate
Warmoeskerken and Smith (1985)	Micro-impeller, photography, average power dissipation	Rushton turbine	Cavity shape and structure, Ratio of gassed to ungassed power against the gas flow rate, liquid radial outflow near the impeller
Sutter *et al.* (1987)	Hydrophones	Rushton turbine	Power spectrum of sound wave time series
Bujalski *et al.* (1990)	Power dissipation	6-Blade down- as well as up-pumping pitched turbine	Ratio of gassed to ungassed power against the gas flow rate

Table 3.1: Review of Previous Work on Identification of Flow Regime Transition

Lu and Ju (1989)	Constant temperature anemometry	Rushton turbine	Cavity structure and size
Warmoeskerken and Smith (1989)	Power dissipation	Smith turbine	Ratio of gassed to ungassed power against the gas flow rate
Saito *et al.* (1992)	Power dissipation	Scaba turbine	Ratio of gassed to ungassed power against the gas flow rate
Rewatkar and Joshi (1993)	Power dissipation	6-Blade down-pumping pitched turbine	Ratio of gassed to ungassed power against the gas flow rate
Sharma *et al.* (1993)	Power dissipation	Rushton turbine, disc turbine (8 blade), 4-blade down- pumping pitched turbine, propeller	Ratio of gassed to ungassed power against the gas flow rate and torque fluctuations
Bombac *et al.* (1997)	Resistivity probe	Rushton turbine	Power spectrum of conductivity time series
Paglianti *et al.* (2000)	Conductance probe	Rushton turbine	Statistical properties of conductance time series

Table 3.2: Available Empirical Correlations for Flow Regime Transition and Power Dissipation for Rushton Turbine

Flow Regime Transition	**Empirical Correlation** (Nienow *et al.*, 1985 and Warmoeskerken and Smith, 1987)	**Power Dissipation** (Smith *et al.*, 1987)
Fully recirculation regime to limited recirculation regime	$Fl_{CD} = 13Fr^2(T/D)^{-5}$	$Pg/P = 1 - 16.7 * Fl * Fr^{0.35}$
Limited recirculation to small 3-3 cavity regime (S33)	$Fl_{S3-3} = 3.8\times10^{-3}\left(\mathrm{Re}^2/Fr\right)^{0.07}(T/D)^{0.5}$	$Pg/P = 1 - 16.7 * Fl * Fr^{0.35}$
Small 3-3 cavity regime (S33) to large 3-3 cavity regime (L33)	$Fl_{L3\text{-}3} = 0.1$	$Pg/P = B - 0.1\left(\frac{A-B}{Fl-0.1}\right) + \frac{(A-B)Fl}{Fl-0.1}$ $A = 1 - 17 * Fl * Fr^{0.35}$ $B = 0.27 + 0.022 * Fr^{-1}$
Large 3-3 cavity regime (L33) to flooding regime	$Fl_F = 30Fr(T/D)^{-3.5}$	$Pg/P = 0.27 + 0.022Fr^{-1}$

regime transitions. However, the transitions between other flow regimes is not that clear and sharp and therefore could not be identified by using a conductance method (Pagalianti *et al.*, 2000). The detail review of the previous studies shows a need to develop new nonintrusive tools with a simple methodology to identify the prevailing flow regimes in gas-liquid stirred reactors. In the present study such an attempt has been made.

3.1.2 Present contribution

The present work was carried out with an objective to characterize the fluid dynamics of gas dispersion in a stirred reactor using nonintrusive techniques such as torque measurement and wall pressure sensors. Measurements were carried out for the Rushton turbine, the Smith turbine (Van't Riet *et al.*, 1976) and the 6-blade down pumping pitched blade turbine (PBTD). An attempt was made to use the variation in instantaneous torque fluctuations to identify the prevailing flow regimes. In the latter part of the work, the analysis of wall pressure fluctuations has been carried out to develop criteria for the identification of the prevailing flow regimes. An attempt has also been made to extract the information on the relevant time scales of the fluid dynamics from the wall pressure fluctuations. The work is organized as follows. The details about the experimental setup, pressure and torque sensors are discussed in the next section. The brief discussion on time series analysis used in the present study and the results and the conclusions of the present study are discussed in the subsequent sections.

3.2 Experimental Setup

The measurements were carried out in a fully baffled, flat bottom acrylic reactor (of diameter, T = 0.7 m and liquid height, H = 0.7 m). A schematic diagram of the experimental setup is shown in Figure 3.2. Four baffles of width T/10 were mounted diametrically opposite and perpendicular to the reactor wall. The shaft of the impeller (d_s = 0.032m) was concentric with the axis of the reactor and was extended till the impeller off-bottom clearance. Rushton and Smith turbines (of diameter, D = 0.2 m; impeller blade width, W = D/4 and impeller blade height, B = D/5) and the 6-blade

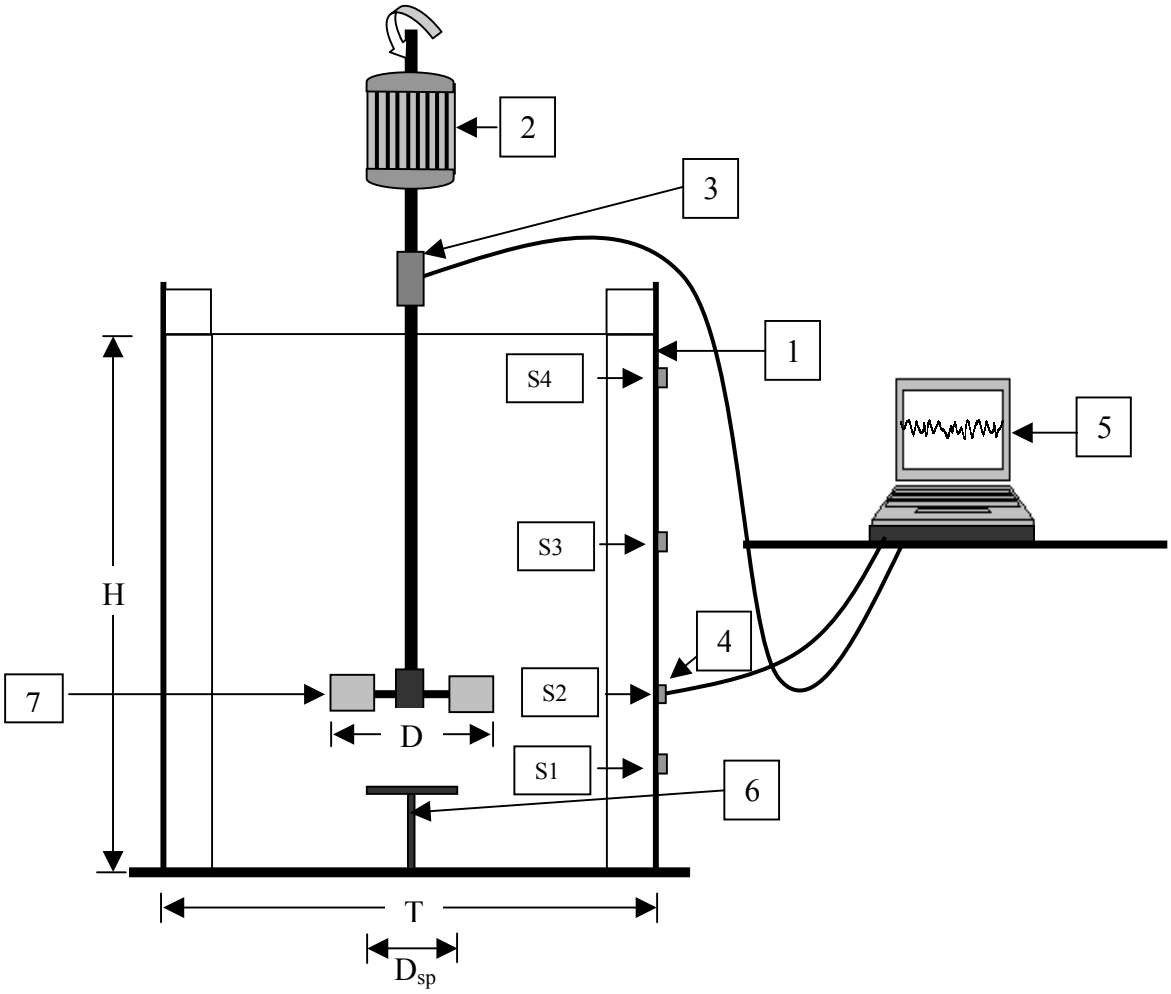

1. Vessel, T = H= 0.7 m
2. Motor
3. Torque sensor with telemetry system
4. Pressure transducer, Si
5. Data acquisition system with personal computer
6. Ring sparger, D_{sp}= 0.16 m, hole dia. = 1 mm
7. Impeller, D = 0.2 m
8. Sensor locations: 0.16 m, 0.23 m, 0.46 m and 0.65 m, all the dimensions are measured from bottom of the vessel

Figure 3.2: Schematic Diagram of the Experimental Set-up

(a) Rushton turbine

(b) Smith turbine

(c) Pitched blade turbine

Figure 3.3: Impellers Used in the Present Study

down pumping pitched blade turbine (of diameter, D = 0.2 m, impeller blade height, B = D/5) were used during experiments (see Figure 3.3). The impeller off-bottom clearance was (C = T/3) measured from the bottom of the reactor to the center of the impeller disc for Rushton and Smith turbines and mid of impeller blade height for pitched blade turbine. The gas was introduced in the reactor through a ring sparger (of diameter, D_{sp} = 0.16 m, 12 holes with 1 mm diameter) and it was located at 0.16 m from the bottom of the reactor. The working fluids were water and compressed air in all the experiments. The measurements were carried out for three values of Froude number 0.6, 0.85 and 1.03 for Rushton turbine (power consumption varied between 0.96 kW/m^3 to 2.2 kW/m^3 for single-phase flow), for two values of Froude numbers (0.41 and 0.6) for the Smith turbine and for four values of Froude number (0.41, 0.5, 0.85 and 1.12) for the pitched blade turbine. The gas flow number was varied between 0 and 0.37 for Rushton turbine, 0 and 0.44 for Smith turbine and 0 and 0.24 for pitched blade turbine. The selected operating conditions for all three turbines represent all the key flow regimes occurring in gas-liquid stirred reactors.

Torque sensor (with a range of 0 to 30 N-m and sensitivity of 66.66 mV/N-m) was used (of Mechanica Systems, India) to measure instantaneous torque values. The torque sensor was a simple Whetstone Bridge of four strain gauges pasted on soft steel metal rod. The strain gauges were excited by a constant voltage 12V supplied through the slip ring. The sensor measured the instantaneous strain values developed in shaft. The measured strain values were then transmitted to data acquisition system in the form of a voltage signal via telemetry system through the same slip ring. Pressure transducer (with range of ± 34.46 kPa, resolution of 0.000482 kPa and sensitivity of 72.54 mV/kPa) was used (of PCB Piezoelectronics Inc., USA, Model 106B50) to measure the wall pressure fluctuations. The pressure sensor was flush mounted on reactor wall at a height of impeller off-bottom clearance for both the impellers. The transducer was powered by ICP battery unit (PCB Piezoelectronics Inc., USA, Model 480E06), which also acted as an amplifier.

Conductivity measurement method was used to measure the mixing time in a gas-liquid stirred reactor. The conductivity cell (of Electronics India Ltd., India, Model 601E) was used to measure the time history of the passive tracer concentration, of 1 molar salt

solution of volume equal to 1% total reactor volume, at a certain position in the reactor. The measured time history (series) of tracer concentration was first amplified and then transmitted to data acquisition system. Ranade *et al.* (1991) have discussed various ways of calculating mixing time from the time history of the tracer concentration. Following Ranade *et al.* (1991), mixing time in the present study was calculated as the time required for the detector tracer concentration to lie within (± 5%) of the final concentration (C_∞).

The instantaneous torque was measured with a sampling frequency of 400 Hz for 800 seconds. The pressure fluctuations were acquired with a sampling frequency of 400 Hz (around 10 data points for blade passage) and the signal was acquired for 200 seconds. The 200 seconds of sample time corresponds to a minimum of 900 revolutions of impeller, indicating sufficient number of cavity (blade) passages to statistically represent the cavity structure present behind impeller blades. The time histories of tracer concentration values were acquired with a sampling frequency of 50 Hz and the signal was acquired for 50 seconds (more than two times that of observed mixing time). Measurements were always performed in the same manner, starting from low to high impeller speeds with stepwise increase in the gas flow rate at a constant impeller speed. The amplified signal from both the sensors was acquired using a laptop computer with 16-bit A/D PCMCIA converter card and data acquisition software 'dAtagate' (of nCode, UK). The acquired time series of torque and wall pressure fluctuations were analyzed by using in-house code '**A**nalysis of **n**onlinear **T**ime **S**eries, **AnTS**' (Sunthankar and Ranade, 1997). The details of different analysis methods used and the interpretation of the analyzed signal are discussed in the following sections.

3.3 Analysis of Time Series

3.3.1 Torque fluctuations

3.3.1.1 Average power consumption

The power number characterizes an impeller in terms of energy dissipation and is an important factor not only for optimizing energy but also for comparing different

impellers. In the present work, the instantaneous torque fluctuations measured using the torque sensor were long time averaged to calculate the average power consumption of an impeller and subsequently the power number.

$$P = 2\pi N \times \frac{1}{n}\left(\sum_{i=1}^{n} T_i'\right)$$

$$N_P = \frac{P}{\rho N^3 D^5} \tag{3.1}$$

Under aerated condition, the aerated power consumption is usually presented as the aerated to non-aerated power ratio, P_g/P. This allows for the identification of the effect of aeration on the impeller power consumption.

3.3.1.2 RMS value of torque fluctuations

The torque time series shows the wide fluctuations in the instantaneous torque values over the average torque value. To understand the effect of the gas flow rate on the fluctuations of time series, the RMS value of the whole time series was calculated. The root mean square or RMS is a statistical measure of the magnitude of a varying quantity. The RMS value is the mean value and its ratio with the average value of the time series provide the information of the fluctuation of the whole time series over the average value of the time series. The RMS value of the torque fluctuations is calculated as:

$$RMS = \sqrt{\frac{\sum_{i=1}^{n}\left(T'_i - T'_{avg}\right)^2}{n}} \tag{3.2}$$

where T'_{avg} is the time average value of the torque, T'_i is the instantaneous value of torque and n is the number of instantaneous torque values.

3.3.2 Wall pressure fluctuations

The dynamics of fluidized beds and bubble column reactors have been studied using wall pressure fluctuations by several investigators (see for example, Franca *et al.*, 1991; Daw and Halow, 1992; van der Stappen *et al.*, 1993; van den Bleek and Schouten,

1993; Schouten and van den Bleek, 1998; Letzel *et al.*, 1997). They have used the embedding techniques based on Takens (1981) study and applied them to time-delay coordinate expansions to provide a way to reconstruct and characterize the underlying dynamics and ultimately to define a criteria for the regime identification. Drahos *et al.* (1991) proposed a simple parametric method for the purpose of on-line flow pattern identification using the auto-regressive model. The focus was ultimately on correlating properties of the time series by means of a set of scaling exponents. Recently, Briens and Briens (2002) have developed a method to study cycle characteristics of a measured time series. They have used V statistics and P statistics (calculated from Hurst analysis) to detect the flow regime transitions in multiphase systems such as risers, gas-solid and gas-liquid-solid fluidized beds. None of the studies has reported the detailed characterization of gas-liquid flows in stirred reactor to provide information of the underlying fluid dynamics and to define criteria for regime identification. In this study we have made such an attempt.

While acquisition of the data time series, a random external noise or internal (noise associated with the measurement system) noise may get added into the real data. This noise gives rise to some high frequency output signal along with the original data, which may corrupt the analysis. Low pass filter (following the algorithm of Press *et al.*, 1987) was used to remove the high frequency noise from the measured time series. It was ensured that low pass filtering does not remove any significant useful information in the signal (the differences in root mean square, RMS, values of filtered and unfiltered series were less than 1-2%). The low pass frequency is calculated as:

$$\text{Low pass frequency} = \text{Sampling frequency/smoothening parameter} \qquad (3.3)$$

Using the Fourier transform the measured time series was converted into array of frequencies. The frequencies higher than the low pass frequency were neglected and a filtered time series was obtained by inversing the Fourier transformation.

Prior to performing the statistical analysis of the experimentally measured time series, the measured time series was normalized with average absolute deviation. The standardized time series with data points y_i with respect to average absolute deviation as:

$$Average(\bar{x}) = \frac{1}{n}\sum_{i=1}^{n} x_i$$

$$Abs.Dev.(\Delta x) = \frac{1}{n}\sum_{i=1}^{n} |x_i - \bar{x}| \qquad (3.4)$$

$$y_i = \frac{x_i - \bar{x}}{\Delta x}$$

Different methods are available to identify the dominant time scales of the flow. The power spectrum analysis of the measured time series is one of the most commonly used and the simplest method to identify the dominant time scales. The power spectral density function (PSD) was calculated using standard Fast Fourier Transform (FFT) algorithm (Press *et al.*, 1987). The power spectrum indicates the relative strengths of different frequencies. For n point sample function of x(t), the FFT is calculated as:

$$x = \sum_{j=0}^{n-1} x_j e^{\frac{2\pi ijk}{n}} \qquad k = 0,.....,n-1 \qquad (3.5)$$

However, in many cases it is not possible to identify the single dominant frequency from the power spectrum. In such situations the Hurst analysis can be used to identify the dominant frequency of the time series. In rescaled range analysis, the time series is divided into number of intervals of length τ and the range, R (cumulative range of deviations from the mean) and the standard deviation, S are calculated for the time lag τ (refer Hurst, 1951 for more details). The empirical relations defining the Hurst Exponent (H) is given as:

$$\frac{R}{S} = \tau^H \qquad (3.6)$$

where R, is the cumulative range of deviations from the mean for the time lag τ and S is the standard deviation (Feder, 1988). A rescaled range is calculated for each interval. The average of the rescaled ranges $(R/S)_\tau$ can then be obtained for all the intervals of length τ. Changing the value of the interval length τ and plotting $\ln(R/S)_\tau$ as a function of $\ln(\tau)$ gives a curve whose slope is the Hurst exponent H. If the time series exhibits cyclic behavior then the Hurst exponent H changes at certain values of the interval length τ and the plot of ln (R/S) vs. ln (τ) is not a straight line (Peter, 1994). The break in this plot corresponds to the dominant frequency of the cycle.

It is not always easy to identify the dominant time scale using such analysis. Two variants, namely V Statistics (Peters, 1994) and P statistics (Briens and Briens, 2002) have been proposed to facilitate the detection of the characteristics time scales. In this work, we have used P statistics, which is defined as:

$$P_\tau = \frac{(R/S)_\tau}{\tau^\gamma} \tag{3.7}$$

where γ is calculated as:

$$\gamma = \frac{\text{Maximum P statistics – maximum of P statistics at the minimum and maximum } \tau}{\text{Maximum of P statistics at the minimum and maximum } \tau} \tag{3.8}$$

3.4 Results and Discussion

3.4.1 Torque fluctuations

3.4.1.1 Power consumption of impellers

The torque sensor was first calibrated using the test facility to confirm the linear dependence of torque on output voltage and to ensure the reproducibility in the measured voltage values for the same applied torque. The sensor was then used to measure the power dissipated by an impeller for single-phase system. The measurements were carried out for the Rushton, Smith and pitched blade turbines at four impeller speeds. The instantaneous torque values were found to fluctuate significantly about the average torque value. For the single-phase flow, the instantaneous torque value fluctuates between (maximum) ± 10% for Rushton turbine, (maximum) ± 15% for Smith turbine and (maximum) ± 15% for pitched blade turbine. The power numbers were calculated from the measured average torque. The experimentally measured power number for Rushton turbine was 5.1 (± 0.25). The experimentally measured value of power number of Rushton turbine was in good agreement with those reported in the literature (see for example Bertrand *et al.*, 1980; reported range of power number is from 5.0 to 6.0). Similarly the power numbers of Smith turbine and down pumping pitched blade turbine were obtained as 2.9 (± 0.15)

and 1.6 (± 0.10) respectively. The experimentally measured value of power number was in good agreement with the values reported by (van't Riet *et al.*, 1976; Bakker, 1992 and Jaworski *et al.*, 1991). The torque sensor was then used to measure the power consumption in the presence of gas.

The introduction of gas decreases impeller pumping and energy dissipation capacity. The fractional reduction in the power dissipated by an impeller with an increase in gas flow rate for a constant impeller speed for Rushton turbine impeller (the ratio of P_g/P) is shown in Figure 3.4a. The comparison of measured fractional reduction in the impeller power with the multiple correlations proposed by Smith *et al.* (1987) is shown in Figure 3.4a (see Table 3.2 for correlations). Smith *et al.* (1987) have proposed empirical correlations to calculate the power dissipated by Rushton turbine operating in different flow regimes. It can be seen from Figure 3.4a that the measured experimental data agrees with the correlations. In the flooding regime (for Froude number equal to 0.6) an increase in the power dissipation by the impeller was observed. Nienow *et al.* (1990) have also reported similar observations in case of the flooding regime.

The power dissipated by Smith turbine in an aerated stirred reactor is shown in Figure 3.4b. It can be seen from Figure 3.4b that the power reduction curve for Smith turbine is significantly different than that of the Rushton turbine. The power curve shows a small increase in the power dissipation for low gassing rates compared to a single-phase flow. Beyond certain gas flow rate, the power dissipation slowly decreases with increasing gas flow rate. The explanation of the observed increase in the power value for low gassing rate is not yet clearly understood. However, the modification in the rolling vortices caused, due to the blade shape and gas accumulation may be the possible reason for the observed increase in the energy dissipation for low gassing rate. In the flooding regime (for Froude number equal to 0.41) a sharp increase in the power dissipation by an impeller was observed. It can be seen that fractional reduction in the power consumption due to gas flow rate is much lower for the case of Smith turbine than the Rushton turbine. Also, for the same impeller speed, the Smith turbine handles more gas compared to Rushton turbine before reaching the flooding condition. Unlike the Rushton turbine, the Smith turbine shows hysterisis in the power dissipation

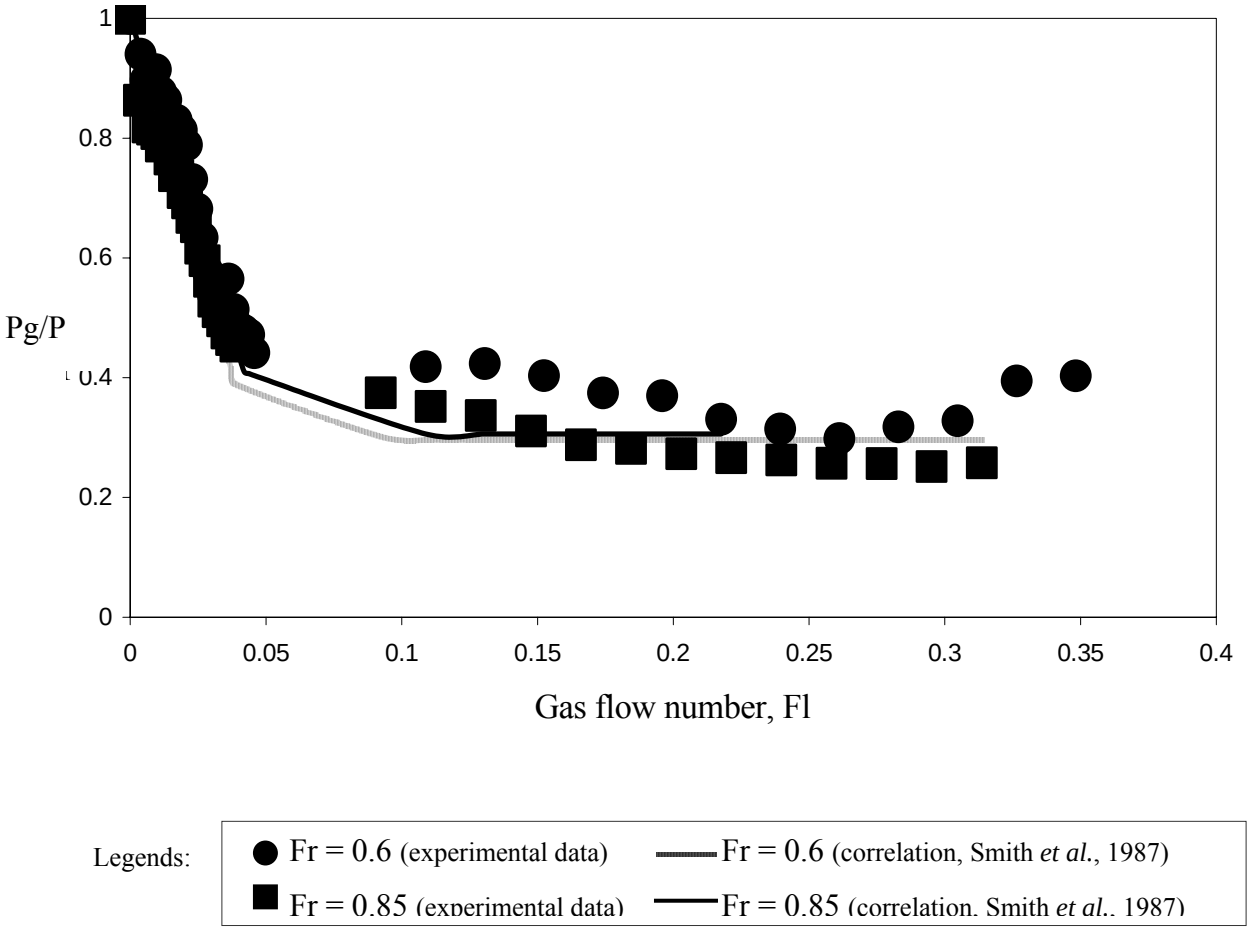

(a) Rushton turbine

Figure 3.4: Experimentally Measured Data of Power Dissipated by an Impeller in an Aerated Conditions

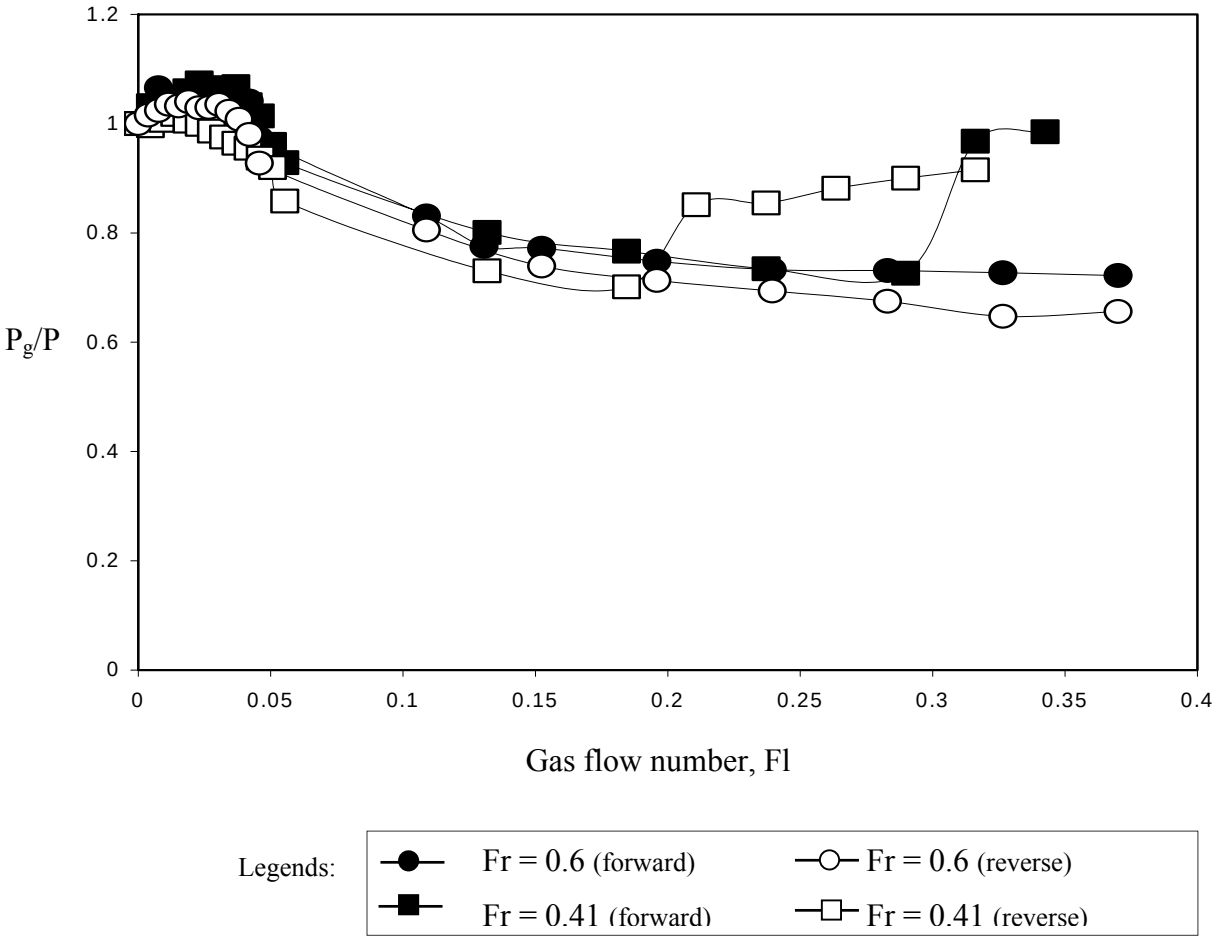

(b) Smith turbine

Figure 3.4: Experimentally Measured Data of Power Dissipated by an Impeller in an Aerated Conditions

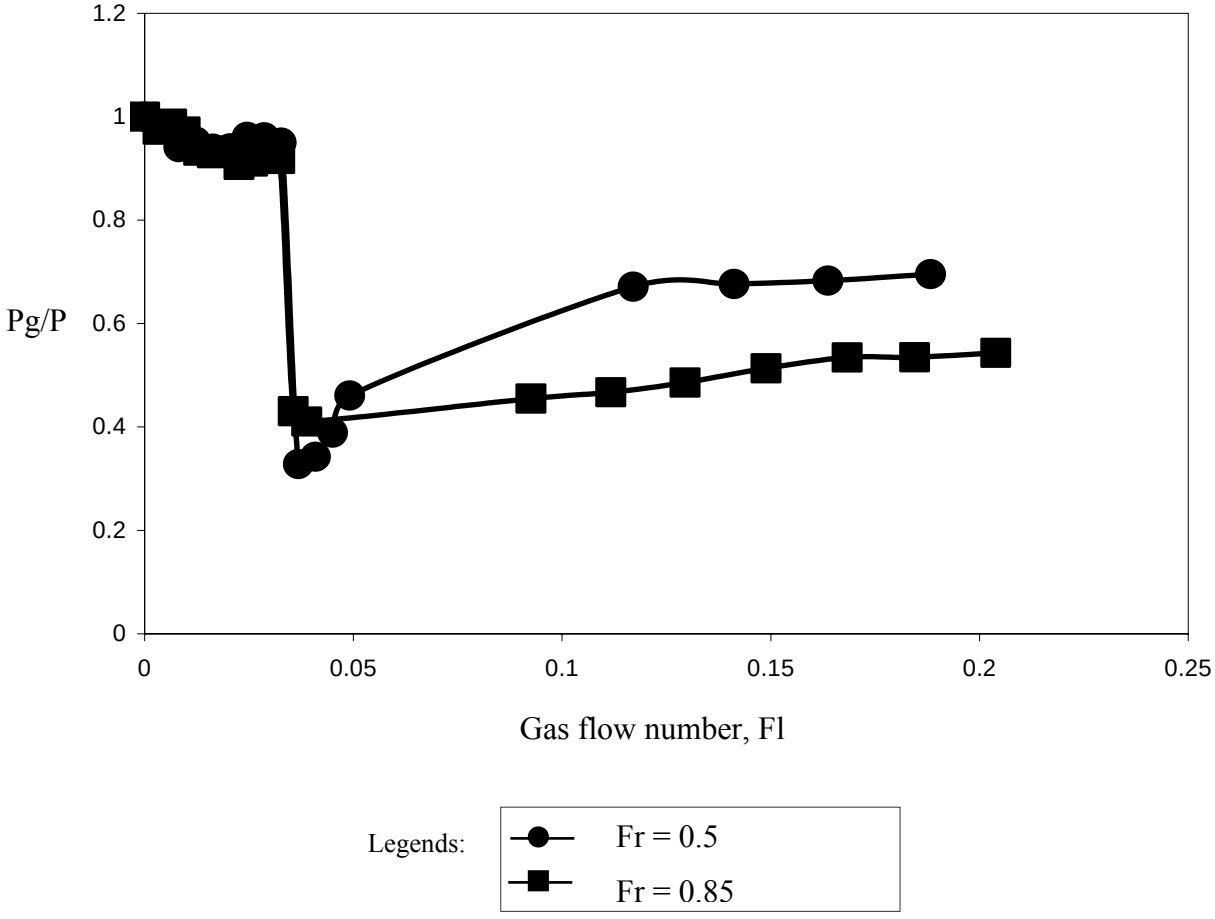

(c) Pitched blade turbine: down- pumping

Figure 3.4: Experimentally Measured Data of Power Dissipated by an Impeller in an Aerated Conditions

variation with gas flow rate. It can be seen from Figure 3.4b that the power reduction curves are distinctly different when the measurements were taken in the forward direction (for same impeller speed the gas flow rate was increased from lower to higher value) and in the backward direction (gas flow rate was decreased from higher to lower value). The flooding-loading transition also found to shift towards the left side (for lower gassing rate) during the measurement in the backward direction. Warmoskerken and Smith (1989) have the reported similar results earlier. This observed hysterisis in the flooding-loading transition was possibly due to inability of an impeller to transform the established large ragged cavities to 3-3 cavity structure.

The effect of aeration on power dissipated by 6-blade down pumping pitched blade turbine is shown in Figure 3.4c. The measured power data show a trend similar to that reported by Rewatkar and Joshi (1993). At low gas flow rates the power dissipated by the impeller was almost the same as single-phase flow (for complete dispersion and recirculation regime). As gas flow rate was increased at a constant impeller speed, the flow exhibited instability and a sharp reduction in the power dissipation by the impeller was observed. The power dissipation curve reaches a minimum value with wide fluctuations in the instantaneous torque values. Rewatkar and Joshi (1993) defined these dispersion conditions as cavity formation regime. The observed operating conditions for the cavity formation regimes are comparable with the range of operating conditions reported by Rewatkar and Joshi (1993). With further increase in the gas flow rate the impeller is unable to disperse the gas in the bulk liquid. Such flow condition in the reactor is commonly known as a flooding regime. In the flooding regime, the liquid recirculation due to the upward rising gas gets generated and is significant. For the case of down pumping impeller, the direction of this liquid circulation is against the direction of the impeller pumping action. This causes an increase in the power consumption in the flooding regime compared to the cavity formation regime (Rewatkar and Joshi, 1993).

The nature of the power reduction curve for down pumping pitched blade turbine made it possible to identify the flow regime transitions occurring in gas-liquid stirred reactors. However for the Rushton and Smith turbines, the drop in the power was more gradual and it was not possible to identify the flow regime transitions other than loading -flooding (large 33 cavity-flooding transition, which is quite sharp) from the

fractional power dissipation curves. The torque time series shows wide fluctuation of the instantaneous torque values over the average torque values, and these fluctuations increase with increase an in the aeration rate. Therefore, the RMS values of torque fluctuations were examined for the different flow regimes.

3.4.1.2 RMS value of torque fluctuations

The measured RMS values of the torque fluctuations for Rushton turbine are shown in Figure 3.5a as a function of gas flow rate. It can be seen from Figure 3.5a that the intensity of fluctuations for low aeration rate was observed to be comparable with the situation of no gas flow. Further increase in the aeration rate leads to loading and subsequently the flooding regime in the reactor. The intensity of fluctuations markedly increases with the aeration rate in the loading regime and show almost constant intensity in the flooding regime. Similarly, the RMS values of torque fluctuations for Smith turbine are shown in Figure 3.5b as a function of gas flow rate. It has been observed that similar to Rushton turbine, in the case of the Smith turbine, RMS values of torque fluctuations in the presence of gas were not found to be different than those observed with the single-phase flow. This indicated that both of these impellers were able to realize stable gas-liquid flows. In contrast to these, in the case of the pitched blade turbine, the instantaneous torque was found to fluctuate widely over the average value in the cavity formation regime. Such wide fluctuations in the torque values are not desirable and may cause structural problems to impeller blades, shaft and other internals.

The measured RMS values of torque fluctuations are shown in Figure 3.5c as a function of gas flow rate. The intensity of torque fluctuations increases with an increase in the gas flow rate for all the regimes. However, a sharp increase in the intensity of fluctuations was observed in the cavity formation regime. The visual examination of the torque-time series shows the oscillation of whole time series over the average torque value. This oscillation of the whole torque time series was due to simultaneous formation and the breakage of the large gas cavities behind impeller blades. In the presence of large cavities, the power dissipated by an impeller reached the minimum value. When these large cavities were sheared away, the power dissipation by the

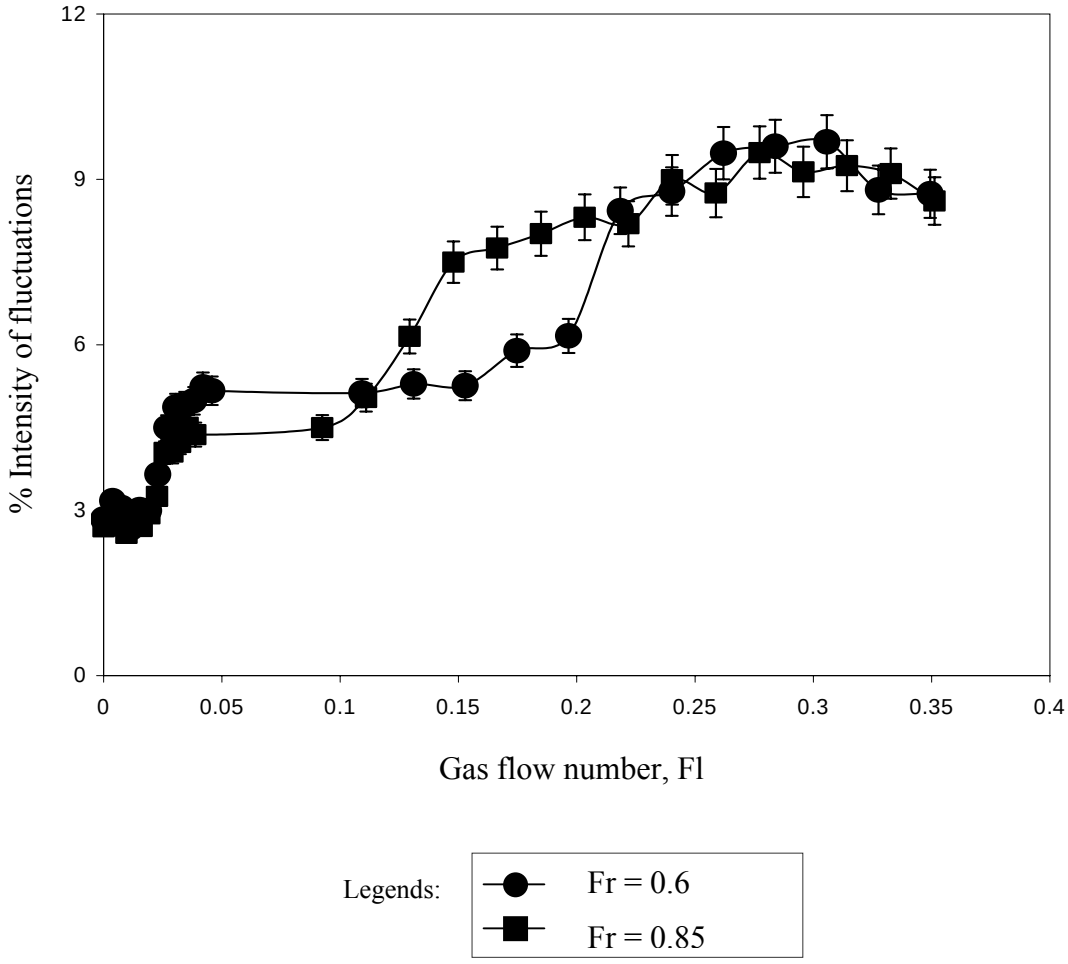

(a) Rushton turbine

Figure 3.5: Experimentally Measured RMS Value of Torque Fluctuations in an Aerated Conditions

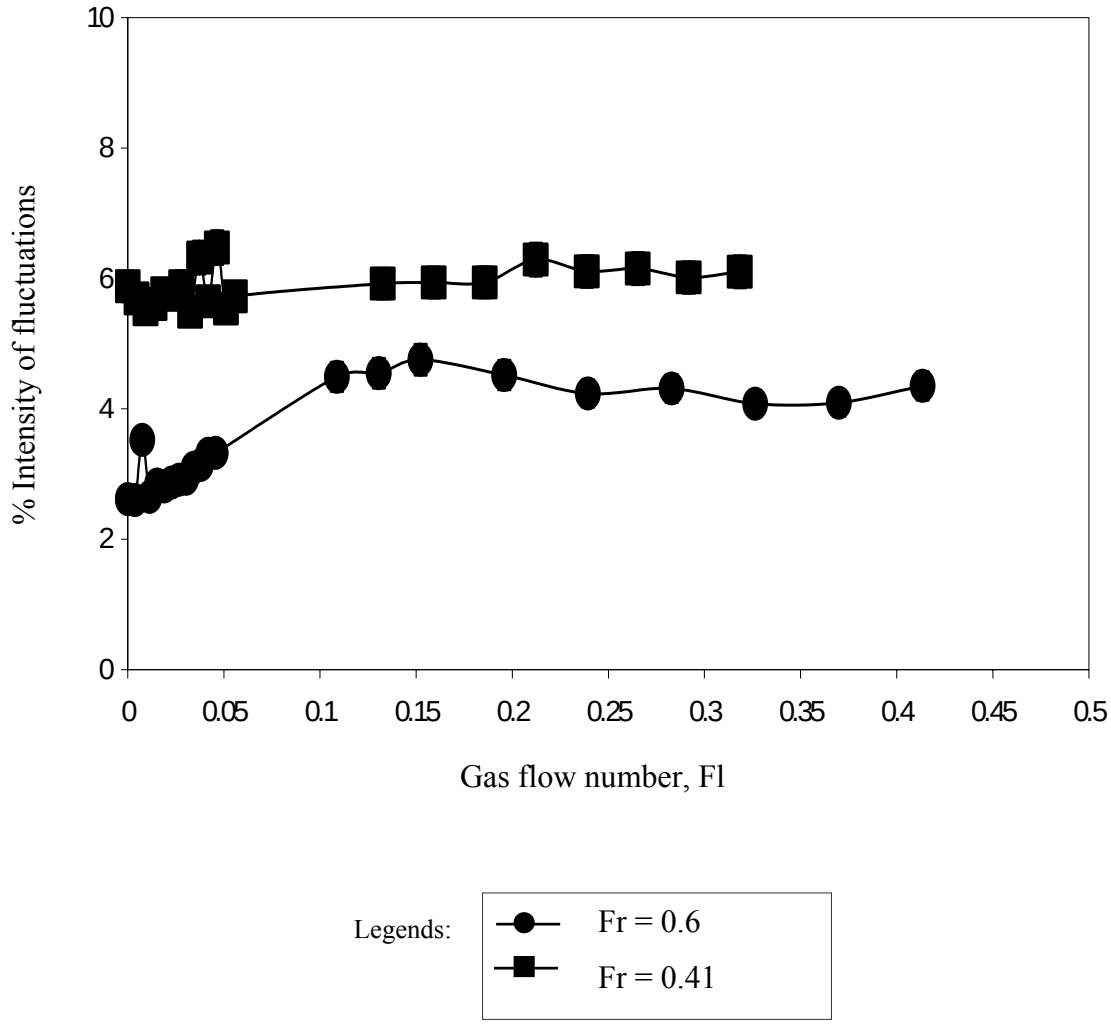

(b) Smith turbine

Figure 3.5: Experimentally Measured RMS Value of Torque Fluctuations in an Aerated Conditions

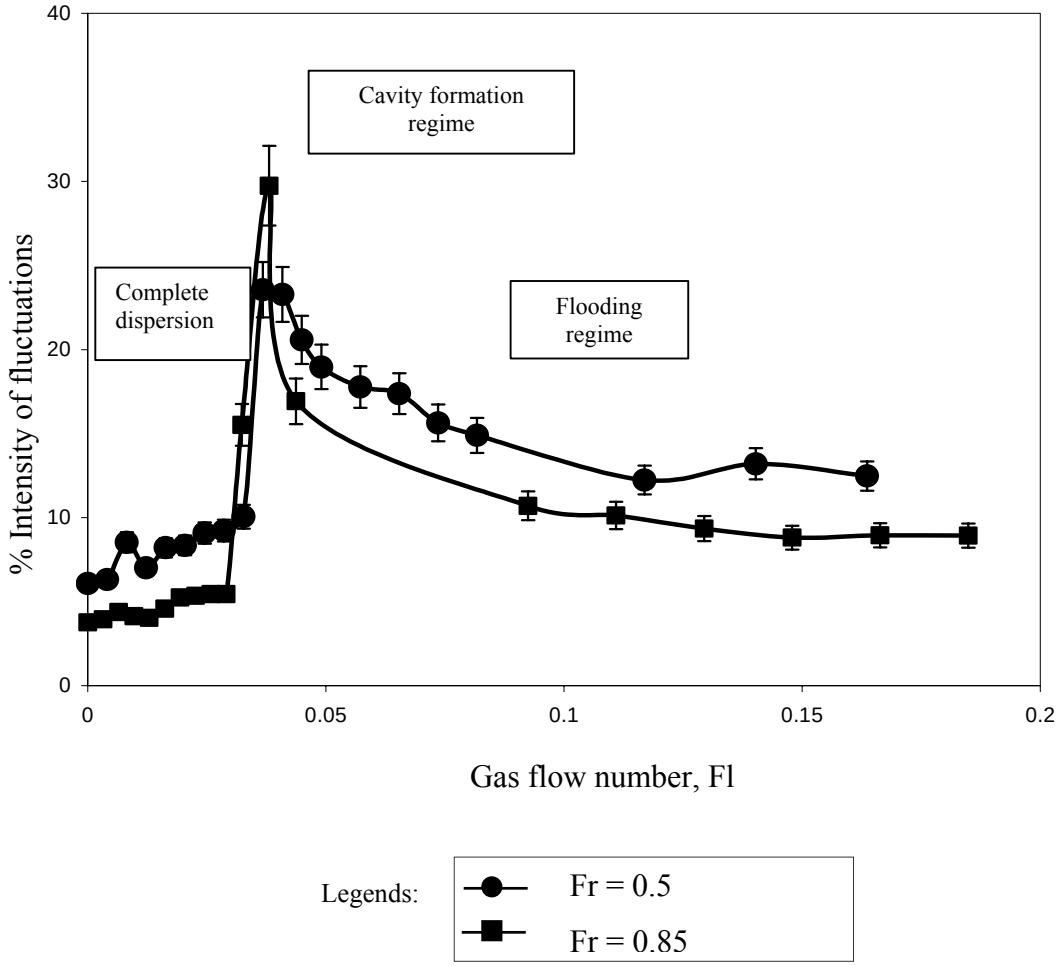

(c) Pitched blade turbine: down- pumping

Figure 3.5: Experimentally Measured RMS Value of Torque Fluctuations in an Aerated Conditions

impeller suddenly increases. Such a sharp increase in the RMS torque can be used to identify the cavity formation regime. With further increase in the gas flow rate the flow conditions in the reactor are transformed into flooding regime. In the flooding regime, RMS torque values are much smaller than the cavity formation regime but are higher than the complete dispersion regime. Though some indication of flow regimes can be obtained based on the RMS torque values of the pitched blade turbines, no clear information about the cavity structure present behind the impeller blades could be obtained from the RMS values. An attempt was made to obtain some information about the cavity structures behind the impeller blades by analyzing the wall pressure fluctuations.

3.4.2 Pressure fluctuations

The pressure field around the impeller blades is linked with the cavity structure present behind the impeller blades. The identification of the change in the pressure field can be related to the change in the cavity structure behind the impeller blades. Therefore, a change in the statistical properties of the pressure fluctuations was used to set up a criterion for the identification of flow regimes.

The preliminary experiments were carried out to understand the influence of the sensor location on acquired data and analysis. The measurements were carried out for four different sensor locations (different axial heights measured from the reactor bottom, see Figure 3.2 for sensor locations) at different gas flow rates with the Rushton turbine. It was observed that the acquired wall pressure fluctuations from the first three sensor positions (s1, s2 and s3) could clearly capture all the flow regimes occurring in gas-liquid reactors. The signal acquired by the fourth sensor (s4), located near the top liquid surface could not capture the transition from fully recirculation to a limited recirculation of gas in the reactor. Thus it is recommended to position wall pressure sensor between the distances equal to impeller off-bottom clearance in both directions measured from the impeller center plane. However, considering the possible extension of the present methodology to multiple impellers, we have mounted the pressure sensor at the distance equal to impeller off-bottom clearance for the subsequent experimental measurements.

The pressure signal was sampled with a frequency 'f_s' equal to 400 Hz and 2^{16} points (more than 900 revolutions of impeller, sufficient to statistically capture and represent the cavity structure present behind impeller blades) constituting a complete time series. The maximum frequency with which the gas filled cavity rotates in the reactor is described by the blade passage frequency. The preliminary analyses of the power spectrum suggested that the frequencies till blade passage frequency were sufficient to identify the prevailing flow regimes. In the present work, the maximum impeller rotational speed equal to 465 rpm was used corresponding to the blade passage frequency of 46.5 Hz. In the present study the low pass filter of frequency equal to 50 Hz was selected for filtering the experimentally measured time series. No significant loss (less than 7% of the total energy) in the information was observed due to filtering. The power spectrum distribution of the pressure time series was then studied.

3.4.2.1 Power spectrum analysis

3.4.2.1.1 Rushton turbine

At a chosen impeller speed (N_i), the gas flow rate (Q_i) was increased stepwise from 0 lpm (single-phase) to the point at which the impeller was no longer able to disperse air (flooded). At each setting of (N_i, Q_i) the pressure time series was recorded after the flow was completely developed and the stable sizes of gas cavities were formed (after 200 rotations of impeller). Similar procedure was repeated for the two other impeller speeds. In this manner more than 100 measurements were taken and transformed into frequency domain using FFT. The power spectra thus obtained are shown in Figure 3.6.

The typical power spectrum distribution of pressure fluctuation for single-phase flow is shown in Figure 3.6a. The flow characteristics in stirred reactor are expected to be characterized by the two main frequencies, viz., impeller rotational frequency and blade passage frequency. In the present study, for the six-blade Rushton turbine, the power spectrum of wall pressure fluctuations showed a peak at impeller rotational frequency. Similar peak at the blade passage frequency was not observed. Flow in the baffled stirred reactors is dominated by a complex interaction between the rotating impeller blades and stationary baffles. For a six-blade turbine, interaction of each blade with surrounding four baffles is asymmetric (due to different relative positions of each

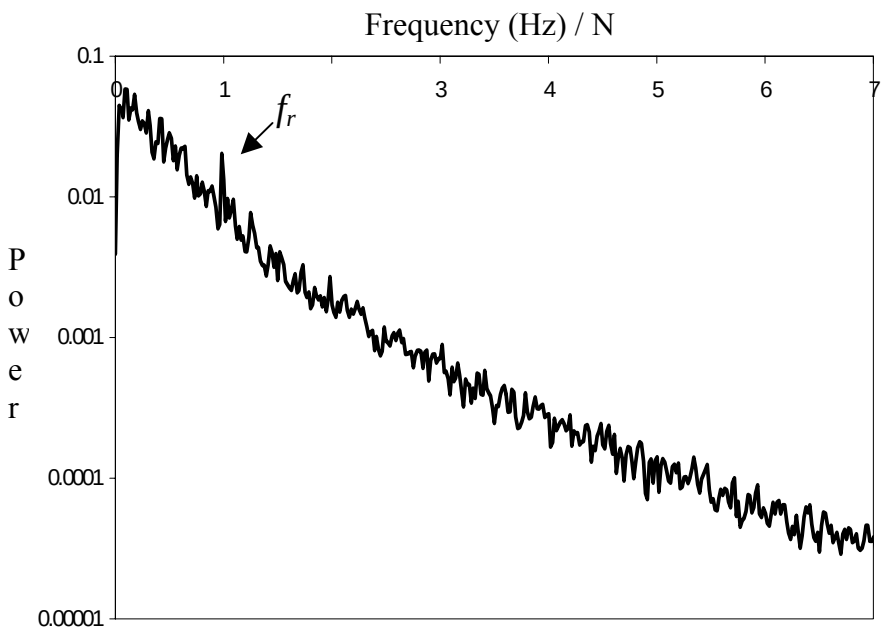

(a) Single-phase flow,
Gas flow number, Fl = 0.0 and Froude number, Fr = 0.6

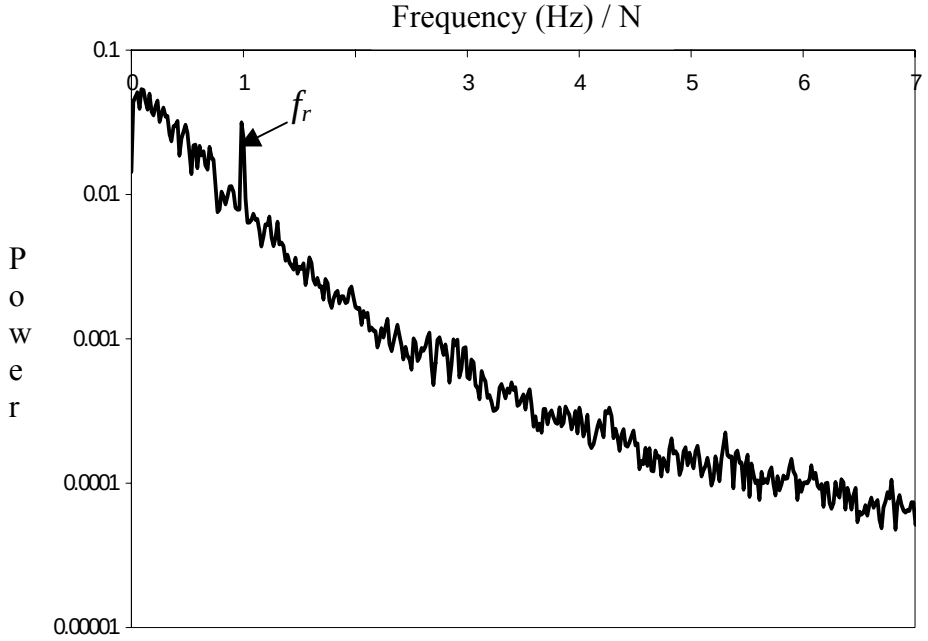

(b) Complete recirculation regime (VC-C),
Gas flow number, Fl = 0.0057 and Froude number, Fr = 0.6

Figure 3.6: Power Spectrum Distribution Computed with 2^{16} Points from Dynamic Pressure p'(t)
for Six Fluid Dynamic Conditions of Rushton Turbine

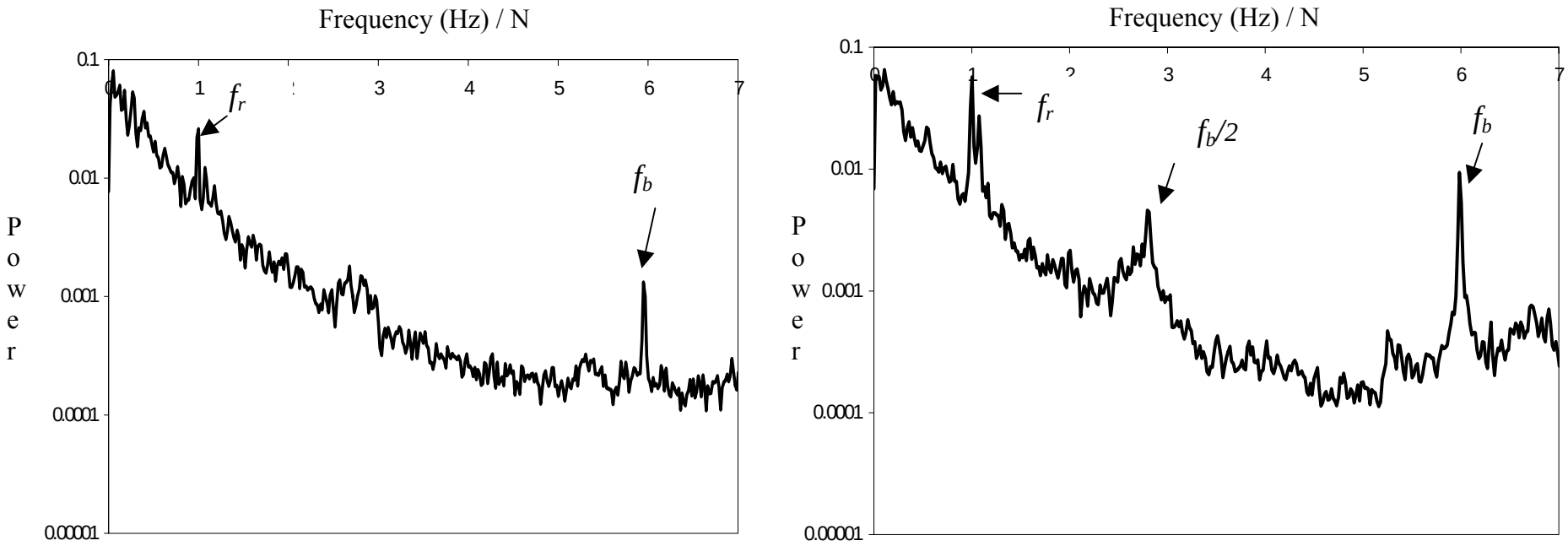

(c) Limited recirculation regime (VC-L),
Gas flow number, Fl = 0.019 and Froude number, Fr = 0.6

(d) Small 3-3 cavity regime (S33),
Gas flow number, Fl = 0.034 and Froude number, Fr = 0.6

Figure 3.6: Power Spectrum Distribution Computed with 2^{16} Points from Dynamic Pressure p'(t)
for Six Fluid Dynamic Conditions of Rushton Turbine

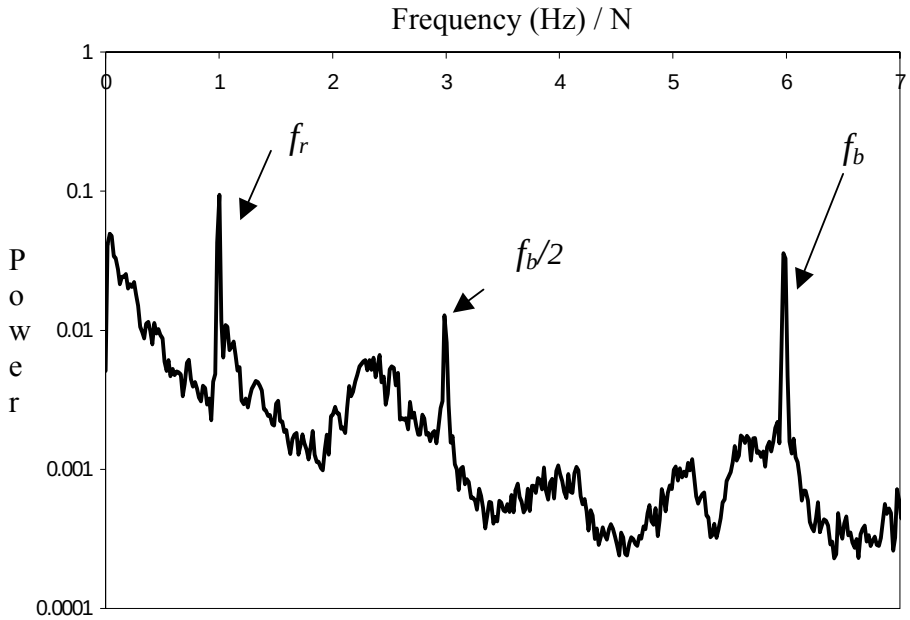

(e) Large 3-3 cavity regime (L33),
Gas flow number, Fl = 0.019 and Froude number, Fr = 0.6

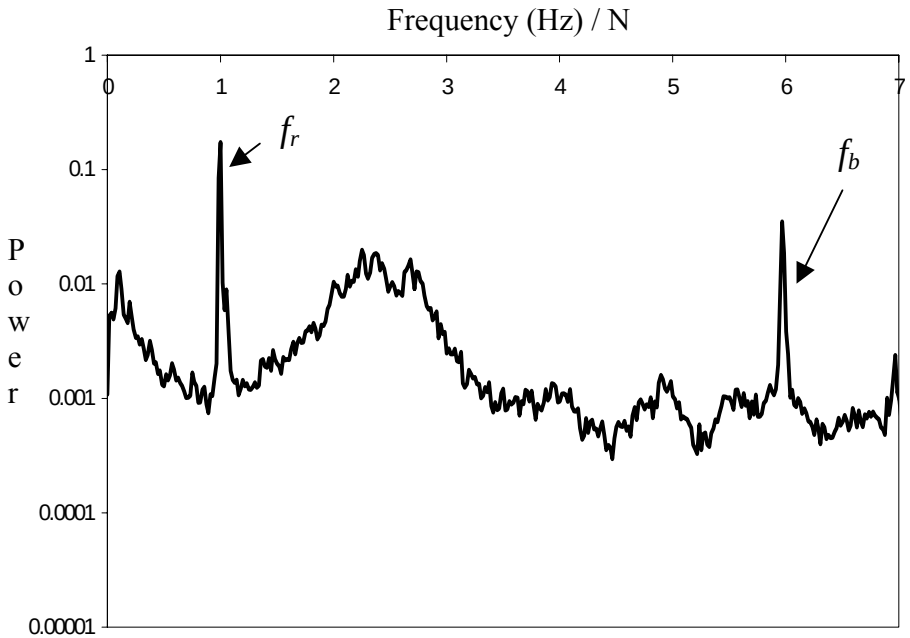

(f) Flooding regime (RC)
Gas flow number, Fl = 0.034 and Froude number, Fr = 0.6

Figure 3.6: Power Spectrum Distribution Computed with 2^{16} Points from Dynamic Pressure p'(t)
for Six Fluid Dynamic Conditions of Rushton Turbine

impeller blade with respect to baffles). This asymmetric interaction leads to a significantly asymmetric pressure distribution around impeller blades. Therefore, the dominant frequency is the impeller rotational frequency and not the blade passage frequency. Note that the measurements in the present work were carried out using a pressure sensor located at the reactor wall. If the pressure sensor is placed very near to rotating blades, it might be possible to see peaks at both impeller rotational frequency and blade passage frequency. For example, the power spectrum reported by Sutter *et al.* (1987) showed peaks at both of these frequencies. They had placed the sensor very close to the impeller tip (13 mm away from impeller tip). When interaction between the rotating blades and baffles is nearly symmetric (like for the case of a four- blade impeller in a fully baffled reactors), it is expected that there will be a peak at blade passage frequency in a power spectrum for such a combination.

The cavity structure present behind the impeller blades may include vortex clinging, one, two, three or six large cavities, which correspond to the VC, 1L, 2L, S33, L33 and RC structures respectively. For low gas flow rate, photographic studies (Bruijn *et al.*, 1974; van't Riet and Smith, 1973 and Takahashi and Nienow *et al.*, 1992) showed vortex-clinging cavity structures to be present behind impeller blades. These clinging cavities are of the same sizes, present on all the blades and follow each other. Nienow *et al.* (1977) defined a criterion to differentiate vortex-clinging (VC) cavity structure into two different flow regimes viz. fully established recirculation (after complete dispersion, recirculation of gas in whole reactor) and limited recirculation (before complete dispersion, recirculation of gas in lower circulation loop). Transformation of the pressure time series into the frequency domain for fully established recirculation regime (VC-C) is shown in Figure 3.6b. It can be seen from Figure 3.6b that similar to single-phase flow, the pressure time series shows a significant peak at frequency equal to impeller rotational speed, 'f_r'. Thus, the fluid dynamics of fully recirculation regime seems to resemble that of a single-phase flow in a reactor. The presence of such small clinging cavities behind the impeller blades might not cause much deviation from the characteristics of a single-phase flow.

With further increase in the gas flow rate, at a constant impeller speed, the flow condition in the reactor was transited to limited recirculation (VC-L) regime. The power spectrum distribution of the pressure time series for the limited recirculation

regime is shown in Figure 3.6c. It can be seen from Figure 3.6c that along with the impeller rotational frequency 'f_r', the blade passage frequency 'f_b' was seen in the power spectrum for limited recirculation regime. The presence of a peak only at blade passage frequency other than the rotational frequency can be used to indicate the presence of identical size cavities behind all impeller blades. However, the low magnitude of the power of blade passage frequency compared to the impeller rotational frequency could relate to the presence of small cavities behind the impeller blades. Therefore, it can be said that the power spectrum shown in Figure 3.6c can be used to identify the limited recirculation regime for the Rushton turbine. The transition of VC-L regime to S33 regime is not direct. The cavity structures like 1L and 2L are observed in few studies (Lu and Ju, 1989). The 1L and 2L regimes lie around the transition line between the VC-L and S33 regimes. In the present work, these cavity structures were not captured in the measured wall pressure fluctuations. Some of the previous studies (for example, Warmoeskerken and Smith, 1985) were also not able to capture these flow regimes explicitly.

Further increase in gas flow rate with the standard Rushton turbine leads to the '3-3' cavity structure (which is commonly used in industrial operations). In general, the '3-3' structure includes a combination of the small '3-3' structure (S33) and a large '3-3' structure (L33). Both these regimes are dependent on the gas flow rate ($0.04 \leq Fl \leq 0.1$ for S33 regime and $Fl \geq 0.1$ for L33 regime). The large cavities are observed with alternating sequence behind impeller blades in '3-3' cavity structure followed by either vortex-clinging cavities (S33 structure) or small cavities (L33 structure). The power spectrum for S33 cavity regime is shown in Figure 3.6d. The power spectrum for S33 regime shows two significant peaks at frequency equal to '$f_b/2$' and at blade passage frequency 'f_b' other than the peak at the rotational frequency 'f_r'. The presence of characteristic frequency f_r represents the impeller rotational frequency. The peaks resulted at frequencies '$f_b/2$' indicate the presence of two different types of cavities present, behind impeller blades and they follow each other in alternate sequence. However, the peak at the blade passage frequency, f_b, corresponds mainly to the shearing of gas cavities behind impeller blades. The pressure sensor at the reactor wall experiences this cavity shearing at the blade passage frequency. Nienow (1990) and Warmoeskerken and Smith (1982) described the L33 structure as a combination of

three large and three small cavities on alternate blades. The power spectrum of the pressure signal in L33 regime is shown in Figure 3.6e. It can be seen from Figure 3.6e that similar to S33 regime, the L33 regime also shows the presence of three characteristic frequencies 'f_r, $f_b/2$ and f_b'. However, there is a distinct difference in the power spectrum of L33 regime and S33 regime. When alternating gas cavities are small (S3-3 regime), the magnitude of a peak at $f_b/2$ is significantly lower than that at f_b. The magnitude of the peak at $f_b/2$ frequency increases as size of the cavities grows and approaches the magnitude of peak at f_b in L33 regime. Smith *et al.* (1987) and Bombac *et al.* (1997) have also used the similar criteria for differentiating between the S33 and L33 regimes.

Since the vast majority of industrial operations are carried out in the L33 regime, the prediction of L33 regime and subsequent transition to flooding condition is of great importance. In flooding condition the impeller action is not sufficient to disperse the gas. Nienow *et al.* (1985) observed that stable L33 structure converts into six violently vibrating large cavities of identical size in the flooding regime. The flooding condition can also be predicted from the rise in the power dissipated by the impeller (Figure 3.4a). A characteristic power spectrum under the flooding condition is shown in Figure 3.6f. Other than impeller rotational frequency 'f_r', a strong/prominent peak at blade passage frequency 'f_b' was clearly seen in the power spectrum. It can be depicted from the power spectrum that six large and identical size cavities present behind all the blades of the impeller under the flooding condition.

The power spectrum of wall pressure fluctuations has shown a significant difference in the pattern of frequency distribution for different flow regimes. The power spectrum of the pressure fluctuations was then analyzed for Smith turbine and pitched blade turbine.

3.4.2.1.2 Smith turbine

The hydrodynamic conditions for Smith turbine are classified into three main flow regimes, viz., vortex–clinging cavity (VC), 3-3 cavity (3-3) and flooding (RC) regime (see Warmoeskerken and Smith, 1989). The wall pressure fluctuations were acquired for two impeller speeds (Fr = 0.41 and 0.6) and gas flow rate (Fl) was varied from 0 to 0.44. The Smith turbine shows the hysterisis for the transition between the 3-3 cavity

and flooding regime. Therefore, all the measurements were carried out in the forward direction (gas flow rate was increased from lower to higher value for a constant impeller speed) as well as in the backward direction (gas flow rate decreased from higher value to a lower value for constant impeller speed).

The power spectrum of the pressure time series for a single-phase flow is shown in Figure 3.7a. Similar to Rushton turbine, the presence of six blades and four baffles resulted into asymmetric interaction, which leads to an asymmetric pressure distribution around the impeller blades. Therefore, only the impeller rotational frequency was observed as a dominant frequency in the power spectrum. The power spectrum of pressure time series for vortex-clinging cavity structure regime is shown in Figure 3.7b. It can be seen from Figure 3.7b that the two significant peaks in the power spectrum at impeller rotational speed 'f_r' and impeller blade passage frequency 'f_b' are present. The magnitude of a peak at a blade passage frequency 'f_b' is lower that that at 'f_r'. This can be attributed to the presence of small vortex-clinging cavities behind the impeller blades. Such pattern can be used for the recognition of the vortex-clinging impeller blades. With further increase in the gas flow rates, the flow regime changes to 3-3 cavity regime. In 3-3 cavity regime, two types of cavities (large cavities and vortex-clinging cavities observed behind the impeller blades and they follow each other in alternate sequence) are observed behind the impeller blades. The peaks resulted at the frequencies of '$f_b/2$' indicate the presence of two different types of cavities present, behind impeller blades (see Figure 3.7c). With further increase in the gas flow rate at constant impeller speed leads to the formation of large cavities behind the impeller blades. The presence of large cavities behind the impeller blades significantly reduces the pumping capacity of the impeller and leads to the flooding conditions in the reactor. The flooding condition can also be predicted from the rise in the power dissipated by impeller (Figure 3.4b). The power spectrum for the flooding regime is shown in Figure 3.7d. It can be seen from Figure 3.7d that the power spectrum shows the presence of only blade passage frequency 'f_b' other than the rotational frequency. The power spectrum thus corresponds to six large cavities (ragged cavities) of identical size present behind each of the impeller blades.

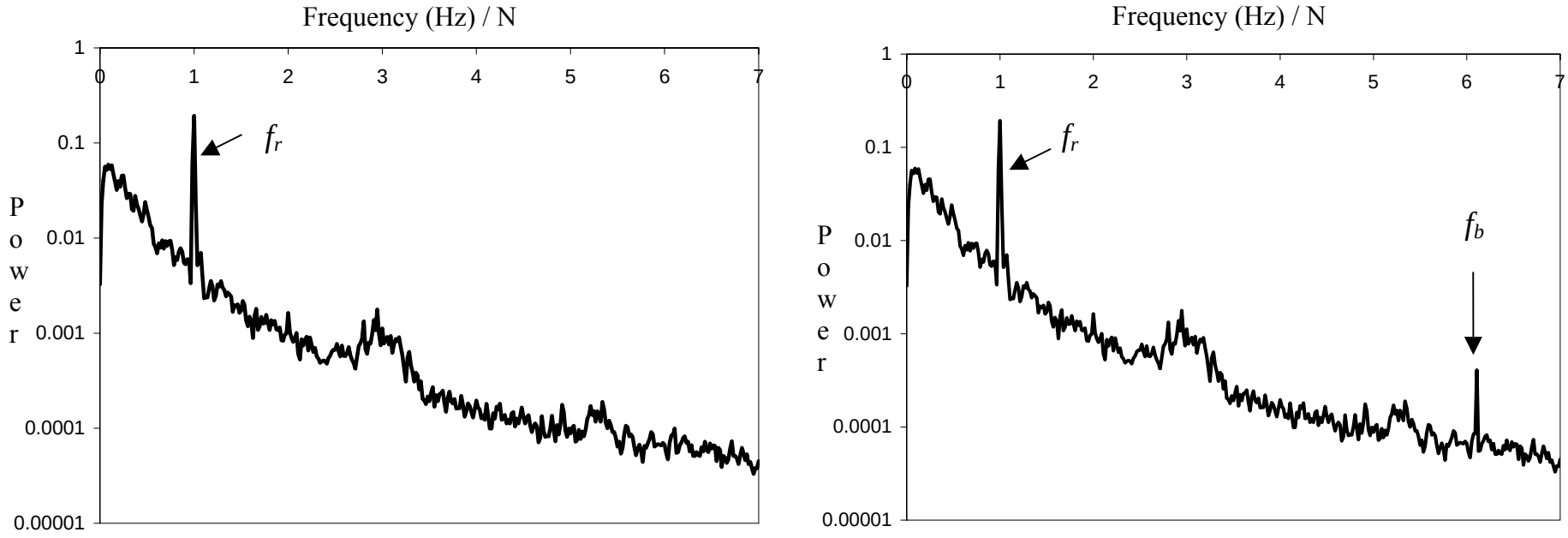

(a) Single-phase flow,
Gas flow number, Fl = 0.0 and Froude number, Fr = 0.6

(b) Vortex-clinging cavity regime,
Gas flow number, Fl = 0.015 and Froude number, Fr = 0.6

Figure 3.7: Power Spectrum Distribution Computed with 2^{16} Points from Dynamic Pressure p'(t) for Four Fluid Dynamic Conditions of Smith Turbine

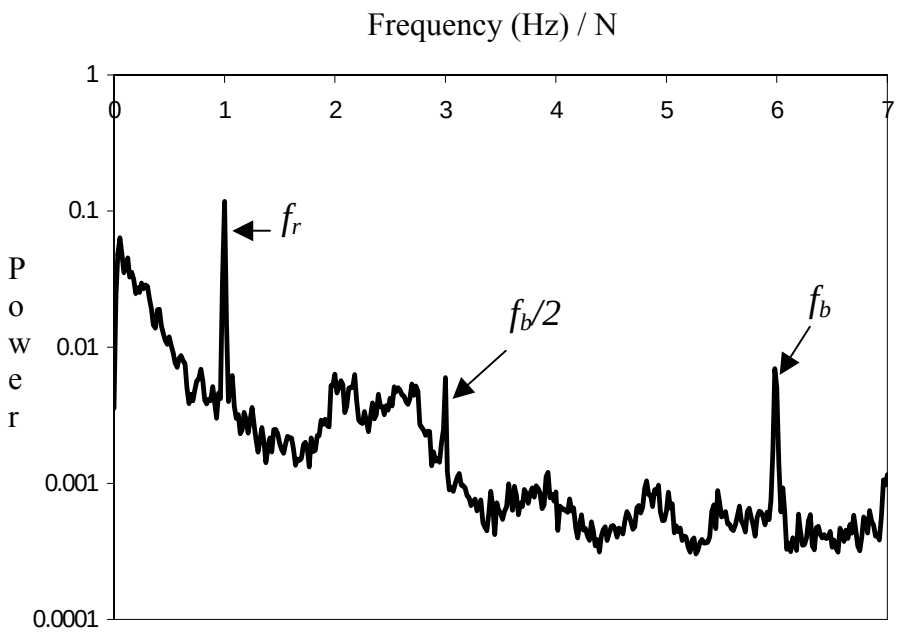

(c) 3-3 cavity regime,
Gas flow number, Fl = 0.13 and Froude number, Fr = 0.6

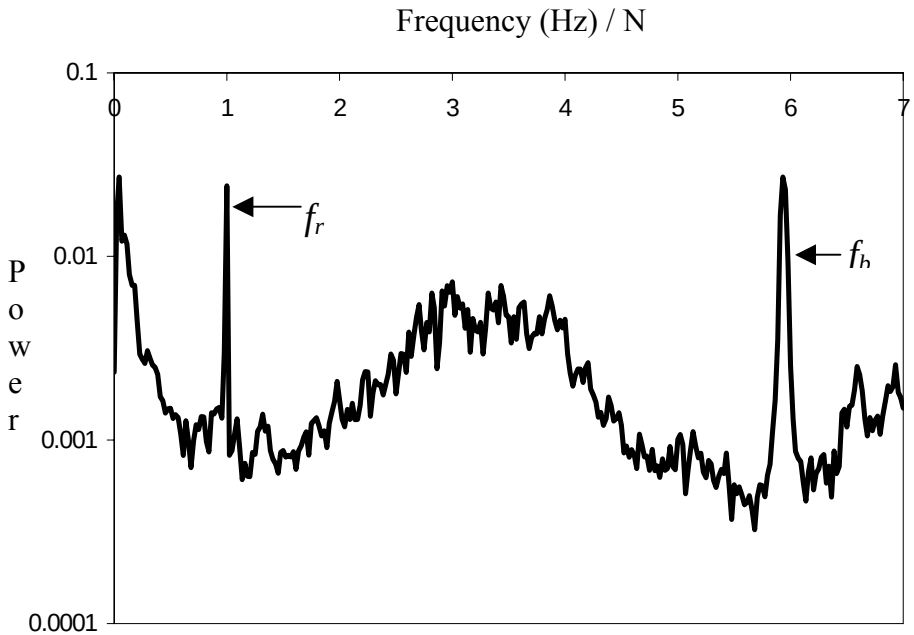

(d) Flooding regime,
Gas flow number, Fl = 0.28 and Froude number, Fr = 0.6

Figure 3.7: Power Spectrum Distribution Computed with 2^{16} Points from Dynamic Pressure p'(t)
for Four Fluid Dynamic Conditions of Smith Turbine

3.4.2.1.3 Down pumping pitched blade turbine

For 6-bladed down pumping pitched blade turbine, the hydrodynamic conditions can be broadly differentiated into two main flow regimes, viz. flooding and complete dispersion. Over a narrow range of operating conditions between these two regimes a third regime (known as cavity formation regime) is present in the reactor. In the present study the wall pressure signal was acquired for four impeller rotational speeds (Fr = 0.415, 0.5, 0.85 and 1.12) and gas flow rate (Fl) was varied from 0 to 0.24.

The power spectrum of the pressure time series for a single-phase flow is shown in Figure 3.8a. Similar to Rushton turbine, the presence of six blades and four baffles resulted into an asymmetric interaction, which leads to an asymmetric pressure distribution around the impeller blades. Therefore, only the impeller rotational frequency was observed as a dominant frequency in the power spectrum. The power spectrum of the pressure time series for a complete dispersion /recirculation regime is shown in Figure 3.8b. It can be seen from Figure 3.8b that the two significant peaks in the power spectrum at impeller rotational speed 'f_r' and impeller blade passage frequency 'f_b' are present. The magnitude of a peak at a blade passage frequency 'f_b' is lower that that at 'f_r'. This can be attributed to the presence of small vortex-clinging cavities behind the impeller blades. Such pattern can be used for the recognition of the completely dispersed and re-circulating condition for the gas phase in the reactor. With further increase in the gas flow rates, the flow regime changes to cavity formation regime. In the cavity formation regime the power dissipated by an impeller reaches to the minimum value (see Figure 3.4c) and an unstable gas dispersion pattern was observed for these operating conditions. In the cavity formation regime, large cavities are formed and simultaneously sheared away from the blade tip. These cavities shear away with different frequencies and may lead to a different number of cavities present behind the impeller blades. This complex cavity structure present behind the impeller blades in the cavity formation regime was manifested in the form of several peaks in the power spectrum at f_b, $5f_b/6$, $2f_b/3$, $f_b/2$, $f_b/3$ and $f_b/6$ (see Figure 3.8c). Further increase in the gas flow rate at constant impeller speed leads to the formation of large cavities behind the impeller blades. The presence of large cavities behind the impeller blades significantly reduces the pumping capacity of the impeller and leads to the

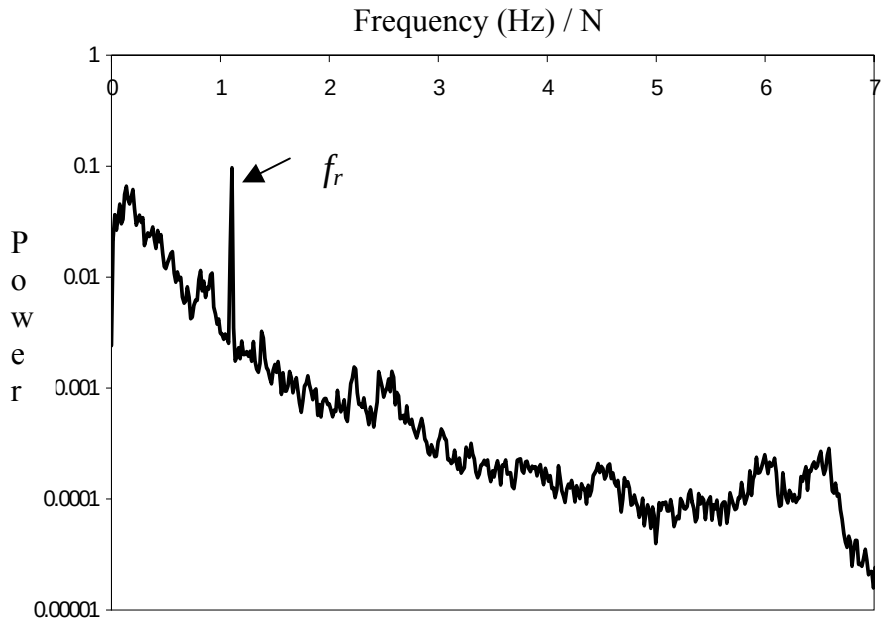

(b) Single-phase flow,
Gas flow number, Fl = 0.0 and Froude number, Fr = 0.85

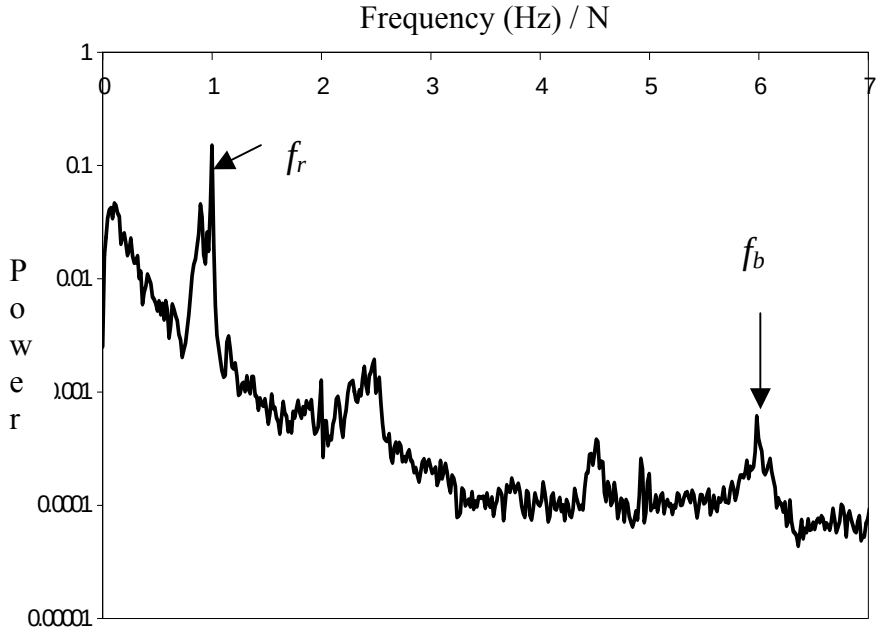

(b) Complete dispersed regime,
Gas flow number, Fl = 0.01 and Froude number, Fr = 0.85

Figure 3.8: Power Spectrum Distribution Computed with 2^{16} Points from Dynamic Pressure p'(t)
for Four Fluid Dynamic Conditions of Pitched Blade Turbine

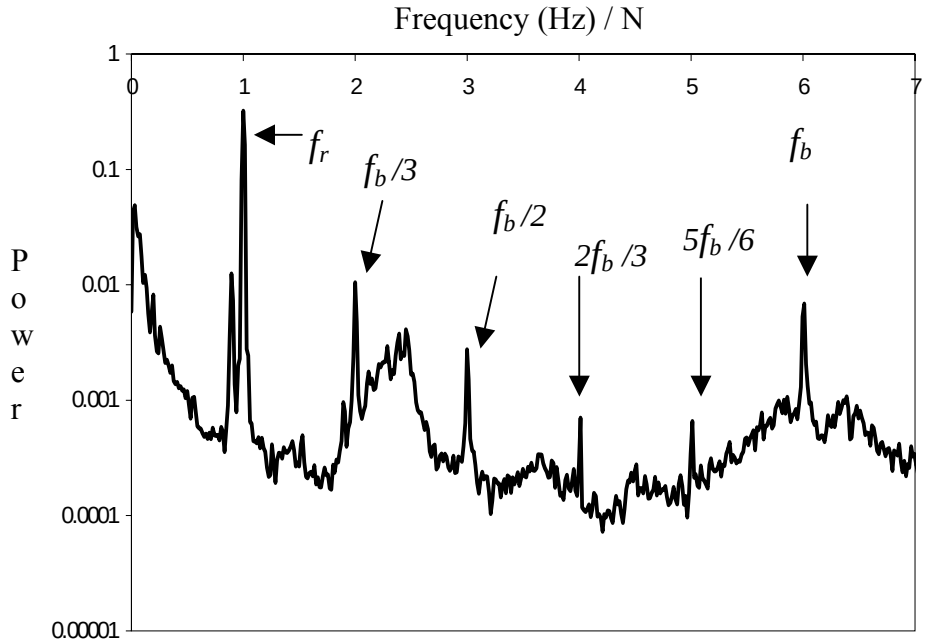

(d) Cavity formation regime,
Gas flow number, Fl = 0.036 and Froude number, Fr = 0.85

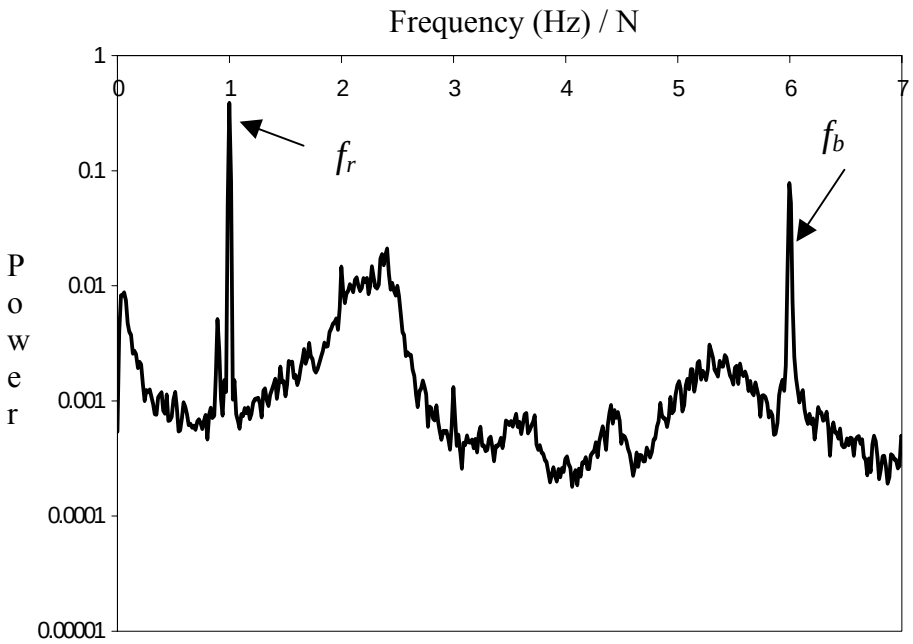

(d) Flooding regime,
Gas flow number, Fl = 0.16 and Froude number, Fr = 0.85

Figure 3.8: Power Spectrum Distribution Computed with 2^{16} Points from Dynamic Pressure p'(t)
for Four Fluid Dynamic Conditions of Pitched Blade Turbine

flooding conditions in the reactor. The power spectrum for flooding regime is shown in Figure 3.8d. It can be seen from Figure 3.8d that the power spectrum shows the presence of only a blade passage frequency 'f_b' other than the rotational frequency. However, the magnitude of the power at blade passage frequency 'f_b' was significant and was almost equal to the power of rotational frequency 'f_r'. The power spectrum thus corresponds to six large cavities (ragged cavities) of identical size present behind all the impeller blades.

The power spectral distribution of the pressure time series have clearly identified the different cavity structures, present behind the impeller blades for all the three impellers. The flow in gas-liquid stirred reactors is a combination of impeller-generated flow and gas-generated flow. For the complete dispersion regime, the impeller-generated flow dominates the fluid dynamics in the reactor. In contrast to this for the flooding regime, the gas-generated flow dominates the overall flow. The intermediate flow regime occurs when both these interact with each other in a complex way. The power spectrum analysis of the pressure fluctuations could not provide the information about the relative strengths of the impeller and gas generated flows. Attempt was made to use the P statistics analysis to get some insight.

3.4.2.2 P statistics analysis

The P statistics of the dynamic pressure time series for Rushton turbine, for Fr = 0.6, was calculated using Equation 3.7. The optimized value of the exponent γ calculated using criterion (Equation 3.8) defined by Briens and Briens (2000) was equal to 0.74 for Fr = 0.6 (and was found to vary in the range of 0.72 to 0.75 for other impeller rotational speeds). Figure 3.9 shows the P statistics of the dynamic pressure for different flow regimes. For the single-phase flow and for both the recirculation regimes the P statistics curve shows the presence of a single peak. For these conditions, the impeller-generated flow controlled the overall fluid dynamics. Therefore, it is possible to assume that the peak predicted by the P statistics for both the recirculation regimes is the characteristic peak of the impeller-generated flow.

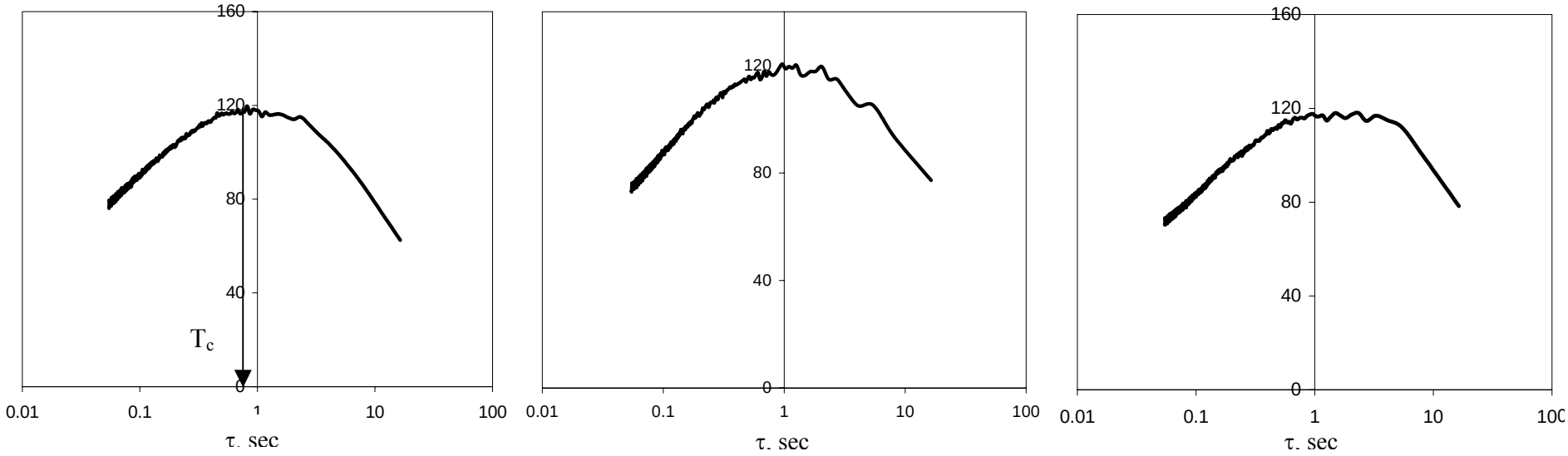

(a) Single-phase, Fl = 0 (b) Complete recirculation, Fl = 0.0057 (c) Limited recirculation, Fl = 0.019

Figure 3.9: P Statistics for the Dynamic Pressure Time Series of Rushton Turbine, Froude number, Fr = 0.6

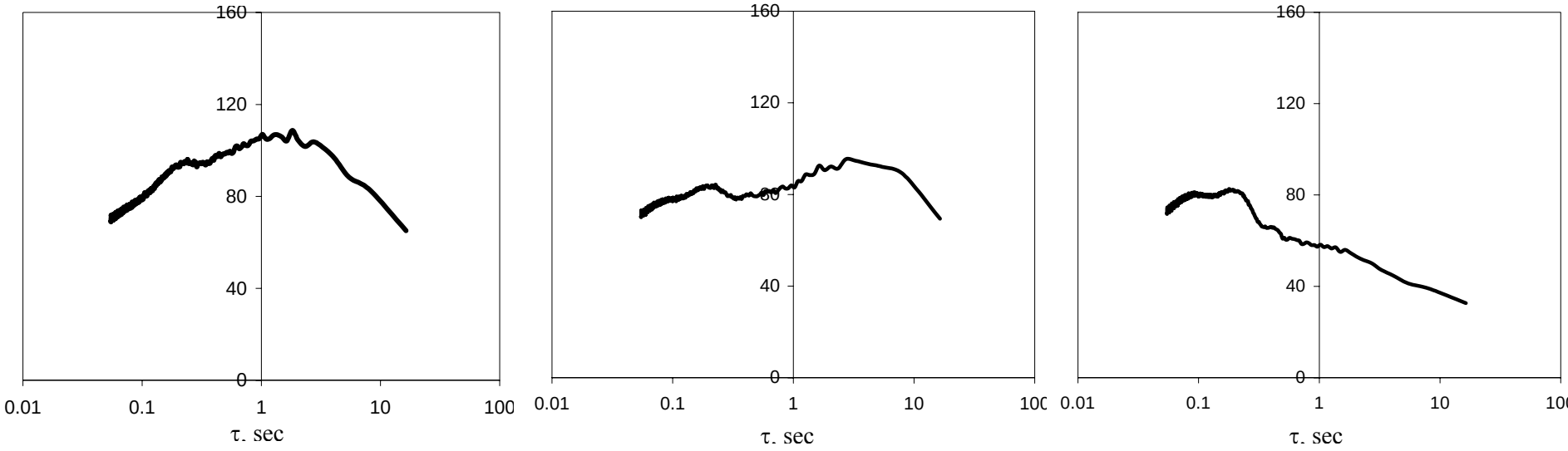

(d) S33 Regime, Fl = 0.0457

(e) L33 regime, Fl = 0.152

(f) Flooding, Fl = 0.348

Figure 3.9: P Statistics for the Dynamic Pressure Time Series of Rushton Turbine, Froude number, Fr = 0.6

The P statistic curves for the S33 and L33 regimes are also shown in Figure 3.9. It can be seen from the Figure 3.9 that the P statistic curves for S33 and L33 regimes show the presence of another peak on the left side of the characteristic peak of the impeller-generated flow. However, the peak of the impeller-generated flow was shifted towards the right as compared with the VC regimes. The presence of second peak was more prominent in the L33 regime compared to the S33 regime. This indicates that the second peak observed in S33 and L33 regimes was due to the contribution of the gas-generated flow in overall fluid dynamics. This assumption was further confirmed from the P statistics curve for the flooding regime. As we know that the flow in a stirred reactor in a flooding regime is controlled by the flow generated by the sparged gas. The second peak, as observed in S33 and L33 regimes, was also seen for the flooding regime with an absence of a peak of impeller-generated flow. Thus it can be said that the qualitative difference between the P statistics curves successfully differentiated the flow regimes and separated the contribution of flow generated by an impeller and the flow generated by the sparged gas in the overall fluid dynamics. The P statistics curves of the pressure fluctuations for the pitched blade turbine and Smith turbine were then analyzed to distinguish the prevailing flow regimes. However, before discussing the flow regime identification using P statistics curves, the P statistics method was used to estimate the effect of gas loading on the impeller-generated liquid flow.

The impeller-generated flow or the pumping capacity of an impeller is one of the important design parameters of stirred reactor. The pumping efficiency of an impeller significantly reduces in the presence of gas and negatively affects the performance of the reactor. The knowledge of the reduction in the pumping efficiency is essential for the quantitative determination of the liquid phase mixing in the reactor. In this work, an attempt was made to estimate the drop in the pumping efficiency of the Rushton turbine for an aerated condition using P statistics curve.

A close look at the P statistic curves for different regimes of Rushton turbine indicated an increase in the characteristic cycle time of an impeller-generated flow with an increase in the gas flow rate. The characteristic cycle time of the impeller-generated liquid flow was estimated from the time scale associated with this peak. The effect of the gas flow rate on the cycle time of the impeller-generated flow is shown in Figure 3.10. It can be seen from Figure 3.10 that the cycle time first increases sharply with an

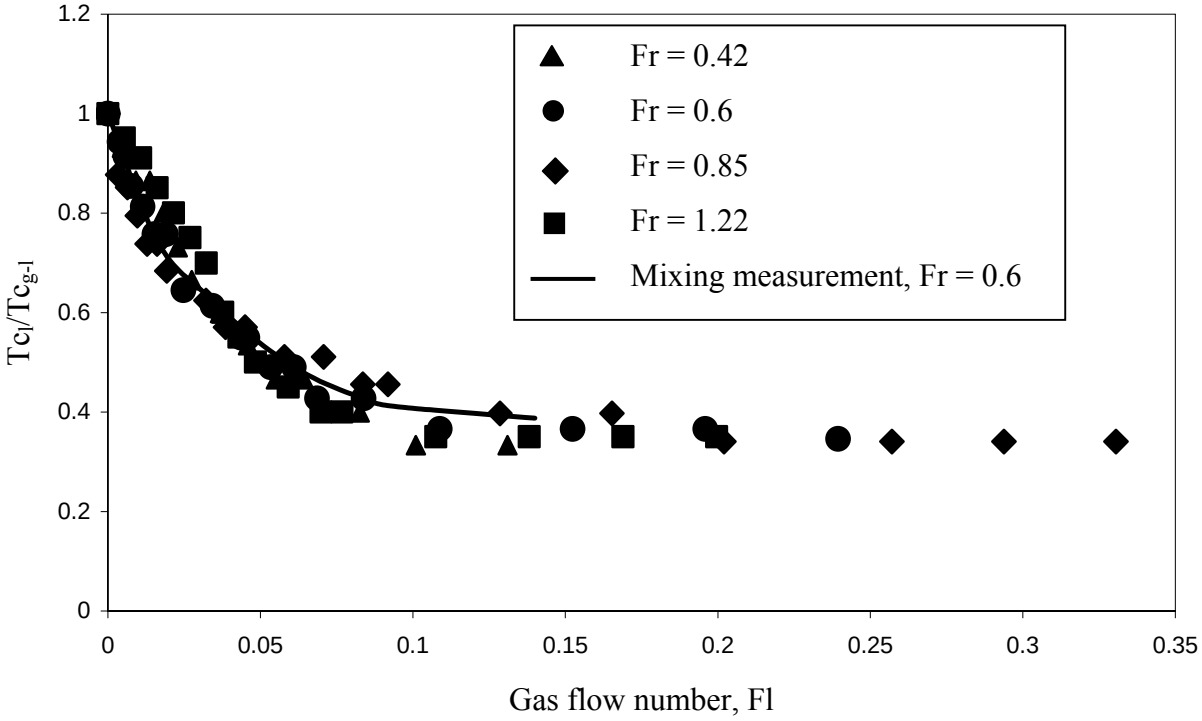

Figure 3.10: Estimation of Drop in Pumping Efficiency of Rushton Turbine in an Aerated Condition Using P statistics

increase in the gas flow rate (ratio of characteristic time scale for single-phase case to that for gas-liquid case decreases). This sharp increase in the cycle time was seen in the recirculation regime. However, in S33 regime the rate of increase in the cycle time was slowed down and almost a constant value of cycle time was then seen in L33 regime. The relative change in the characteristic cycle time can be related to corresponding change in circulation/mixing time for the gas-liquid stirred reactor. To verify this, the mixing time measurements were carried out for Froude number equal to 0.6 and the gas flow rate was varied from 0 to 0.12. The fractional increase in the mixing time was then compared with the fractional increase in the characteristic cycle time of the impeller-generated flow. It can be seen from Figure 3.10 that the fractional increase in the mixing time (reduction in the ratio of mixing time obtained for single-phase flow to that for gas-liquid flow) follows the fractional increase in the cycle times of impeller-generated flow. Thus the P statistics of pressure fluctuation can be used to estimate the increase in the circulation/mixing time with gas flow rate in a gas-liquid stirred reactor.

The P statistics of the pressure fluctuations were then used to identify the prevailing flow regimes for down pumping pitched blade turbine and Smith turbine. The P statistics curves for Smith turbine for three distinct regimes are shown in Figure 3.11a. It can be seen from Figure 3.11a that the P statistic curve successfully identified the prevailing flow regimes of Smith turbine. The P statistic curve for vortex-clinging (fully dispersed) regime is shown in Figure 3.11a (i). Unlike the Rushton turbine, the P statistics curve shows the presence of two peaks for completely dispersed condition for Smith turbine. However, the cycle, representing the impeller- generated liquid flow is dominating and controls the overall fluid dynamics. The gas- generated flow shows a small contribution to the overall fluid dynamics. The P statistics curve for the 3-3 cavity (loading) flow regime shows slightly higher contribution of gas-generated flow on fluid dynamics compared to voterx-clinging regime. However, still the impeller-generated flow controls the overall fluid dynamics (see Figure 3.11a (ii)). With further increase in the gas flow rate, the flow condition in the reactor transformed into the flooding regime. Similar to the Rushton turbine, the P statistics curve for Smith turbine shows a presence of gas-generated flow cycle for the flooding regime (see Figure 3.11a (iii)). With further increase in the gas flow rate, the flow condition in the reactor transformed into the flooding regime. The P statistics curves for the six-blade down-pumping pitched blade turbine operating in the different flow regimes are shown in

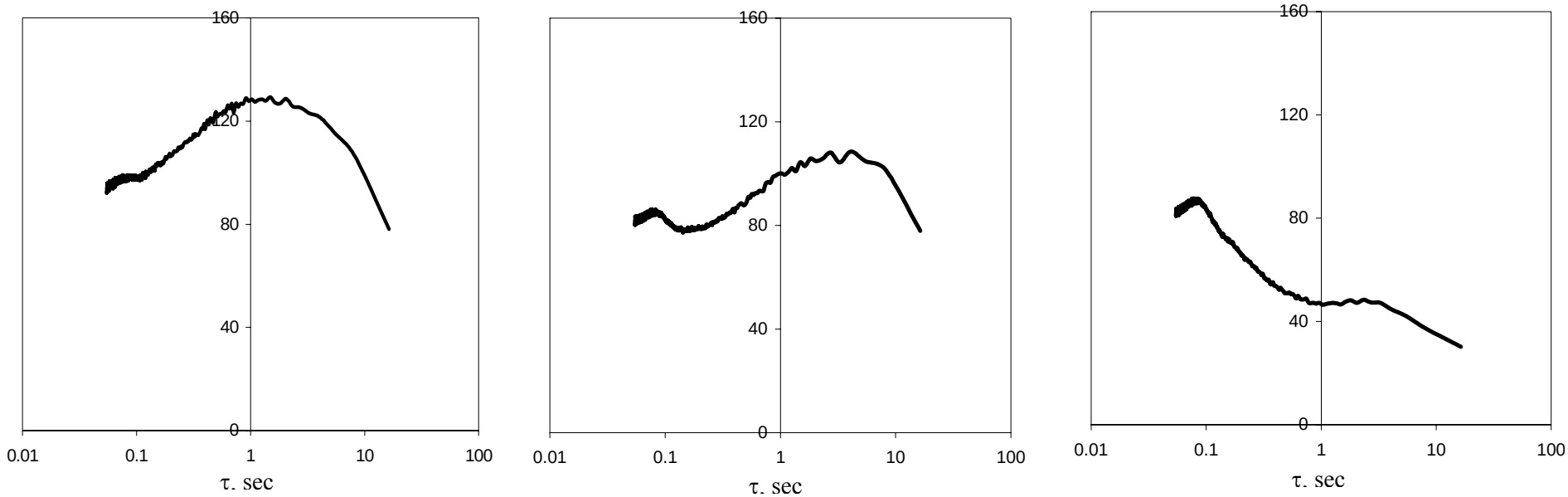

(a) VC regime,
Gas flow number, Fl = 0.015

(b) 3-3 regime,
Gas flow number, Fl = 0.13

(c) Flooding regime,
Gas flow number, Fl = 0.28

(a) Smith turbine, Froude number, Fr = 0.6

Figure 3.11: P statistics for the Dynamic Pressure Time series

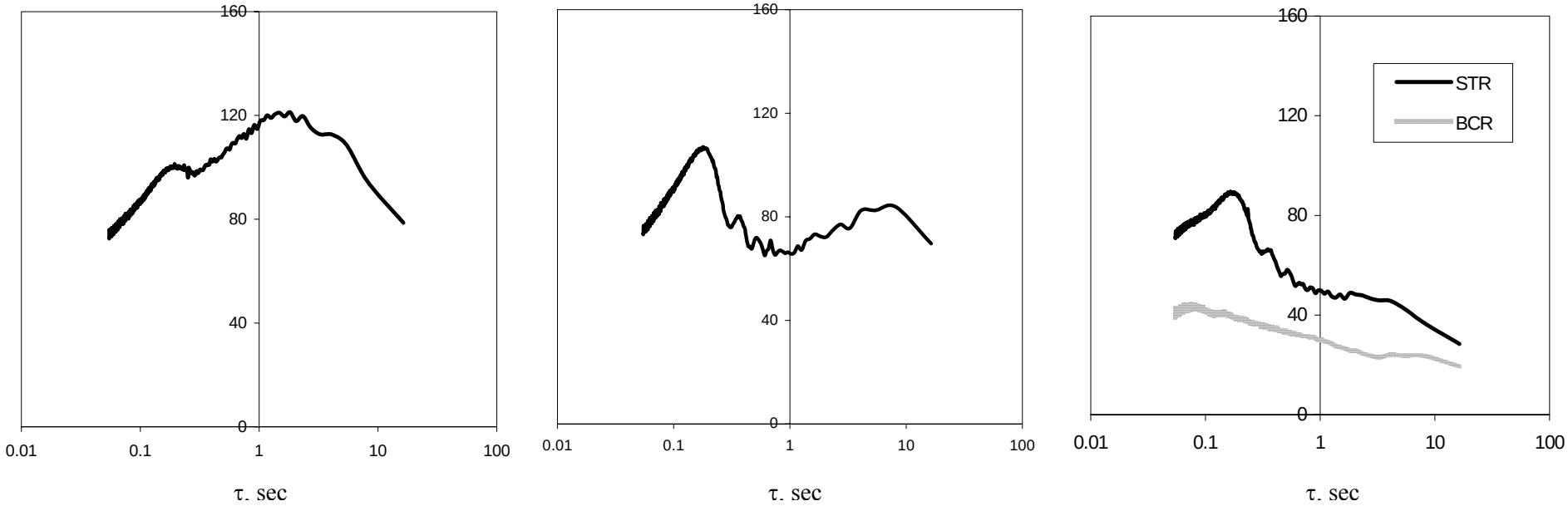

(a) Complete dispersion regime, Gas flow number, Fl = 0.01

(b) Cavity formation regime, Gas flow number, Fl = 0.036

(c) Flooding regime, Gas flow number, Fl = 0.16

(b) Pitched blade turbine, Froude number, Fr = 0.85

Figure 3.11: P statistics for the Dynamic Pressure Time series

Figure 3.11b. It can be seen that the P statistic curves successfully identified the fully dispersed (vortex-clinging), cavity formation and the flooding regimes. Similar to Smith turbine, the P statistics for vortex-clinging cavity structure for the pitched blade turbine shows the presence of two peaks. The cycle representing the impeller-generated liquid flow is dominating and controls the overall fluid dynamics. The gas-generated flow shows a small contribution in the overall fluid dynamics. The contribution of the gas-generated flow in an overall fluid dynamics is increased in the cavity formation regime. The cavity formation regime shows, almost equal contribution by the impeller- and gas-generated flows to the overall fluid dynamics (see Figure 3.11b (ii). However, in the flooding regime, the gas- generated flow controls the overall fluid dynamics.

The flooding condition in a stirred reactor is similar to bubble column reactor because of the dominant contribution of a gas driven flow in the overall fluid dynamics. To confirm this, the pressure time series was acquired in a gas-liquid stirred reactor without an impeller rotation to resemble bubble column reactor with H/D = 1. The P statistics of the pressure time series of flooding regime was then compared [see Figure 3.11b (iii)] with that of the bubble column reactor to show an excellent agreement. The observed difference in the P statistics curve between the two systems could be attributed to the presence of the impeller rotation in a stirred reactor. This observation supports the above analysis of time scales based on P statistics.

The flow regimes, identified in the present work for the Smith turbine are then compared with the reported flow regime map (Warmoeskerken and Smith, 1989) in Figure 3.12a. It can be seen that the transition to flooding regime was found to be earlier than the reported map. It should be noted that in the present work the impeller diameter was smaller than T/3, which may cause such an early transition to flooding. Similar behavior was also observed with the Rushton turbine. Similarly the flow regime map based on the analyzed experimental data for the pitched blade turbine (power dissipation, power spectrum and P statistics of pressure fluctuations) is shown in Figure 3.12b. It can be seen that from Figure 3.12b that the region for the cavity formation regime/ unstable flow regime move towards the right side of the map and get enlarged with an increase in the impeller rotational speed. These observations are consistent with the experimental study reported by Chapman *et al.* (1983) for four blade pitched blade

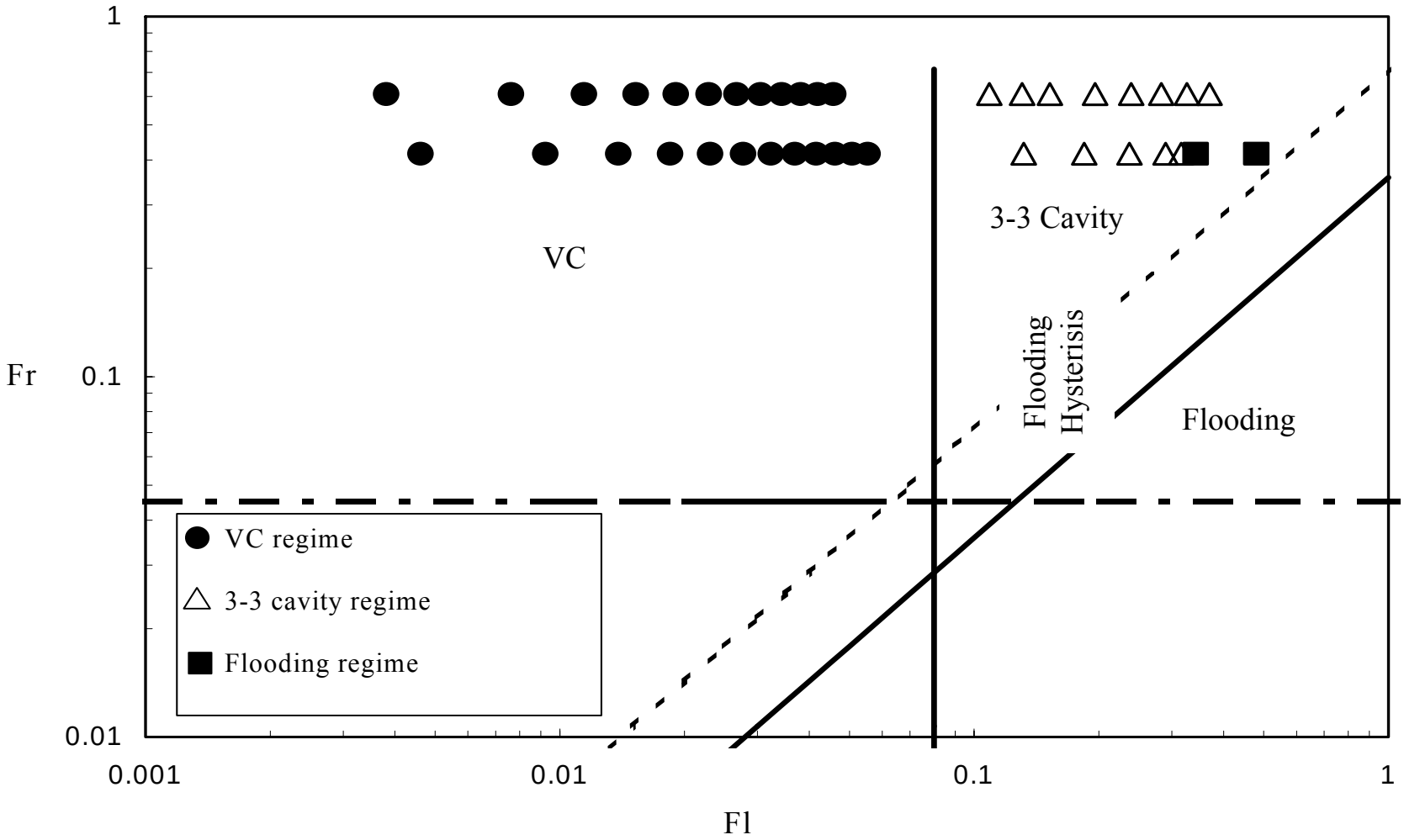

(a) Smith turbine (Flow regime map from Warmoeskerken and Smith, 1989)

Figure 3.12: Flow Regime Map based on Cavity Structure Developed behind Impeller Blades

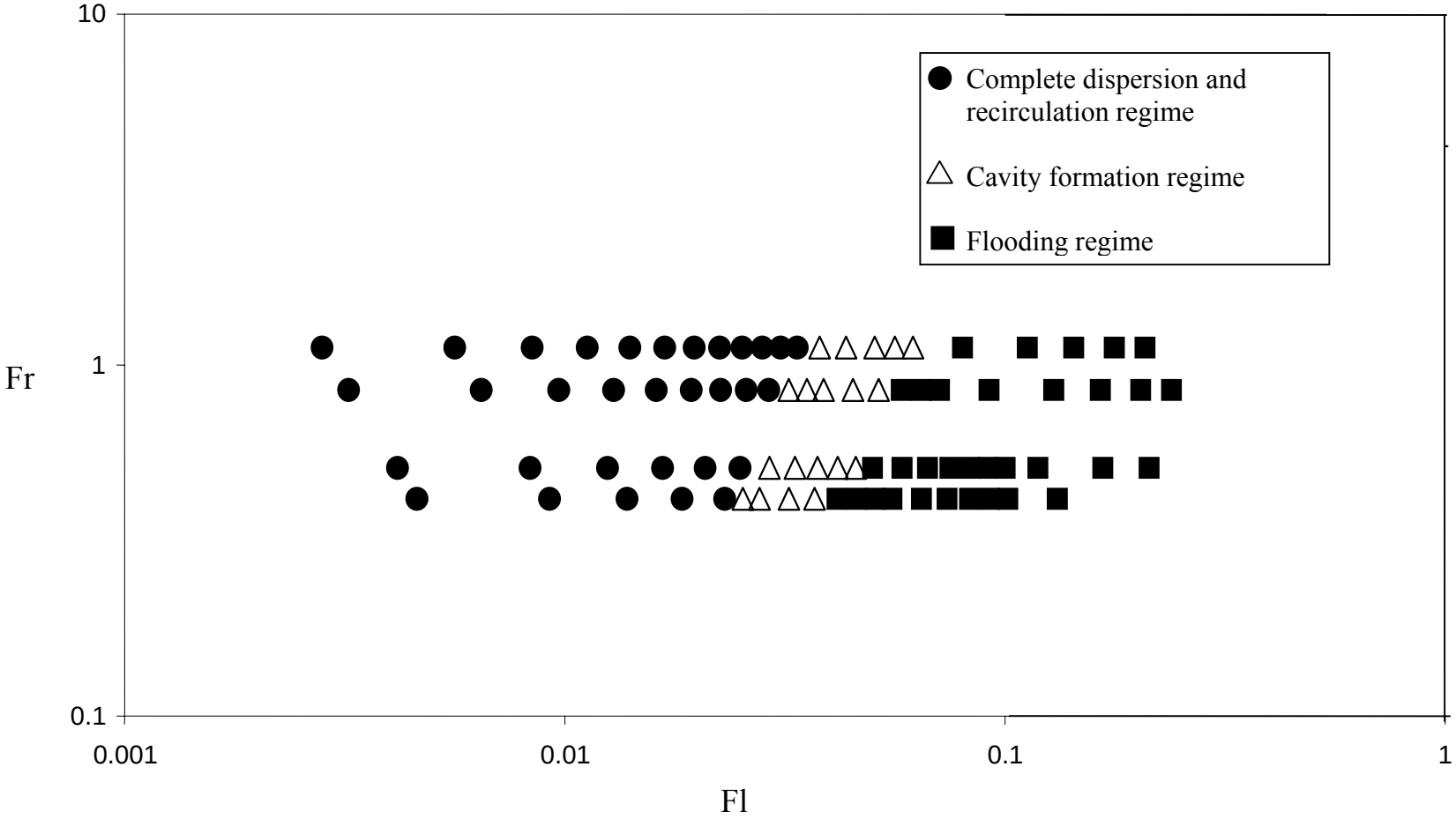

(b) Pitched blade turbine

Figure 3.12: Flow Regime Map based on Cavity Structure Developed behind Impeller Blades

turbine. The reproducibility of the results was verified for the other two more impeller speeds (given in section 3.2) for all the three turbines. All possible cavity structures were repeatedly recognized in all the cases.

Overall the methods presented here could be successfully used to understand the influence of the gas flow rate on flow regimes, cavity structures and characteristic time scales. It was also shown that the exact location of the pressure sensor is not critical as long as it is not very close to the top surface. The methods are based on the statistical analysis of the torque and pressure fluctuations, which are directly related to the gas cavity structures behind the impeller blade. The detection of these fluctuations is not a function of fluid properties, opaqueness and the scale of the reactor. The techniques presented here could be used with commercially available industrial torque and pressure sensors. The analysis and detection of the flow regimes is fairly straightforward and unambiguous. Therefore the methods proposed in the present work look promising for their applications to industrial gas-liquid stirred reactors. The techniques (especially based on the wall pressure fluctuations) could also be useful for on-line detection and for providing early warnings of regime transitions due to the changes in the process (operating) parameters.

3.5 Summary and Conclusion

In the present study, non-intrusive techniques based on the wall pressure sensor and torque sensor, were successfully used for the characterization of gas-liquid flows in a stirred reactor. Along with the information of the average power consumption, the torque fluctuations provided the information of transition to flooding regime for all three impeller. For pitched blade turbine, the power reduction curve as well as the RMS values of torque fluctuations clearly identified flow regime transition. However, the power reduction curve did not clearly identified the regime transition points for the Rushton and Smith turbine and also failed to provide the quantitative information on the cavity structure present behind the impeller blades.

The wall pressure fluctuations were then measured at the reactor wall for the Rushton, Smith and pitched blade turbine. The power spectrum distribution and the P statistics of the pressure fluctuations clearly identified the prevailing flow regimes for the turbines

considered in the present study. Along with the identification of the flow regimes, the power spectrum of the pressure fluctuations provided the knowledge of the cavity structure present behind the impeller blades. The P statistics analysis of the pressure fluctuations quantitatively estimated the drop in the pumping efficiency for the aerated conditions and the relative contributions of gas-driven and impeller-driven liquid flows to the overall fluid dynamics in the stirred reactor.

Overall, it can be concluded that the pressure transducer and torque sensor successfully identified the prevailing flow regimes and extracted the relevant and valuable information of fluid dynamics without disturbing the flow.

PART II

COMPUTATIONAL MODELLING

Chapter 4

COMPUTATIONAL MODELLING OF GAS-LIQUID FLOWS

4.1 Introduction

From the last two decades, many studies have reported the CFD simulation of (single as well as multiphase) flow field in a stirred reactor (excellently reviewed by Ranade, 2002). However, most of the studies have reported the results on a single-phase flow in stirred reactor. The presence of the secondary phase, especially gas-phase, significantly increases the complexity of the CFD simulation. Despite these complexities few attempts have been made to simulate the gas-liquid flows in stirred reactor. Table 4.1 shows a brief overview of the studies concerning the simulation of the gas-liquid flows in a stirred reactor. Critical analysis of these past studies shows several discrepancies. The most important differences between the simulations concern the turbulence modelling, impeller modelling approaches, grid size and most important, the modelling of interphase closure terms. In this chapter we have first presented the brief review of the different impeller modelling approaches, turbulence models and the multiphase modelling approaches available for the simulation of gas-liquid flows in a stirred reactor. The impeller as well as multiphase modelling approaches and the turbulence model used in present study is discussed thereafter.

4.2 Impeller Modelling Approaches

The relative motion between the stationary baffles and the rotating impeller blades makes a complete simulation of the flow field in stirred reactor computationally awkward. Different approaches have been suggested to numerically simulate the flow in a stirred reactor. Four types of approaches are widely used in practice to model the flow generated by a rotating impeller in the reactor. They are, black box approach, sliding grid approach, multiple reference frame or inner-outer approach and snapshot approach. The schematic of all four types is shown in Figure 4.1.

Most of the flow simulations of the stirred reactor published before 1995 were based on steady state analysis (reviewed by Ranade, 1995) using the black box approach. In this approach the impeller region is excluded from the computational domain. This approach requires the specification of the impeller boundary conditions (mean velocities and turbulent characteristics) on the impeller swept surface, which need to be determined experimentally. Although, this approach is reasonably successful in

Table 4.1: Review of Previous Work on Numerical Simulation of Gas-Liquid Flows

Author	**Impeller modelling approach**	**Interphase coupling**	**Turbulence model**	**Parameters studied**
Gosman *et al.* (1992)	Impeller boundary conditions (IBC)	Two-way	Standard k-ε	Gas and liquid flow field
Bakker and van den Akker (1994)	IBC	One-way	Algebraic stress model	Gas holdup and bubble size distribution
Rousar *et al.* (1994)	IBC	One way	Standard k-ε	Gas holdup, bubble size distribution and gas flow field
Ranade and van den Akker (1994)	Snapshot approach (SA)	Two-way	Standard k-ε	Liquid flow field
Morud and Hjertager (1996)	IBC (two-dimensional model)	Two-way	Standard k-ε	Gas flow field
Friberg (1998)	Sliding grid (SG)	Two-way	Standard k-ε	Liquid and gas flow field
Ranade and Deshpande (1999)	SA	Two-way	Standard k-ε	Gas accumulation behind impeller blades
Lane *et al.* (1999)	Multiple reference frame (MRF)	Two-way	Standard k-ε	Gas holdup distribution and bubble size distribution
Lo (2000)	MRF	Two-way	Standard k-ε	Gas holdup distribution and bubble size distribution
Lane *et al.* (2000)	MRF	Two-way	Standard k-ε	Interphase drag force and gas holdup distribution

Table 4.1: Review of Previous Work on Numerical Simulation of Gas-Liquid Flows

Ranade *et al.* (2001b)	SA	Two-way	Standard k-ε	Flow around impeller blades
Ranade *et al.* (2001c)	SA	Two-way and volume of fluid simulations	Standard k-ε	Gas cavity behind impeller blades
Aubin (2001)	MRF	Two-way	Standard k-ε	Liquid flow field
Deen *et al.* (2002)	SG	Two-way	Standard k-ε	Flow around impeller blades
Laakkonen *et al.* (2004)	SG	Two-way	Standard k-ε	Bubble size distribution
Lane *et al.* (2005)	MRF	Two-way	Standard k-ε	Gas holdup distribution and bubble size distribution

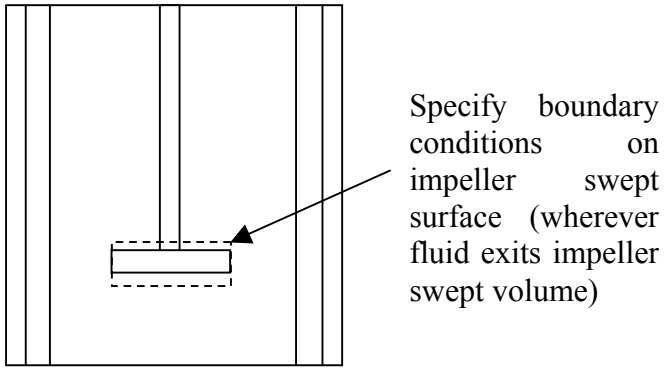

(a) Black box approach

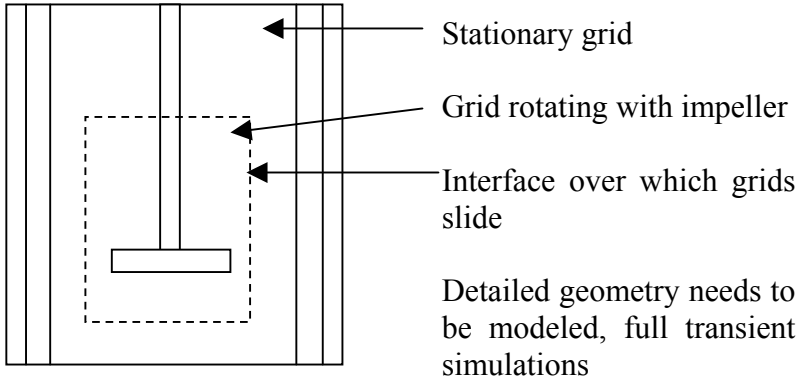

(b) Sliding mesh approach

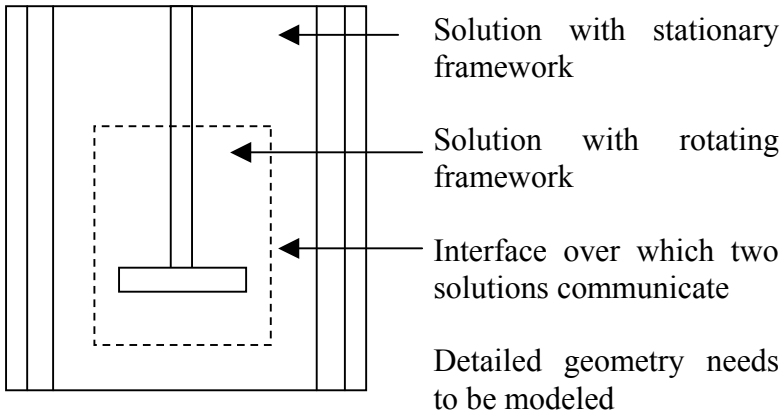

(c) Multiple reference frame or inner-outer approach

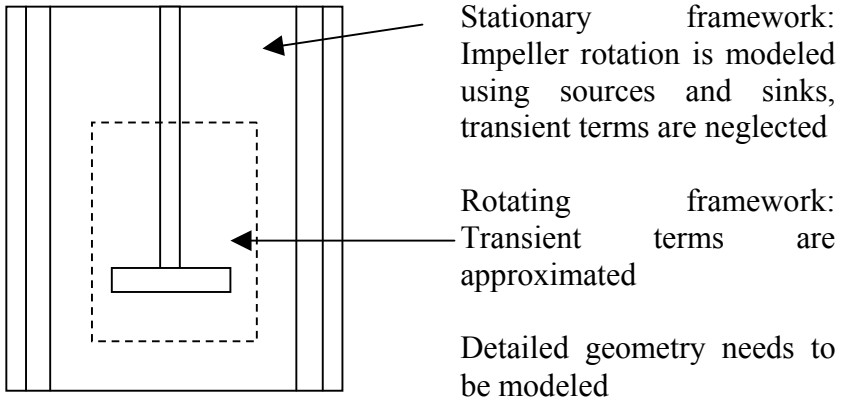

(d) Snapshot approach

Figure 4.1 Approaches for Modelling Impeller Rotation in Stirred Reactor (from Ranade, 2002)

predicting the flow field in the bulk of the reactor, its usefulness is inherently limited. Gosman *et al.* (1992); Rousar *et al.* (1994) have used the black box approach to simulate the gas-liquid flows in stirred reactor. Although, the computational model has predicted the liquid phase velocity field with reasonable accuracy, but there are few main weak points of the black box approach. The weak points are listed below:

- The numerical simulations using this approach can be extended, at best, to geometries similar or close to that for which the experimental data is available.
- The flow field near the impeller blades depend on the overall tank geometry, so that the impeller cannot be uniquely characterized.
- Extension of this approach to multiphase flows and to industrial scale reactor is not feasible because it is virtually impossible to obtain accurate boundary conditions.

This limits the use of this approach to make 'a priory' simulations of flow in stirred reactor.

To eliminate some of the limitations discussed above, attempts have been made to propose the alternate approaches to allow the explicit simulation of the whole flow field without the use of experimental data and to model the flow within the impeller region. Luo *et al.* (1993) solved the time-dependant form of governing transport equations in two domains. These two domains are fixed to the respective frames of reference, the outer one being stationary and the inner one is rotating with impeller. At the interface, the mesh was allowed shear and/or slide to accommodate the relative motion. This approach is commonly known as sliding grid and/or deforming grid approach (Perng and Murthy, 1993). The detailed geometry of the impeller needs to be modeled: impeller blades are modeled as solid rotating walls. The flow within the impeller blades is solved using the usual transport equations. The sliding mesh approach has the potential to generate 'a priory' prediction without requiring any experimental input. It can therefore be used as a design tool to screen different configurations. The sliding grid approach is available with the commercial CFD packages such as FLUENT (of Fluent Inc., USA) and so on. Friberg (1998) and Deen *et al.* (2002) used the sliding mesh approach to simulate the gas-liquid flows generated by Rushton turbine. However, following considerations make the sliding mesh approach less attractive:

- It relies on the solution of the full time varying flow in a reactor. This increases the computational requirement by an order of magnitude compared with the steady state simulations.
- Excessive computational requirement put the restrictions on the computational grids used for the simulation of the flow. Such limitations may make predictions of the flow characteristics such as turbulent kinetic energy dissipation rate, shear rates near impeller blades etc. less accurate.

For most engineering applications, knowledge of the full time varying flow field (which becomes cyclically repeating after certain number of impeller rotations) may not be necessary. It may, therefore, be desirable to develop an approach, which allows 'a priori' simulations of flow generated by an impeller of any shape with as much computational requirements as that of steady state simulations. Such an approach can then be used as a design tool for screening different alternative reactor configurations. Luo *et al.* (1994) observed that, although the flow in a stirred reactor is generally unsteady, but there is a particular radial location at/after, which for all practical purposes steady flow conditions could be assumed. This fact was then exploited to develop the approximate impeller modelling approaches. There are mainly two approaches for approximating unsteady flow in stirred reactors. In both of these approaches, a fictitious cylindrical zone with a radius more than that of impeller blade tips and less than inner edges of the baffles and height sufficient to include an entire impeller is defined (see Figure 5.1c and 5.1d). Full geometry needs to be modeled in both these approaches and the impeller blades are modeled as solid walls.

The first approach is known as the “multiple reference frame (MRF)” approach. In MRF approach, the whole reactor is divided into two regions: an inner region attached to the rotating impeller and shaft and an outer region attached to the stationary baffles and the reactor. The model equations for the inner region are solved using a rotating framework, whereas the equations for the outer region are solved using stationary framework. The solutions from both regions are matched at the interface between the rotating and stationary region via velocity transformation from one frame to the other. This velocity-matching step implicitly involves the assumption of the steady flow

conditions at the interface. Two approaches are available for modelling the communication between two regions (Marshall *et al.*, 1996). In the first approach, the flow characteristics are circumferentially averaged at the interface and then used as boundary condition for the other region. However, in the second approach, no averaging is carried out and the continuity of absolute velocity is forced to provide the neighbouring values of velocity for the region under consideration. The location of the boundary between the inner and outer regions may have some influence on the simulated results. Therefore, while implementing MRF approach, location of the interface have to be selected appropriately. The MRF approach was used in numerical studies of Lane *et al.* (1999, 2000), Lo (2000) and Aubin (2001) to simulate gas-liquid flows in a stirred reactor. Like sliding grid approach, the MRF approach is also available with commercial CFD packages such as FLUENT (of Fluent Inc., U.S.A.) and hence not discussed in detail.

The second approach is based on ignoring the relative motion between the impeller blades and baffles and taking a snapshot of the flow for a fixed relative position of the impeller blades and baffles. Ranade and van den Akker (1994) have proposed and validated the computational snapshot approach for liquid only and gas-liquid flows in stirred reactor. Ranade (2002) have used the same approach to simulate the gas-liquid flows generated by different types of impellers. In the present study same snapshot approach is used to simulate the gas-liquid flows in a stirred reactor. In the computational snapshot approach, the impeller blades are modeled as the stationary solid walls and the flow is simulated in a stationary framework for the specific impeller blade positions. The appropriate source and sink terms are specified around the impeller blades to simulate the flow generated by an impeller. If necessary, the simulations are carried out for different specific positions of the impeller blades to obtain the ensemble-average results over different blade positions. In the snapshot approach, the complete domain is divided into two regions, similar to MRF approach. In the inner region, attached to the impeller blades, time derivative terms are approximated in terms of spatial derivatives. However, in the outer region, the time derivative terms are usually quite small in magnitude in comparison with the other terms in the governing equations and are, therefore, neglected. In the present study, the snapshot approach was used to simulate the impeller rotation in reactor. The formulation of the snapshot approach is discussed in the following sub-section.

4.2.1 Computational snapshot approach

The flow generated by an impeller is governed by the pressure and centrifugal force generated by a rotating impeller. The blade rotation causes suction of the fluid at the back- side of blades and equivalent ejection of the fluid from the front side of the blades. This phenomenon of the ejection and suction needs to be modeled correctly to simulate the impeller rotation in steady framework proposed in computational snapshot approach. The development of appropriate representation of rotating impeller in a steady framework is discussed below. It is assumed that the flow is fully developed. It means that in a frame rotating with blades, profiles within impeller blades do not change with time.

Consider a finite volume representation of a basic conservation equation for a general variable, ϕ for phase q as:

$$\frac{\partial}{\partial t}\left(V_{cell}\rho_q\alpha_q\phi_q\right)+\left(area\rho_q\alpha_q U\phi_q\right)_e-\left(area\rho_q\alpha_q U\phi_q\right)_w+\ldots\ldots\ldots=$$

$$\left(area\Gamma_{\phi_q}\frac{\partial\phi_q}{\partial x}\right)-\ldots\ldots\ldots+S_{\phi_q} \qquad (4.1)$$

All the terms appearing in Equation (4.1) are formulated following the usual practice of finite volume method except the first term containing the time derivative. Usually, a volume of computational cell, V_{cell}, is considered as constant and is written outside the time derivative. For the discussion on computational snapshot approach, it is useful to consider the above form. In snapshot approach, instead of considering the moving grid, the time derivative term in above equation is approximated and a steady framework is used to solve Equation (4.1).

Consider evaluation of Equation (4.1) in a steady framework by assuming the cyclically repetitive flow between the impeller blades. As mentioned earlier, in snapshot approach, blades are considered stationary at one position. For an instant, when blades of rotating impeller coincide with the position of blades considered in snapshot simulation, the following equation is solved in a steady framework:

$$\left(area\rho_q\alpha_q U\phi_q\right)_e - \left(area\rho_q\alpha_q U\phi_q\right)_w + ... =$$
$$\left(area\Gamma_{\phi_q}\frac{\partial\phi_q}{\partial x}\right) - ..... + S_{\phi_q} - \frac{\partial}{\partial t}\left(V_{cell}\rho_q\alpha_q\phi_q\right) \quad (4.2)$$

It is necessary to approximate the time derivative terms appearing in this equation. By separating the variables, one can write the time derivative term as (for constant density fluid):

$$\frac{\partial}{\partial t}\left(V_{cell}\,\rho_q\alpha_q\,\phi_q\right) = V_{cell}\alpha_q\,\rho_q\frac{\partial}{\partial t}\left(\phi_q\right) + \rho_q\,\phi_q\frac{\partial}{\partial t}\left(\alpha_q V_{cell}\right) \quad (4.3)$$

Generally in a fixed grid simulation, volume of any computational cell remains constant. This can be applied to all the computational cells used in the snapshot approach except those directly attached to the front and backsides of blades. As the impeller rotates, the volume of cells attached to the front side of the blade decreases. Correspondingly, the volume of computational cells attached to the backside of impeller blade increases (see Figure 4.2). The rate of increase or decrease can directly be calculated from the area of interface between computational cells and impeller blade and the velocity with which impeller is rotating. Thus, for the computational cells attached to front and backside of impeller blades, the second term of the right hand side of Equation (4.3) can be written as:

$$\rho_k\,\phi_k\frac{\partial}{\partial t}\left(\alpha_k V_{cell}\right) = \rho_k\,\phi_k\alpha_k\left(2\,\pi\,N\,r\right)A_{bc} \quad (4.4)$$

where N is impeller rotational speed in revolutions per unit time. The bracketed quantity from the right hand side is the tangential velocity of the impeller blades at radial location, r, and A_{bc}, is the projection of area of the interface between computational cell and impeller blade on a plane normal to the tangential velocity. Please note that for the computational cells attached to the front side, volume decreases with time and therefore, there will be negative sign on the right hand side of Equation (4.4). For the mass continuity equation, that is, when ϕ is unity, Equation (4.4) represents the mass source and sink at the front and backsides respectively.

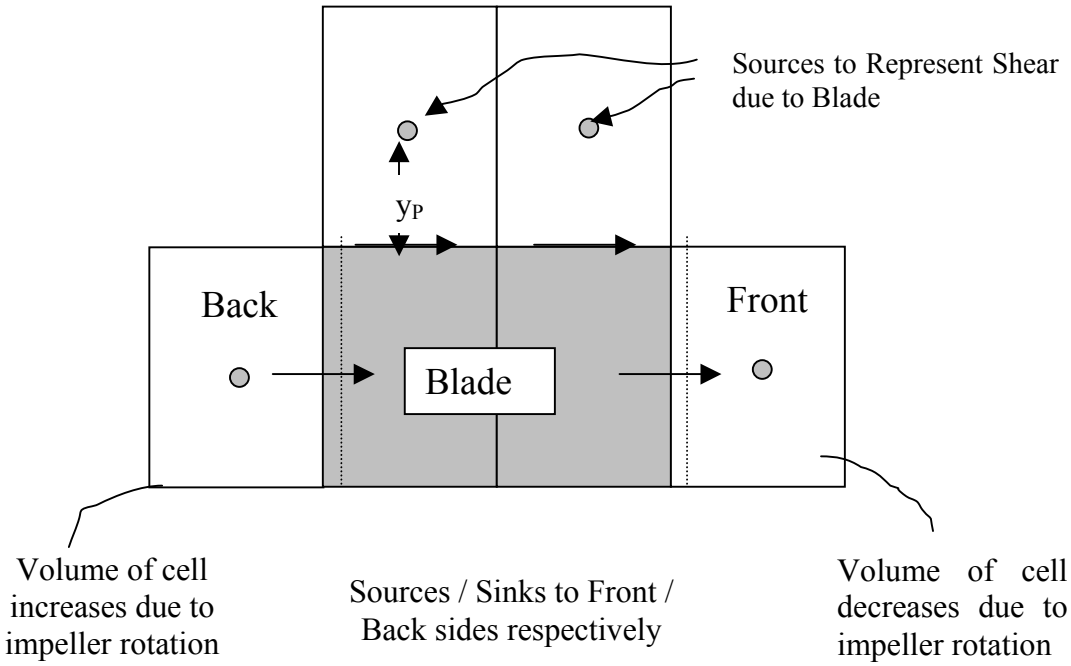

Figure 4.2: Computational Snapshot Approach (from Ranade, 2002)

Using the assumption of cyclically repetitive flow within the impeller region, the first term of the right hand side of Equation (4.3) can be approximated as:

$$V_{cell}\alpha_q \rho_q \frac{\partial}{\partial t}\left(\phi_q\right) = -V_{cell}\,\alpha_q \rho_q \left(2\pi N\right)\frac{\partial}{\partial \theta}\left(\phi_q\right) \tag{4.5}$$

Such cyclically repetitive flow will occur only in certain region around the rotating impeller. Baffles at the walls destroy such cyclically repetitive flow. Fortunately, for the region where such cyclically repetitive flow does not exist, the magnitude of time derivative terms is quite small compared to other terms in Equation (4.1) and therefore, the time derivative terms may be neglected. As there is no other way to find in which region, flow will be cyclically repetitive without solving the full time varying equations, this region has to be specified based on available empirical information. Simulations carried out with this approach, however, indicate that the predicted results are not very sensitive to the choice of the assumed region of cyclically repetitive flow. Equations (4.4) and (4.5) can be used to simulate flow generated by a rotating impeller in a steady state framework.

In addition, since the impeller blades are modeled as stationary walls, it is also necessary to include additional source terms to computational cells attached to the edges of impeller blades representing the shear caused by the rotating impeller blades (Figure 4.2). For all the computational cells attached to the four thin edges of the impeller blade, a momentum source needs to be added while solving for the tangential velocity. Though standard wall function formulation is not strictly applicable to very thin walls, it may be used in the absence of better information to define such momentum source as:

$$S_W = \left[\frac{\kappa\, y^+}{\ln\left(E\, y^+\right)}\right]\mu_l \frac{W_{BLD}}{y_P}\left(A_B\right) \tag{4.6}$$

where W_{BLD} is the tangential velocity of the blade averaged over A_B, which is the contact area between computational cell and impeller blade. y^+ is the dimensionless distance from the wall, defined as:

$$y^+ = \frac{C_D^{1/4} \rho_l k^{1/2} y_P}{\mu} \quad (4.7)$$

If the calculated value of y^+ is less than 11.225, the near wall cell center lies in the viscous sub-layer and therefore, the factor in the square bracket of Equation (4.6) is set to unity.

4.3 Multiphase Modelling Approaches

Over the past 10 years CFD based models are increasingly used by chemical industry for process analysis and optimization. Most of these processes involve single or multiphase flows with complex geometries, which may be accompanied by heat and mass transfer and chemical reactions. The complex interaction between the mass transfer, fluid flow and chemical reactions in the process equipment makes the overall prediction of the performance and the scale-up very difficult. It is therefore, of very important to develop understanding and predictive capability for simulating multiphase flow processes for better development of reactor technologies.

There are three main approaches available for the modelling of the multiphase flows:

(a) Volume of fluid approach (Eulerian framework for both the phases with reformulation of interface forces on volumetric basis).
(b) Eulerian-Lagrangian approach (Eulerian framework for the continuous phase and the Lagrangian framework for the disperse phase.
(c) Eulerian-Eulerian approach (without explicit accounting of interface between phases)

Basic concepts of these approaches are shown schematically in Figure 4.3 and are briefly discussed below.

The first approach, volume of fluid approach (VOF), is conceptually the simplest approach. In this approach, motion of all the phases is modeled by formulating local, instantaneous conservation equations for mass, momentum and energy. Such local instantaneous conservation equations can be solved using appropriate jump boundary

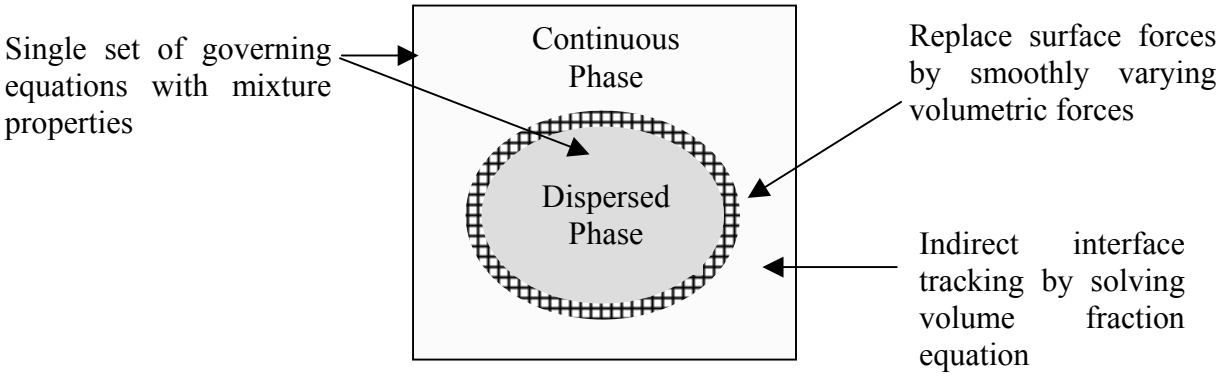

(a) Volume of fluid (VOF) Approach

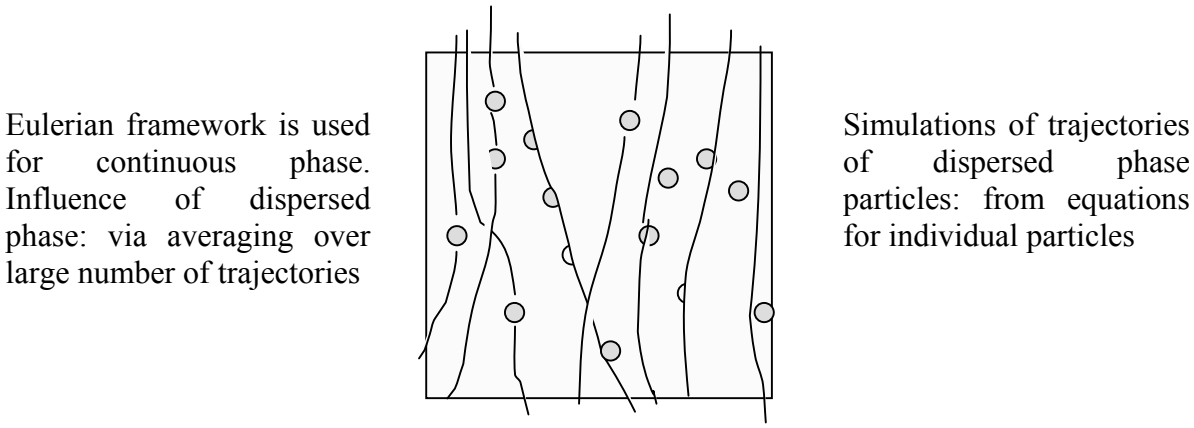

(b) Eulerian-Lagrangian Approach

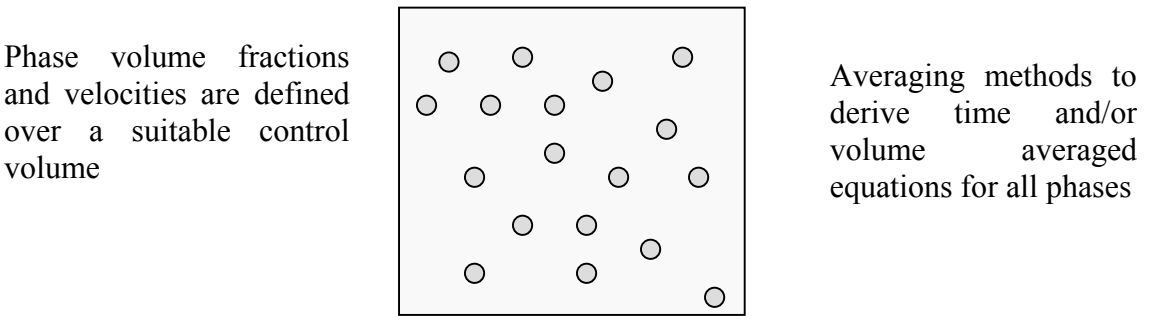

(c) Eulerian-Eulerian Approach

Figure 4.3: Modeling Approaches for Multiphase Flows (from Ranade, 2002)

conditions at the interface. However, interface between different phases may not remain stationary and imposing boundary conditions at such an interface becomes a very complicated moving boundary problem. To avoid this, instead of directly tracking the deforming and moving interface, VOF approach tracks motion of all the phases, from which motion of the interface is inferred indirectly. All the interfacial forces, therefore, have to be replaced by smoothly varying volumetric forces. If the shape and flow processes occurring near the interface are of interest, VOF approach should be used. Some of the interface related forces, like surface or adhesion forces, could be modeled accurately using this approach. This approach is, however, limited to the modelling of the processes having smallest length and time scales, for example rising of single gas bubble (Deen *et al.*, 2004), cavity shape behind the impeller blades (Ranade *et al.*, 2001c) and so on. The VOF approach can provide valuable information for developing the appropriate closures for the bubble-liquid interaction.

For systems at larger time and space scales, Eulerain-Lagrangian (EL) approach is used. In this approach, the motion of continuous phase is modeled by using Eulerian framework. The motions of dispersed phase particles (trajectories) are explicitly simulated in a Lagrangian framework. Averaging over large number of trajectories is then carried out to derive the required information for the modelling of continuous phase. In this approach, particle level processes like reactions, heat and mass transfer etc. can be simulated in adequate detail. In the case of turbulent flows, it is necessary to simulate very large number of particle trajectories to obtain meaningful averages. Therefore, even with this approach, when number of particles to be simulated increase, computational resources get stretched. The approach is, therefore, suitable for simulating dispersed multiphase flows containing low (< 10%) volume fraction of the dispersed phases. This approach can be used to extract the Lagrangian information of flow, which can provide an insight into local circulation patterns present in the reactor (Khopkar *et al.*, 2005). Similarly this approach can be use to study the interaction of the gas bubbles with the trailing vortices in a stirred reactor. In the present study, we have used this approach to calculate the circulation time distribution of the liquid phase to explain the mixing process occurring in the gas-liquid reactor. The formulation of Eulerian-Lagrangian approach is discussed in Chapter 8.

For the denser dispersed phase flows with largest time and space scales, the Eulerian-

Eulerian (EE) approach is used to model the two phases. The framework of this approach is based on the assumption of the interpenetrating continuum. The discrete character of the underlying process is averaged out to provide a model involving a continuum associated with the dispersed phase particles. This approach is, therefore, the most difficult one to understand conceptually, requiring extensive modelling efforts. Various averaging issues will have to be addressed while formulating the governing equations in this approach. If modeled successfully, this approach can be applied to multiphase flow processes containing large volume fractions of dispersed phase. It may, therefore, be extended to modelling and simulation of complex industrial multiphase reactors consisting of large number of dispersed particles. In all the reported studies, Eulerian-Eulerian approach was used to simulate the gas-liquid flows. In the present study, the same approach was used. The formulation of Eulerian-Eulerian approach is discussed in Chapter 5.

4.4 Turbulence Modelling

For most of the industrial applications, stirred reactors are usually operated in the turbulent flow regime. Although for engineering purposes the knowledge of the detail turbulent fluctuations is not required, but the effects of the turbulence on the mean flow are sought (for example, bubble breakup, particle collision). Different turbulence models (classical models: based on time-averaged Reynolds equations and Large eddy simulation: based on space-filtered equations) are available in literature to model the turbulent gas-liquid flows in process equipment.

The brief review of the published studies show that in most of the reported studies k-ε turbulence model was widely used to model the turbulence in the dispersed two phase in stirred reactor (see the brief review presented in Table 4.1). The k-ε model assumes the presence of isotropic turbulence. However, the turbulence in the stirred reactor is far from the isotropic. Apart from the anisotropic turbulence generation due to the strong rotational character of the flow, the flow in stirred reactor is periodic. To account for the anisotropic turbulence in the flow field, Bakker and van den Akker (1994) used Algebraic Stress model (ASM) for modelling the turbulence. Although, the ASM provide the cheap method to account for Reynolds stress anisotropy with slightly more

computational cost than k-ε turbulence model, the ASM is not as widely validated as the standard k-ε turbulence model. Despite the known deficiencies, the overall performance of the standard k-ε turbulence model for simulating flows in stirred vessels is adequate for many engineering applications (see for example, Ranade 2002 and references cited therein), the k-ε turbulence model was used in the present study. The formulation of k-ε turbulence model for dispersed two-phase flow is discussed in Chapter 5.

4.5 Methodology of Present Work

In the present thesis, we have simulated the gas-liquid flows generated by different types of impeller in stirred reactor using Eulerian-Eulerian approach. Initial Eulerian-Eulerian simulations were carried for gas-liquid flow generated by a Rushton turbine. The influence of different interphase forces especially interphase drag force was studied in detail. We have later developed a two-dimensional sub-model to understand the influence of free stream turbulence and presence of neighboring bubbles on the bubble drag coefficient.. The model predictions of sub-model were used to evaluate and modify the available drag force correlation. The modified correlation was then incorporated in the developed computational model and the gas-liquid flows were simulated for three different operating conditions representing the three different distinct flow regimes (Chapter 5). We have also simulated the gas-liquid flow generated by different impellers [Scaba turbine (Chapter 5); pitched blade turbine, down- as well as up- pumping and paddle turbine (Chapter 6)]. The computational model was then used to understand the flow around the impeller blades. Finally an attempt was made to understand the similarities and the differences between the flow generated by these impellers.

Chapter 5

FLOW GENERATED BY RADIAL FLOW IMPELLERS

5.1 Introduction

Reactions between gas and liquid phases are commonly carried out in chemical and allied industries. Stirred reactors are widely used to carry out these reactions because they offer adequate flexibility and control to tailor their fluid dynamics. To derive the benefits of the degrees of freedom offered by stirred reactors, it is essential to establish a relationship between process performance and fluid dynamics, on one hand, and hardware configuration and operating conditions with fluid dynamics, on the other hand.

Despite the widespread use of the stirred reactors, the relationship between fluid dynamics and hardware is not adequately understood. Design engineers are still compelled to use empirical information. This is especially true for multiphase flows in stirred reactors. Gas-liquid flows in a stirred reactor exhibit different flow regimes depending on scale, impeller details (type, diameter, location, rotational speed) and gas flow rate. In this work, the scope is restricted to study the gas-liquid flows generated by the standard Rushton turbine in a fully baffled reactor. Traditionally, empirical correlations are used to estimate prevailing flow regimes and corresponding flow characteristics. For example, Warmoeskerken and Smith (1985) have presented a flow regime map for gas-liquid flows generated by a single Rushton turbine in a fully baffled reactor. The map (shown in Figure 5.1) shows four main flow regimes: (a) vortex clinging (VC) cavities, (b) three large and three-vortex clinging (S33) cavities, (c) three large and three small (L33) cavities and (d) ragged cavity (RC) structures. Flow characteristics of these regimes differ significantly. Empirical correlations are also used to estimate overall/global parameters characterizing the flow (like power dissipation, volume fraction, mixing time and so on). However, such overall characteristics conceal variations within the reactor. Such localized information may be crucial for successful design of process equipment (for example, to avoid oxygen starvation in oxidation reactor). Besides this, availability of the relevant empirical information is often a problem either due to the cost or due to the constraints on time. Considering this, it would be most useful to develop computational models, which will allow prediction of detailed quantitative information about the prevailing flow characteristics.

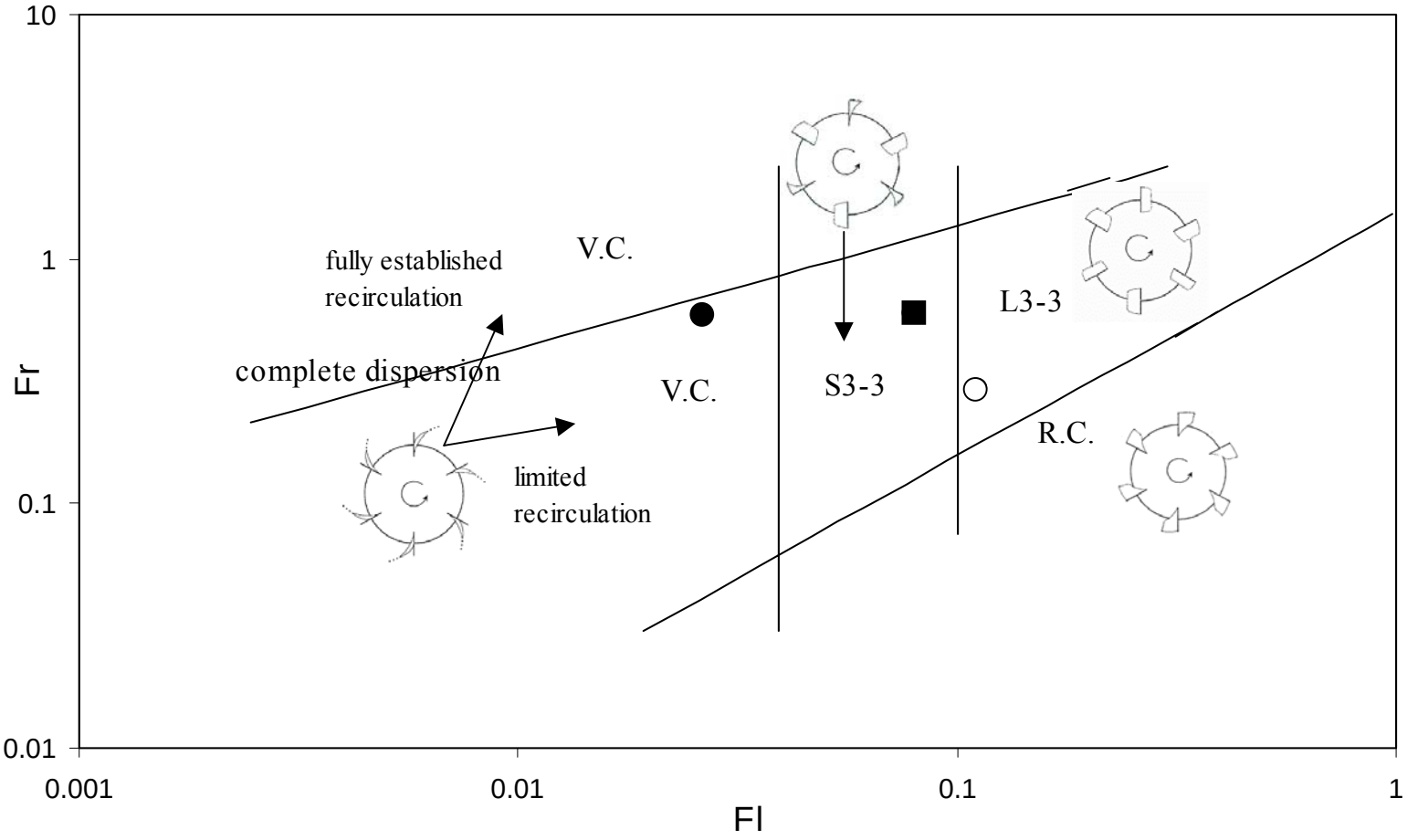

Figure 5.1: Flow Regime Map for Rushton Turbine (from Warmoeskerken and Smith, 1985),
Symbols denote operating conditions selected for simulations.

5.1.1 Previous work

A brief review of recent literature shows substantial progress in simulating flows in stirred reactors using computational fluid dynamics (CFD). CFD models were shown to be successful in simulating single-phase flow generated by impeller(s) of any shape in complex reactors (see for example, Ranade, 2002 and references cited therein). For multiphase flows, the complexity of modelling increases considerably and this remains an area for further research and development. Despite the complexity, several attempts have been made to simulate the gas-liquid flows in stirred reactors (for example, Gosman *et al.*, 1992; Morud and Hjertager, 1996; Bakker and van den Akker, 1994; Ranade and van den Akker, 1994; Ranade and Deshpande, 1999; Lane *et al.*, 1999 Lane *et al.*, 2000; Ranade *et al.* 2001b; Laakkonen *et al.*, 2004 and Lane *et al.*, 2005). Although some degree of success is reported, a number of limitations are apparent.

Earlier studies were carried out with rather inadequate number of computational cells and were qualitative in nature (see for example, Gosman *et al.*, 1992; Ranade and van den Akker, 1994). Most of the published simulations used single bubble diameter for whole reactor. Recently, Laakkonen (2004) and Lane *et al.* (2005) used a variable bubble size model based on coalescence and breakage processes. These multi-fluid models with coalescence-breakup processes increase the demands on computational resources by an order of magnitude and often are forced to use rather smaller number of computational cells (less than 80000 cells). Adequate grid resolution (usually more than 300000 cells) is however, essential to correctly simulate flow around impeller blades (Ranade and Tayaliya, 2000). Ranade and Deshpande (1999) and Ranade *et al.* (2001b) studied the influence of gas flow rate on trailing vortices of Rushton turbine. The predicted results showed the accumulation of gas behind impeller blades. However the focus was on near impeller region and whether the models are able to simulate different flow regimes quantitatively was not studied.

Apart from the simulation of trailing vortices and flow around the impeller blades, the published studies also highlight the importance of appropriate inter-phase drag force formulation (see for example, Bakker and van den Akker, 1994; Brucato *et al.*, 1998; Lane *et al.*, 2000; Pinelli *et al.*, 2004; Lane *et al.*, 2005). Inter-phase drag coefficient was found to affect both, the distribution of gas hold-up and total holdup of gas.

Though several correlations are available to estimate inter-phase drag coefficient, adequate guidelines to select appropriate model for inter-phase drag force for all the regimes of gas-liquid flow in a stirred reactor are not available. It is necessary to systematically evaluate these different inter-phase drag force models with reference to different flow regimes in gas-liquid stirred reactors. None of the previous studies were able to quantitatively simulate different prevailing flow regimes. Present work is carried out with this motivation. The detail contributions of the present work are discussed below.

5.1.2 Present contribution

In the present work, simulations were therefore carried out using two fluid model with the standard k-ε turbulence model to understand the key characteristics of the gas-liquid flow generated by the standard Rushton turbine for three different operating conditions representing three different distinct flow regimes.

As stated earlier, the previous studies highlighted the influence of the prevailing turbulence on the interphase drag force. The accurate estimation of interphase drag force is important for adequate prediction of gas holdup distribution. A separate sub-model was therefore developed to quantitatively understand the influence of turbulence and the presence of neighboring bubbles on drag acting on bubbles. This sub-model was used to identify an appropriate correlation for estimating the inter-phase drag force. The appropriate drag coefficient formulation was then used while simulating the gas-liquid flows in a stirred reactor.

The standard k-ε turbulence model was used to simulate turbulent gas-liquid flows in a stirred reactor. The commercial CFD software, FLUENT version 4.5 (of Fluent Inc., USA) with appropriate user defined subroutines, was used to simulate the turbulent two-phase flow. The computational snapshot approach was used to simulate the impeller rotation. The computational model was then used to understand the influence of interphase drag force formulation and virtual mass force on the predicted pattern of gas holdup distribution. The model predictions were evaluated by comparing predictions with the experimental data presented by Bombac *et al.* (1997) over three

different flow regimes. Bombac *et al.* (1997) have used phase detection technique to identify flow regimes and have provided one of the most detailed data set on gas hold-up distribution within the reactor. In order to complement the available information, simulations were carried out for a flat bottom stirred reactor with the geometrical specifications same as that used by Bombac *et al.* (1997). The computational model was also used to study the flow around impeller blades and understand the effect of the extent of gas accumulation on the structure of trailing vortices and the turbulent kinetic energy dissipation rate.

The gas cavities formed behind the impeller blades of Rushton turbine significantly reduce the pumping capacity and the power dissipated by the impeller, therefore having negative effects on the performance (Bruijn *et al.*, 1974). Since the discovery of these inherent problems of the Rushton turbine, there has been constant interest to improve the performance of aerated stirred reactors by modifying the impeller blade shape. The flow around impeller blades is a complex function of the impeller blade shape. In the present study the developed computational model was then used to understand the influence of the blade shape on the liquid flow generated by the Rushton turbine and Scaba turbine. The model predictions were evaluated by comparing predictions with the experimental data presented by Khopkar *et al.* (2004). In order to complement the available information, simulations were carried out for a dished bottom stirred reactor with the geometrical specifications same as that used by Khopkar *et al.* (2004).

5.2 Mathematical Modelling

5.2.1 Model equations

In a gas-liquid stirred reactor, the sparged gas interacts with the trailing vortices behind the impeller blades and forms gas cavities behind impeller blades. The cavities are then sheared at the tips and smaller bubbles are formed which are dispersed in the reactor. The size of the bubbles emanating from the cavity tip is controlled by the size of the cavity, breakage of cavity and the turbulence level around the cavity. Unfortunately no direct experimental data for turbulent kinetic energy dissipation rate is available for validating the available cavity breakage models. In principle, cavity formation behind impeller blades and their shearing at the tip can be simulated by employing volume of

fluid (VOF) approach. First attempt to carry out such simulations was made some years ago (Ranade *et al.*, 2001c). Unfortunately, the computing demands for such simulations are enormous and it was not possible to track the formation of smaller bubbles accurately. It is unrealistic at present to extend such models for simulating gas-liquid flow in stirred reactors. Therefore, in the present study the Eulerian-Eulerian approach was used.

In a gas-liquid stirred reactor, gas bubbles of different sizes co-exist. Very fine bubbles are observed in impeller discharge stream (< 1 mm) where as bubbles of the size of few mm (~5 mm) are observed in the region away from impeller (Barigou and Greaves, 1992). The width of bubble size distribution depends upon the turbulence level and prevailing flow regime. Considering that the importance of the correct prediction of the slip velocity, it might be necessary to use appropriate bubble sizes. The multi-fluid model with appropriate breakage and coalescence rates (see for example, Buwa and Ranade, 2002), which are able to simulate evolution of bubble size distribution within the reactor, may provide a better way to simulate the gas-liquid flow in stirred reactor. Unfortunately the available experimental data of bubble size distribution in stirred reactor is not adequate to calculate the parameters appearing in coalescence and break-up kernels.

Apart from the uncertainties in parameters of coalescence and break-up kernels and cavity modelling, there is significant uncertainty in estimation of inter-phase forces on gas bubbles in the presence of other bubbles and high levels of turbulence prevailing in the reactor. Considering these issues and the present state of understanding, the option of using multi-fluid computational model for stirred reactors, which requires an order of magnitude more computational resources, was not thought to be very effective. Instead, an approach of using a two-fluid model with a single bubble size for the whole reactor (and lump all the uncertainties into the inter-phase drag coefficient) was adopted here. The bubble size used in the present study and the basis for selection of the bubble size is discussed in the next sub-section.

For most of the operating regimes shown in Figure 5.1, gas-liquid flows in stirred reactor are turbulent. Therefore, the Reynolds averaged mass and momentum balance

equations for each phase in turbulent flow regime were written as (without considering mass transfer):

$$\frac{\partial(\alpha_q \rho_q)}{\partial t} + \nabla.\left(\alpha_q \rho_q \vec{U}_{q,i} - \rho_q D_{12} \nabla \alpha_q\right) = 0 \tag{5.1}$$

$$\frac{\partial\left(\alpha_q \rho_q \vec{U}_{q,i}\right)}{\partial t} + \nabla.\left(\alpha_q \rho_q \vec{U}_{q,i} \times \vec{U}_{q,i}\right) = - \alpha_q \nabla \vec{p} - \nabla.\left(\alpha_q \overline{\overline{\tau}}_{q,ij}^{(lam)}\right) - \nabla.\left(\alpha_q \overline{\overline{\tau}}_{q,ij}^{(t)}\right) + \alpha_q \rho_q g_i + \vec{F}_{12,i} \tag{5.2}$$

Here q= 1 and q= 2 denote the continuous phase (liquid) and the dispersed phase (gas), respectively and i is the direction. $\vec{U}_q$ and α_q are the time-averaged values of the velocity and volume fraction of phase q, respectively. It should be noted that time-averaged pressure, $\vec{p}$, is shared by both the phases and, therefore, appears in the governing equations of all the phases. ρ_q is the density of the phase q and D_{12} is the turbulent diffusivity of dispersed phase. $\vec{F}_{12,i}$ is the time-averaged inter-phase force in i direction and is discussed later in this section. $\alpha_q \rho_q g_i$ is the external body force on the phase q. $\overline{\overline{\tau}}_{q,ij}^{(lam)}$ is the stress tensor in the phase q due to the viscosity and $\overline{\overline{\tau}}_{q,ij}^{(t)}$ is the Reynolds stress tensor of phase q (representing contributions of correlation of fluctuating velocities in momentum transfer). In this work, we used Boussinesq's eddy viscosity hypothesis to relate the Reynolds stresses with gradients of time averaged velocity as:

$$\overline{\overline{\tau}}_{q,ij}^{(t)} = \mu_{tq}\left(\left(\nabla \vec{U}_{q,i} + \left(\nabla \vec{U}_{q,i}\right)^T\right) - \frac{2}{3} I\left(\nabla \vec{U}_{q,i}\right)\right) \tag{5.3}$$

Here, μ_{tq} is the turbulent viscosity of the phase q and I is the unit tensor. Despite the known deficiencies, the overall performance of the standard k-ε turbulence model for simulating flows in stirred reactors is adequate for many engineering applications (see for example, Ranade 2002 and references cited therein). In the present work, we have therefore used the standard k-ε turbulence model to estimate the turbulent viscosity of the liquid phase. The governing equations for turbulent kinetic energy, k and turbulent energy dissipation rate,ε, were solved only for the liquid phase and are listed below:

$$\frac{\partial}{\partial t}\left(\alpha_l \rho_l \phi_l\right) + \nabla.\left(\alpha_l \rho_l \vec{U}_{l,i} \phi_l\right) = -\nabla.\left(\alpha_l \frac{\mu_{tl}}{\sigma_{\phi l}} \nabla \phi_l\right) + S_{\phi,l} \tag{5.4}$$

where ϕ_l can be the turbulent kinetic energy or turbulent energy dissipation rate in liquid phase. The symbol $\sigma_{\phi l}$ denotes turbulent Prandtl number for variable ϕ. $S_{\phi l}$ is the corresponding source term for ϕ in the liquid phase. Source terms for turbulent kinetic energy and dissipation can be written as:

$$\begin{aligned} S_{kl} &= \alpha_l \rho_l \left[\left(G_l + G_{el}\right) - \varepsilon_l\right] \\ S_{\varepsilon,l} &= \alpha_l \rho_l \frac{\varepsilon_l}{k_l}\left[C_1\left(G_l + G_{el}\right) - C_2 \varepsilon_l\right] \end{aligned} \tag{5.5}$$

where G_l is the generation in liquid phase and G_{el} is extra generation (or dissipation) of turbulence in liquid phase. Generation due to mean velocity gradients, G_l and $\mu_{t,l}$, turbulent viscosity was calculated as:

$$G_l = \frac{1}{2}\mu_{tl}\left(\nabla \vec{U}_{l,i} + \left(\nabla \vec{U}_{l,i}\right)^T\right)^2 \qquad \mu_{tl} = \frac{\rho_l C_\varpi {k_l}^2}{\varepsilon_l} \tag{5.6}$$

Following the general practice, we have used the same values of parameters proposed for single-phase flow (C_1= 1.44, C_2= 1.92, C_ω= 0.09, σ_k= 1.0, σ_ε= 1.3) to simulate the turbulence in two-phase flow.

Extra-generation or damping of turbulence due to the presence of dispersed phase particles is represented by G_{el}. Kataoka *et al.* (1992) have analyzed the influence of the gas bubbles on the liquid phase turbulence. Motion of larger bubbles generates extra turbulence. However, their analysis indicates that the extra dissipation due to small-scale interfacial structures almost compensates the extra generation of turbulence due to large bubbles. Numerical experiments on bubble columns also indicate that one may neglect the contribution of extra turbulence generation (Ranade, 1997). Therefore, in the case of stirred reactors, where impeller rotation generates significantly higher turbulence than that observed in bubble columns, the contribution of the additional turbulence generation due to bubbles could be neglected. In the present work, therefore, G_{el} was set to zero. Standard values of the k-ε model parameters were used in the

present simulations. No separate equations were solved for modeling turbulence in the dispersed phase. Instead, the turbulent viscosity of the dispersed phase was estimated from the knowledge of turbulent viscosity of liquid phase as:

$$\mu_{tg} = \frac{\rho_g}{\rho_l} \mu_{tl} \tag{5.7}$$

In the Reynolds averaging procedure, the turbulent dispersion of dispersed phase was modeled using the turbulent diffusivity, D_{12}, in mass balance equation (Equation 5.1). The numerical study of Lane *et al.* (2000) indicated that the turbulent dispersion terms were significant only in the impeller discharge stream. Even near the impeller, the influence of dispersion terms on predicted results was not quantitatively significant (difference was less than 5%). It should be noted that only turbulent eddies larger than bubble diameter will contribute to the dispersion. Under the usual operating conditions of gas-liquid flow in laboratory scale stirred reactors (with smaller impeller blades leading to smaller scales of energy containing eddies), the contribution of eddies larger than bubbles is unlikely to be significant. Considering these results, the turbulent dispersion of dispersed phase was not considered in the present study (the third term in the left hand side of Equation 5.1 was neglected).

Inter-phase coupling terms make two-phase flows fundamentally different from single-phase flows. The formulation of time-averaged $\vec{F}_{12,i}$, therefore, must proceed carefully. The interphase momentum exchange term consists of four different interphase forces: Basset history force, lift force, virtual mass force and drag force (see Ranade, 1992 for more details). Basset force arises due to the development of a boundary layer around bubbles and is relevant only for unsteady flows. Basset force involves a history integral, which is time-consuming to evaluate and in most cases, its magnitude is much smaller than the interphase drag force. Bubbles experience lift force due to vorticity and shear in continuous phase flow field. Lift force is proportional to the vector product of the slip velocity and the curl of liquid velocity. Lift force is significant if the velocity gradients are large. In stirred reactors, velocity gradients are significant mainly near the impeller. In the bulk region of the reactor, the velocity gradients are not large. In the vicinity of impeller, pressure gradients and interphase drag forces would mainly dominate motion of bubbles. An order of magnitude analysis indicates that the

magnitude of lift force is much smaller than the interphase drag force (Lane *et al.*, 2000). The virtual mass force needs to be considered when a secondary phase accelerates relative to the primary phase. It becomes significant, when the secondary phase density is much smaller than the continuous phase density (as in gas-liquid stirred reactor or bubble column reactor). Considering this, in the present work, Basset and lift forces were not considered. The virtual mass and drag force terms were included in the interphase momentum exchange term as:

$$\vec{F}_{12,i} = \vec{F}_{D,i} + \vec{F}_{VM,i} \tag{5.8}$$

The virtual mass term in i direction is given as:

$$\vec{F}_{VM,i} = \alpha_2 \rho_1 C_{VM} \left(\frac{D\vec{U}_{2,i}}{Dt} - \frac{D\vec{U}_{1,i}}{Dt} \right) \tag{5.9}$$

where C_{VM} is virtual mass coefficient. In the present work, the value of C_{VM} was set to 0.5.

The inter-phase drag force exerted on phase 2 in i direction is given by:

$$\vec{F}_{D,i} = -\frac{3\alpha_1 \alpha_2 \rho_1 C_D \left(\sum \left(\vec{U}_{2,i} - \vec{U}_{1,i} \right)^2 \right)^{0.5} \left(\vec{U}_{2,i} - \vec{U}_{1,i} \right)}{4 d_b} \tag{5.10}$$

As discussed earlier, the estimation of drag force is critical for accurate prediction of gas distribution within stirred reactors. Most of the available correlations to estimate drag coefficient appearing in Equation (5.10) relate the value of drag coefficient to bubble Reynolds number. These correlations are valid for a single bubble rising in a stagnant liquid. In this work, the value of drag coefficient for a single bubble rising in a stagnant liquid, C_{D0} was estimated using the following correlation of Tsuchiya *et al.* (1997):

$$C_{D0} = \max\left\{ \left(\frac{2.667 * Eo}{Eo + 4.0} \right), \left(\frac{24}{\mathrm{Re}_b} * \left(1 + 0.15 * \mathrm{Re}_b^{0.687} \right) \right) \right\} \quad \text{and} \quad Eo = \frac{g(\rho_l - \rho_g) {d_b}^2}{\sigma_l} \tag{5.11}$$

It is likely that the presence of neighboring bubbles affects the drag coefficient of a bubble. Ishii and Zuber (1979) studied the effect of neighboring particles or bubbles on drag coefficient and proposed a correction factor as a square of continuous phase holdup. Gas volume fraction in the bulk region of the tank is less than 5% in most of the cases studied by Bombac *et al.* (1997). For such situations, the magnitude of drag reduction estimated by Ishii and Zuber (1979) correlation is less than 10%. Therefore, in this work the correction factor due to the presence of other bubbles was not considered. Unlike a case of a bubble flowing through a stagnant liquid, where flow around a bubble is dominated by the motion of that bubble, in stirred reactors, bubbles experience significantly higher turbulence generated by impellers. Unless, the influence of this prevailing turbulence on bubble drag coefficient is accounted, the CFD model will not predict the pattern of gas holdup distribution adequately. Relatively few attempts (experimental as well as numerical) have been made to understand the influence of prevailing turbulence on drag coefficient (see for example, Clift and Gauvin, 1971; Bakker and van den Akker, 1994; Brucato *et al.*, 1998; Pinelli *et al.*, 2004; Lane *et al.*, 2005). Bakker and van den Akker (1994), Brucato *et al.* (1998) and Lane *et al.* (2005) have attempted to relate the influence of turbulence on drag coefficient to the characteristic spatio-temporal scales of prevailing turbulence and therefore seem to be promising. These are briefly discussed here.

Bakker and van den Akker (1994) have attempted to relate the influence of turbulence on drag coefficient by using a modified Reynolds number in a usual correlation developed for the stagnant liquid. Their proposal is given in Equation (5.12):

$$C_D = \frac{24}{\mathrm{Re}^*}\left[1 + 0.15\left(\mathrm{Re}^*\right)^{0.687}\right] \qquad \because \mathrm{Re}^* = \frac{\rho_l U_{slip} d_b}{\mu_l + \frac{2}{9}\mu_t} \tag{5.12}$$

It should be noted that the effective viscosity is calculated by adding some fraction of turbulent viscosity to the molecular viscosity. The fraction is an adjustable parameter and the value of 2/9 is recommended.

Brucato *et al.* (1998) attempted to relate the influence of turbulence on drag coefficient to the ratio of the particle size and the Kolmogorov length scale of the turbulence as (based on their experiments with solid particles in Taylor Couette apparatus):

$$\frac{C_D - C_{D0}}{C_{D0}} = K\left(\frac{d_b}{\lambda}\right)^3 \tag{5.13}$$

where C_D is the drag coefficient in turbulent liquid, C_{D0} is the drag coefficient in stagnant liquid, d_b is bubble/ particle diameter and λ is the Kolmogorov length scale (based on volume averaged energy dissipation rate). The correlation constant K was reported to be 8.67×10^{-04}. It should be noted that despite significantly non-uniform distribution of ε in a Taylor-Couette apparatus, the correlation was based on volume averaged energy dissipation rate. This makes the direct extension of the correlation to different configurations difficult and may necessitate a use of different multiplier than that proposed by Brucato at al. (1998). The experimental data presented by Brucato *et al.* (1998) also clearly show a systematic trend of decreasing value of multiplier with an increase in the particle size (see Figure 11 of Brucato *et al.*, 1998, where particles of 63-71 micron, of 212-250 microns and of 425-500 micron show trends with decreasing intercept with an increase in particle size). This trend indicates that the value of *K* for bubbles (which are much larger than solid particle considered in their work) will be much lower than that proposed by Brucato *et al.* (1998). Recent study of Lane *et al.* (2000) also support the lower value of K. Lane *et al.* (2002) found better agreement with experimental data using 100 times smaller value of K. No clear guidelines are however available on deciding an appropriate value of K.

Recently, Lane *et al.* (2005) correlated the available data of settling velocity of particles and the rise velocity of bubbles in a turbulent flow with particle relaxation time (τ_p) and integral time scale of turbulence (T_L) as:

$$\frac{C_D}{C_{D0}} = \left[1 - 1.4\left(\frac{\tau_p}{T_L}\right)^{0.7} \exp\left(-0.6\frac{\tau_p}{T_L}\right)\right]^{-2} \tag{5.14}$$

The experimental data used for the correlation was taken for particle or bubble sizes less than 1000 microns. The adequacy of the proposed correlation for larger particles of size 4000 microns is not known. The proposed correlation predicts a decrease in the drag coefficient values for higher values of ratio of two time scales. No experimental data supporting this trend was reported.

Considering the importance of accurate accounting of the prevailing turbulence in the simulation of gas-liquid flow in stirred reactors, the three alternative proposals (Equation 5.12, 5.13 and 5.14) were investigated further in this study. For gaining a better understanding of the influence of prevailing turbulence on drag coefficient, flow of liquid over a regular array of bubbles has been considered. For reducing demands on computational resources, the flow was modeled in a two-dimensional solution domain using a 'unit cell' approach (discussed later in more detail). This means, flow through a bank of regularly arranged cylinders was computationally studied. Influence of Reynolds number, volume fraction of bubbles and prevailing turbulence level on drag coefficient was investigated. The standard k-ε turbulence model was used to simulate the turbulence in the flow. The level of prevailing turbulence was varied by specifying different magnitudes of additional source for turbulence generation by following Equation (5.15):

$$G = \frac{1}{2}\mu_t\left(\nabla\vec{U}_i + \left(\nabla\vec{U}_i\right)^T\right)^2 + f_e \qquad (5.15)$$

where, f_e is the extra source of turbulence. By manipulating the value of such extra source, volume averaged values of the effective viscosity, Kolmogorov length scales and integral time scales of turbulence were varied over a range of interest. The trends observed in the two-dimensional model are expected to be valid for the three-dimensional flow over bubbles. The predicted effects on the drag coefficients were therefore used to identify an appropriate correlation for estimating inter-phase drag force on bubbles in a turbulent flow. The developed correlation was then evaluated for simulating gas-liquid flows in a stirred reactor by comparing simulated results with the experimental data of Bombac *et al.* (1997).

The gas-liquid flow in stirred reactor was simulated using the computational snapshot approach. The details of the snapshot approach are discussed in Chapter 4 and hence not repeated here. In snapshot approach, the choice of blade positions with respect to baffle positions is rather arbitrary. Ranade and van den Akker (1994) have studied the sensitivity of simulated results with the exact position of blades relative to baffles by comparing predicted results of five snapshots. Their results clearly indicate that though local values may differ for different relative positions, angle averaged results are not sensitive to the actual positioning of impeller blades. They also compared ensemble-averaged results (over five snapshots) for the mid-baffle plane with angle- averaged results. For the region away from the impeller, both the averaging methods yield almost the same results. Predicted values of overall characteristics like pumping number and power number are also not sensitive to relative positions of impeller blades and baffles. Therefore, only one snapshot was considered in the present work.

5.2.2 Solution domain and boundary conditions

5.2.2.1 Flow through regularly arranged cylindrical objects

A 'unit cell' approach was used to model the single-phase flow through regularly arranged cylindrical objects (applicability of unit cell approach to model flows through regular array is recently discussed by Gunjal *et al.*, 2005). Cylinders were arranged in a regular square array (see Figure 5.2). The spacing between the cylinders was calculated by specifying the relevant value of volume fraction. Figure 5.2 shows cylindrical objects having diameter (d_b) equal to 5×10^{-3} m with volume fraction equal to 15%. The unit cell approach uses the geometrical symmetry to significantly reduce the computational requirements (also shown in Figure 5.2). All sides of the unit cell were defined as periodic walls. Considering the negligible shear exerted by the gas flow within bubble on the surrounding liquid, the walls of the cylindrical objects were defined as zero shear walls. Simulations were carried out for different Reynolds numbers (by specifying different values of liquid mass flow rates through the unit cell), volume fractions (by considering different geometries) and levels of prevailing turbulence (by specifying different magnitudes of extra generation, f). In the stirred

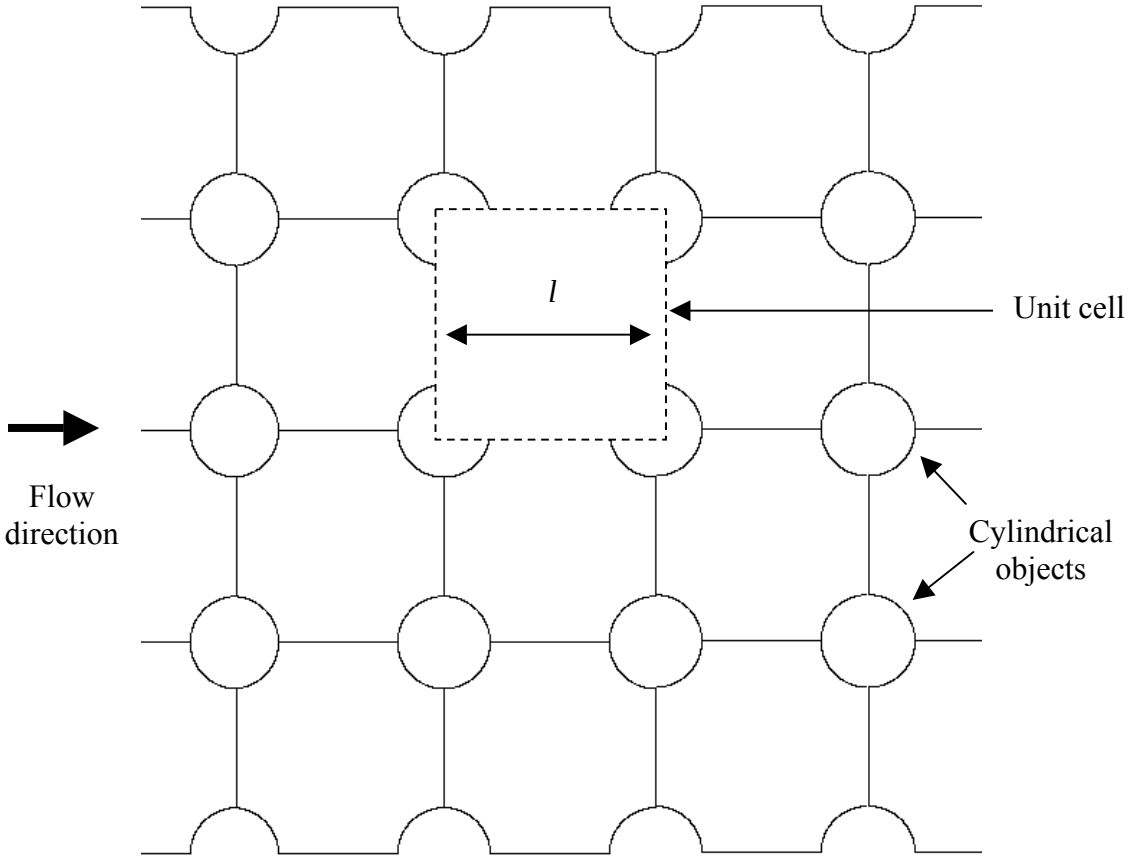

$$l = \sqrt{\frac{\pi/4\, d_b^{\,2}}{\varepsilon_g}}$$

d_b: diameter of cylindrical object
ε_g: gas holdup

Grid Details	:
Total grid	: 199,809
x × y	: 447 × 447

Figure 5.2: Solution Domain for Flow through Regular Array of Cylinders

reactor, bubble Reynolds number varies in the range of 200 to 800. The mass flow rate of the liquid was then calculated as:

$$u_\infty = \frac{\mathrm{Re}\,\mu}{\rho d_b} \qquad m = \rho u_\infty A_f \tag{5.16}$$

where, A_f is the flow area ($\propto$ l shown in Figure 5.2) and m, is the mass flow rate of the liquid. The direction of net flow of liquid was set as shown in Figure 5.2. The simulations were carried out for three Reynolds numbers (200, 500 and 800) and for two values of volume fraction of gas (5% and 15%). The turbulent flow around the cylinders with zero shear walls was simulated using FLUENT 6.1.22 (of Fluent Inc., USA). The magnitude of f was varied in the range of 0 kg/s^3-m to 5000 kg/s^3-m to cover the variation in the Kolmogorov length scale between 1×10^{-04} to 1×10^{-06}m, as usually observed in stirred reactors.

The prediction of flow characteristics, especially turbulence quantities are sensitive to the number of grid nodes, grid distribution within the solution domain and the discretization scheme. In the present work, we used QUICK (Quadratic Upstream Interpolation for Convective Kinetics) discretization scheme with limiter function (SUPERBEE of Roe, 1985) to avoid non-physical oscillations. A commercial grid-generation tool, GAMBIT 2.0 (of Fluent Inc., USA) was used to model the geometry and to generate the body-fitted grids. The geometry was modeled with eight different grid size distributions with total number of computational cells ranging from 5,000 to 800,000. The predicted results are discussed in the next section.

5.2.2.2 Gas-liquid stirred reactor

In the present work, experimental setup used by Bombac *et al.* (1997) was considered. All the relevant dimensions like impeller diameter, impeller off-bottom clearance, reactor height and diameter, sparger location and diameter and so on were same as used by Bombac *et al.* (1997). Absence/presence of bottom bearing was assumed to have a negligible effect on gas holdup distribution pattern. Hence, to simplify the modelling of geometry, bottom bearing was not considered in present work. The system investigated, consists of a cylindrical, flat-bottomed reactor (of diameter, T = 0.45 m, height, H =

0.45 m). Four baffles of width T/12 were mounted perpendicular to the reactor wall with a gap of 0.007 m. The shaft of the impeller was concentric with the axis of the reactor and extended till the bottom of the reactor. A standard Rushton turbine (of diameter, $D_i = T/3$) was used for all the simulations. The impeller off-bottom clearance was ($C = T/4$) measured from the bottom of reactor.

Considering the symmetry of the geometry, half of the reactor was considered as a solution domain (see Figure 5.3). It should be noted that, even if the geometry is symmetric, flow might not be symmetric. For example, flow regimes S33 and L33 do not exhibit half plane symmetry. However, in the present work, simulations were carried out with half of the reactor to reduce computational demands. The objective was to examine whether the computational model is able to capture the variation in gas accumulation for different flow regimes correctly if not the asymmetry. The baffles were considered at angles of 45^o and 135^o. Impeller was positioned in such a way that three blades were located at angles of 30^o, 90^o and 150^o. As discussed by Ranade (2002), the computational snapshot approach divides the solution domain in an inner region, in which time derivative terms are approximated using spatial derivatives and an outer region, in which time derivative terms are neglected. The boundary between the inner and outer region needs to be selected in such a way that the predicted results are not sensitive to its actual location. Fortunately, for the standard impellers with impeller diameter of about one third of reactor diameter, the predicted results are not sensitive to the actual location of the boundary between inner and outer region (Ranade 2002 and references cited therein). In the present work, for all the simulations, the boundary of the inner region was positioned at $r = 0.138$ m and $0.09 \text{ m} \leq z \leq 0.265$ m (where z is axial distance from the bottom of the reactor).

The ring sparger (of diameter $d_{sp} = T/3$) was located at 0.075 m from the bottom of the reactor. The sparger was modelled as a solid wall and a mass source for gas phase was specified one cell above sparger to simulate gas introduction in the reactor. Special boundary conditions are needed to simulate gas-liquid interface at the top through which bubbles escape the solution domain. Recently, Ranade (2002) has discussed different possible approaches to treat gas-liquid interface in detail. We have modelled top surface of the dispersion as velocity inlet. The outgoing (axial) velocity of gas

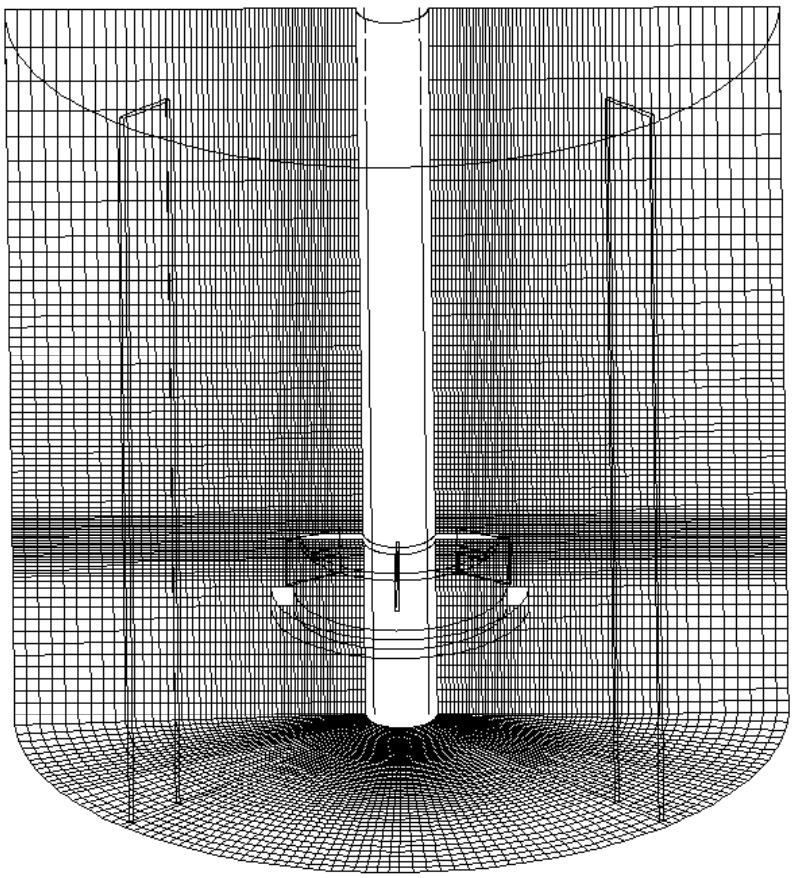

Grid Details	:
$r \times \theta \times z$	: $63 \times 98 \times 82$
Impeller blade	: $18 \times 1 \times 19$
Inner region	: $15 \leq k \leq 65$ $j \leq 45$

Figure 5.3: Computational Grid and Solution Domain of Stirred Reactor

bubbles was set equal to the terminal rise velocity of gas bubbles (estimated as 0.2 m/s for air bubbles). Normal liquid velocity was set to zero. Implicit assumption here is that gas bubbles escape the dispersion with terminal rise velocity. Since the liquid velocity near the top gas-liquid interface is small and the overall volume fraction of gas is also small (< 5%), this assumption is reasonable. It should be noted that even after defining top surface as an inlet, gas volume fraction at the top surface is a free variable.

It would have been appropriate to specify the value of effective bubble size in the computational model by using experimental data. Unfortunately, Bombac *et al.* (1997) did not measure the bubble size distribution in their experimental study. Barigou and Greaves (1992) have reported experimentally measured bubble size distribution for the stirred reactor of diameter 1m (of size T = H = 1m, C = T/4 and D_i = T/3; operating range-Fr: 0.37-0.765, Fl: 0.015-0.06). Their experimental data clearly indicates that the bubble size in the bulk region of the reactor varies between 3.5 mm to 4.5 mm for high gas flow rate. The reported values of Sauter mean diameter, D_{32}, for the cases relevant to those studied by Bombac *et al.* (1997) are about 4 mm. [D_{32} =3.75 mm for Fl = 0.04 & Fr = 0.765 and D_{32} = 4.24 mm for Fl = 0.056 & Fr = 0.37]. We have therefore used effective bubble size as 4 mm for the S33 and L33 regimes. For the VC regime, where higher impeller speed was used, a bubble size of 3 mm was used in the simulations. Fluid properties were set as those of water and air for primary and secondary phase respectively.

It is very important to use an adequate number of computational cells while numerically solving the governing equations over the solution domain. The prediction of turbulence quantities is especially sensitive to the number of grid nodes and grid distribution within the solution domain. Our previous work (Ranade *et al.*, 2001a) as well as other published work (for example, Ng *et al.*, 1998, Wechsler *et al.* 1999) gives adequate information to understand the influence of number of grids on the predicted results. It was demonstrated that, in order to capture the details of flow near impeller, it is necessary to use at least 200 grid nodes to resolve the blade surface. Based on the previous experience and some preliminary numerical experiments, the numerical simulations for gas-liquid flows in stirred reactor for all three operating conditions were carried out for grid size ($r \times \theta \times z$: 63 × 98 × 82). In the present work we have used (r ×

θ × z: 18 × 1 × 19) grid nodes covering the impeller blade. The boundary of the inner region was positioned at $j \leq 45$ and $15 \leq k \leq 65$ (where j is cell number in radial direction from shaft and k is cell number in axial direction from the bottom of the reactor). The computational grid used in the present work is shown in Figure 5.3. In the present work, QUICK discretization scheme with SUPERBEE limiter function (to avoid non-physical oscillations) was used. Standard wall functions were used to specify wall boundary conditions. The computational results are discussed in the following section.

5.3 Results and Discussion

5.3.1 Influence of prevailing turbulence on drag coefficient

Preliminary simulations of flow through regularly arranged cylindrical objects were first carried out for all eight-grid size distributions, varied from 5,000 to 800,000 computational cells. Based on these numerical simulations, it was found that about 200,000 computational cells were sufficient to predict the flow adequately (the difference between the predicted values of pressure drop for 200,000 and 800,000 grid nodes was found to be within 7% of the pressure drop value for 800,000 grid nodes). Therefore, all the further simulations were carried out with the grid size of about 200,000.

Typical predicted results for the gas holdup value equal to 15%, Reynolds number equal to 200 and for without any source for extra turbulence are shown in Figure 5.4 in the form of velocity vectors and the contours of predicted pressure and turbulent kinetic energy. The predicted velocity field around the cylindrical objects is shown in Figure 5.4a(i). The predicted velocity field shows the presence of wake behind the cylindrical objects. The predicted pressure and turbulent kinetic energy distribution around the cylindrical objects is shown in Figure 5.4b(i) and 5.4c(i). The predicted results show the presence of high pressure and high turbulent kinetic energy region near the nose of the cylindrical objects. The approach and computational models were validated (not shown here for the sake of brevity) by comparing predicted results with published correlations of Dybbs and Edward (1984) and Prakash *et al.* (1987). The computational

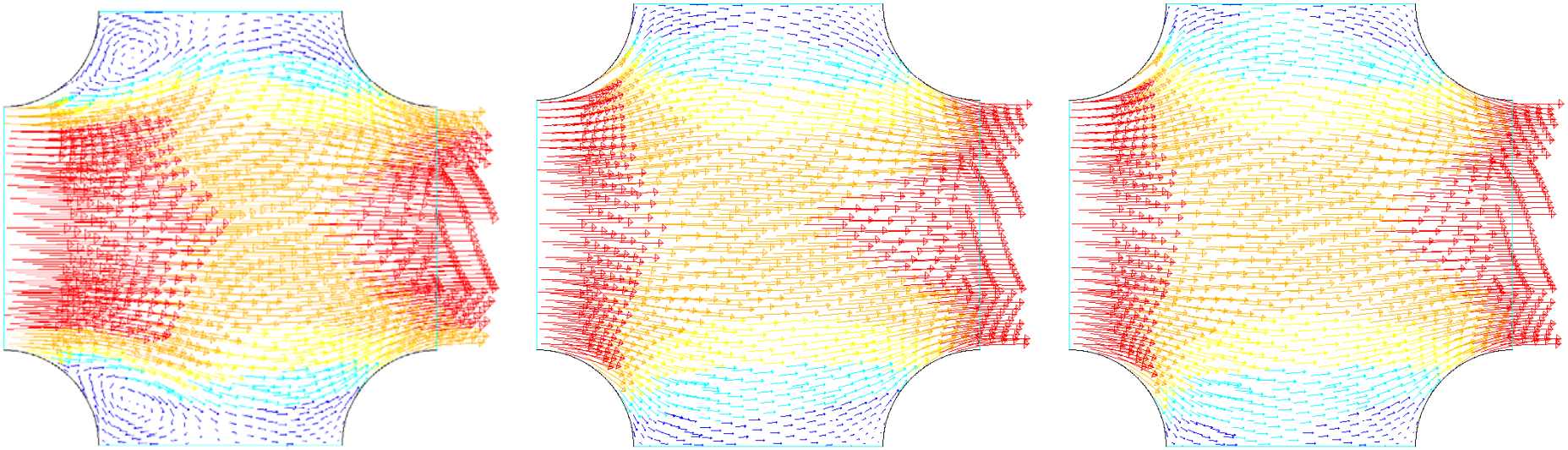

(i) $\lambda = 1.32\times10^{-4}$ m, $f_e = 0$ kg/s^3-m (ii) $\lambda = 1.02\times10^{-4}$ m, $f_e = 2$ kg/s^3-m (iii) $\lambda = 9.5\times10^{-5}$ m, $f_e = 5$ kg/s^3-m

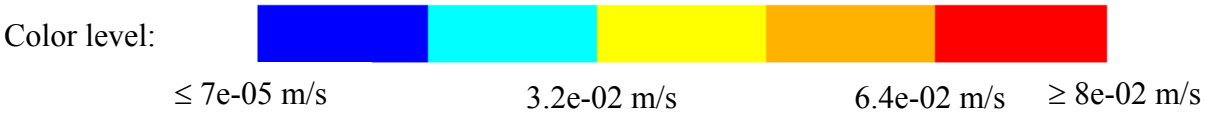

(a) Velocity field around the cylindrical objects

Figure 5.4: Simulated Flow through Array of Cylinders [Continue on next page]

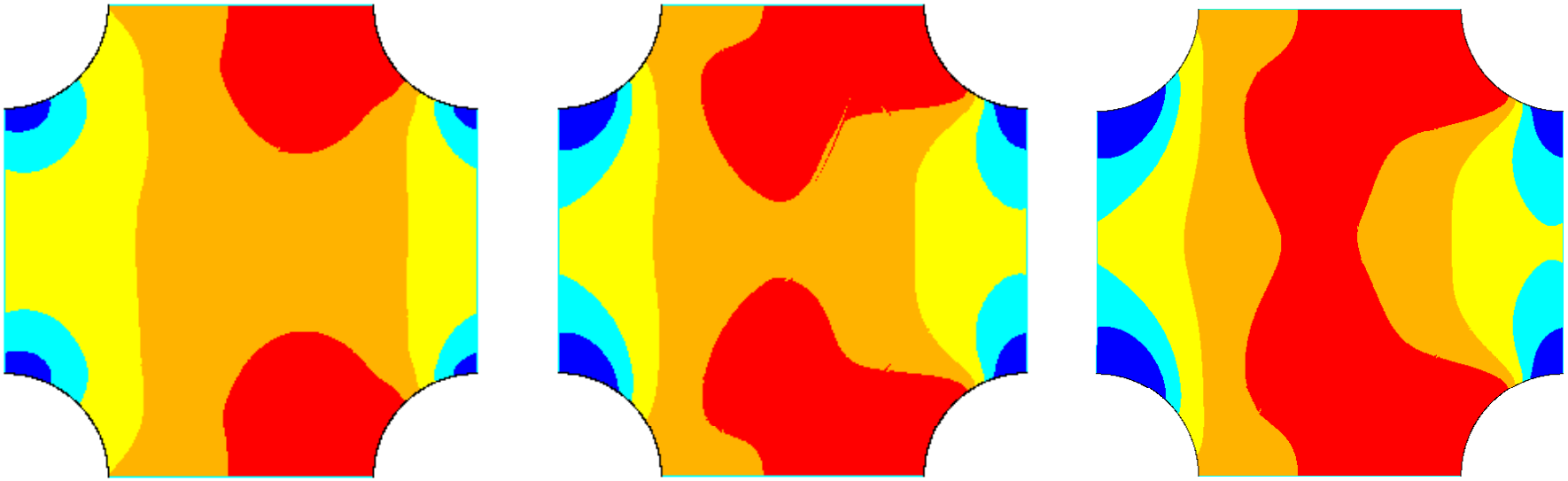

(i) $\lambda = 1.32\times10^{-4}$ m, $f_e = 0$ kg/s^3-m (ii) $\lambda = 1.02\times10^{-4}$ m, $f_e = 2$ kg/s^3-m (iii) $\lambda = 9.5\times10^{-5}$ m, $f_e = 5$ kg/s^3-m

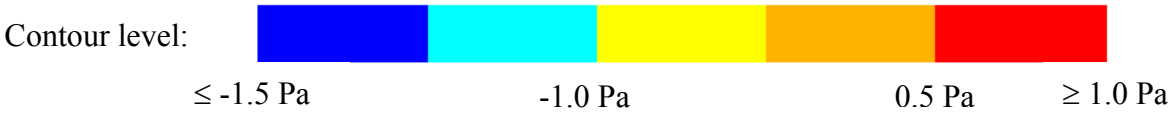

(b) Pressure field around the cylindrical objects

Figure 5.4: Simulated Flow through Array of Cylinders [Continue on next page]

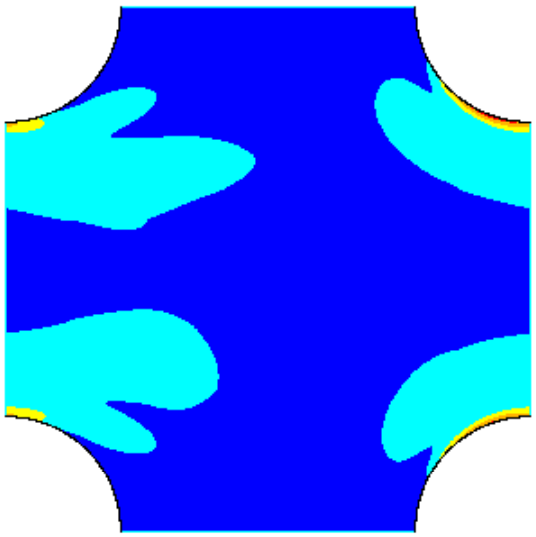

(i) $\lambda = 1.32\times10^{-4}$ m, $f_e = 0$ kg/s^3-m

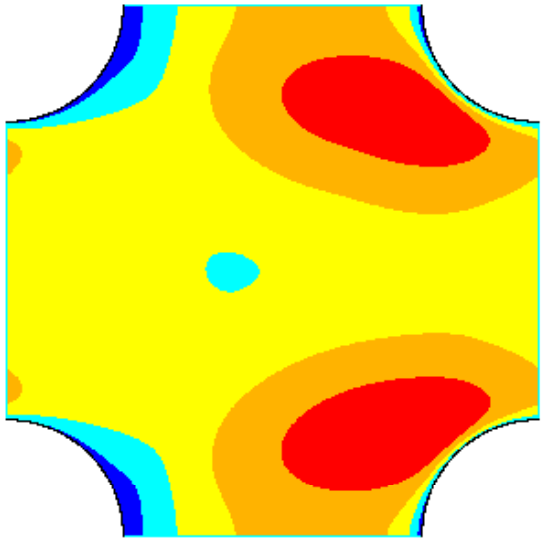

(ii) $\lambda = 1.02\times10^{-4}$ m, $f_e = 2$ kg/s^3-m

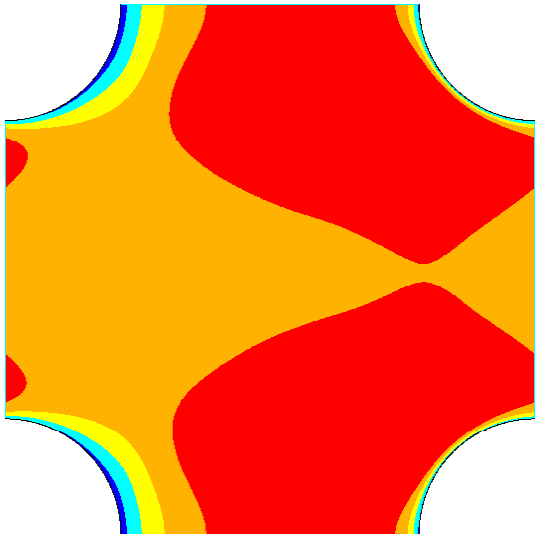

(iii) $\lambda = 9.5\times10^{-5}$ m, $f_e = 5$ kg/s^3-m

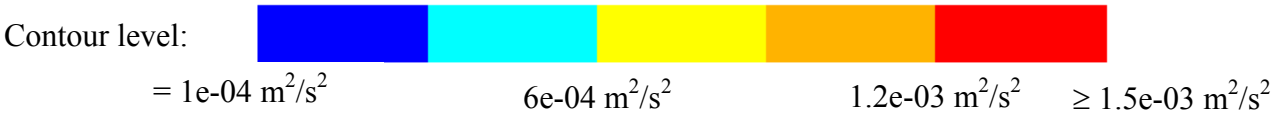

(c) Turbulent kinetic energy field around cylindrical objects

Figure 5.4: Simulated Flow through Array of Cylinders

model was then extended to understand the influence of free stream turbulence on the bubble drag coefficient.

An additional source for turbulent kinetic energy was specified using a user-defined function to simulate the presence of extra turbulence in flowing liquid. The magnitude of this source term was varied to cover the variation of Kolmogorov length scales of turbulence in the range of 1×10^{-04} to 1×10^{-06}, as usually observed in stirred reactor. The predicted results show significant increase in the pressure drop values with increase in the level of turbulence. The comparison of the predicted results for with and without extra turbulence (Figure 5.4) shows significant change in the flow field around the cylindrical objects. As the level of prevailing turbulence increases, the high-pressure region in front of the cylinders increases resulting into higher form drag. The values of drag coefficients for these different cases were calculated from the predicted pressure drop (see Gunjal *et al.*, 2005 for more details). The predicted increase in drag coefficient with an increase in the prevailing turbulence is consistent with the previously reported experimental studies (see for example, Uhlherr and Sinclair, 1970; Clift and Gauvin, 1971; Magelli *et al.*, 1990).

For quantitative analysis of influence of prevailing turbulence, the approach of Brucato *et al.* (1998) was selected. The results predicted by the CFD model were compared with the correlations of Brucato *et al.* (1998), Pinelli *et al.* (2004), Bakker and van den Akker (1994) and Lane *et al.* (2005) in Figure 5.5. The comparison brings out several salient points. It can be seen from Figure 5.5 that the predicted values for the smaller solid (noted by solid triangles) particles (these simulations were carried out by following similar approach with no slip boundary conditions at the walls of cylinders) follow trends of correlation of Brucato *et al.* (1998). As Reynolds number increases, the predicted values shift towards right indicating decrease in the magnitude of proportionality constant in the correlation of Brucato *et al.* (1998). This is consistent with the experimental data reported by them. The predicted results deviate from the trends estimated by correlations of Pinelli *et al.* (2004) and Lane *et al.* (2005) for higher ratios of d_b/λ. These correlations were therefore not considered further.

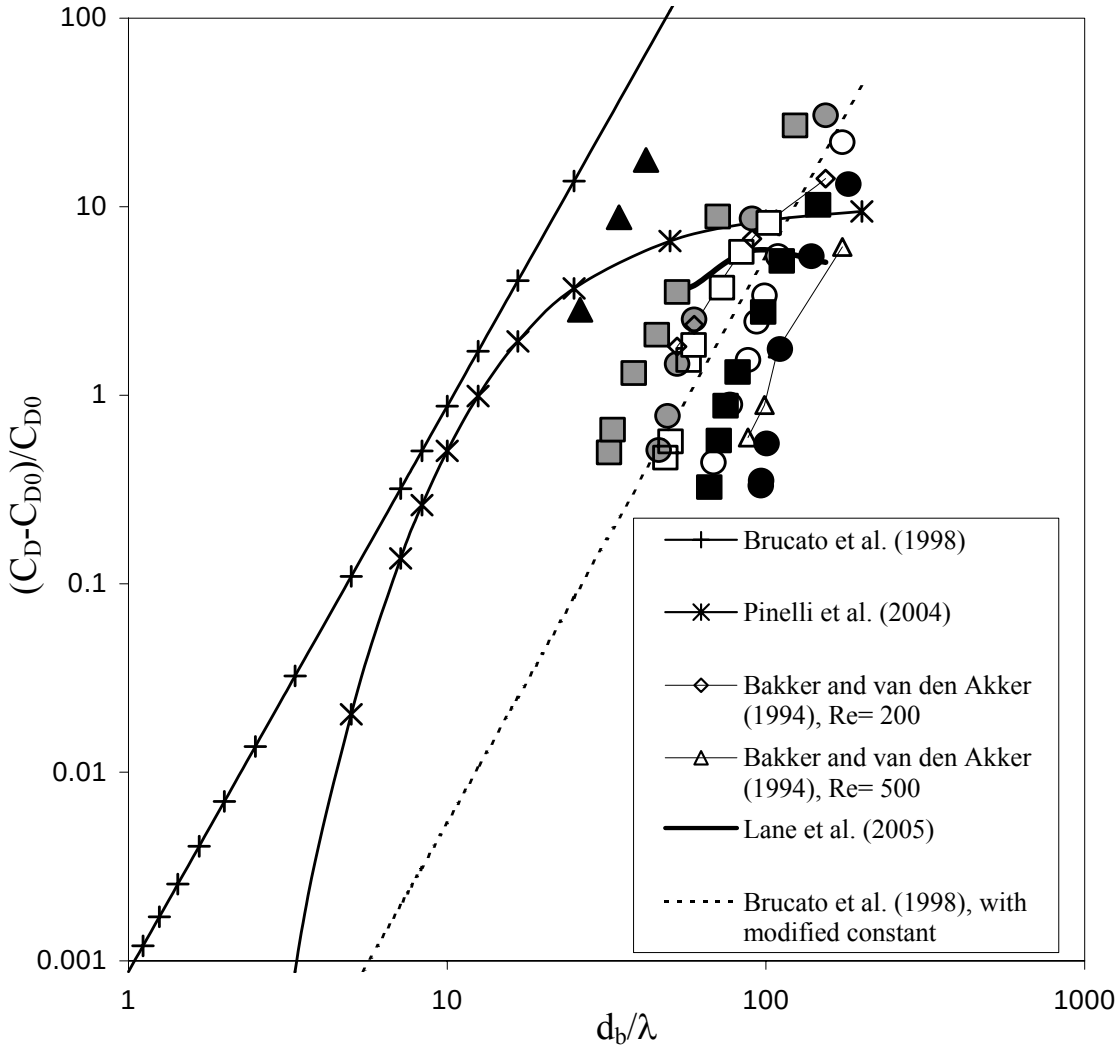

Legends:

Reynolds Number	Volume fraction 5%	Volume fraction 15%
200	■	●
500	□	○
800	■	●
50, with 500 μm solid particles	-	▲

Figure 5.5: Influence of Turbulence, Reynolds Number and Volume Fraction on Drag Coefficient

The predicted results clearly indicate that in addition to d_b/λ, the fractional increase in the drag coefficient is also function of bubble Reynolds number and the volume fraction. Considering the range of volume fractions, its influence can be neglected. It can be seen from Figure 5.5 that the CFD predictions show reasonable agreement with the estimations based on correlation of Bakker and van den Akker (Equation 5.12). While applying the correlation of Bakker and van den Akker (Equation 5.12), volume averaged value of turbulent viscosity was used. Importantly, this correlation captures the influence of Reynolds number as well as influence of prevailing turbulence on the drag coefficient. Considering the rather narrow range of bubble Reynolds numbers relevant to gas-liquid flows in stirred reactors, the influence of the bubble Reynolds number might be ignored as done by Brucato *et al.* (1998). The predicted results however require much lower proportionality constant and can be correlated (modified correlation of Brucato *et al.*) as:

$$\frac{C_D - C_{D0}}{C_{D0}} = 6.5 \times 10^{-6} \left(\frac{d_b}{\lambda} \right)^3 \tag{5.17}$$

where C_D is the drag coefficient in turbulent liquid and C_{D0} is the drag coefficient in liquid without additional turbulence. The predictions of Equation (5.17) are shown by dotted line in Figure 5.5. The trends observed in the numerical results presented in Figure 5.5 support the reduced value of the multiplier for higher Reynolds numbers. Recently reported numerical study of Lane *et al.* (2000) also provides empirical support for lower value of K as in Equation (5.17). The correlation of Bakker and van den Akker (1994) and Equation (5.17) (both based on volume averaged properties) were evaluated for estimating effective drag coefficients for gas-liquid flow in a stirred reactor by comparing simulated results with the experimental data of Bombac *et al.* (1997).

5.3.2 Gas-liquid flows in stirred reactor

Gas-liquid flow generated by the Rushton turbine in a stirred reactor was simulated for an impeller rotational speed (N) of 266 rpm and volumetric gas flowrate (Q_g) equal to 1.667×10^{-3} m^3/s (Fl = 0.1114 and Fr = 0.3005). Before discussing the details of the predicted results, the influence of grid size, the effect of interphase drag force

formulation on the gas holdup distribution, total gas holdup and the influence of virtual mass were studied in detail.

5.3.2.1 Influence of grid size

As stated in previous section, the prevailing level of turbulence influences the drag coefficient and ultimately affects the pattern of gas distribution and total gas holdup. Therefore, accurate prediction of turbulent quantities becomes essential for the correct estimation of interphase drag coefficient. The predictions of turbulent quantities are usually quite sensitive to the number of grid nodes used in the solution domain. Preliminary simulations were therefore carried out to identify adequate number and distribution of grids. Equation (5.17) used to calculate drag coefficient. In the present work, three grid sizes, coarse grid ($r \times \theta \times z$: $25 \times 44 \times 43$: 47 K), medium grid ($r \times \theta \times z$: $51 \times 82 \times 57$: 238 K) and fine grid ($r \times \theta \times z$: $63 \times 98 \times 82$: 506 K) were considered to study the effect of grid size on the predicted gas holdup distribution. The predicted gas holdup distribution for all the three grid distributions are shown in Figure 5.6. It can be seen from Figure 5.6 that the predicted gas holdup distribution in the impeller discharge stream significantly changes for the coarse grid (47 K) to a medium grid (240 K). However, relatively small change was observed in predicted gas holdup distribution at impeller discharge stream for medium grid (240 K) and fine grid (500 K). Similarly, the relative change in the volume averaged energy dissipation rates, when moved from medium grid to fine grid was much less (< 14%) than when moved from coarse grid to medium grid (~60%). The predicted values of the total gas holdup, turbulent kinetic energy and energy dissipation rate are listed in Table 5.1 to explain the influence of the grid size on the predicted values. Overall, it can be said that the fine grid (~500 K grids) used in the present work adequately captures the key features of flow generated in stirred reactors. All the subsequent simulations were therefore carried out with the fine grid ($r \times \theta \times z$: $63 \times 98 \times 82$).

5.3.2.2 Influence of inter-phase drag force

Adequate prediction of the slip velocity is a key issue in simulating gas distribution and flow regimes in stirred reactors. Apart from the value of the empirical constants,

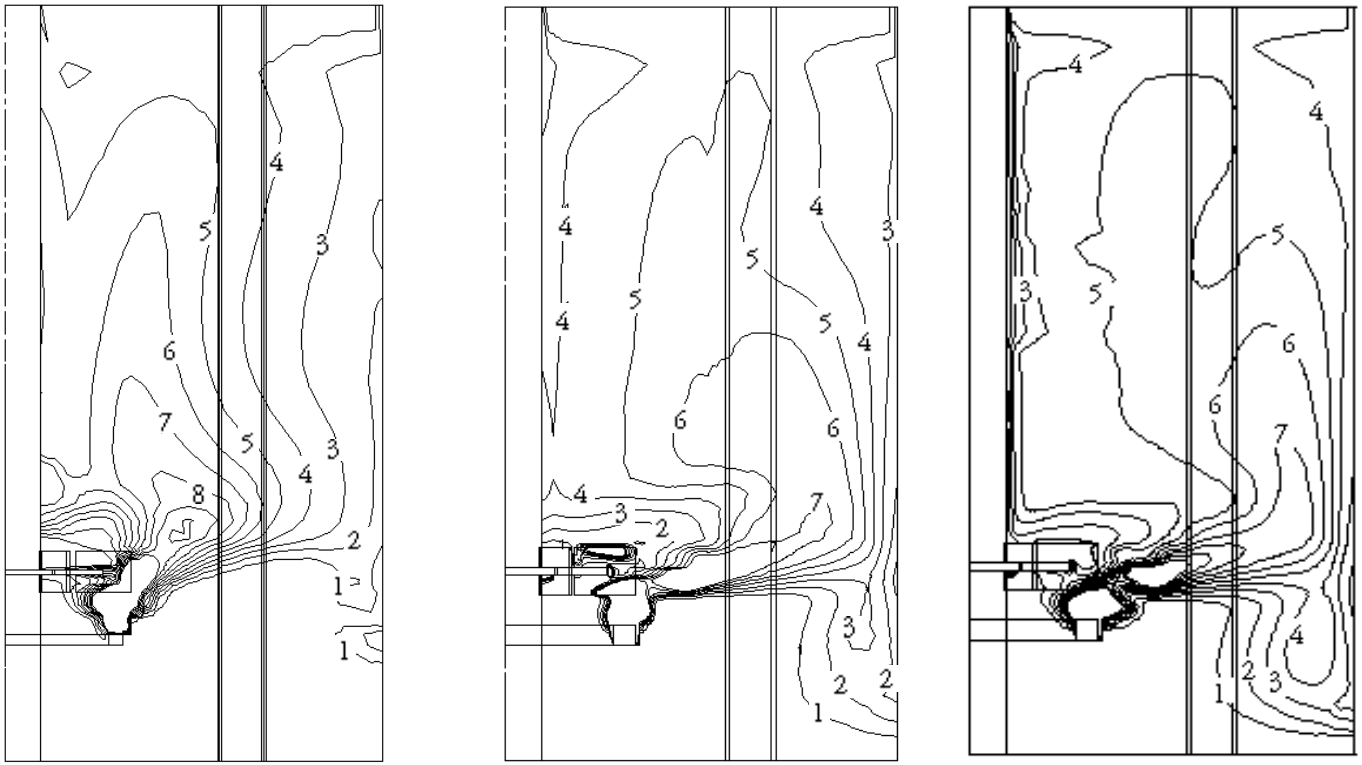

(a) Coarse grid (47,000) (b) Medium grid (240, 000) (c) Fine grid (500, 000)

(Contour labels denote the actual values of gas holdup, in percentage)

Figure 5.6: Influence of Number of Computational Cells on Predicted Gas Hold-up Distribution for L33 Flow Regime, Fl = 0.1114 and Fr = 0.3005

Table 5.1: Influence of Grid Size on the Predicted Volume Averaged Values

Grid Size	Turbulent kinetic energy, m^2/s^2	Turbulent energy dissipation rate, m^2/s^3	Total gas holdup, in percentage
47, 000	0.0075	0.0495	2.84
240, 000	0.0109	0.1232	3.65
500, 000	0.01132	0.1428	3.97

appropriate value of the turbulent energy dissipation rate and turbulent viscosity need to be used in Equation (5.12 and 5.17). The quantitative comparison of the predicted results obtained with the drag coefficients estimated with volume average values of Kolmogorov scale and turbulent viscosity and the experimental data (Bombac *et al.*, 1997) is shown in Figure 5.7b and 5.7c.

It can be seen from Figures 5.7a and 5.7b that the gas holdup distribution predicted based on Equation (5.12) shows fairly different gas distribution than the experimental data (shown in Figure 5.7a). The major disagreement was observed in the region below the impeller. The impeller generated flow was not sufficient to circulate gas in a lower circulation loop. The computational model have under-predicted total gas holdup (predicted hold-up was 2.55% compared to the experimental measurement of 3.3%). The predicted results based on Equation (5.17) are closer to the experimental data (see Figures 5.7a and 5.7c). This model resulted in over prediction of total gas holdup (predicted hold-up was 3.97% compared to the experimental measurement of 3.3%). Despite the over prediction, the predicted gas hold-up distribution showed better agreement with the data than predicted by Equation (5.12). All the subsequent simulations were therefore carried out with the turbulent correction term for interphase drag coefficient calculated using Equation (5.17).

5.3.2.3 Effect of virtual mass

The virtual mass effect is significant when the secondary phase density is much smaller than the primary phase density. The effect of the virtual mass force was studied before discussing the quantitative comparison of the predicted results with experimental data for other flow regimes. The predicted gas holdup distributions obtained with and without considering virtual mass force are shown in Figure 5.8. It can be seen form Figure 5.8 that the influence of the virtual mass force on the predicted pattern of gas distribution was significant only in the impeller discharge stream. However, the influence of virtual mass force was not found to be significant in the bulk of the reactor. Therefore, for all further simulations, the virtual mass force was not considered.

5.3.2.4 Gas holdup distribution in L33, S33 and VC flow regimes

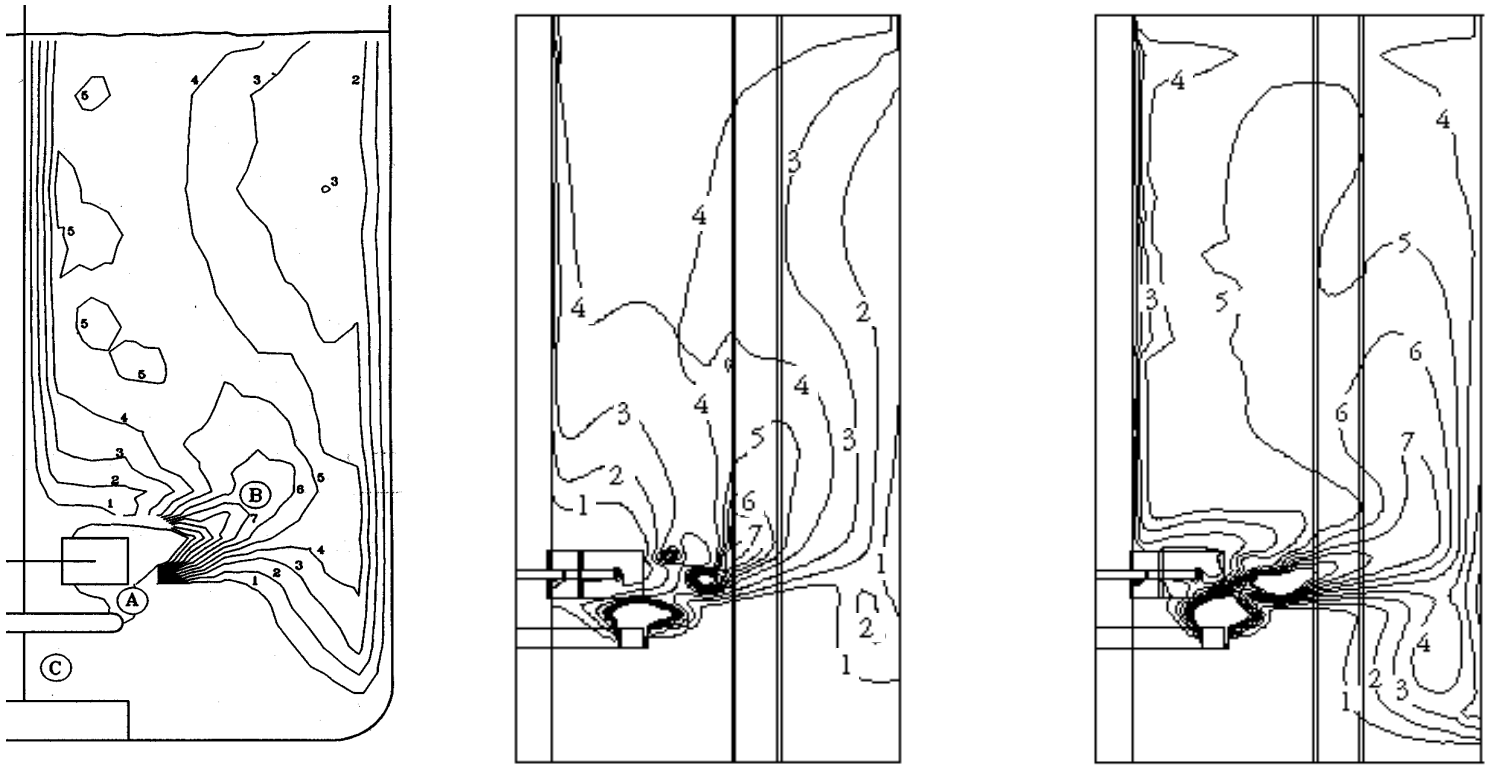

(a) Experimental (Bombac *et al.*, 1997)

(b) Predicted results with Bakker and van den Akker correlation, (Equation 12)

(c) Predicted results with modified Brucato *et al.* correlation, (Equation 17)

(Contour labels denote the actual values of gas holdup, in percentage)

Figure 5.7: Comparison of Experimental and Predicted Gas Hold-up Distribution at Mid-baffle Plane for L33 Flow Regime, Fl = 0.1114 and Fr = 0.3005

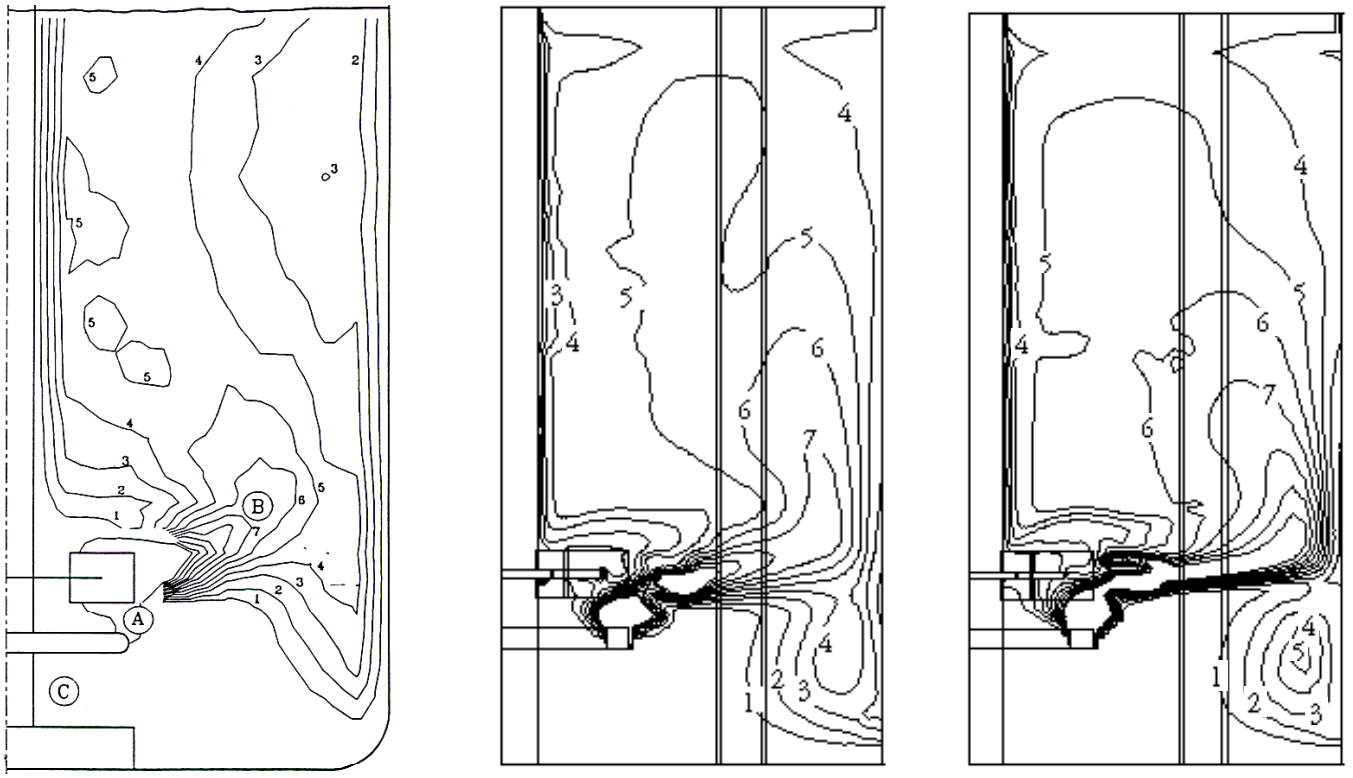

(a) Experimental: mid-baffle plane, (Bombac *et al.*, 1997)

(b) Predicted, without virtual mass effect: mid-baffle plane

(c) Predicted, with virtual mass effect: mid-baffle plane

(Contour labels denote the actual values of gas holdup, in percentage)

Figure 5.8: Comparison of Predicted Gas Hold-up Profiles for With and Without Virtual Mass Effect for L33 Flow Regime, Fl = 0.1114 and Fr = 0.3005

Gas-liquid flows generated by the Rushton turbine in a stirred reactor were simulated for three gas flow regimes representing L33 (Fl = 0.1114 and Fr = 0.3005), S33 (Fl = 0.0788 and Fr = 0.6) and VC (Fl = 0.026267 and Fr = 0.6). As discussed in previous subsection, Equation (5.17) based on the volume averaged dissipation rate and Kolmogorov scale was used to calculate effective drag coefficients. The comparisons of predicted gas holdup distributions with the experimental results at mid-baffle plane are shown in Figure 5.7 (L33) and Figure 5.9 (S33 and VC). It can be seen from these figures that, the predicted gas holdup distribution for L33, S33 and VC flow regimes are in reasonably good agreement with the experimental data. However, the computational model has over predicted the values of the total gas holdup. The predicted value of total gas holdup (4.85%) was higher than the reported experimental value (4.2%) for S33 flow regime. Similarly the predicted value of total gas holdup (2.63%) was higher than the experimental data (2.2%) for VC flow regime.

The comparisons of axial profiles of radially averaged gas holdup for all the three regimes are shown in Figure 5.10. It can be seen from Figure 5.10 that the computational model over predicts the values of the gas holdup in the region above the impeller for all the three regimes. The maximum value of predicted radially averaged gas holdup occurs at an axial distance of 0.117 m for L33 and 0.107 m for S33 as well as VC regimes compared to the experimentally observed distance of 0.13 m for L33 and 0.1125 m for S33 as well as VC regimes. The predicted values of gas holdups at this maximum are under predicted (7.3% for L33, 7.94% for S33 and 3.82 for VC) compared with the experimental value (~ 8.1% for L33, ~8.8% for S33 and ~4.1% for VC). The quantitative comparison of angle averaged values of predicted gas holdup and experimental data at three different axial locations for all the three are shown in Figure 5.11. It can be seen from Figure 5.11 that, the comparisons of predicted values of gas holdup and experimental data are reasonably good for all the three regimes. The computational model was thus able to simulate all the three regimes reasonably well.

5.3.2.5 Gross characteristics

Predicted influence of the gas flow rate on gross characteristics, power and pumping numbers are also of interest. Pumping and power numbers were calculated from simulated results as:

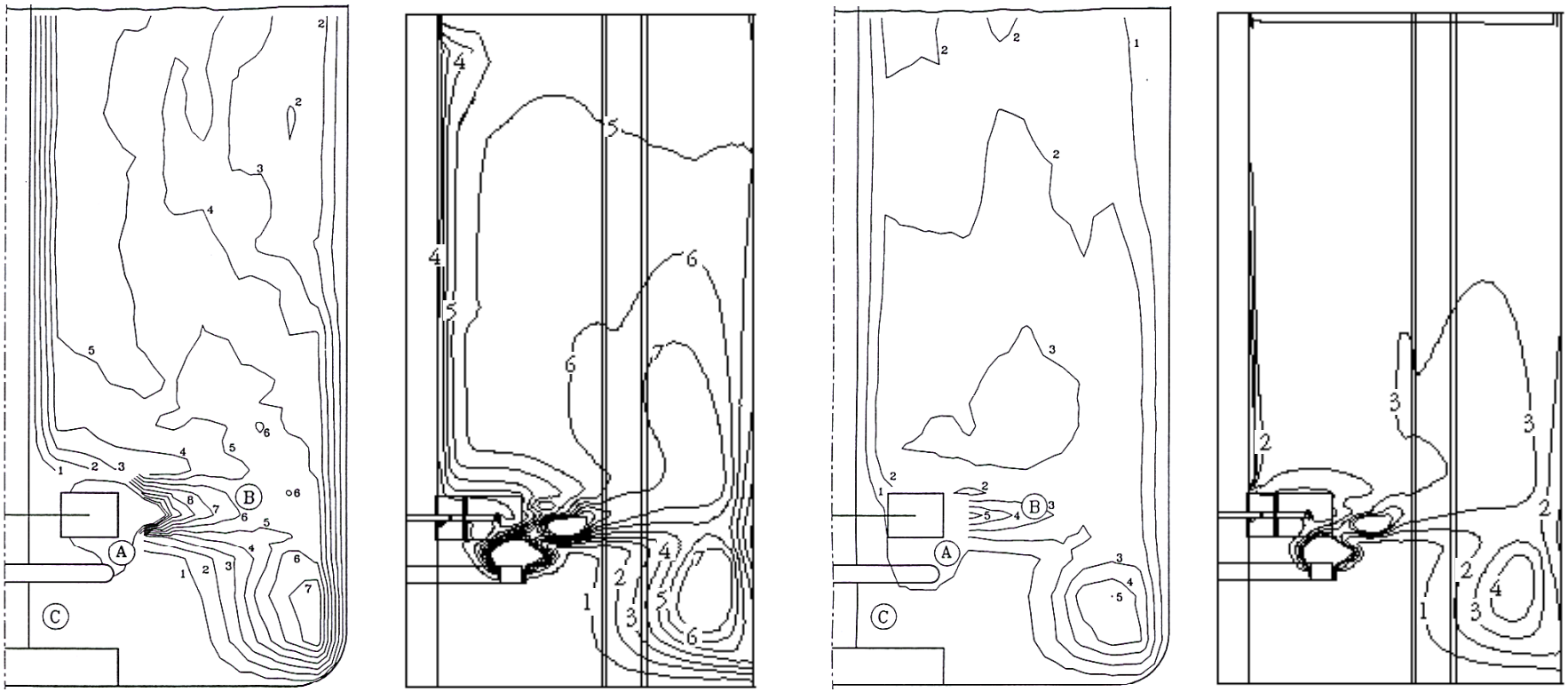

(a) Experimental, S33 flow regime, Fl = 0.0788 and Fr = 0.3005 (mid-baffle)

(b) Predicted, S33 flow regime, Fl = 0.0788 and Fr = 0.6 (mid-baffle)

(c) Experimental, VC flow regime, Fl = 0.026267 and Fr = 0.6 (mid-baffle)

(d) Predicted, VC flow regime, Fl = 0.026267 and Fr = 0.6 (mid-baffle)

(Contour labels denote the actual values of gas holdup, in percentage)

Figure 5.9: Comparison of Experimental and Predicted Gas Hold-up Distribution for S33 and VC Flow Regimes

(Experimental data of Bombac *et al.*, 1997)

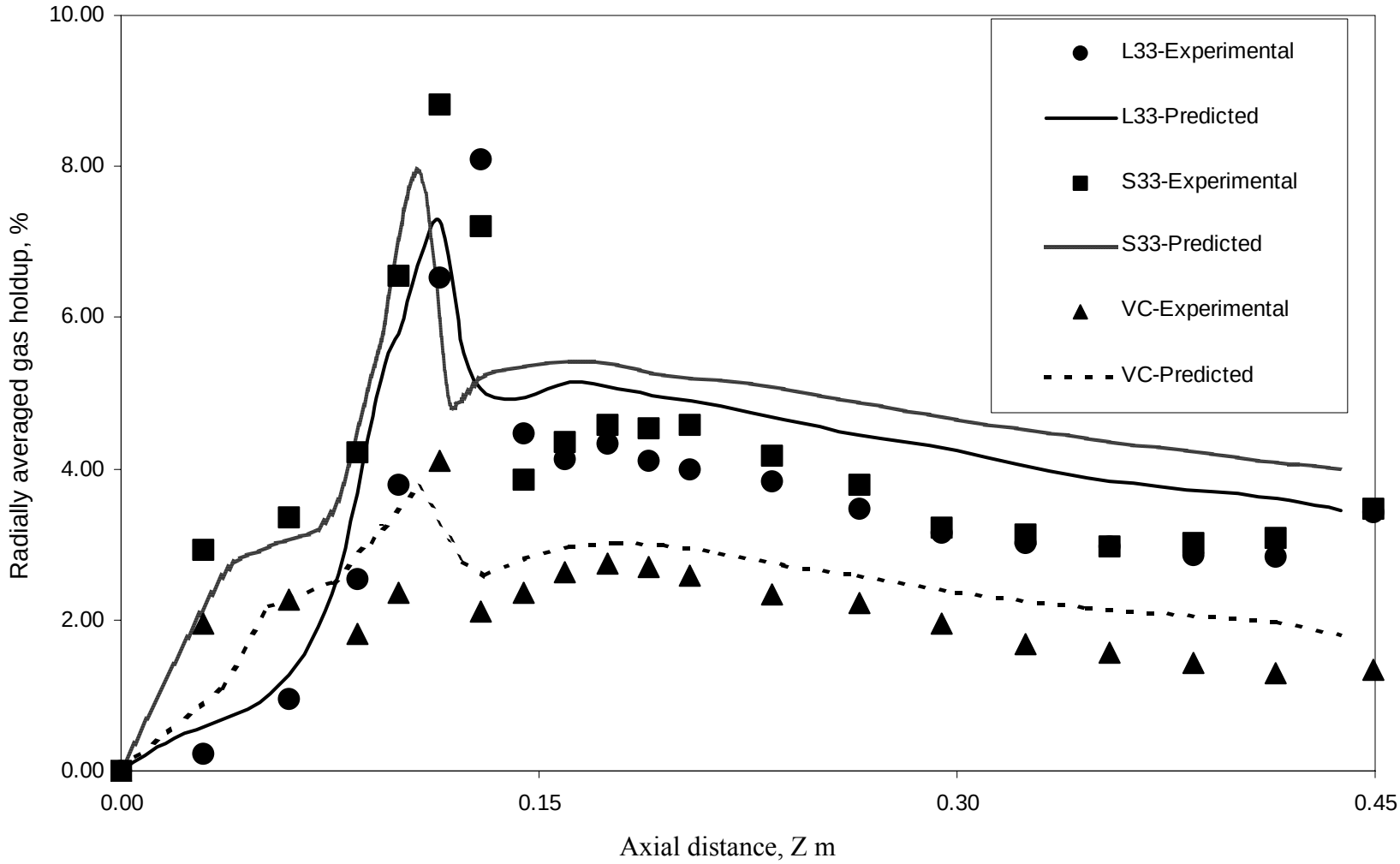

Figure 5.10: Comparison of Predicted Axial Profile of Radially Averaged Gas Hold-up with Experimental Data for L33, S33 and VC Flow Regimes, Symbol denotes the experimental data of Bombac *et al.*, 1997

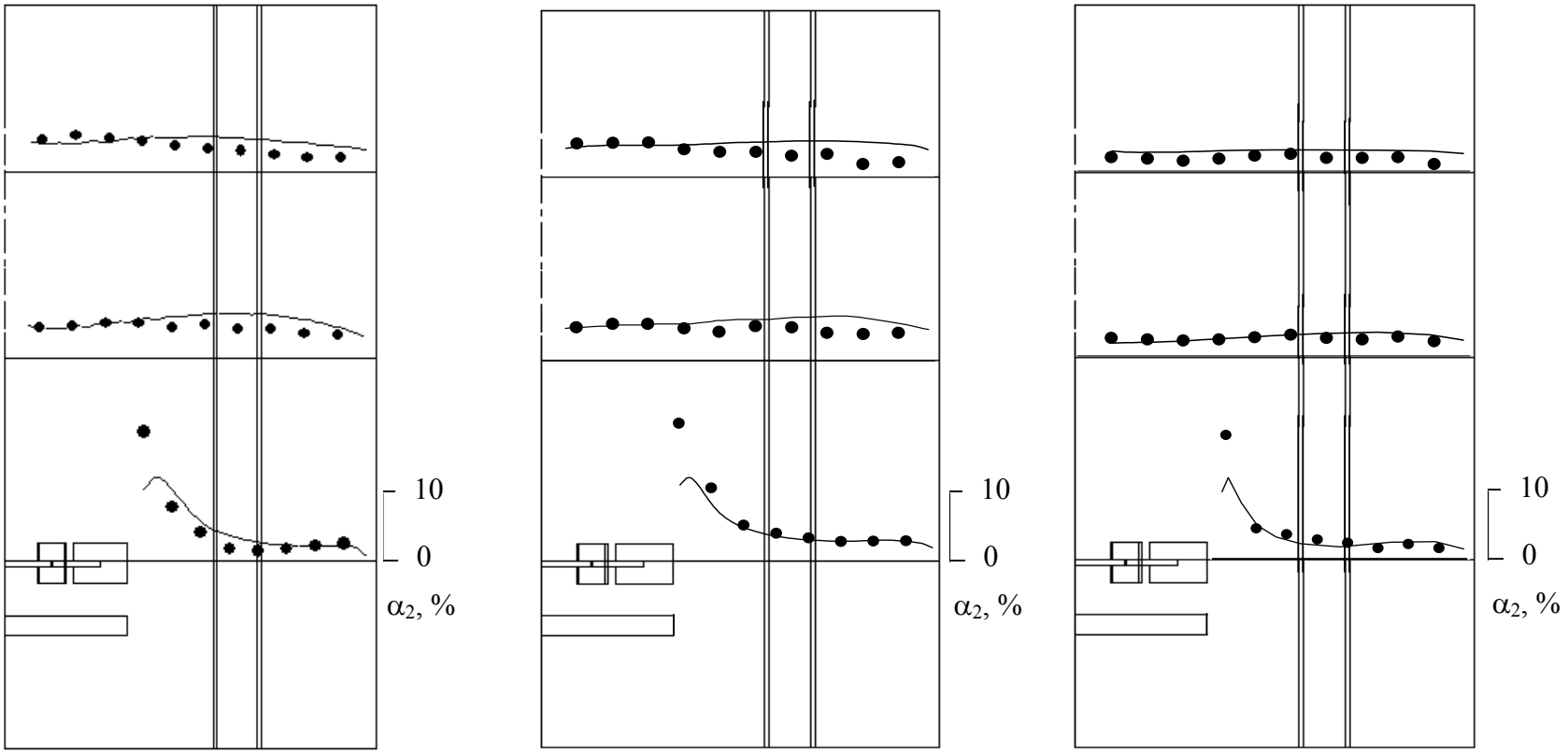

(a) L33 flow regime
Fl = 0.1114 and Fr = 0.3005

(b) S33 flow regime
Fl = 0.0788 and Fr = 0.6

(c) VC flow regime
Fl = 0.026267 and Fr = 0.6

Legends:

● Experimental data (Bombac *et al.*, 1997)
—— Predicted results

Figure 5.11: Comparison of Predicted Angle Averaged Values of Gas Hold-up (α_2) with Experimental Data for L33, S33 and VC Flow Regimes

$$N_Q = \frac{2\int_{-B/2}^{B/2}\int_{0}^{\pi} \alpha_l r_i U_r \, d\theta dz}{ND_i^3} \tag{5.18}$$

$$N_P = \frac{2\int_V \alpha_l \rho \varepsilon dV}{\rho N^3 D_i^5} \tag{5.19}$$

where B is blade height, D_i is impeller diameter, N is impeller speed, r_i is impeller radius and U_r is radial velocity. The calculated values of pumping and power number from the simulated results are listed in Table 5.2. As the gas flow rate increases, impeller pumping as well as power dissipation decreases. The extent of decrease increases with an increase in the gas flow rate (or in other words, as flow regime changes from VC to S33 and further to L33). Bombac *et al.* (1997) have not reported their experimental values of power dissipation or pumping number. In absence of such a data, the predicted values were compared with the estimates of empirical correlations proposed by Calderbank (1958), Hughmark (1976) and Cui *et al.* (1996). While demonstrating the qualitative trend, the CFD model under predicts the decrease in power dissipation in the presence of gas compared to the estimates of these correlations. CFD model, however, could correctly capture the overall gas hold-up distribution and can therefore simulate different flow regimes of gas-liquid flow in stirred reactors.

5.3.2.6 Gas-liquid flow around impeller blades

It would be useful to examine the details of the predicted results near impeller blades to identify the differences in the flow structure of different flow regimes. Predicted flow characteristics near the impeller blades are shown in Figure 5.12 (iso-surfaces of gas volume fraction) and Figure 5.13 (contours of gas volume fraction, vorticity and turbulent kinetic energy dissipation rate) for three flow conditions.

It can be seen from Figure 5.12 that, the computational model successfully captured the gas accumulation in low-pressure region behind the impeller blades. The sparged gas interacts with trailing vortices and gets accumulated in the low-pressure region associated with the vortices. The contours and iso-surface of gas volume fraction indicate that, large portion of the gas in impeller swept region gets accumulated in low-

Table 5.2: Gross Characteristics of an Aerated Stirred Reactor

Operating Conditions	Total gas holdup (%)		Predicted Results		Influence of gas on power number, N_{Pg} / N_P				Influence of gas on pumping number, Predicted N_{Qg} / N_Q
	Predicted	Experimental (Bombac *et al.* 1997)	N_{Pg}	N_{Qg}	Predicted by CFD	Predicted by empirical correlations			
						Calderbank (1958)	Hughmark (1976)	Cui *et al.* (1996)	
Single-phase Flow	-	-	4.15	0.66	-	-	-	-	-
VC Flow Regime (Fl = 0.026267 & Fr = 0.6)	2.63	2.20	2.76	0.615	0.66	0.67	0.64	0.61	0.93
S33 Flow Regime (Fl = 0.0788 & Fr = 0.6)	4.85	4.20	2.196	0.6	0.53	0.47	0.49	0.41	0.9
L33 Flow Regime (Fl = 0.1114 & Fr = 0.3005)	3.97	3.30	1.66	0.49	0.4	0.41	0.51	0.41	0.74

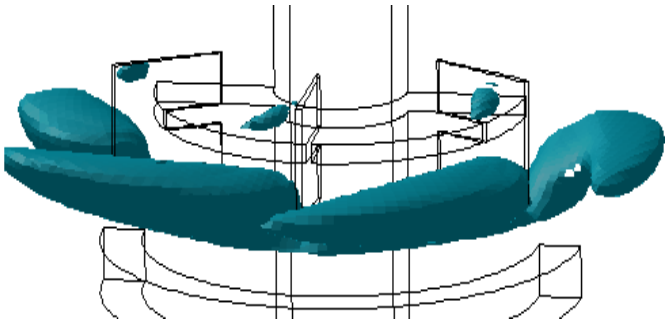

(a) L33 flow regime
Fl = 0.1114 and Fr = 0.3005

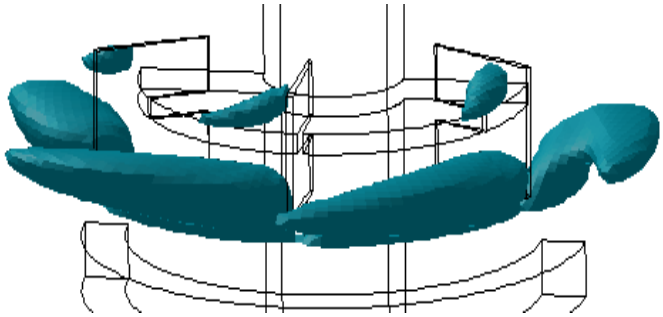

(b) S33 flow regime
Fl = 0.0788 and Fr = 0.6

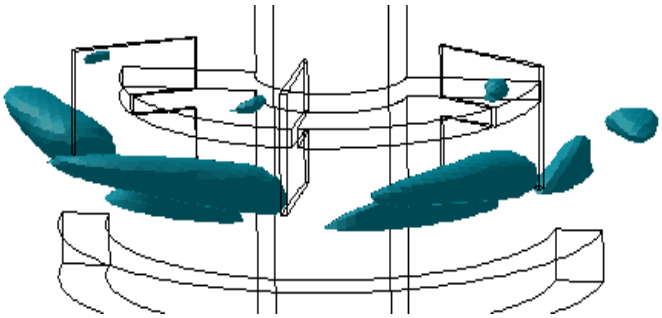

(c) VC flow regime
Fl = 0.026267 and Fr = 0.6

Iso- surface of gas volume fraction for $\alpha_2 = 0.15$
(Impeller is moving in anti-clockwise direction)

Figure 5.12: Predicted Accumulation of Gas Hold-up (α_2) behind Impeller Blades for L33, S33 and VC Flow Regimes

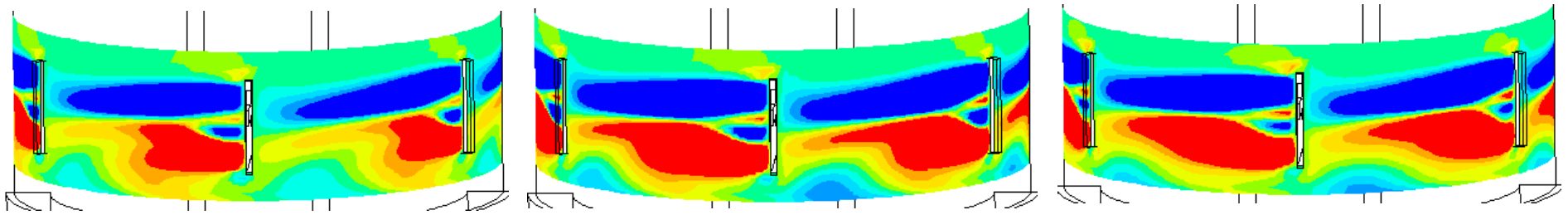

(i) L33 Flow Regime,
Fl = 0.1114 and Fr = 0.3005

(ii) S33 Flow Regime,
Fl = 0.0788 and Fr = 0.6

(iii) VC Flow Regime,
Fl = 0.026267 and Fr = 0.6

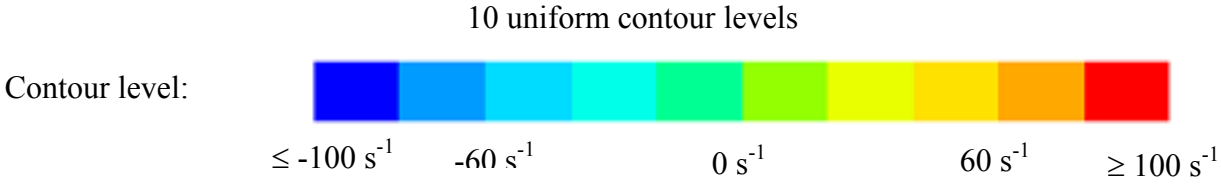

(a) Z-vorticity
(Impeller is moving from left to right)

Figure 5.13: Details of Predicted Flow Characteristics near Impeller Blades [Continue on next page]

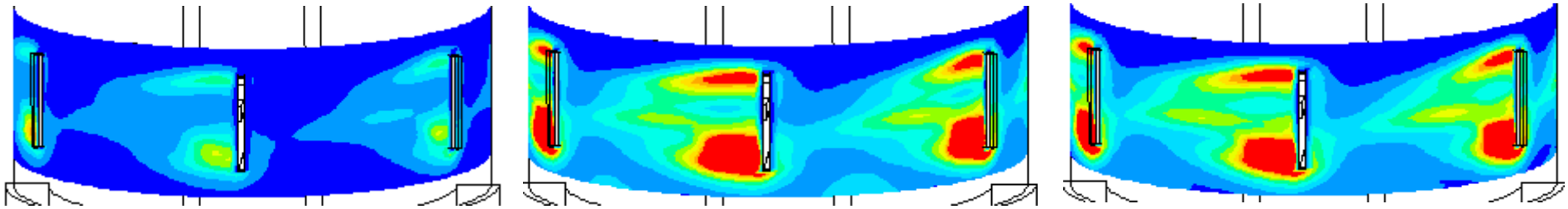

(i) L33 Flow Regime,
Fl = 0.1114 and Fr = 0.3005

(ii) S33 Flow Regime,
Fl = 0.0788 and Fr = 0.6

(iii) VC Flow Regime,
Fl = 0.026267 and Fr = 0.6

10 uniform contour levels

Contour level:

=0.0001 m^2/s^3 4 m^2/s^3 10 m^2/s^3 16 m^2/s^3 ≥ 20 m^2/s^3

(b) Turbulent kinetic energy dissipation rate

(Impeller is moving from left to right)

Figure 5.13: Details of Predicted Flow Characteristics near Impeller Blades

pressure region associated with lower trailing vortex. The examination of flow and gas accumulation around impeller blades provides clues of prevailing flow regime. The iso-surface of gas volume fraction (iso-value = 0.15) shown of three flow regimes, clearly indicates the progressive decrease in the quantity of gas accumulated behind impeller blades as one progresses from L33 regime to VC regime via S33 regime. The computational model did not capture the asymmetry in cavity shape for L33 and S33 flow regimes. The physical reasons for the possible asymmetry in the cavity shapes are not yet clear and further work is needed to capture alternating cavity structure/ gas accumulation behind impeller blades. The predicted results indicate that, the computational model qualitatively captures the changes in the gas accumulation as the flow regime changed.

The predicted contours of vorticity and energy dissipation rate demonstrate the complex flow field within impeller blades (Figure 5.13a and 5.13b). It can be seen that, for L33 and S33 flow regimes the sparged gas interacts with the lower trailing vortex and disrupt the lower trailing vortex. High gas accumulation in the vortex core region may be the possible reason for the disruption of lower trailing vortex in L33 and S33 flow regimes. Similar behavior was not observed for VC flow regime. The predicted contours of dissipation rate showed an increase in the dissipation as the flow regime changes from L33 to VC (Figure 5.13b). The power dissipated within the impeller region significantly reduces with an increase in the gas accumulation behind the impeller blades.

The critical analysis of the predicted results points out that the agreement between the predicted and experimental results in not very good in the impeller discharge stream. In all the three cases the computational model under predicted gas holdup in the impeller discharge stream. In the present work single bubble diameter was used to simulate gas-liquid flow in stirred reactor. Considering that the importance of right prediction of the slip velocity, it might be necessary to use appropriate bubble sizes in the different regions of the reactor. The population balance model with appropriate breakage and coalescence rates (see for example, Buwa and Ranade, 2002), which is able to simulate the evolution of bubble size distribution within the reactor, may lead to a better agreement with the experimental data. Such a model will require an order of magnitude more computing resources. Despite some of the deficiencies, the computational model

developed in this work was able to simulate observed gas hold-up distribution for the three distinct flow regimes for the first time. The model was also shown to capture correct trends in the accumulation of gas behind the impeller blades and the reduction in the power dissipation in the presence of gas. The obtained results will provide a useful basis for extending the computational models for different applications like mixing in gas-liquid stirred reactors. The developed computational model was then further extended to understand the influence of blade shape on the flow around the impeller blades.

5.3.3 Influence of blade shape

In most of the process applications, the Rushton turbine is widely used for dispersing gas in the liquid bulk. For this impeller, the sparged gas interacts with trailing vortices present behind the impeller blades and accumulates in a vortex core region of trailing vortices. This gas accumulation forms gas pockets behind the impeller blades, which are also known as gas cavities. These gas cavities significantly reduce the pumping capacity and the power dissipated by the impeller, therefore having negative effects on the performance of the stirred reactor (Bruijn *et al.*, 1974). Since the discovery of these inherent problems of the Rushton turbine, there has been constant interest to improve the performance of aerated stirred reactors by modifying the impeller blade shape. Van't Riet *et al.* (1976) observed a remarkable improvement in the loss of power draw under aeration by replacing the six flat blades of the Rushton turbine with six half-pipe segments (Smith turbine). This change in blade shape modifies the structure of the trailing vortices and reduces their strength. This in turn reduces the extent of gas accumulation behind impeller blades.

The blade shape proposed by Van't Riet *et al.* (1976) was considered as the initial design of the Scaba Radial Flow Gas Dispersing Turbine (6SRGT). The experimental study carried out by Saito *et al.* (1992) shows the excellent capability of the Scaba turbine to disperse gas. At an equivalent power input and impeller size, the Scaba turbine handles approximately three times as more gas compared with the Rushton turbine before the loaded condition changes to the flooded regime. Also, the ratio of the aerated power to the non-aerated power of the Scaba turbine does not drop upon gassing and remains close to one (Saito *et al.*, 1992). The efficient gas dispersion

capability of the Scaba turbine was linked with the cavity structure developed behind the impeller blades. Similar to the Rushton turbine (Nienow *et al.*, 1977 and Nienow, 1990), the Scaba turbine also supports the ventilated cavities of different shapes. Saito *et al.* (1992) defined three cavity structures, viz. vortex clinging, 3-3 (3 vortex clinging and big clinging) and big clinging cavities, are present behind impeller blades of Scaba turbine depending upon the gas flow rate and impeller rotational speed. The absence of big cavities was the possible reason for the lower drop in power consumption value in aerated condition and good gas dispersion efficiency. Moreover, the gas holdup, the mixing time and the mass transfer coefficient of the Scaba turbine are broadly equivalent to those of an equal-sized Rushton turbine for an equal power and superficial gas velocity (Nienow, 1998). These excellent characteristics of gas dispersion capability, power and mixing make the Scaba turbine an attractive alternative to the Rushton turbine for use in the process industry.

In the present work, the gas-liquid flow generated by a Scaba and Rushton turbine has been simulated. The model predictions were compared with the angle resolved flow fields (liquid and gas-liquid flow) generated by the Scaba turbine measured by Khopkar *et al.* (2004) using PIV in order to better understand the flow around the blades for single phase, as well as gas-liquid flow. Finally an attempt was made to compare the flow around impeller blades of the Rushton turbine and the Scaba turbine to bring out the similarities and the differences between the both the turbines. The comparison study will help us to identify the possible reasons for the advantages observed for Scaba turbine over Rushton turbine.

5.3.3.1 Computational model

The two-fluid model discussed in section 5.2.1 was used to simulate the gas-liquid flow generated by Scaba turbine in stirred reactor. Equation 5.17 was used to estimate the bubble drag coefficient. The gas-liquid flow in the stirred reactor was simulated using the computational snapshot approach. The computational snapshot approach was implemented in the commercial CFD code FLUENT 4.5 (of Fluent Inc., USA) using user-defined subroutines.

Considering the geometrical symmetry, half of the reactor was considered as a solution domain (see Figure 5.14). The baffles were considered at angles of 45^o and 135^o. The impeller was positioned in such a way that the three blades were located at angles of 30^o, 90^o and 150^o (measured from the center-line of the impeller blade). As discussed in chapter 4, the computational snapshot approach divides the solution domain into an inner region, in which time derivative terms are approximated using spatial derivatives and an outer region, in which time derivative terms are neglected. The boundary between the inner and outer regions needs to be selected in such a way that the predicted results are not sensitive to its actual location. For all the simulations, the boundary of the inner region was positioned at $r = 0.065$ m and $0.05 \text{ m} \leq z \leq 0.15$ m (where z is the axial distance from the bottom of the reactor).

In the snapshot approach, the sparger is modeled as a solid wall. The mass source of the gas phase was specified one cell above the sparger to simulate gas introduction into the reactor. The top surface of the dispersion was modeled as a velocity inlet. The outgoing (axial) velocity of gas bubbles was set equal to the terminal rise velocity of gas bubbles (estimated as 0.2 m/s for air bubbles). All the other velocity components for gas and liquid phase were set to zero). Implicit assumption here is that gas bubbles escape the dispersion with terminal rise velocity. Since the liquid velocity near the top gas-liquid interface is small and the overall volume fraction of gas is also small (< 5%), this assumption is reasonable. The mass and momentum conservation equations for the gas phase were solved and the gas distribution within the reactor was predicted. The mass conservation was verified by comparing the integral gas mass flow rate across various horizontal planes with the input gas mass flow rate at the sparger. In the present work, a single bubble size was specified (4 mm) over whole reactor domain for all the simulations. Fluid properties were set to those of water and air for the primary and secondary phases, respectively.

A commercial grid-generation tool, GAMBIT 2.0 (of Fluent Inc., USA) was used to model the geometry and to generate the body-fitted grids. It is very important to use an adequate number of computational cells while numerically solving the governing equations over the solution domain. Based on the previous experience, the numerical simulations for the gas-liquid flows in stirred reactors were carried out for grid size of

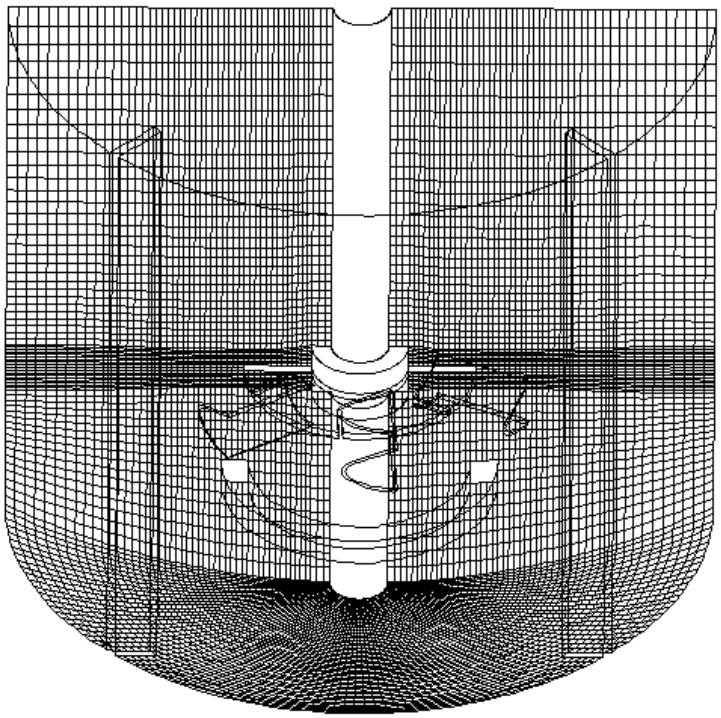

Grid Details	:
$r \times \theta \times z$	: $52 \times 95 \times 67$
Impeller blade	: $18 \times 1 \times 18$
Inner region	: $13 \leq k \leq 55$ $j \leq 40$

Figure 5.14: Computational Grid and Solution Domain

(r × θ × z: 46 × 96 × 72). In the present work, we have used (r × θ × z: 21 × 2 × 10) grid nodes covering the impeller blade. The boundary of the inner region was positioned at $j \leq 35$ and $19 \leq k \leq 60$ (where j is the cell number in the radial direction from the shaft and k is the cell number in the axial direction from the bottom of the reactor). The computational grid used in the present work is shown in Figure 5.14. Differencing of the advection terms has been carried out using the QUICK discretization scheme with the SUPERBEE limiter function (to avoid non-physical oscillations). Standard wall functions were used to specify wall boundary conditions. The developed computational model then used to understand the flow generated by Scaba turbine and Rushton turbine. The predicted results for the Scaba turbine were also compared with the experimental data reported by Khopkar *et al.* (2004).

5.3.3.2 Single-phase flow

The flow generated by the Scaba turbine in a stirred reactor was simulated for an impeller rotational speed of 300 rpm. Without using any impeller boundary conditions, the snapshot approach was able to simulate the flow generated by the impeller. The comparison of predicted velocity field of Scaba turbine (angle averaged to eliminate the influence of specific blade position) with the experimental PIV data (reported by Khopkar *et al.*, 2004) is shown in Figure 5.15. The radial velocity jet with two-loop flow structure (similar to Rushton turbine) seen in the experimental flow field is captured in the simulations. The simulated flow field shows two small re-circulating loops (attached to the inner edge of the impeller blades) below and above the disc. A small reverse loop below the hub, which is seen in the experimental flow field, is however not captured in the simulation. The pumping number for the Scaba turbine was calculated using Equation 5.18. The calculated value of the pumping number for the Scaba turbine from the simulated results (0.63) is higher than the experimental value determined by PIV (0.47) and that reported in the literature (0.52) [Kovacs *et al.*, 2001].

In order to understand the effect of blade shape on the flow, the flow generated by the Rushton turbine in a stirred reactor was simulated for the same geometry and for the same grid resolution. The predicted flow fields were then used to identify the

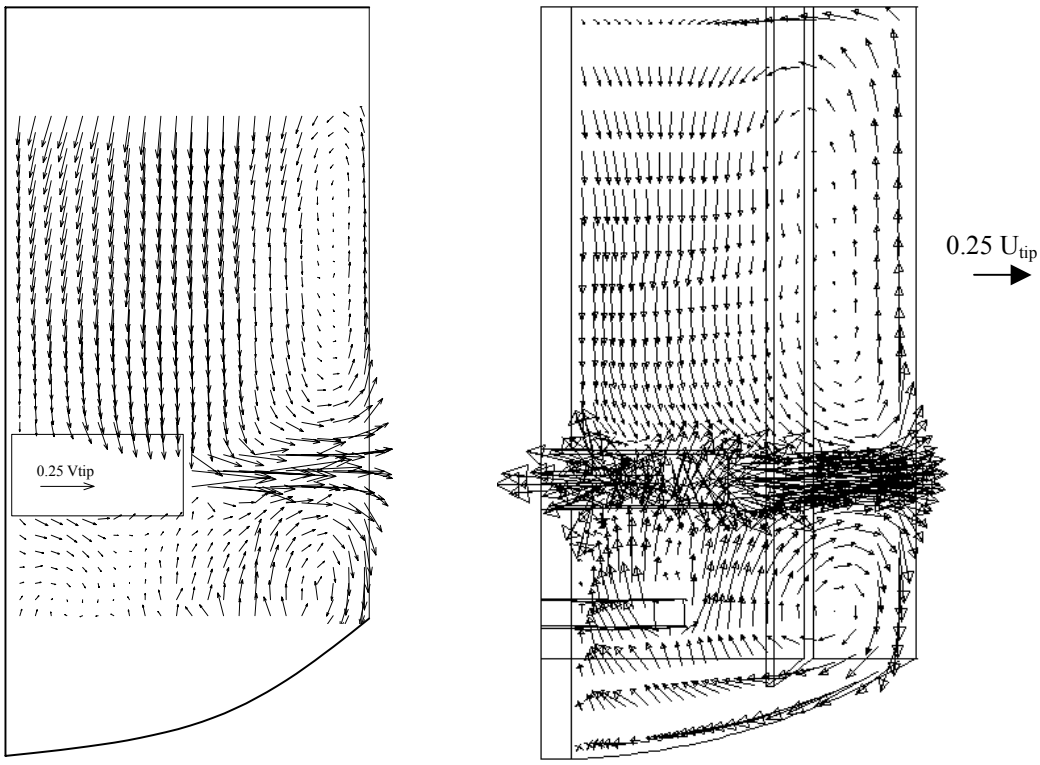

(a) Experimental: mid-baffle plane
(Experimental data, Khopkar *et al.*, 2004)

(b) Predicted: mid-baffle plane

Figure 5.15: Mean Flow Field at the *r*-*z* Plane for Single-phase Flow, N = 300 rpm and U_{tip} = 1.5 m/s

differences in flow field generated by these two turbines. To do this, the distribution of flow quantities around the impeller blade and along the blade height was analysed. The azimuthally averaged axial profiles of the predicted radial velocity and the turbulent kinetic energy for the two turbines are compared in Figure 5.16. It can be seen from Figures 5.16a that despite the differences in the blade curvature of the two impellers, the azimuthally averaged velocity profiles do not differ significantly. The predicted profiles of the radial velocity almost overlap, although for the Scaba turbine, the predicted velocity profiles near the impeller tip show a well-defined peak at $z/b = 0.5$. When comparing the predicted values with the experimental data, it can be seen that the computational model over predicts the radial velocity values in the impeller discharge stream.

The predicted turbulent kinetic energy distribution for both the turbines is shown in Figure 5.16b-(i). It can be seen that the predicted distribution of kinetic energy (azimuthally averaged) in the impeller discharge stream is different for both turbines, highlighting the effect of the blade shape. In the case of the Rushton turbine, two maxima at around z/b = 0.25 and 0.75 are observed. These observations have already been reported by other authors (Ng *et al.*, 1998) and are related to the presence of trailing vortices. In the case of Scaba turbine, a sharp peak at z/b = 0.54 is observed. Kovacs *et al.* (2001) similarly reported a peak at z/b = 0.5. The comparison of predicted values with the experimental data (Figure 5.16b-(ii)) shows that the computational model under predicts the turbulent kinetic energy values. This is a common finding when k-ε turbulence models are used. The use of more complex models, like Reynolds stress models, may not lead to any significant improvement (Jenne and Reuss *et al.*, 1999). Recent work, however, shows that correct kinetic energy values in stirred tanks can be obtained via Large Eddy Simulations (LES) (Kilander and Rasmuson, 2003 and Yeoh *et al.*, 2003). Such simulations, however, still require a significant amount of CPU time and therefore are not yet fine-tuned for fast process design. Nevertheless, the simulated results presented in this work enable correct qualitative comparisons between agitator types. The computational model was further used to understand the influence of the blade shape on the flow around the impeller blades of Rushton turbine and Scaba turbine.

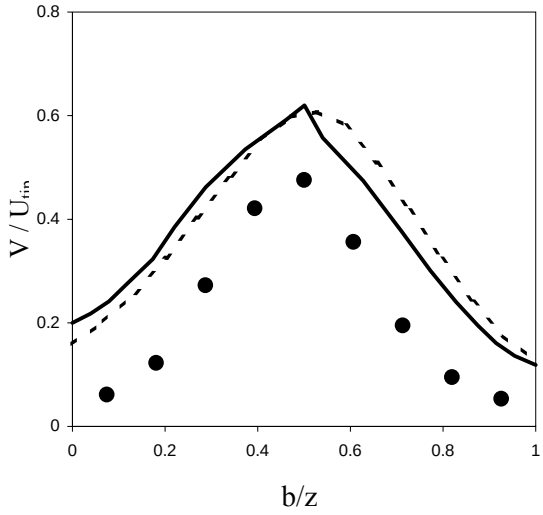

(i) r/ R = 0.63

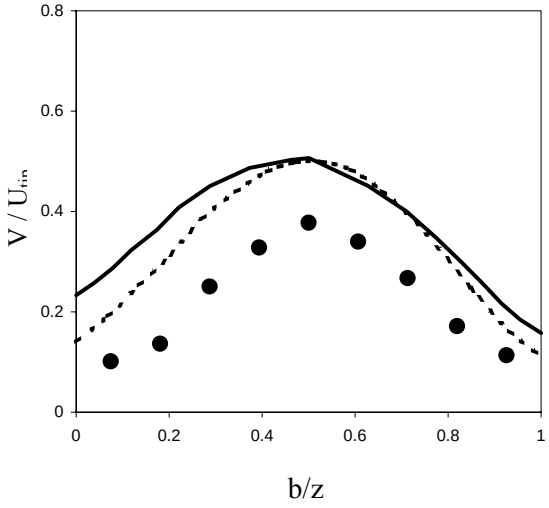

(ii) r/ R = 0.745

(a) Axial profiles of radial velocity

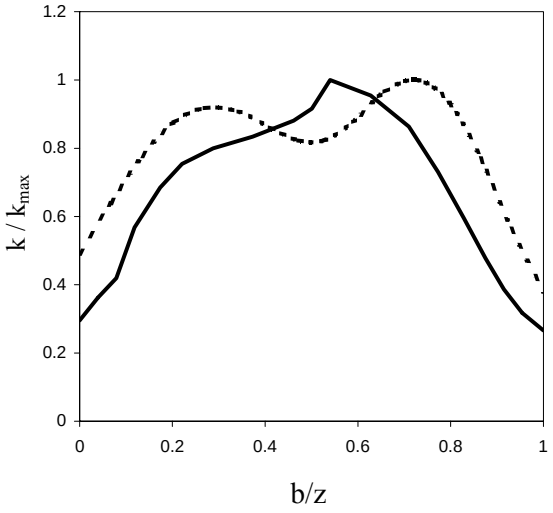

(i) Comparison of two turbines

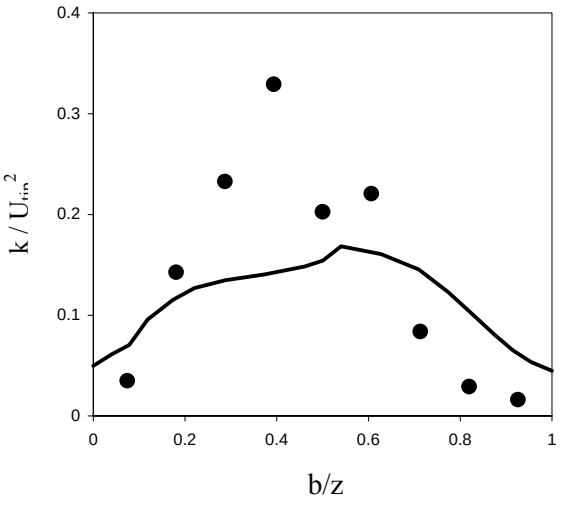

(ii) Comparison with experimental data

(b) Axial profiles of turbulent kinetic energy

Legends:	Scaba turbine	Rushton turbine	Experimental data, (Khopkar *et al.*, 2004)

Figure 5.16: Comparison of Predicted Results with Experimental Data for Single-Phase Flow, N = 300 rpm and U_{tip} = 1.5 m/s

The predicted pressure distribution around the impeller blades and the iso-surface of z-vorticity for both the turbines are shown in Figure 5.17. It can be seen from Figure 5.17a that similar to Rushton turbine, the Scaba turbine also shows the presence of two trailing vortices behind the impeller blades (not seen in presented view). However, the model predictions show the small, low strength vortices are present behind the Scaba turbine compared to the Rushton turbine. Similarly, the predicted pressure distribution around impeller blades of both the turbines are shown in Figure 5.17b. It can be seen from Figure 5.17b that the predicted pressure field indicated the presence of smaller low-pressure region behind the impeller blades of Scaba turbine and the low-pressure regions are attached to the top and bottom edges of the turbine. The smaller low-pressure regions generated behind the blades of the Scaba turbine and the consequent small low strength trailing vortices are the major reasons for the reduction of the gas accumulation behind the impeller blades of this impeller and thus its improved performance compared to the Rushton turbine.

5.3.3.3 Gas-liquid flow

The gas-liquid flow generated by the Scaba turbine in the stirred reactor was simulated for a gas flow number (Fl) of 0.004 and Froude number (Fr) of 0.242. This corresponds to a volumetric gas flow rate (Q_g) of 1.715×10^{-5} m^3/s and an impeller rotational speed of 300 rpm. Under these operating conditions, the gas is completely dispersed in the reactor. The predicted radial velocity field is used for calculating the flow (pumping) number. The calculated value of pumping number from the simulated results (0.59) is higher than the measured experimental value of 0.44. The predicted gas hold-up distribution at mid-baffle plane is shown in Figure 5.18a. It can be seen that the computational model captures the complete dispersion of gas in the reactor. The predicted gas holdup distribution shows higher values of gas hold-up in the lower circulation loop, indicating recirculation of the gas in the lower part of the reactor. The computational model was further used to study the effect of the aeration rate on the gas dispersion performance of Scaba turbine. The gas-liquid flows in stirred reactor were simulated for two higher aeration rates (Fl = 0.04 and Fl = 0.1), while the impeller speed was kept constant. The predicted gas hold-up distribution for high gas loading (Fl = 0.1) is shown in Figure 5.18b. It can be seen that even for high gas loading, the Scaba

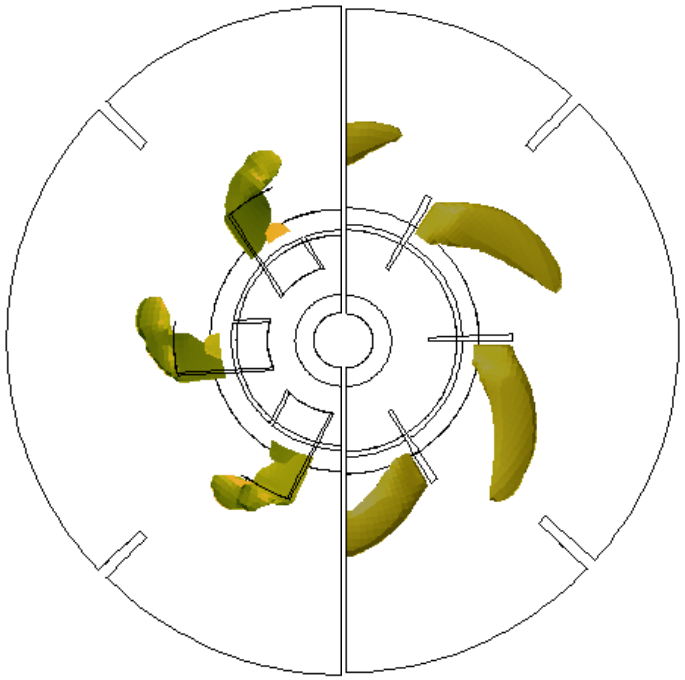

(a) Iso-surface of Z-vorticity (L.H.S.: Scaba turbine and R.H.S.: Rushton turbine), $\omega D_i/U_{tip} = -30$

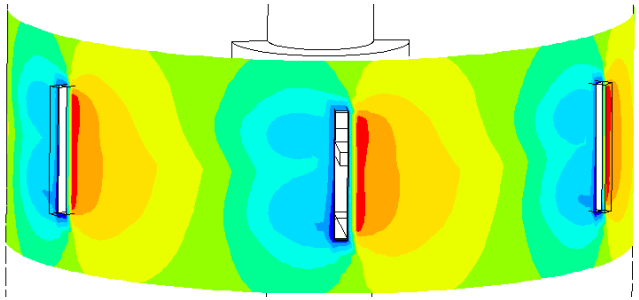

(i) Pressure distribution around the Rushton turbine (10 uniform contours, blue ≡ -700, red ≡ 800)

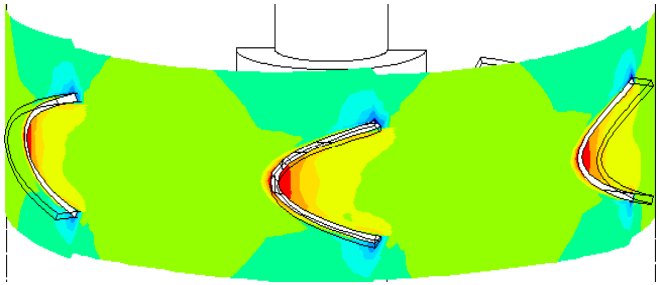

(ii) Pressure distribution around the Scaba Turbine (10 uniform contours, blue ≡ -2700, red ≡3800)

(Impeller is moving from left to right)

Figure 5.17: Flow Field around the Impeller Blades for Single-phase Flow, N = 300 rpm and U_{tip} = 1.5 m/s

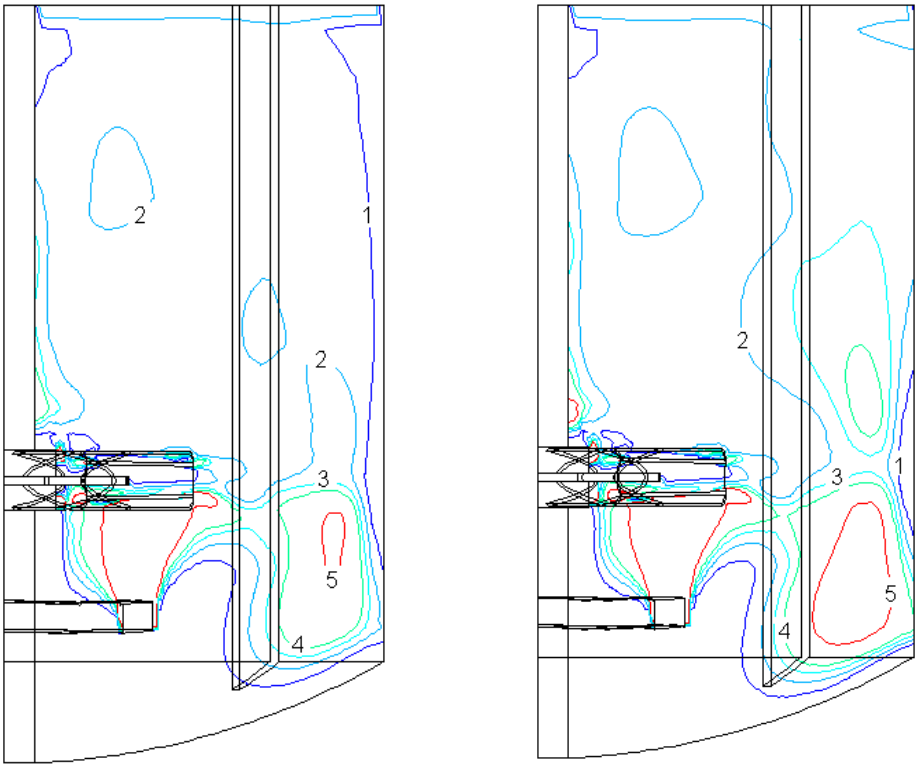

(a) Fl = 0.004 (mid-baffle plane)

(b) Fl = 0.1 (mid-baffle plane)

(Contour labels denote the actual values of gas holdup, in percentage)

Figure 5.18: Predicted Gas Holdup Distribution at the r-z Plane for Gas-Liquid Flow, Fr = 0.242

turbine provides good dispersion of the gas and significant gas hold-up in the lower circulation loop.

The predicted gas hold-up distributions around the impeller blades of the Scaba turbine for three gas flow rates are shown in Figure 5.19. It can be seen that the computational model captures the gas accumulation behind the impeller blades. The sparged gas interacts with the lower trailing vortices and accumulates in the low-pressure region associated with the lower trailing vortex of each blade. It is also observed that even at very high gas flow rates (Figure 5.19b&c) the gas accumulation structure (size and the magnitude) hardly changes. The little change in the quantity of the gas accumulation behind impeller blades for higher gas loading explains the so-called advantages of Scaba turbine over the Rushton turbine for gas dispersion applications. The presence of small and clinging cavities ensures a lower drop in the pumping capacity and power dissipation of the impeller. These observations are valid for small and pilot plant scale reactors. However, for large or industrial scale reactor, the ratio of characteristic length scales of impeller blades and the gas bubble are strikingly different as compared to small reactor. Therefore, the interaction of gas bubbles with the trailing vortices and the structure of the cavities might be significantly different for industrial scale as compared to small reactor. Though some indirect evidence of this is available, but no systematic study of influence of the scale on relative performance of the Scaba turbine is available. Therefore, there is a clear need to understand the influence of the scale, on the relative performance of the Scaba turbine. CFD based model may make useful contribution to understand the influence of the scale of the operation on the impeller performance.

5.4 Summary and Conclusions

A comprehensive computational model based on the Eulerian-Eulerian approach was developed to simulate gas-liquid flows in a stirred reactor. The preliminary simulations of gas-liquid flows in a stirred reactor highlighted the importance of appropriate modelling of the interphase drag force. A CFD based two-dimensional model problem was then developed to understand the influence of free stream turbulence and the presence of neighboring bubbles on the bubble drag coefficient. This sub-model was used to identify an appropriate correlation for estimating the inter-phase drag force. The

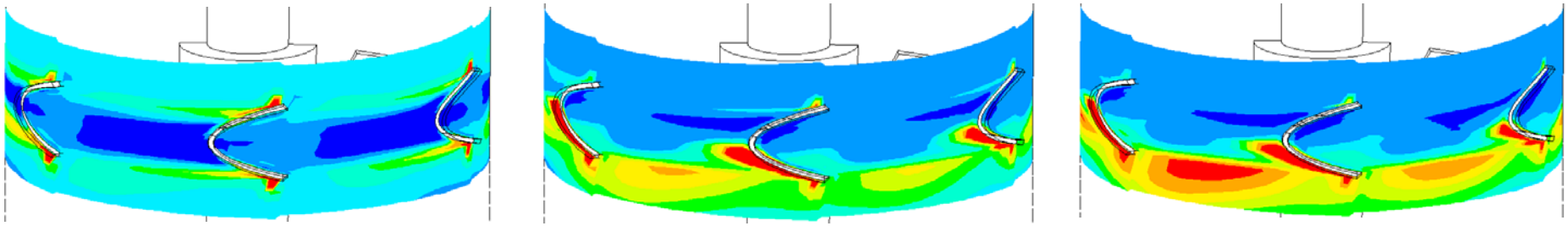

(a) Fl = 0.004 (10 uniform contours, blue ≡ 0.005, Red ≥ 0.1)

(b) Fl = 0.04 (10 uniform contours, blue ≡ 0.01, Red ≥ 0.25)

(c) Fl = 0.1 (10 uniform contours, blue ≡ 0.01, Red ≥ 0.25)

Figure 5.19: Predicted Gas Holdup Distribution around Impeller Blades, Fr = 0.242

two-fluid model along with the standard k-ε model of turbulence was then developed to simulate gas-liquid flows. The model was used to simulate gas holdup distribution in stirred reactor operating in VC, S33 and L33 flow regimes. The predicted results were compared with the experimental data of Bombac *et al.* (1998). Along with the gas holdup distribution, the computational model was able to predict the influence of the gas flow rate/ flow regime on the gross impeller characteristics like impeller pumping number and power number. The computational model was then used to examine flow structures around impeller blades for different flow regimes. The model was able to capture accumulation of gas behind the impeller blades and their influence on the structure of trailing vortices. It was however not possible to predict the exact shape of the gas cavities present behind the blades.

The developed computational model was further used to identify the similarity and the differences between the flow generated by a modern radial flow impeller, Scaba turbine and the standard Rushton turbine. The CFD simulations have enabled the similarities and the differences between the single-phase flows generated by the Rushton and Scaba turbines to be identified. The computational model correctly captures the overall flow field generated by both turbines. The predicted results also indicate a difference in the axial profiles of velocities, which decays as one moves away from the impeller plane. The difference between the shapes of the axial profiles of turbulent quantities for the two turbines is significant and is related to the strength and size of the trailing vortices generated by the different impellers. The predicted smaller low-pressure region and smaller and low-strength trailing vortices present behind the blades of Scaba turbine confirms the observed better performance of the Scaba turbine compared to Rushton turbine. The gas-liquid flow in the stirred reactor was then simulated for three gas flow rates (Fl = 0.004, Fl = 0.04 and Fl = 0.1). With respect to the gas phase, the computational model was able to capture the complete dispersion of the gas. The predicted gas accumulation behind the impeller blades indicated only a small change in the magnitude of gas accumulation even for higher gas flow rate explaining the so-called possible advantage of Scaba turbine over Rushton turbine.

Overall, the model appears to capture most of the key features of the single phase, as well as the gas-liquid flow. The developed model was further used to simulate the gas-

liquid flow generated by an axial flow impeller, before extending to address some of the key reactor engineering issues.

Chapter 6

FLOW GENERATED BY AXIAL FLOW IMPELLERS

6.1 Introduction

Stirred reactors are often used in the process industries for dispersing gas into bulk liquid. In many cases, radial flow impellers like Rushton turbine are used for such applications. These radial impellers generate more head (shear rate) than the flow for a given power consumption per unit mass than axial impellers. The generated high shear rate is useful for dispersing the sparged gas into smaller gas bubbles. However, in many gas dispersion applications, the bulk flow generated by an impeller may be just as important as the head (shear rate) developed by an impeller. Sufficient bulk flow is crucial for the circulation and distribution of gas bubbles throughout the entire reactor and also for adequate heat transfer, mixing process and solid suspension (in case of three phase systems). Axial flow impellers, like pitched blade turbines, have a good balance between generated head and generated flow, and therefore are being increasingly used for the gas-liquid applications in stirred reactors.

6.1.1 Previous work

Previous workers (see for example, Chapman *et al.*, 1983; Bujalski *et al.*, 1988; Cooke *et al.*, 1988 and references cited therein) have studied the global parameters, such as total gas hold-up and flow regime transition in an aerated stirred reactor equipped with a down- pumping pitched blade turbine. Although reasonable information required for the design and operability of stirred reactors was given, these studies did not provide any local information. The local information on gas volume fractions and flow fields is crucial for many gas-liquid applications. Experimental techniques, like laser Doppler anemometer, LDA, (Mishra and Joshi, 1994) or particle image velocimetry, PIV, (Aubin *et al.*, 2004) have been used to obtain such local information in stirred tanks. However, these studies were carried out with low volume fraction of gas holdup present in the reactor due to inherent limitation associated with these optical techniques (Deen *et al.*, 2001). Also the need for transparent reactor and time required for the installation and measurement restricted the use of these techniques for laboratory scale geometries.

It is therefore, essential to develop and validate the computational models to simulate the flow in stirred reactors for their subsequent use for design and process improvement. CFD has already shown to be successful in simulating single-phase flow

generated by impeller(s) of various shapes in complex reactors (Ranade, 2002). Gas-liquid flows in stirred tanks, however, exhibit increased complexity making simulation by CFD a much more difficult task. Despite such complexities, several attempts have been made in recent years to develop computational models of gas-liquid flows in stirred reactors (see for example, Ranade and van den Akker, 1994; Bakker and van den Akker, 1994; Morud and Hjertager, 1996; Ranade and Deshpande, 1997, Lane *et al.* 2000, Ranade *et al.*, 2001b and Lane *et al.*, 2004). The focus of these studies was to correctly predict the gas-liquid flow characteristics over the whole reactor and understand the flow around impeller blades. It is interesting to note that almost all of the above studies were restricted to the flow generated by radial flow impeller. However, very few attempts have been made to simulate the gas-liquid flow generated by down- pumping pitched blade turbine.

Bakker and van den Akker (1994) first time simulated the gas-liquid flow generated by the down- pumping pitched blade turbine. They have first simulated the single-phase flow in stirred reactor using commercial CFD software FLUENT (of Fluent Inc., USA). The simulated single-phase flow pattern, including the turbulence distribution was then used as input for an in-house code GHOST (Gas Holdup Simulation Tool). The gas holdup distribution over the reactor was then calculated on the basis of balance equations for gas. A mathematical model for bubble breakup and coalescence based on local turbulent intensity and local dissipation rate was incorporated in the GHOST. They have calculated local gas holdup distribution, bubble size distribution, interfacial area distribution and local mass transfer rate over the reactor. However, they have assumed negligible influence of the gas on the liquid flow. This assumption is only valid for the reactors operating with low gas holdup values. The bubble drag coefficient was calculated using modified Reynolds number based on effective viscosity (summation of molecular viscosity and turbulent viscosity). However, the recent studies of Lane *et al.* (2000) have shown that the bubble drag coefficient proposed by Bakker and van den Akker (1994) did not predict the gas holdup distribution accurately. Also, the assumption of negligible influence of the gas on the liquid flows limits the application of proposed model for simulating gas-liquid flows for higher gas loading.

Recently, Ranade *et al.* (2002) has simulated the gas-liquid flow in stirred reactor using two-fluid model. They have captured the presence of trailing vortices and gas

accumulation behind the impeller. Though the developed models have shown the promise in simulating trailing vortices and gas accumulation behind the impeller blades, the ability of these model to correctly simulate the gas holdup distribution and liquid phase flow characteristics is yet to be studied. For any progress in the development of these models, the simulated results on liquid velocities and phase holdup are need to compared with the experimental data. Present work is carried out with this motivation. The detail contributions of the present work are discussed below.

6.1.2 Present work

In the present work, simulations were therefore carried out using a two-fluid model with the standard k-ε turbulence model to understand key characteristics of the flow generated by the down- pumping pitched blade turbine. The commercial CFD software, FLUENT version 4.5 (of Fluent Inc., USA) with appropriate user defined subroutines, was used to simulate the turbulent two-phase flow. The computational snapshot approach was used to simulate the impeller rotation. The interphase drag force formulation, proposed in Chapter 5, was used while simulating the gas-liquid flow generated by a down- pumping pitched blade turbine. In order to complement the available information, simulations were carried out for a dished bottom stirred reactor with the geometrical specifications same as that used by Aubin *et al. (2004)*. The model predictions were compared with the PIV measurements reported by Aubin *et al. (2004)* and Khopkar *et al.* (2003). The computational model was used to study the flow around impeller blades and understand the effect of extent of gas accumulation on the structure of trailing vortices.

Pitched blade turbines can be operated in up- as well as down- pumping mode. The chosen mode of pumping has its own advantages in process application, depending on the process demands. Bujalski *et al.* (1988) have reported that up- pumping mode is better than down- pumping mode. However, many think this to be paradoxical since intuitively down- pumping mode appears to be more beneficial than the up- pumping mode for dispersing gas. Computational models may make useful contributions to understand the gas dispersion capabilities of axial flow impellers and interaction of pumping mode on other variables like the scale of operation and prevailing flow

regime. The developed computational model has then been used to understand the effect of blade angle/pumping direction on the performance of impeller (flow around impeller blades, pumping number and power dissipated by an impeller). Apart from a down- ($\theta = 45°$) and up- ($\theta = -45°$) flow pitched blade turbine, the mean position, paddle (straight) blade turbine ($\theta = 0°$) has also been considered in the present study. An attempt was made to bring out the differences and the similarities between the flow generated by these three impellers. Such study will be useful while selecting the pitched blade turbines for specific operation. The computational model and the results are discussed in following sections.

6.2 Computational Model

6.2.1 Model equations

For simulating gas-liquid flow in a stirred reactor, a two-fluid model based on the Eulerian - Eulerian approach was used in this work. The governing equations for each phase in Eulerian-Eulerian approach and for the standard k-ε turbulence model are given in Chapter 5 and therefore not repeated here.

In Eulerian-Eulerian approach, the correct modelling of the interphase momentum exchange terms controls the predictive capability of the computational model. The interphase momentum exchange term consists of four different interphase forces: the Basset force, the virtual mass force, the lift force and the interphase drag force. In most cases, the magnitude of the Basset force is much smaller than that of the interphase drag force. In the bulk region of the reactor, the velocity gradients are not large. Near the impeller, pressure gradients and interphase drag forces mainly dominate the motion of the bubbles. An order of magnitude analysis indicates that the magnitude of the lift force is much smaller than the interphase drag force. The numerical studies reported in previous chapter indicate that the effect of the virtual mass force is not significant in the bulk region of the stirred reactor. Considering these results, only the inter-phase drag force was retained in the inter-phase momentum exchange terms in the present study.

The inter-phase drag force exerted on phase 2 in the *i* direction is given by:

$$F_{q_i} = F_{D2i} = -\frac{3\alpha_1\alpha_2\rho_1 C_D\left(\sum\left(\vec{U}_{2i}-\vec{U}_{1i}\right)^2\right)^{0.5}\left(\vec{U}_{2i}-\vec{U}_{1i}\right)}{4d_b} \tag{6.1}$$

In gas-liquid stirred reactors the interphase drag coefficient, C_D, is a complex function of the drag coefficient in a stagnant liquid, the gas holdup and prevailing turbulence. The influence of the free stream turbulence on the bubble drag coefficient is numerically studied in the chapter 5. Following this, we have used the following correlation (Equation 6.2) for the calculation of the drag coefficient in turbulent flow:

$$\frac{C_D - C_{D0}}{C_{D0}} = K\left(\frac{d_b}{\lambda}\right)^3 \tag{6.2}$$

$$C_{D0} = \max\left\{\left(\frac{2.667 * Eo}{Eo + 4.0}\right), \left(\frac{24}{\mathrm{Re}_b} * \left(1 + 0.15 * \mathrm{Re}_b^{0.687}\right)\right)\right\}$$

where, λ is the Kolmogorov length scale, d_b is the bubble diameter and K is an empirical constant, which was set to 6.5×10^{-6}. Equation (6.2) thus accounts for the increased drag coefficient due to prevailing liquid phase turbulence.

The gas-liquid flow in the stirred reactor was simulated using the computational snapshot approach. In this approach, the impeller blades are considered as fixed at one particular position (similar to taking a snapshot of the rotating impeller) with respect to the baffles. The formulation of snapshot approach for the simulation of two-phase flow is discussed in Chapter 4 and therefore it is not repeated here. The flow is simulated for a specific blade position with respect to the baffles. The results obtained with a specific snapshot position were not found to be significantly different from the ensemble average of a number of snapshots (see Ranade and van den Akker, 1994 for more details). The computational snapshot approach was implemented in the commercial CFD code FLUENT 4.5 (of Fluent Inc., USA) using user-defined subroutines.

6.2.2 Solution domain and boundary conditions

In the present work, the experimental set-up used by Aubin *et al.* (2004) was considered. All the relevant dimensions like the impeller diameter, the reactor shape

and diameter and so on were the same as the one used by Aubin *et al.* (2004). The system investigated consists of a stirred cylindrical reactor, with a dished bottom (diameter, T= height, H= 0.19 m, R_c= 0.19 m) with four baffles (width= T/10= 0.019 m) equally spaced around the reactor periphery and a ring sparger (d_{sp}= 0.076 m, located at 0.047 m from bottom). The shaft (diameter d_s= 0.008 m) of the impeller was concentric with the reactor axis and extended till the bottom of the reactor. Axial flow impellers (pitched blade turbine operating in down- [PBTD] and up- pumping mode [PBTU]) and Paddle turbine, of diameter, D= 0.095 m, were used for all simulations. The impeller off-bottom clearance was (C= 0.0667 m, measured from the lowest impeller swept plane).

Considering the geometrical symmetry, half of the reactor was considered as a solution domain (see Figure 6.1). The baffles were considered at angles of 45^o and 135^o. The impeller was positioned in such a way that three blades were located at angles of 30^o, 90^o and 150^o (measured from center line of impeller blade). As discussed in chapter 4, the computational snapshot approach divides the solution domain into an inner region, in which time derivative terms are approximated using spatial derivatives and an outer region, in which time derivative terms are neglected. The boundary between the inner and outer regions needs to be selected in such a way that the predicted results are not sensitive to its actual location. In the present work, for all the simulations, the boundary of the inner region was positioned at r = 0.065 m and 0.05 m $\leq$ z $\leq$ 0.15 m (where *z* is the axial distance from the bottom of the reactor).

In the present work, the sparger is modeled as a solid wall. The mass source of the gas phase was specified one cell above the sparger to simulate gas introduction into the reactor. Special boundary conditions are needed to simulate gas-liquid interface at the top through which bubbles escape the solution domain. Recently, Ranade (2002) has discussed different possible approaches to treat gas-liquid interface in detail. We have modeled the top surface of the dispersion as a velocity inlet. The outgoing (axial) velocity of gas bubbles was set equal to the terminal rise velocity of gas bubbles (estimated as 0.2 m/s for air bubbles). All the other velocity components for gas and liquid phase were set to zero). Implicit assumption here is that gas bubbles escape the

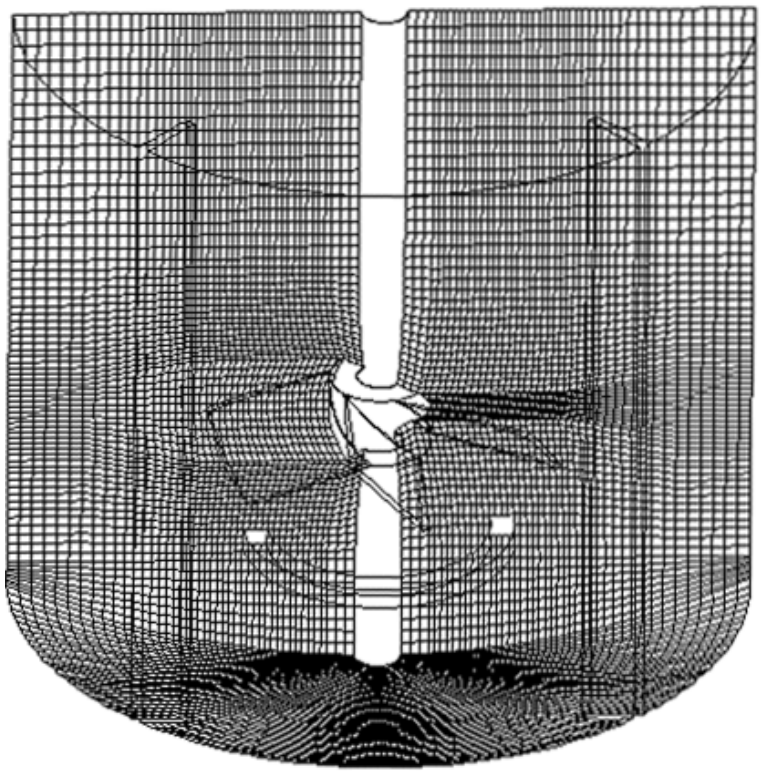

Grid Details	:
$r \times \theta \times z$	: $46 \times 96 \times 72$
Impeller blade	: $21 \times 2 \times 10$
Inner region	: $19 \leq k \leq 60$ $j \leq 35$

Figure 6.1: Computational Grid and Solution Domain

dispersion with terminal rise velocity. Since the liquid velocity near the top gas-liquid interface is small and the overall volume fraction of gas is also small (< 5%), this assumption is reasonable. It should be noted that even after defining top surface as an inlet, gas volume fraction at the top surface is a free variable. The mass and momentum conservation equations for the gas phase were solved and the gas distribution within the reactor was predicted. The mass conservation was verified by comparing the integral gas mass flow rate across various horizontal planes with the input gas mass flow rate at the sparger.

In a gas-liquid stirred reactor, there is a wide distribution of bubble sizes. The prevailing bubble size distribution in a gas-liquid stirred reactor is controlled by several parameters like reactor configuration, impeller speed and gas flow rate. It is possible to develop a detailed multi-fluid computational model using population balance framework to account for bubble size distribution. However, the use of multi-fluid models based on the population balances increase the computational demands by manifolds. Unfortunately available experimental data of bubble size distribution in stirred reactor is not adequate to calculate the parameters appearing in the coalescence and break-up kernels. Considering these issues, in the present work, a single bubble size was specified (4 mm) over whole reactor domain for all the simulations. Fluid properties were set to those of water and air for the primary and secondary phases, respectively.

A commercial grid-generation tool, GAMBIT 2.0 (of Fluent Inc., USA) was used to model the geometry and to generate the body-fitted grids. It is very important to use an adequate number of computational cells while numerically solving the governing equations over the solution domain. The prediction of turbulence quantities is especially sensitive to the number of grid nodes and grid distribution within the solution domain. The previous work of Ranade *et al.* (2001a) as well as other published work (Ng *et al.*, 1998 and Wechsler *et al.*, 1999) gives adequate information on the influence of the grid on the predicted results. It was demonstrated that, in order to capture the details of the flow near impeller, it is necessary to use at least 200 grid nodes to resolve the blade surface. Based on the previous experience, the numerical simulations for the gas-liquid flows in stirred reactors were carried out for grid size of

($r \times \theta \times z$: $46 \times 96 \times 72$). In the present work, we have used ($r \times \theta \times z$: $21 \times 2 \times 10$) grid nodes to resolve the blade surface. In the present work, we have used ($r \times \theta \times z$: $21 \times 2 \times 10$) grid nodes covering the impeller blade. The boundary of the inner region was positioned at $j \leq 35$ and $19 \leq k \leq 60$ (where j is the cell number in the radial direction from the shaft and k is the cell number in the axial direction from the bottom of the reactor). The computational grid used in the present work is shown in Figure 6.1.

Differencing of the advection terms has been carried out using the QUICK discretization scheme with the SUPERBEE limiter function (to avoid non-physical oscillations). Standard wall functions were used to specify wall boundary conditions. Different criteria like the reduction of the residuals, gas mass flow rate through various horizontal planes and variation of overall gas hold-up and energy dissipation rates were used to ensure adequate convergence. The validation of computational results with the reported experimental data is discussed in the following section.

6.3 Results and Discussion

6.3.1 Single-phase flow

6.3.1.1 Bulk flow characteristics

The flow generated by the pitched blade turbine in a stirred reactor operating in the down- pumping mode was simulated for an impeller rotational speed of 300 rpm. Without using any impeller boundary conditions, the snapshot approach was able to simulate the flow generated by the impeller. The comparison of the predicted velocity field and experimental PIV data (reported by Aubin *et al.*, 2004) at mid-baffle position is shown in Figure 6.2. A high velocity jet emanating from the bottom of the impeller and a small reverse loop below the hub, seen in the experimental flow field, was captured in the simulations.

Quantitative comparison of the predicted results and the experimental data of Aubin *et al.* (2004) are shown in Figure 6.3. It can be seen from Figure 6.3a that the comparison

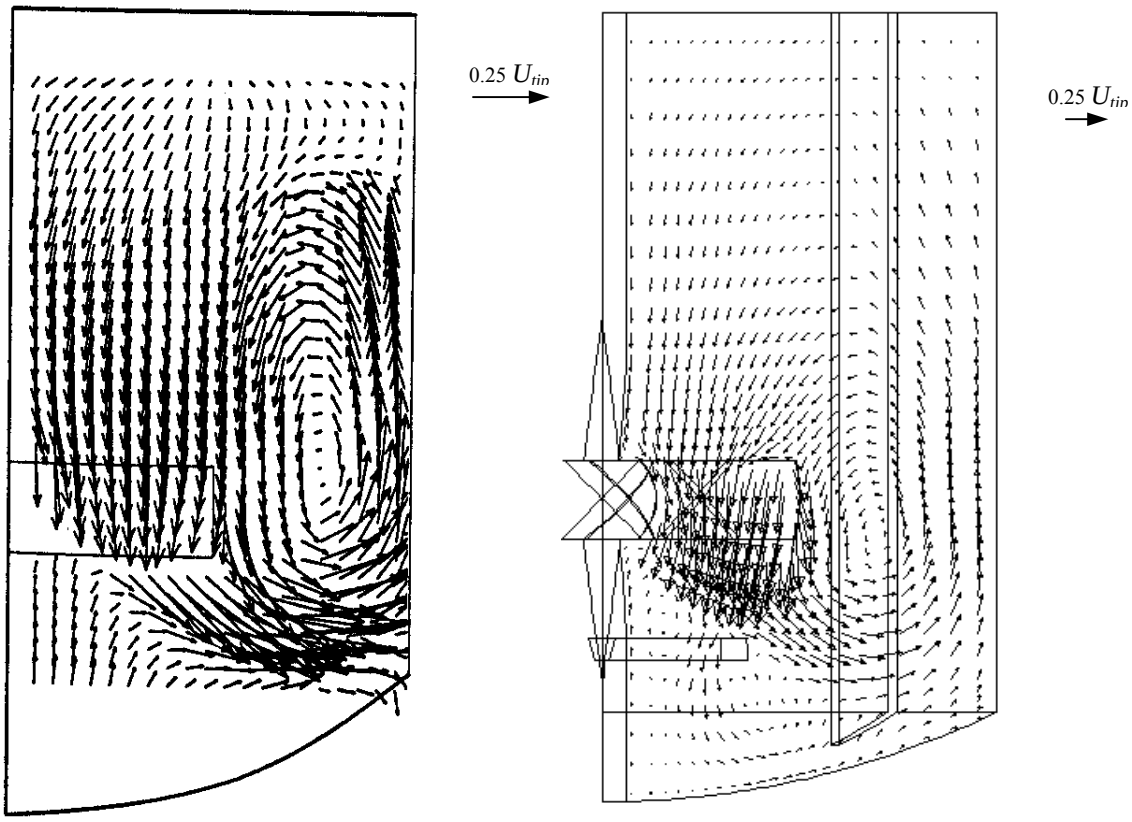

(a) Experimental (mid-baffle plane) (b) Predicted (mid-baffle plane)

Figure 6.2: Mean Flow Field at the *r-z* Plane for Single-phase Flow, N = 300 rpm and U_{tip} = 1.5 m/s.

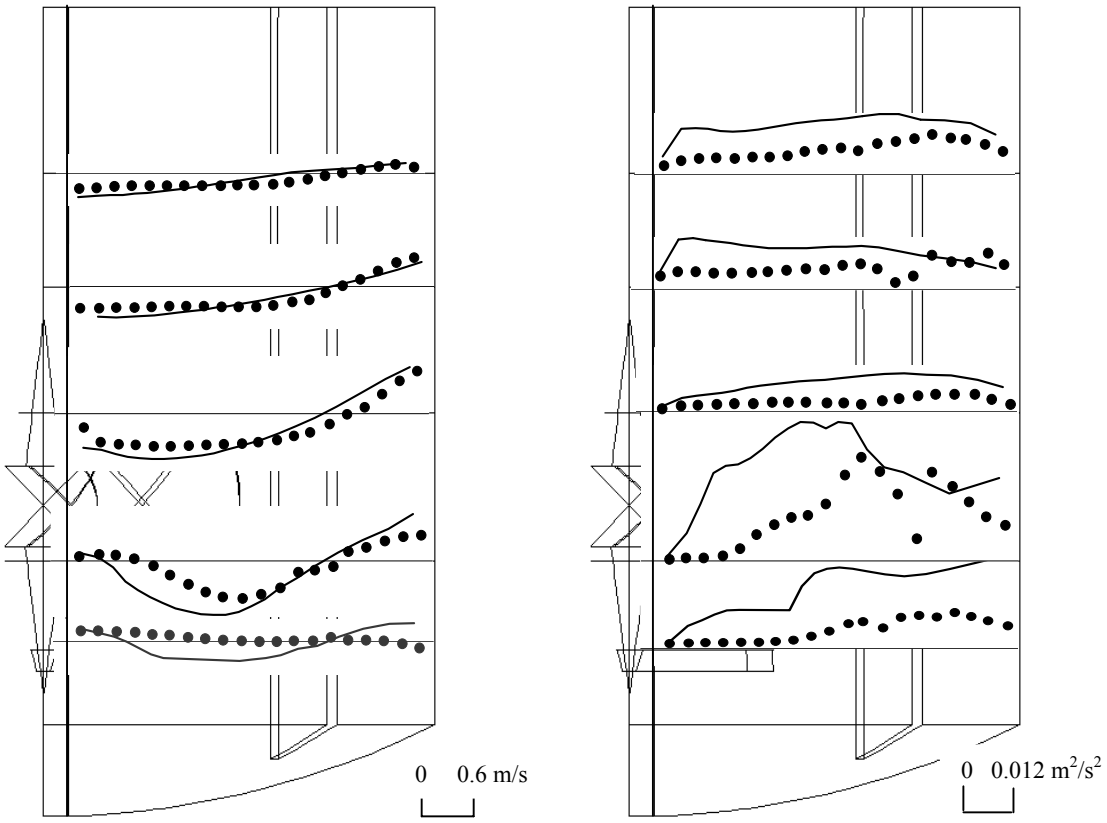

(a) Axial Velocity (b) Turbulent Kinetic Energy

Legends:

●	Experimental data (Aubin *et al*., 2002)
——	Predicted results

Figure 6.3: Comparison of Predicted Results and Experimental Data for Single-phase Flow, N = 300 rpm, U_{tip} = 1.5 m/s

between the predicted values of the axial velocity and experimental data is satisfactory, except for a small region below the impeller. The measured and predicted axial velocity field was used for calculating the flow (or pumping) number for the pitched blade turbine as:

$$N_Q = \frac{2\int \pi r U dr}{N D_i^{\,3}} \tag{6.3}$$

The limits of integration for the radial distance are from the surface of the shaft to the impeller radius. The predicted pumping number for the pitched blade turbine (0.71) is in good agreement with the reported experimental value of 0.68 (Aubin *et al.*, 2004).

The values of turbulent kinetic energy are rather over predicted (Figure 6.3b), especially in the region below the impeller (in the impeller discharge flow stream). Reasons for these discrepancies are not obvious. The use of more complex models, like the Reynolds stress models, did not show any significant improvement over the standard k-ε model for the case of flow generated by the Rushton turbine (see Jenne and Reuss, 1999). Correct prediction of turbulence levels is important for applications controlled by turbulence quantities like dispersion of bubbles or micro-mixing. Fortunately, even in many of such applications, the relevant processes depend on the fractional power of turbulence energy dissipation rate (for example, prediction of Sauter mean diameter depends on $\varepsilon^{0.4}$). Thus 30% over-prediction of energy dissipation rates lead to a smaller (14%) error in Sauter mean diameter. Therefore, the observed discrepancies may not be a serious impediment to many reactor-engineering applications. We have therefore, extended the computational model to study the gas-liquid flow generated by the pitched blade turbine operating in down- pumping mode in a stirred reactor. However, before we discuss the simulations of gas-liquid flow, it is useful to examine the flow characteristics near the blades of the pitched blade turbine for the case of liquid-only flow.

6.3.1.2 Flow around impeller blades

The down- pumping 6-blade pitched turbine generates a high velocity jet moving downwards. An iso-surface of the axial velocity around the impeller blades was used to study the flow emanated from the pitched blade turbine. It can be seen from Figure 6.4a that the jet emanating from the front side is faster than that emanating from the backside of the blade. The jet flowing downwards from the front side of the blade appears to interact with the trailing vortex attached to the backside of the blade. The movement of the blade generates a high-pressure region ahead of the blade leading edge, and a low-pressure region behind the blade.

Such a pressure difference leads to a trailing vortex behind the impeller blades. A single trailing vortex was detected behind each of the blades of the pitched blade turbine. An iso-surface of predicted Z-vorticity (ω) for the pitched blade turbine is shown in Figure 6.4b. It can be seen from Figure 6.4b that a single trailing vortex is attached to the backside of impeller blade and flows downwards as it moves away from the leading impeller blade. To examine the flow structure around impeller blades, the predicted mean velocity field and an angle-resolved experimental data (obtained from PIV measurements reported by Khopkar *et al.*, 2003) behind impeller blade is shown in Figure 6.5. The presence of a trailing vortex and its movement within the impeller stream are clearly evident. The comparison of the predicted results with the experimental data shows a good agreement (qualitative as well as quantitative). The predicted strength of the trailing vortex is found to be somewhat lower than the experimental value, which leads to a relatively early dissipation of the trailing vortex in the simulation.

A quantitative comparison of the axial velocity at 20° behind the impeller blade with the experimental data of Khopkar *et al.* (2003) at three different axial locations is shown in Figure 6.6. It can be seen from Figure 6.6 that the computational model over-predicts the axial velocity values near the impeller blade in the impeller swept region. This may be a consequence of the specific blade position considered in the present work. The comparison improves as one moves radially away from impeller blade. After establishing that the computational model is reasonably successful for single-phase flow, it was extended to simulate the gas-liquid flow in the stirred reactor.

(a) Iso-surface of Axial Velocity Jet (U/U_{tip} = 0.6, in down-ward direction)

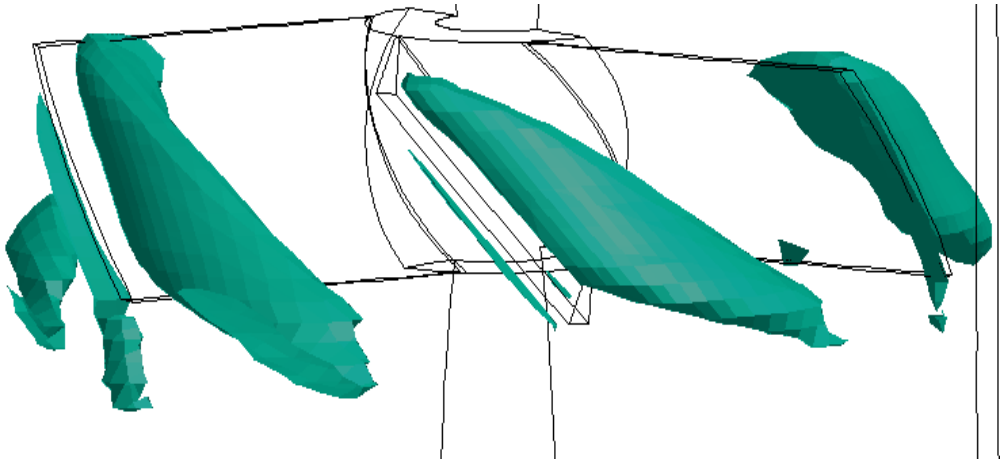

(b) Iso-surface of Z-Vorticity ($\omega D_i/U_{tip}$ = -5)

(Impeller is moving from right to left)

Figure 6.4: Flow Field around the Impeller Blades for Single-phase Flow, N = 300 rpm and U_{tip} = 1.5 m/s

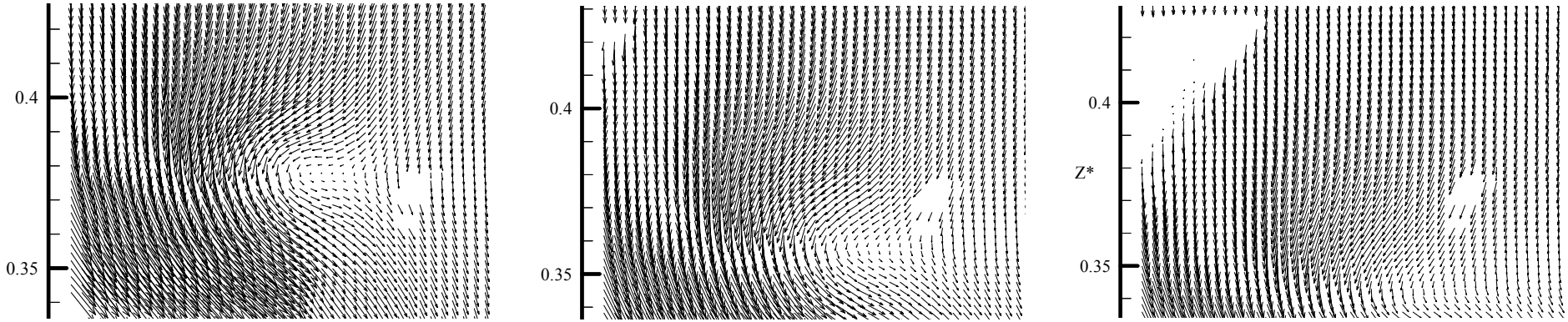

(i) 10° behind the impeller blade (ii) 20° behind the impeller blade (iii) 30° behind the impeller blade

(a) Experimental Data (Khopkar et al., 2003)

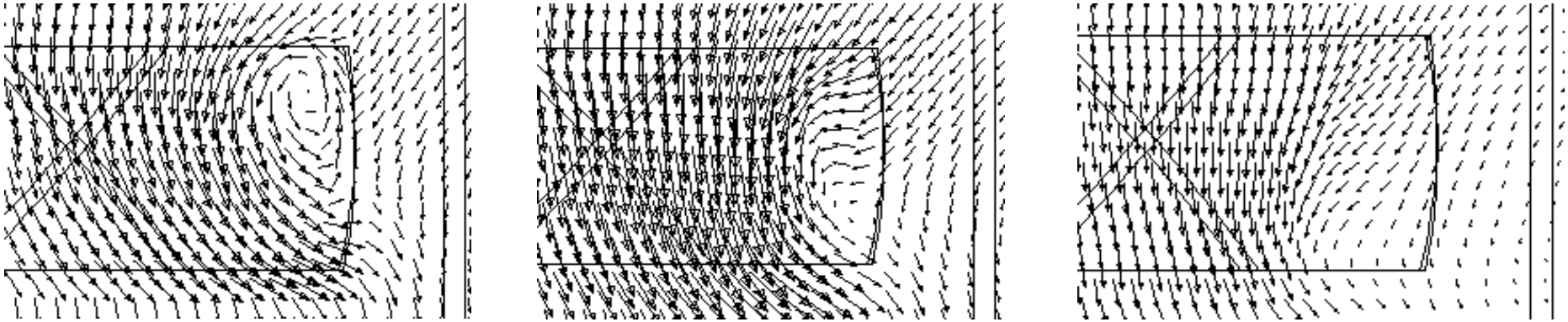

(i) 10° behind the impeller blade (ii) 20° behind the impeller blade (c) 30° behind the impeller blade

(b) Predicted Results

Figure 6.5: Flow Field near the Impeller Blades (single phase flow), N = 300 rpm and U_{tip} = 1.5 m/s

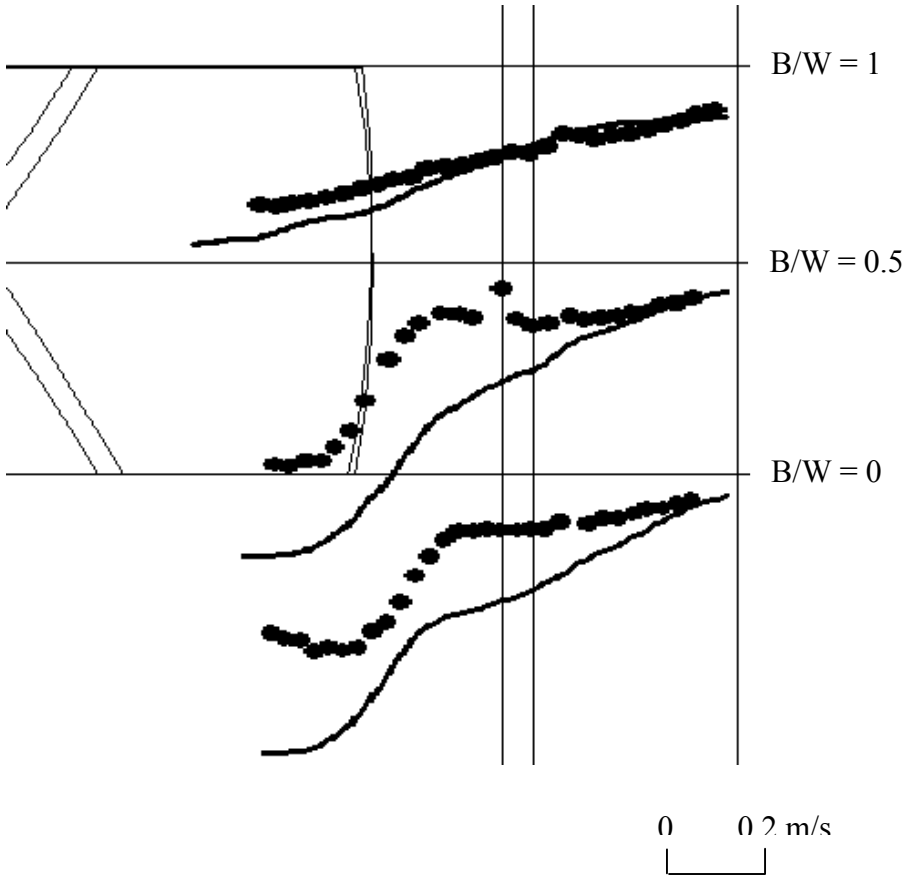

(20° behind the impeller blade)

Figure 6.6: Comparison of Simulated Axial Velocity with Experimental Data (single phase flow), N = 300 rpm and U_{tip} = 1.5 m/s

6.3.2 Gas-liquid flows

6.3.2.1 Bulk flow characteristics

Gas-liquid flow generated by the 6-blade down- pumping pitched blade turbine in the stirred reactor was simulated first for a gas flow number of 0.01 [corresponding to a volumetric gas flow rate (Q_g) of 4.29×10^{-5} m^3/s and an impeller rotational speed equal to 300 rpm]. Under these operating conditions, gas was completely dispersed in the reactor (see Aubin *et al.*, 2004 for more details). The comparison of the predicted liquid velocity field with the experimental PIV data (at mid-baffle position) is shown in Figure 6.7. Similarly to the single-phase flow, the high velocity jet emanating from the bottom of the impeller seen in the experimental flow field is captured in the simulations. The predicted velocity field shows a reduction in liquid velocity magnitudes for the case of gas-liquid flow compared with the liquid-only flow.

The quantitative comparisons of predicted values of the liquid phase axial velocity for the liquid-only and gas-liquid flow cases with experimental data are shown in Figures 6.8a and 6.8b. It can be seen from Figures 6.8a and 6.8b that the computational model captured the inward shift of the location of the maximum axial velocity after aeration. Although the comparison between the predicted results and the experimental data is not as good as observed in the single phase flow case, the computational model captures key features of the gas-liquid flow with reasonable accuracy. A quantitative comparison of the predicted kinetic energy with the experimental data is shown in Figures 6.9a and 6.9b. It can be seen from Figures 6.9a and 6.9b that the computational model over-predicts the values of the turbulent kinetic energy. It is interesting to note that the predicted values of turbulent kinetic energy for the gas-liquid flow are higher than the predicted values for the single-phase flow in some regions.

The predicted influence of gas flow rate on gross characteristics, power and pumping numbers are also of interest. The power number was calculated by using predicted results of turbulent energy dissipation rates as:

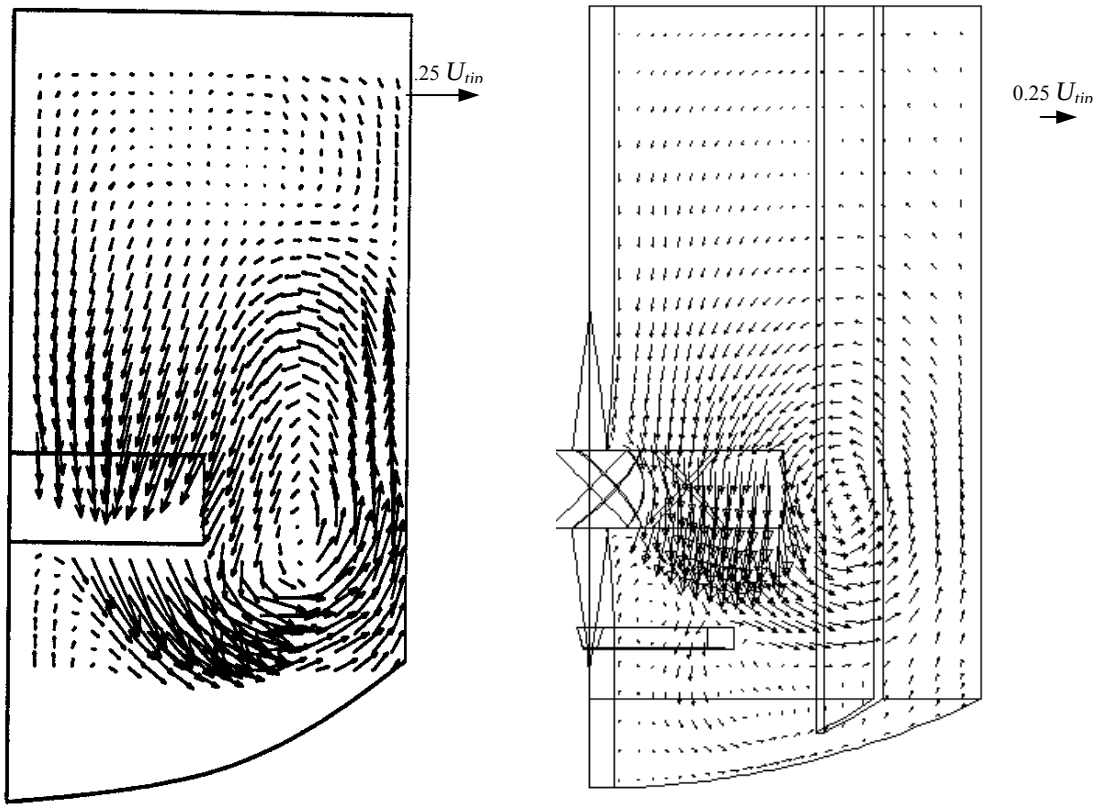

(a) Experimental (mid-baffle plane) (b) Predicted (mid-baffle plane)

Figure 6.7: Mean Liquid Flow Field at the *r*-*z* Plane for Gas-Liquid Flow, Fl = 0.01 and Fr = 0.242

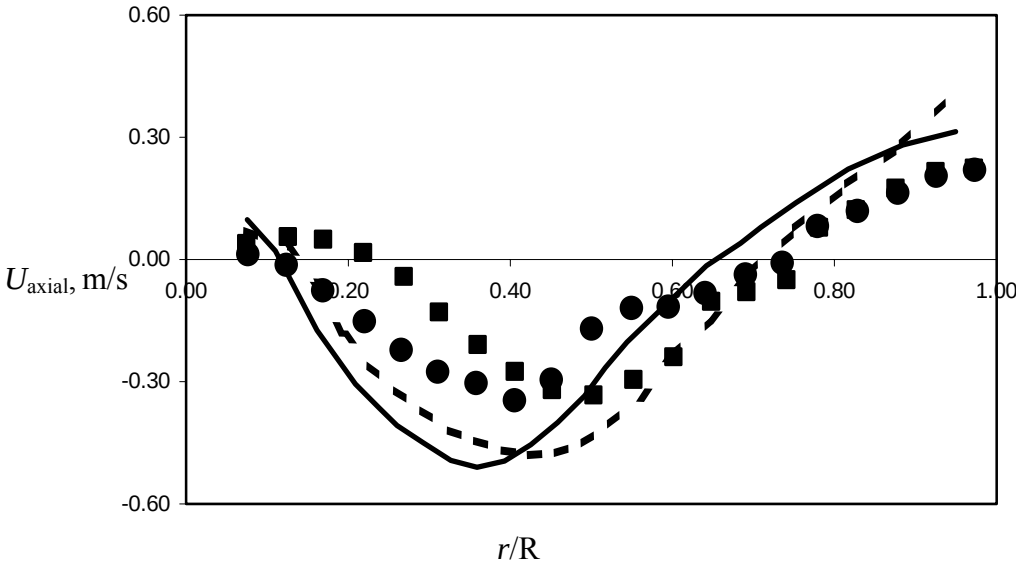

(a) Axial Velocity of liquid, z/T = 0.31

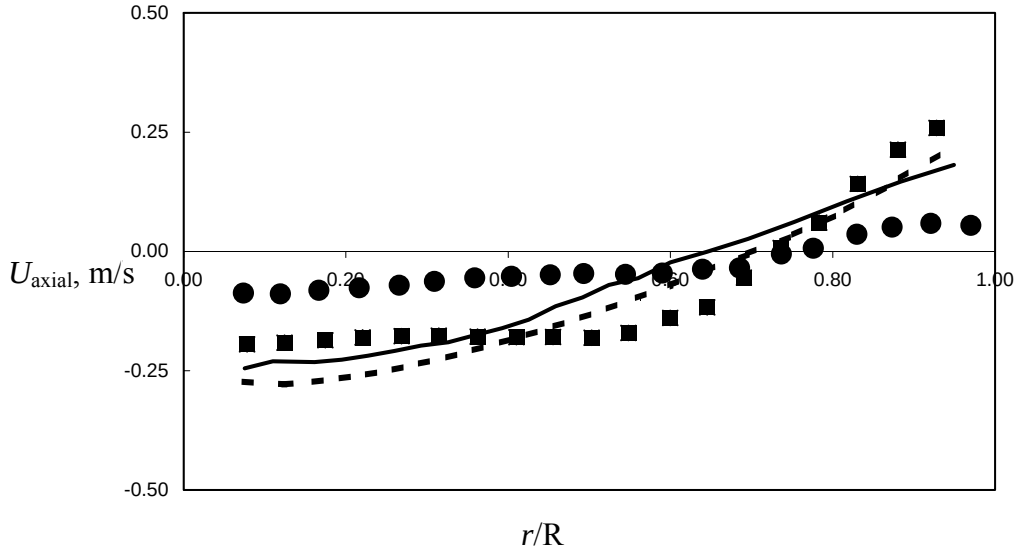

(b) Axial Velocity of liquid, z/T = 0.65

Legends:		
	■ Data of Aubin *et al*. (2002), L flow	- - Predicted results, L flow
	● Data of Aubin *et al*. (2002), GL flow	—— Predicted results, GL flow

Figure 6.8: Comparison of Predicted Results and Experimental Data for Gas-Liquid Flow, Fl = 0.01 and Fr = 0.242

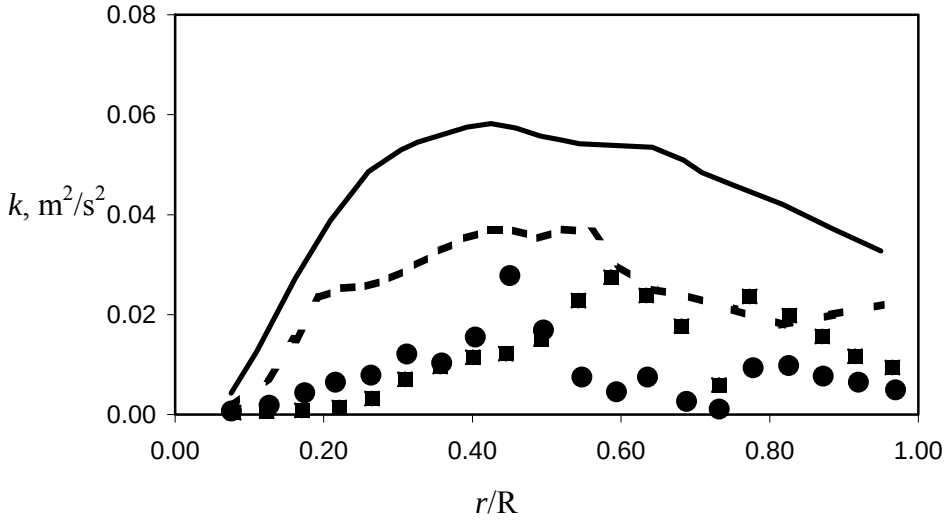

(c) Turbulent Kinetic Energy, z/T = 0.31

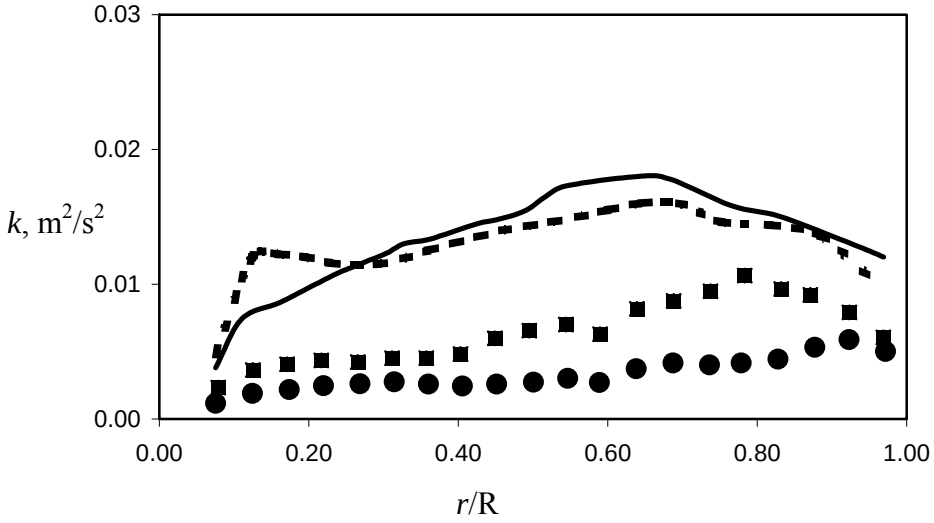

(b) Turbulent Kinetic Energy, z/T = 0.65

Legends:

Data of Aubin *et al*. (2002), L flow	Predicted results, L flow
Data of Aubin *et al*. (2002), GL flow	Predicted results, GL flow

Figure 6.9: Comparison of Predicted Results and Experimental Data for Gas-Liquid Flow, Fl = 0.01 and Fr = 0.242

$$N_P = \frac{2\int_V \alpha_l \rho \varepsilon dV}{\rho N^3 D_i^5} \qquad (6.4)$$

The experimentally measured and predicted values of the pumping and power number are listed in Table 6.1. As the gas flow rate increases, impeller pumping as well as power dissipation decreases. The CFD model predicts the decrease in power dissipation and pumping capacity in the presence of gas.

The predicted gas holdup distribution and the mean gas velocity field at the mid-baffle plane are shown in Figure 6.10. It can be seen from Figure 6.10 that the computational model captures the indirect loading of the impeller. This agrees well with the experimental observations of Aubin (2001) and the previous experimental studies by Bujalski *et al.* (1988). The predicted gas holdup distribution is shown in Figure 6.10b. The computational model correctly captures the complete dispersion of gas in the stirred reactor. The predicted value of the total gas holdup (4.2%) was somewhat higher than the reported experimental value (3.7%).

6.3.2.2 Flow around impeller blades

In a gas-liquid stirred reactor, the addition of gas phase affects the performance of the impeller and particularly its pumping capacity. Therefore, it is important to study the influence of gas on the flow near the impeller blades. Even for a low gas flow number like 0.01, Aubin *et al.* (2004) observed several difficulties to obtain correct PIV measurements around the impeller blades. The high gas holdup behind the impeller blades significantly reduces the accuracy of the PIV measurements. Therefore, Khopkar *et al.* (2003) carried out angle resolved PIV measurements at a lower volumetric gas flow rate, equal to 4.29×10^{-6} m^3/s with an impeller rotational speed of 300 rpm (Fl = 0.001 and Fr = 0.242). The gas-liquid flow generated by a down- pumping pitched blade turbine was again simulated for lower value of volumetric gas flow rate equal to 4.29×10^{-6} m^3/s with an impeller rotational speed of 300 rpm (Fl = 0.001 and Fr = 0.242). The comparison of the reported experimentally measured angle-resolved liquid velocity field and the predicted results is shown in Figure 6.11. The experimentally

Table 6.1: Gross Characteristics, Fl = 0.01 and Fr = 0.242

Turbine	Pumping Number				Gas Holdup, %	
	Experimental*		Predicted		Experimental*	Predicted
	L	G-L	L	G-L		
Down-	0.68	0.59	0.71	0.63	3.7	4.2
Paddle	-	-	0.62	0.55	-	2.9
Up-	0.72	-	0.69	0.62	5.8	7.2

(* Experimental data from Aubin *et al.*, 2004)

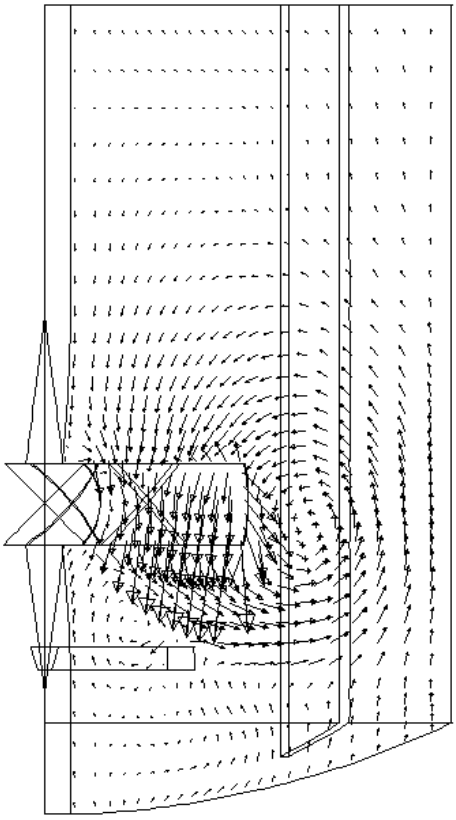

(a) Predicted Gas Flow Field (mid-baffle plane)

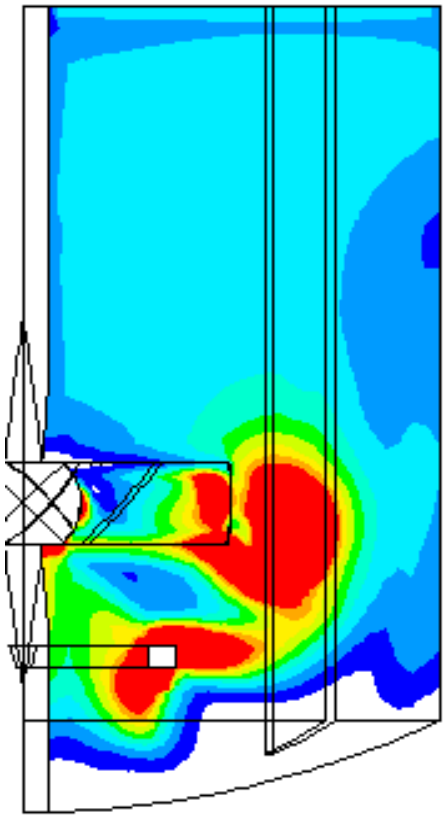

(b) Predicted Gas Holdup Distribution (mid-baffle plane)

(10 uniform contours; minimum gas volume fraction, blue = 0.01 and maximum gas volume fraction, red ≥ 0.1)

Figure 6.10: Predicted Gas Flow Field at the *r-z* Plane for Gas-Liquid Flow, Fl = 0.01 and Fr = 0.242

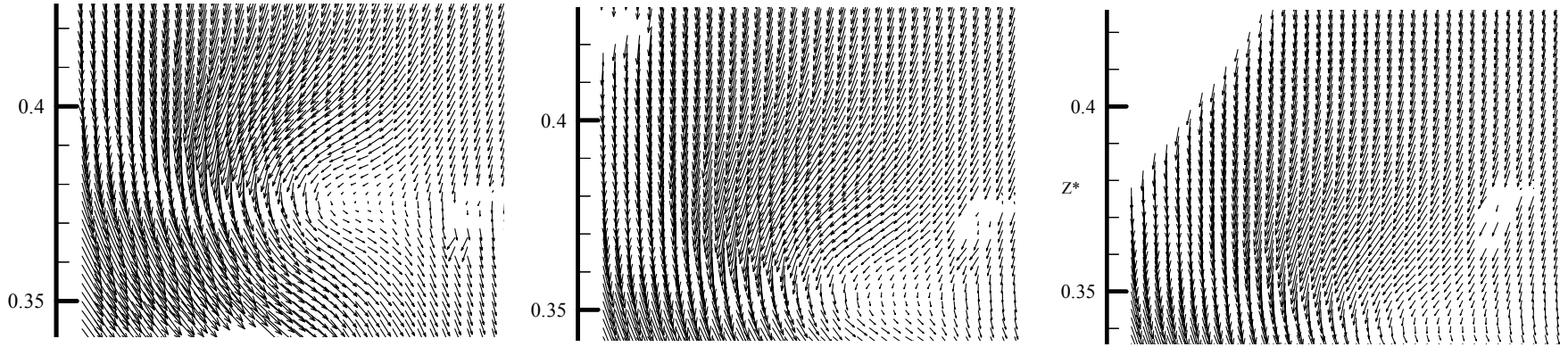

(i) 10° behind the impeller blade (ii) 20° behind the impeller blade (iii) 30° behind the impeller blade

(a) Experimental data (Khopkar et al., 2003)

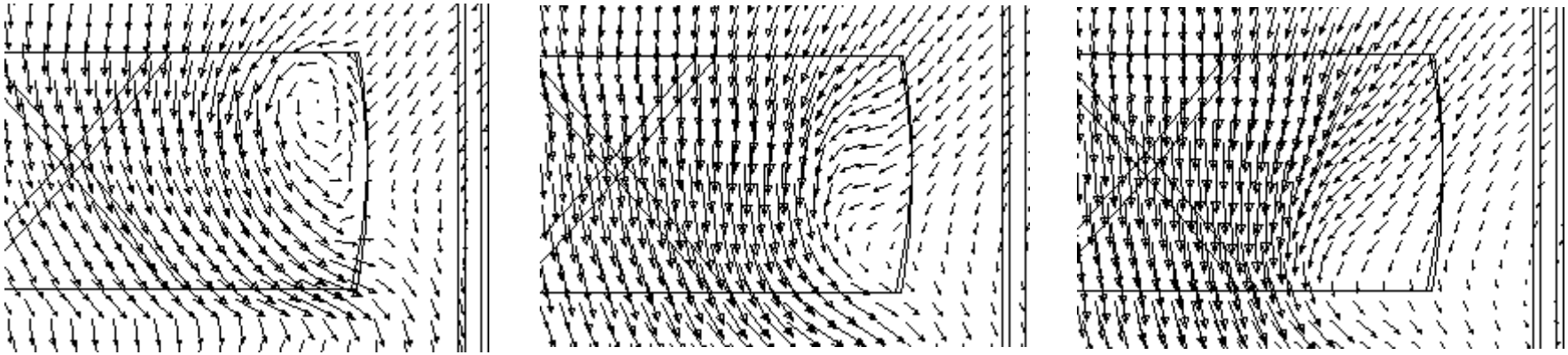

(i) 10° behind the impeller blade (ii) 10° behind the impeller blade (iii) 20° behind the impeller blade

(b) Predicted results

Figure 6.11: Liquid Flow Field near the Impeller Blades (gas-liquid flow), Fl = 0.001 and Fr = 0.242

measured angle-resolved liquid velocity field behind the impeller blade is shown in Figure 6.11a. The liquid velocity field shows a presence of a single trailing vortex behind the blade. Compared with the single-phase flow results (Figure 6.5), the strength of the trailing vortex is reduced after the introduction of gas. The predicted velocity fields at three different r-z planes near the impeller blades are shown in Figure 6.11b. The computational model captures the trailing vortex and its movement in the impeller region correctly. It also correctly captures the reduction in the strength of the trailing vortex after aeration.

The predicted contours of gas hold-up at three different r-z planes near the impeller blade are shown in Figure 6.12. It can be seen that just behind the leading blade gas accumulates in the core region of the trailing vortex. The computational model also captures the movement of this gas pocket with the trailing vortex. A quantitative comparison of the predicted values of the axial velocity and the experimental data at 20° behind the impeller blade is shown in Figure 6.13. It can be seen from Figure 6.13 that the computational model over-predicts the axial velocity values. Similarly to the single-phase flow, the comparison improves as one moves away from the impeller blade.

Although it was not possible to study experimentally the flow near the impeller blades at higher gas flow rate, the computational model was used to examine the influence of a higher gas flow rate on the flow near the impeller blades. The predicted velocity fields at three different r-z planes and the gas hold-up distribution near the impeller blades are shown in Figure 6.14 for a gas flow number of 0.01. It can be seen from Figure 6.14a that the strength of the trailing vortex is further reduced at the higher gas flow rate. It is also seen that at this high gas flow rate, the trailing vortex gets disrupted. The predicted gas accumulation behind the impeller blade is shown in Figure 6.14b. The contours shown in Figure 6.14b clearly show the accumulation of gas behind the blades in the region of the trailing vortex. This accumulation increases with an increase in the gas flow rate and thus, the large gas accumulation behind impeller blades is the main reason for the disruption of trailing vortex.

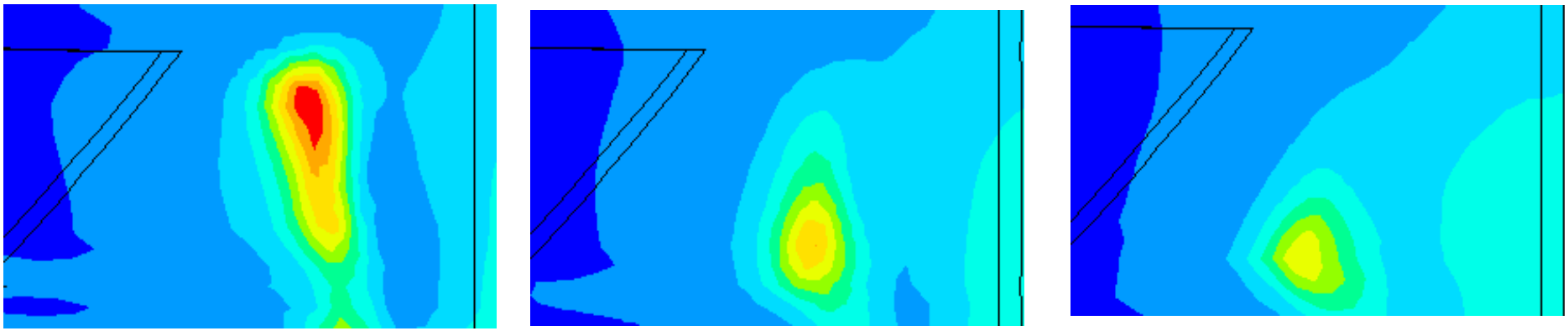

(i) 10° behind the impeller blade (ii) 20° behind the impeller blade (iii) 30° behind the impeller blade

(Blue ≡ 0.01, Red ≥ 0.15)

Figure 6.12: Predicted Gas Accumulation behind Impeller Blades

Fl = 0.001 and Fr = 0.242

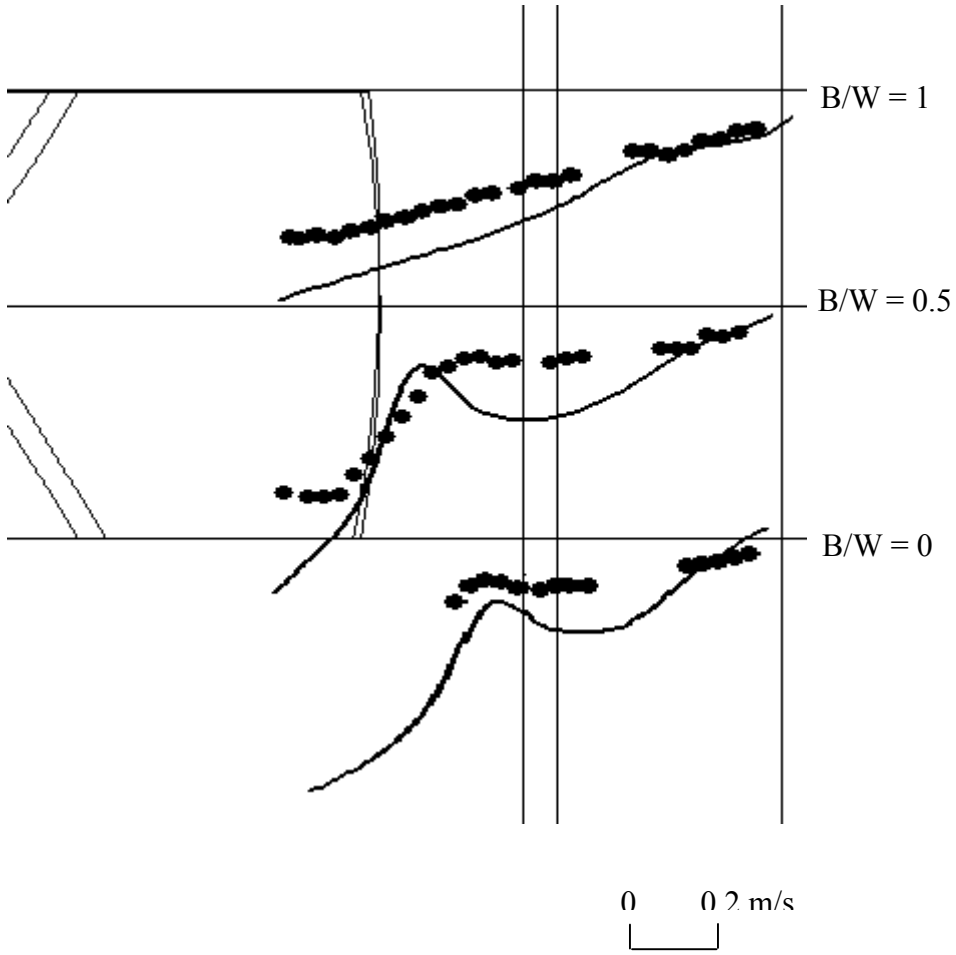

Legends:

● Experimental data (Khopkar et al., 2003)
—— Predicted results

(20° behind the impeller blade)

Figure 6.13: Comparison of Simulated Axial Velocity of Liquid with Experimental Data, Fl = 0.001 and Fr = 0.242

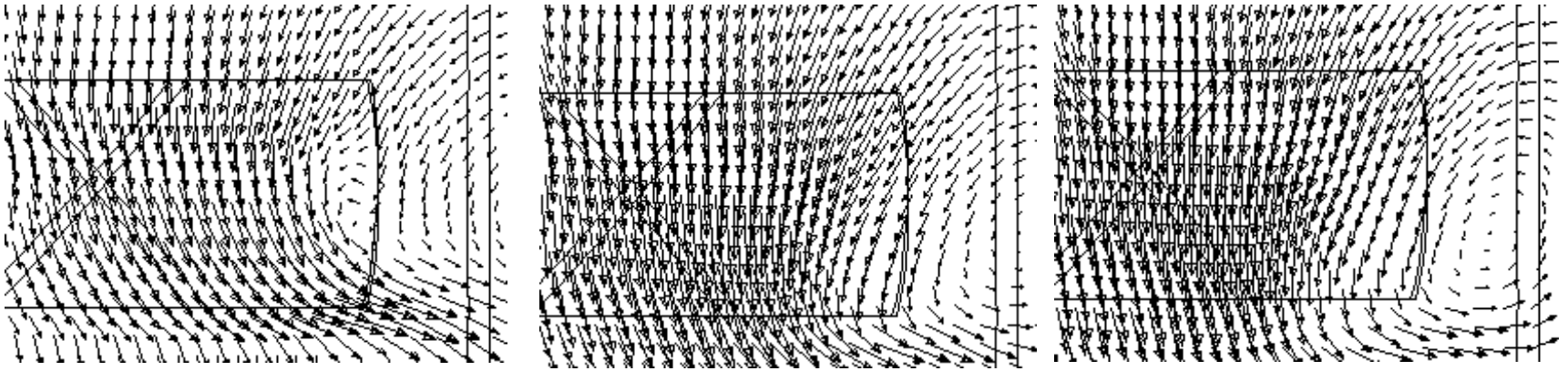

(i) 10° behind the impeller blade (ii) 20° behind the impeller blade (iii) 30° behind the impeller blade

(a) Predicted Velocity Field near the Impeller Blades

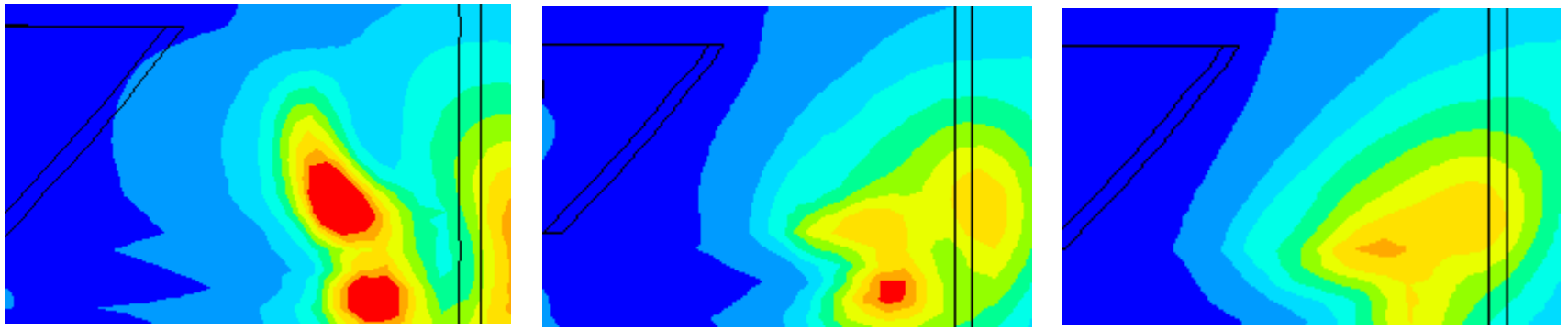

(i) 10° behind the impeller blade (ii) 20° behind the impeller blade (iii) 30° behind the impeller blade

(b) Predicted Gas Accumulation behind the Impeller Blades
(Blue ≡ 0.01, Red ≥ 0.25)

Figure 6.14: Predicted Flow Field near the Impeller Blades, Fl = 0.01 and Fr = 0.242

Overall, it may be said that computational model developed in the present work captures the essential features of the gas-liquid flow generated by a down- pumping pitched blade turbine. The pumping direction is one of the degree of freedom available for a design engineer while operating stirred reactor, equipped with an axial flow impeller. The pumping direction significantly changes the fluid dynamics in the reactor and can lead to different performance. However, few uncertainties are present while selecting the impeller-pumping mode to obtain a better performance specifically in gas-liquid operation. The developed computational model was then further used to understand the implication of the pumping direction on the gas-liquid flows generated by pitched blade turbine.

6.3.3 Effect of blade angle/ pumping direction

The flow generated by an axial flow impeller shows the complex interactions between the impeller pumping mode, scale of operation, reactor hardware and the operating conditions. These interactions significantly increase the complexity of the fluid dynamics. Therefore, to understand and manipulate the performance of the gas-liquid stirred reactor equipped with an axial flow impeller, one must understand the contribution of each of the parameters on the fluid dynamics. Computational models may make useful contributions to understand the gas dispersion capabilities of axial impellers and interaction of pumping mode on other variables like the scale of operation, prevailing flow regimes and overall performance of an impeller. The developed computational model was then used to simulate the flow generated by up-pumping turbine (θ = -45°) and the paddle (straight) blade turbine (θ = 0°) of having same size as that of down- pumping pitched blade turbine. The model predictions were then used to understand the flow characteristics of these three impellers and an attempt has been made to clearly bring out the similarities and differences between the flow generated by these three impellers.

6.3.3.1 Bulk flow characteristics

The previously discussed computational model was then used to simulate the gas-liquid flow generated by an up- pumping and the paddle blade turbines. The gas-liquid flow

was simulated for an impeller rotational speed (N) of 300 rpm and volumetric gas flow rate (Q_g) of 4.29×10^{-5} m^3/s (Fl = 0.01 and Fr = 0.242). Under these operating conditions, gas was completely dispersed in the reactor for up- pumping mode (Aubin, 2001). The predicted liquid phase flow field for up- pumping pitched turbine and paddle turbine are shown in Figures 6.15a and 6.15b respectively. It can be seen from Figure 6.15a that unlike down- pumping pitched blade turbine, the up- pumping turbine generates two-loop structure of the liquid flow field. A high velocity jet emanating from the top of the impeller and a second loop above the first loop is captured in the simulations. The first loop emanating from the top of the impeller move fast and helps in circulating the gas in the below impeller region. This circulation loop significantly improves the performance of up- pumping turbine for gas dispersion and found to suspend the solids effectively (see Nienow, 1998). Similarly, the predicted liquid velocity field for paddle turbine is shown in Figure 6.15b. It cane be seen from Figure 6.15b that the paddle turbine generates almost identical two loop structure like Rushton turbine. However, the predicted velocity field shows slight downward movement of the liquid in impeller discharge stream.

Aubin *et al.* (2004) has measured the liquid phase bulk flow characteristics for up-pumping turbine. The quantitative comparison of the predicted liquid field for up-pumping turbine with the experimental data of Aubin *et al.* (2004) is shown in Figure 6.16. The comparison between the predicted results and the experimental data is reasonable. The computational model captured the key features of the gas-liquid flow with reasonable accuracy. The over-prediction in the axial velocity values was observed in the impeller discharge stream and lower circulation loop. The good agreement between the predicted values of the axial velocities and the experimental data was observed in the upper circulation loop. A quantitative comparison of the predicted kinetic energy with the experimental data is shown in Figure 6.16b. It can be seen from Figures 6.16b that the computational model over-predicts the values of turbulent kinetic energy in the lower circulation loop and the agreement improves in the upper circulation loop. The overall comparison of the predicted liquid flow field for single as well as gas-liquid flow show a negligible influence of gas on the liquid flow in the upper circulation loop not shown in Figure). Aubin *et al.* (2004) has also reported the similar observation in their experimental study for up- pumping turbine.

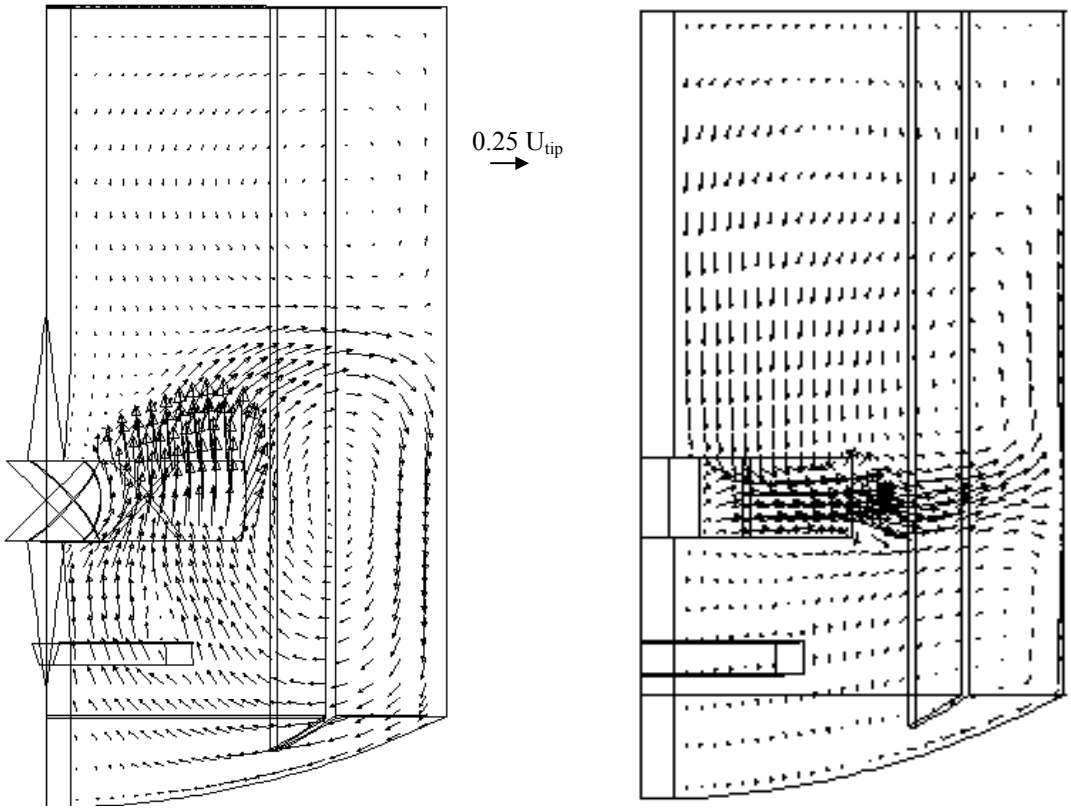

(a) Up- pumping pitched blade turbine (mid-baffle plane)

(b) Paddle turbine (mid-baffle plane)

Figure 6.15: Simulated Liquid Velocity Flow Field at the r-z Plane, Fl = 0.01 and Fr = 0.242

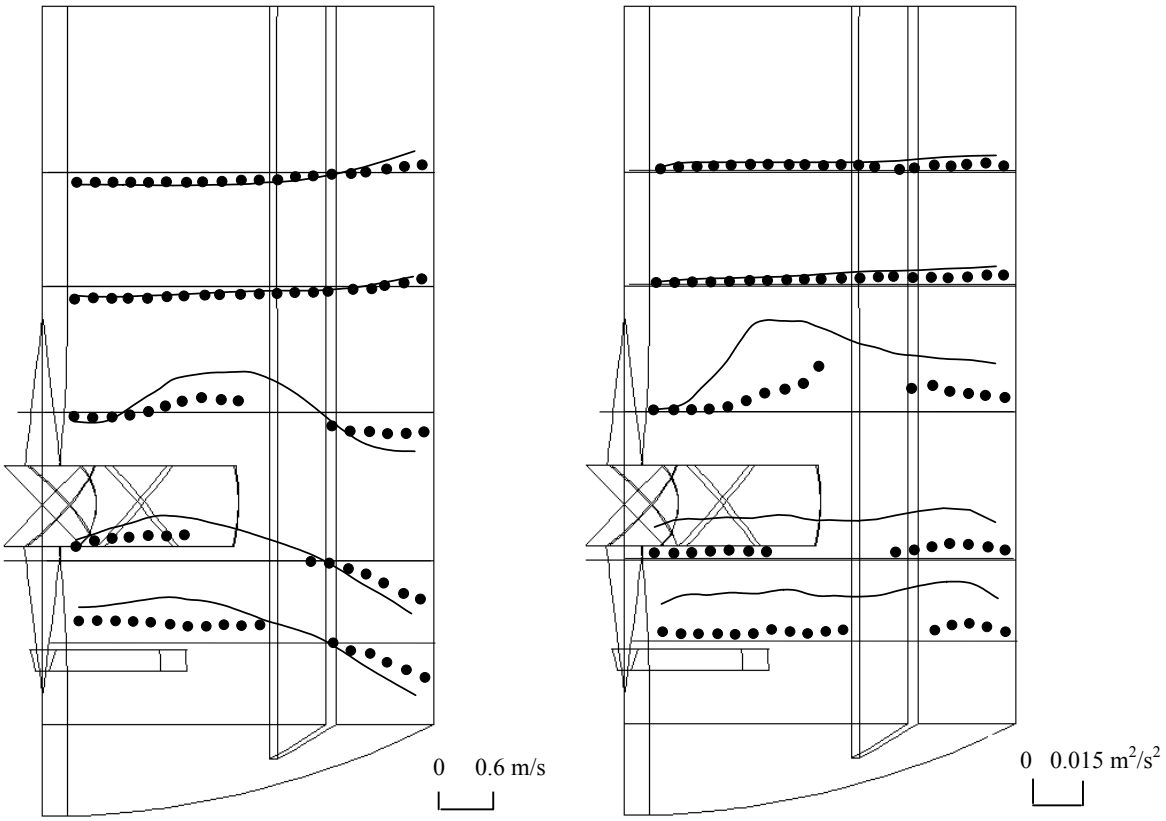

(a) Axial Velocity (b) Turbulent Kinetic Energy

Legends:

● Experimental data (Aubin *et al*., 2004)
—— Predicted results

Figure 6.16: Comparison of Predicted Results and Experimental Data for Gas-Liquid Flow, Fl = 0.01 and Fr = 0.242

The predicted gas holdup distributions for the down- as well as up- pumping pitched blade and the paddle turbines are shown in Figure 6.17. It can be seen from Figure 6.17 that the simulated gas holdup distribution show the complete dispersion condition for the up- as well as down- pumping pitched blade turbines, however, the paddle turbine was unable to achieve the complete dispersion condition for the same operating conditions. Compared to other turbines, the up-pumping impeller show higher values of gas holdup in the below impeller region. In case of up- pumping pitched blade turbine, the downward flowing liquid circulates the gas bubbles in region below the impeller and increases the residence time of gas bubbles in the reactor. This increase in the residence of the gas bubbles resulted into the higher values of the gas holdup in the reactor. The observations obtained from the CFD predictions for down- and up-pumping turbine are in good agreement with the experimental observations of Aubin *et al.* (2004). The predicted values of the average gas holdup (for down-pumping α_g = 4.2 % and for up-pumping α_g = 7.2 %) were higher than the reported experimental values (3.7 % and 5.8 %) respectively. The predicted value of the gas holdup for paddle turbine was found to be 2.8 %, lowest in comparison with the other two turbines. For up-pumping mode, total gas holdup value almost 1.6 times that of down-pumping mode was observed. The predicted gas holdup distribution indicates that the up-pumping turbine is more efficient than other two turbines for gas-liquid operation.

6.3.3.2 Flow around impeller blades

As stated earlier, in gas-liquid stirred reactor, the sparged gas interacts with the trailing vortices behind the impeller blades and affects the performance of the impeller particularly its pumping and power dissipation capacity. However, other than the operating conditions, impeller rotational speed and the volumetric gas flow rate, the hardware parameters such as impeller dimension, impeller pumping and relative dimension of impeller and the ring sparger, specifically for down- pumping impeller control the interaction of the sparged gas with the trailing vortices. Therefore, one may observe different level of gas accumulation, drop in the pumping and power dissipation capacity for the same size impeller having different pumping direction. The computational model was used to study the flow around the impeller blades of up-

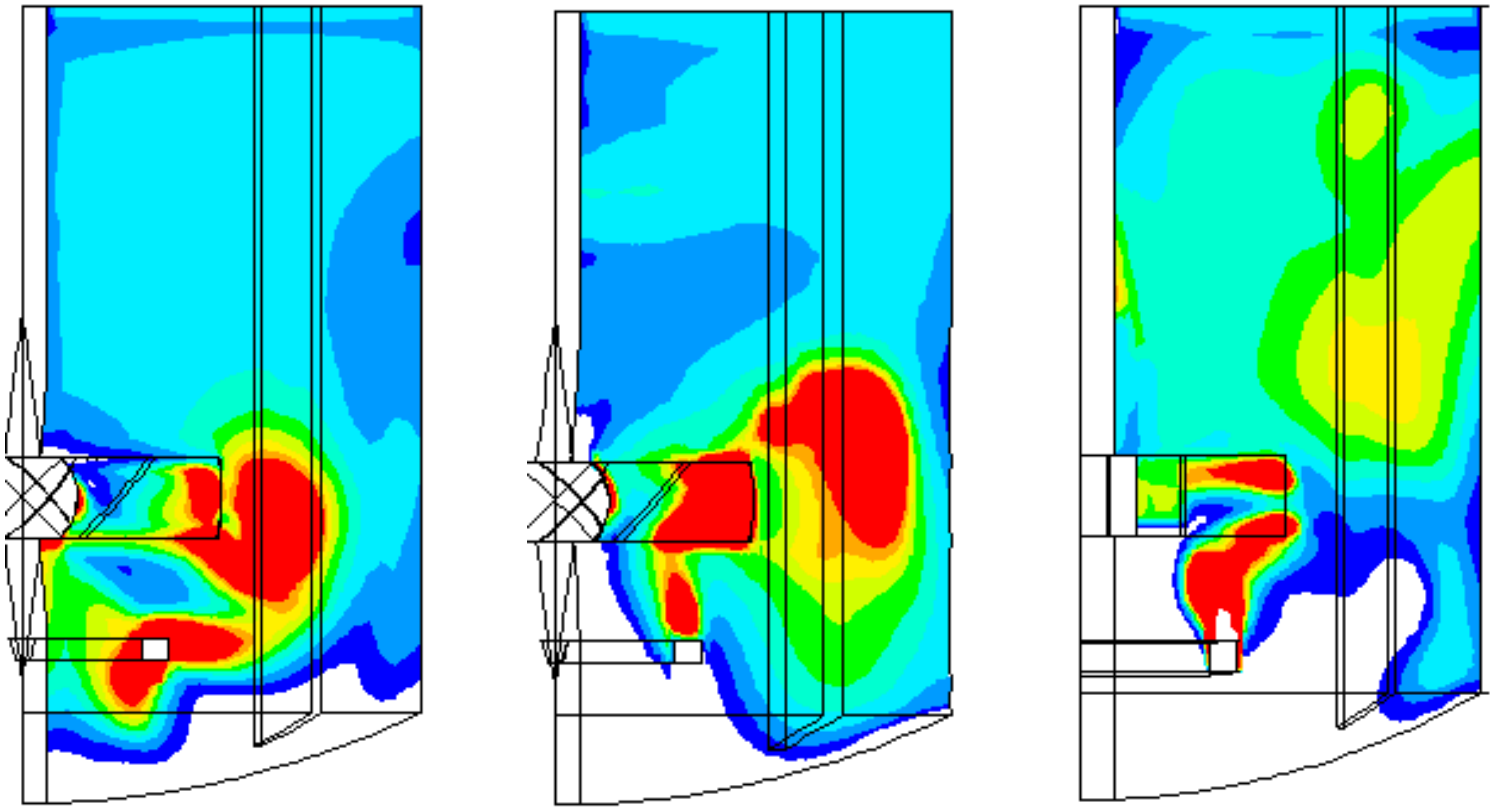

(a) Down- pumping pitched blade turbine (PBTD)

(b) Up- pumping pitched blade turbine (PBTU)

(c) Paddle turbine

10 uniform contours; blue = 0.01 and red ≥ 0.1 (0.15 for PBTU)

Figure 6.17: Predicted Gas Holdup Distribution at the r-z Plane for Gas-Liquid Flow, Fl = 0.01 and Fr = 0.242

pumping, down- pumping and paddle turbine to understand the influence of the pumping mode on the impeller performance.

The iso-surface of the z-vorticity behind the impeller blades was examined to explain the exact movement of the trailing vortices in impeller discharge stream. It can be seen from Figure 6.18 that like the down- pumping pitched blade turbine, the up- pumping turbine shows the presence of a single trailing vortex behind the impeller blades and the trailing vortex flows in the pumping direction as it moves away from the leading impeller blade. Whereas for the paddle impeller, a pair of vortices exists, which moves in radially outward direction. The close –up of the predicted liquid velocity field at 10° behind the impeller blades of the down-, up- pitched as well as paddle turbines is examined to understand the flow around impeller blades. It can be seen from Figure 6.18 that the predicted velocity field captured the location of the vortex with respect to the impeller blade for all three impellers. However, for paddle turbine, the predicted velocity field around impeller blades shows asymmetry in location of the vortex (see Figure 6.18). The location of the lower vortex is slightly radially outward and downward compare to the upper vortex. The asymmetry in the vortex structure was thought to be due to the interaction of the flow approaching from above and below impeller plane. This asymmetry in the vortex structure may be lead to the observed slight downward movement of the impeller discharge stream. The predicted results show that, the mode of pumping and the blade angle significantly influences the structure of trailing vortices present behind the impeller blades and therefore, the flow generated by the turbines.

Different ways of post-processing of simulated results, for example, particle streak lines around impeller blades, facilitate detailed analysis of differences and similarities of flow generated by different impellers. These details are not reported here for the sake of brevity. As an example of possible analysis, the predicted gas holdup distribution around impeller blades is shown in Figure 6.19. The predicted gas holdup distribution for down-pumping pitched turbine is shown in Figure 6.19a. The accumulated gas in the vortex core region flows with trailing vortex in downward direction as it moves away from the leading impeller blade. The predicted gas holdup distribution for paddle

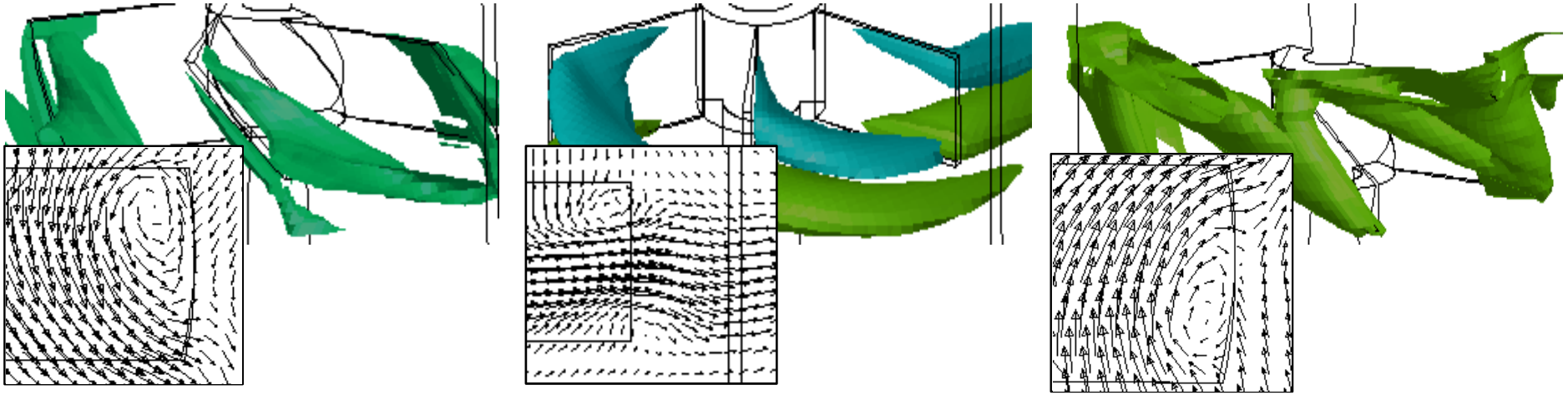

(a) PBTD ($\omega = -80\ s^{-1}$) (b) Paddle Turbine ($-100\ s^{-1} < \omega < 100\ s^{-1}$) (c) PBTU ($\omega = 80\ s^{-1}$)

(Impeller is moving from right to left for PBTD and Paddle turbine and left to right for PBTU)

Figure 6.18: Flow around Impeller Blades, Fl = 0.01 and Fr = 0.242

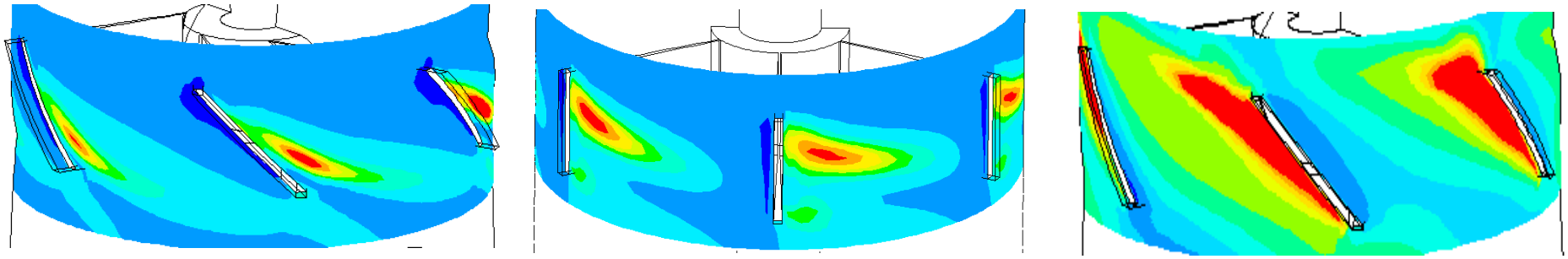

(a) PBTD (b) Paddle Turbine (c) PBTU

(Impeller is moving from right to left for PBTD and Paddle turbine and left to right for PBTU)

10 uniform contours; blue = 0.01 and red ≥ 0.3

Figure 6.19: Predicted Gas Holdup Distribution around Impeller Blades, Fl = 0.01 and Fr = 0.242

turbine and up-pumping turbine are shown in Figure 6.19b and 6.19c respectively. In the case of paddle turbine, higher gas holdup values were observed in upper trailing vortex compared to the lower one. For up-pumping turbine, the accumulated gas, flows with trailing vortex in the upward direction as it moves away from the leading impeller blade. The amount of gas accumulation behind impeller blades is more for up-pumping turbine as compared to the other two turbines for the same aeration rate. Higher values of gas holdup were observed in impeller swept region for up-pumping turbine. In spite of high gas accumulation, the pumping efficiency of up-pumping turbine was observed to fall more slowly than down-pumping turbine, which allows up- pumping turbine to handle more gas compare to the down- pumping and paddle turbine to achieve flooding condition for same impeller speed. This is probably due to the flow generated by the up- pumping turbine is in same direction of the buoyancy of the gas bubbles. Therefore, the motion of gas bubbles has comparatively less effect on the impeller action/efficiency, which lead to slow fall in the pumping efficiency of impeller in spite of high gas accumulation.

6.4 Summary and Conclusions

Eulerian-Eulerian model with standard k-ε turbulence model has been used to simulate the turbulent gas-liquid flows generated by the down- pumping pitched blade turbine for two gas flow rates (Fl = 0.01 and 0.001) and for the same impeller rotational speed (Fr = 0.242). With higher order discretization and the adequate grid resolution, the model was found to capture the key features of the flow including the small reverse loop in the lower part of the tank, presence of trailing vortex and the gas accumulation behind the impeller blades for both the gas flow rates. For lower gas flow rate like PIV results the model prediction shows the presence of coherent structure of gas accumulation regions up to about 20° behind the impeller blade. However, for higher value of gas flow rate, the model has predicted the disruption of the trailing vortex due to high gas accumulation. In addition, it was also found to simulate the overall pumping number and the decrease in the pumping capacity of impeller with aeration reasonably well. The quantitative comparison of the model predictions with the reported experimental data shows over-prediction of axial velocities and turbulent kinetic energy in the impeller discharge stream. This is probably due to inadequate modelling of the

turbulence in the two-phase flow. However, with respect to the gas phase, the computational model was able to capture the complete dispersion of gas and the indirect loading of the impeller, although it slightly over predicts (by 15%) the total gas volume fraction in the reactor.

The computational model has then been used to understand the influence of the blade angle or the pumping mode on the performance of the impeller. The gas-liquid flows in the stirred reactor were simulated for Fl = 0.01 and Fr = 0.242. The computational model correctly captured the overall flow field generated by the pitched blade turbine operating in up- as well as down-pumping mode and the paddle turbine. The computational model was used to examine the flow structure around the impeller blades. The model appears to capture most of the key features of the gas-liquid flows, including the presence, structure and the movement of the trailing vortices and the accumulation of gas behind the impeller blades. The predicted liquid flow field around impeller blades shows the asymmetry in the flow for paddle turbine, which may lead to a slight downward movement of the impeller discharge stream. The predicted gas accumulation behind the impeller blades shows higher values of gas holdup in the impeller swept region for up-pumping turbine compared to down- pumping turbine and the paddle turbine. In spite of high gas accumulation, the pumping efficiency of up-pumping turbine was found to be more efficient than other two turbines for gas-liquid operation.

The ratio of the impeller scale with the bubble diameter determines the interaction of sparged gas with the trailing vortex and the amount of gas accumulation behind the impeller blades. However, this ratio will be significantly higher for the industrial scale reactor and may observe significantly different performance of impellers for similar conditions. Therefore, the influence of the scale on the performance of impeller has to be confirmed before the selection of an impeller. The CFD based model may make useful contributions to understand the influence of scale on the impeller performance. Similar models were also shown to predict successfully different flow regimes of gas-liquid flow generated by Rusthon turbine. These models were further used to address reactor-engineering issues like simulation of liquid phase mixing in tall stirred reactors and the results are discussed in Chapter 8.

PART III

APPLICATION TO REACTOR ENGINEERING

Chapter 7

FLOW IN A CONTINUOUSLY OPERATED STIRRED REACTOR

7.1 Introduction

Mixing and transport processes are the key issues in design of a stirred reactor, especially for the processes involving multiple reactions, where the selectivity of the desired product is important. Under such circumstances, fluid mixing often decides the reactor performance. Although mixing in a stirred tank is extensively studied to understand the underlying physics of mass, momentum and energy transport, the interaction of the operating parameters and reactor hardware with the fluid dynamics is not well understood. Because of the lack of understanding, many industrial operations are inefficient and wasteful. This incurs considerable costs, for example, loss of production time and raw materials, an inability to maintain the product quality and the need for the pilot plants. A detailed knowledge of the power, velocity and mixing characteristics for the given stirred tank configurations is therefore required for better operation.

For most of the industrial applications, continuous flow stirred reactor is widely used. In continuous flow stirred reactor the fluid mixing is a complex function of the local flow field, operating parameters and the reactor hardware. The empirical correlations used in usual practice does not completely include the detail reactor hardware configuration while estimating the time scale of the mixing process. It is therefore, essential to understand the effect of hardware parameters on the mixing process and to evaluate different alternative design configurations for the possible enhancement of the reactor performance. In the present work, we have focused on developing CFD based models to understand the flow characteristics in a continuous flow stirred reactor. The influence of the impeller speed, feed rate and location of inlet/outlet on the mixing process and on the extent of non-ideality of flow was studied in detail.

Very few studies have reported the experimental measurements in continuously operated stirred reactor. However, all the reported studies are restricted to the single-phase flow. Therefore, in absence of experimental data for gas-liquid system, in the present study, we have used the developed CFD model to study the single-phase flow generated by the Mixel TT impeller in a stirred reactor operating in batch as well as in continuous mode of operation. Computational model with multiple reference frame approach was used to simulate the liquid flow generated by an impeller in a stirred

reactor. The model predictions were compared with the reported experimental data (Mavros *et al.*, 2000), measured using laser Doppler velocimetry (LDV). Mavros *et al.* (2000) had carried out experiments in stirred reactor operating in batch as well as continuous mode of operation. They have not studied the flow around impeller blades and the interaction of incoming liquid jet with the impeller generated flow. The developed computational model was then used to understand the interaction of the jet emanating from the feed pipe with the impeller-generated flow and the possible effect of inlet-outlet nozzles configuration on the mixing process occurring in the reactor. The computational model and the predicted results discussed in this work will be useful for understanding flow characteristics in a continuous stirred reactor.

7.2 Computational Model

The interaction of the rotating impeller blades and of the stationary baffles generates an inherently unsteady flow. Various approaches are available for simulating flow in a stirred reactor. As discussed in Chapter 4, quasi-steady state approaches like the "multiple reference frame" (MRF) approach or the "computational snapshot" approach are adequate for simulating the flow generated by the Mixel TT impeller. In this work, the MRF approach was selected. The details of the MRF approach are discussed below.

In MRF approach, the whole reactor is divided into two regions: an inner region attached to the rotating impeller and shaft and an outer region attached to the stationary baffles and the reactor. The model equations for the inner region are solved using a rotating framework, whereas the equations for the outer region are solved using a stationary framework. The solution is matched at the interface between the rotating and stationary region via velocity transformation from one frame to the other. This velocity-matching step implicitly involves the assumption of steady flow conditions at the interface. Two approaches are available for modelling the communication between two regions (Marshall *et al.*, 1996). In the first approach, flow characteristics are circumferentially averaged at the interface and then used as boundary condition for the other region. In the second approach, no averaging is carried out and the continuity of absolute velocity was forced to provide the neighbouring values of velocity for the region under consideration. In the present work second approach was used for communicating the two regions (see Fluent 6.0 User guide for the governing

equations). While implementing the MRF approach, several issues such as the extent and position of the inner region, the number of computational cells, the discretization schemes, the turbulence model, the specific position of impeller blades and so on need appropriate selection. The basis for this is discussed below.

In the present work, the geometric configuration of the experimental set-up used by Mavros *et al.* (2000) was considered. All the relevant dimensions like the impeller diameter, the reactor shape and diameter and so on were the same as the ones used by Mavros *et al.* (2000). The system investigated consists of a stirred cylindrical reactor, with a dished bottom (diameter, T = height, H = 0.19 m, radius of curvature, R_c = 0.19 m) with four baffles (width = T/10 = 0.019 m) equally spaced around the reactor periphery. The shaft (diameter d_s = 0.008 m) of the impeller was concentric with the reactor axis and extended till the bottom of the reactor.

An axial flow Mixel TT impeller (diameter, D = 0.095 m) was used for all the simulations. The Impeller off-bottom clearance was 0.095 m (measured from the agitator mid-plane). For the continuous-flow mode, the inlet pipe (diameter d_{in} = 0.01 m) was located above the impeller, with its tip 0.048 m below the liquid surface and 0.011 m away from the shaft. The liquid outlet (diameter, d_{out} = 0.05 m) was located at the center of the bottom of the reactor. Considering the geometry and the intended extension to a continuous-flow system, the whole reactor was considered as the solution domain. Location of the boundary between inner and outer regions may have some influence on predicted results (Ranade and Tayalia, 2000, Ranade *et al.* 2001a). To minimise such influence, in the present work, the boundary of the inner region was positioned at r = 0.064 m (exactly in between the impeller blade tip and inner edge of the baffle) and 0.04 m ≤ z ≤ 0.13 m (where z is axial distance from the bottom of the reactor). The solution domain and the inner region considered in the simulations are shown in Figure 7.1.

A commercial grid-generation tool, GAMBIT 1.3 (of Fluent Inc., USA) was used to model the geometry and to generate the body-fitted grids. It is very important to use an adequate number of computational cells while numerically solving the governing equations over the solution domain. The prediction of turbulence quantities is sensitive

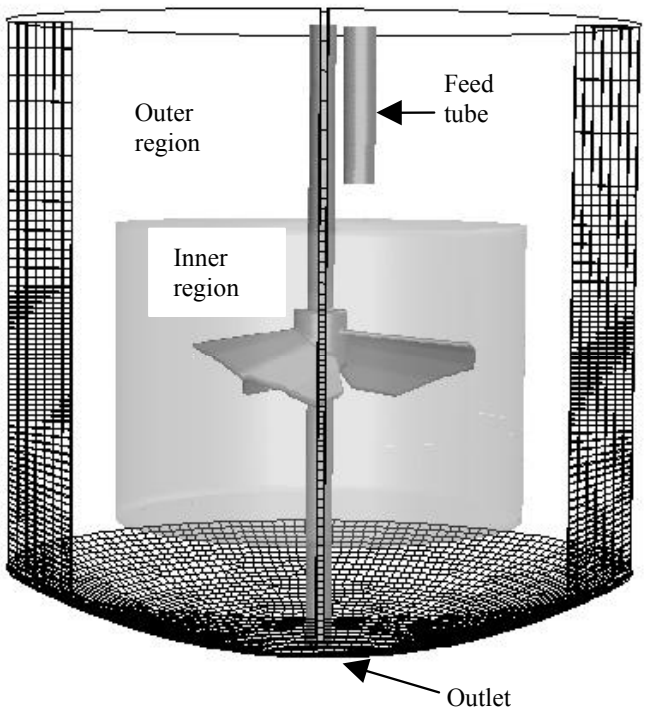

(a) Solution Domain

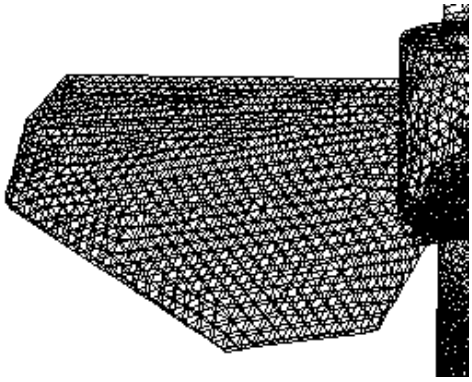

(b) Grid Distribution on Impeller Blade

Grid Details :	
r × θ × z	: 60 × 75 × 63
Total Grid	: 283,500 Cells
Inner Region	: 0.05 m < z < 0.13 m
	r < 0.072 m
	140,844 Cells
Outer Region	: 142,656 Cells

Figure 7.1 Solution Domain and Computational Grid

to the number of grid nodes and grid distribution within the solution domain. The previously published work (for example, Ng *et al.*, 1998; Wechsler *et al.*, 1999; Ranade *et al.*, 2001a) gives adequate information to understand the influence of the grids on the predicted results. It was demonstrated that, in order to capture the trailing vortices accurately, it is necessary to use at least 200 grid nodes to resolve the blade surface. Based on some preliminary numerical experiments, about 283,500 computational cells were used for the simulations of the batch and continuous operations. The used solution domain and the typical grid distribution are shown in Figure 7.1. In the present work, we used QUICK (Quadratic Upstream Interpolation for Convective Kinetics) discretization scheme with limiter function (SUPERBEE of Roe, 1985) to avoid non-physical oscillations. The results (discussed in the following section) seem to indicate that the number of grid nodes used are sufficient to capture most of the important features of the flow generated by the Mixel TT impeller.

The standard k-ε model was used to model the prevailing turbulence. Wall functions were used to specify wall boundary conditions. The top surface of the liquid pool was assumed to be flat and was modelled as symmetry (zero normal velocity and zero shear). For the continuous-flow mode, the face of the inlet pipe is defined as inlet. The uniform inlet liquid velocity (corresponding to a liquid flow rate, $Q_l = 2.01667\times10^{-4}$ m^3/s) was specified. The turbulence intensity of 10% and turbulent length scale ($l = 0.07*R_{in,}$ where R_{in} is the hydraulic radius of the feed tube) was specified at the inlet, to model the turbulence in the incoming liquid. The outlet of the reactor was modelled as zero gradient boundary condition. The gradients normal to the outlet boundary were set to zero for all the variables except pressure. If the direction normal to the outlet boundary is denoted by y, the outlet boundary condition can be expressed as:

$$\frac{\partial \phi}{\partial y} = 0 \tag{7.1}$$

It should be noted that in quasi-steady state approaches, like, MRF or the computational snapshot approach, a specific position of the impeller blades with respect to the other stationary internals is considered. In most experimental studies, flow measurements are carried out for a fixed position for several impeller rotations. Thus, the measured flow

characteristics are essentially averaged over different relative impeller blade positions with respect to the stationary internals. In order to make meaningful comparisons, it would be necessary to carry out simulations at different blade positions and then use ensemble-averaged results over these different simulations for the comparison. However, the previous work for batch reactors with geometrically simple impellers like Rushton turbine has shown not much difference between angle-averaged profiles and ensemble averaged profiles (see for example, Ranade and van den Akker, 1994). In the present case, however, it was observed that the complicated shape of the impeller and interaction of inlet liquid jet with the impeller stream leads to some differences in ensemble averaged results and angle-averaged results. We have therefore carried out simulations at three different relative positions of impeller blade with respect to baffles and inlet/outlet. It may be noted that one simulation provides data at four mid-baffle planes for a specific position of impeller blades with respect to baffles and inlet/outlet. The results from three simulations were used to obtain ensemble-averaged profiles at mid-baffle plane (based on total 12 planes). For batch operations the predicted results were ensemble averaged over all twelve mid-baffle planes and then compared with the experimental data.

For continuous-flow operation, number of different relative blade positions with respect to the feed inlet and baffles respectively are possible. Initially, different relative blade positions with respect to the feed inlet were considered to understand the interaction of incoming feed with the impeller blades. In these three cases, the specific position of impeller blades with respect to baffles were kept the same. Then three different relative positions of impeller blades with respect to baffles were considered and the predicted results were ensemble averaged for comparison with the experimental data. In all the cases, the feed inlet was located at the mid-baffle plane as in the experiments. The five configurations considered in this work are shown in Figure 7.2. These five configurations can adequately represent the flow in a continuous-flow stirred reactor.

A commercial CFD code, FLUENT 5.3 (of Fluent Inc., USA) was used to carry out the flow simulations. The fluid properties were set as: viscosity of liquid (μ) = 0.0009 Pa.s and density of liquid (ρ) = 1000.0 kg/m^3. For initiating computations, all variables except k and ε were set to zero. The initial values of k and ε were set to 0.0001 with

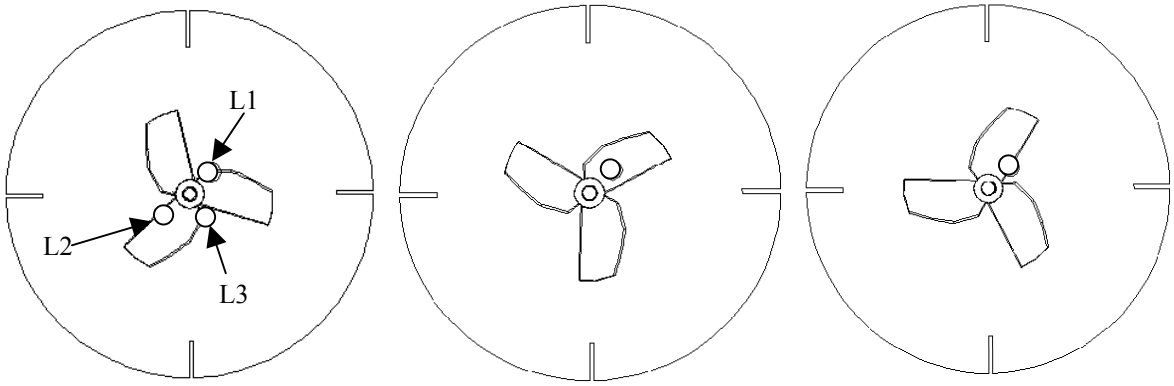

Position 1 (L configurations) Position 2 Position 3

Figure 7.2 Three Specific Positions of Impeller Blades, Feed tube and Baffles

appropriate units. The initial conditions did not affect the converged results. Computations were carried out for two impeller rotational speeds (180 rpm and 360 rpm) and one liquid inlet flow rate ($Q_l = 2.01667\times10^{-4}$ m^3/s). All computations were carried out till the normalized residues fall below 0.0001.

Converged flow results were used for further simulations of the liquid mixing in the stirred reactor. For simulating mixing in a continuous-flow operation, a square pulse of tracer was introduced in the inlet stream for 1 s. The evolution of the tracer concentration field within the reactor and its outlet concentration with respect to time were simulated and studied. The time step used for all the mixing simulations was 0.01 seconds. The species transport equations were solved for adequate time to ensure the complete removal of tracer material from the reactor (more than four times the mean residence time, $\tau = 25.23$ s). The simulated tracer concentration fields and the residence time distributions were analysed to examine the possible non-ideal flow behaviour. The computational results are discussed in the following section.

7.3 Results and Discussion

7.3.1 Batch operation

7.3.1.1 Bulk flow characteristics

The flow generated by the Mixel TT impeller in a batch reactor was simulated for an impeller rotation speed of 360 rpm. Without using any impeller boundary conditions, the multiple reference frame (MRF) approach was able to simulate the axial flow pattern generated by the impeller. The comparison of the predicted velocity field (ensemble averaged to eliminate the influence of specific blade position) and experimental LDV data (mid-baffle position) is shown in Figure 7.3. A high velocity jet emanating from the bottom of the impeller and a small reverse loop below the hub, seen in the experimental flow field, were clearly captured in the simulation.

Quantitative comparison of the predicted results and the experimental data of Mavros *et al.* (2000) are shown in Figure 7.4. It can be seen from Figure 7.4a that, the comparison

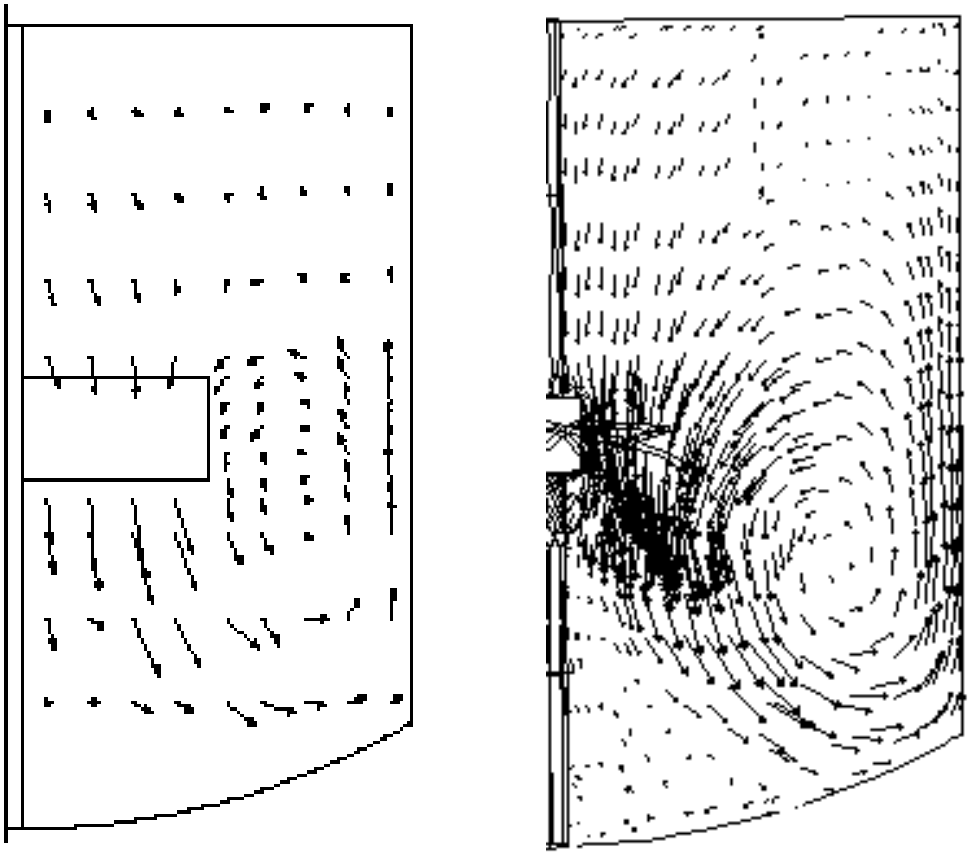

(a) Experimental (mid-baffle plane) (b) Predicted (mid-baffle plane)

Figure 7.3: Mean Flow Field at r-z Plane for Batch Operation,
N= 360 rpm and U_{tip}= 1.7907 m/s

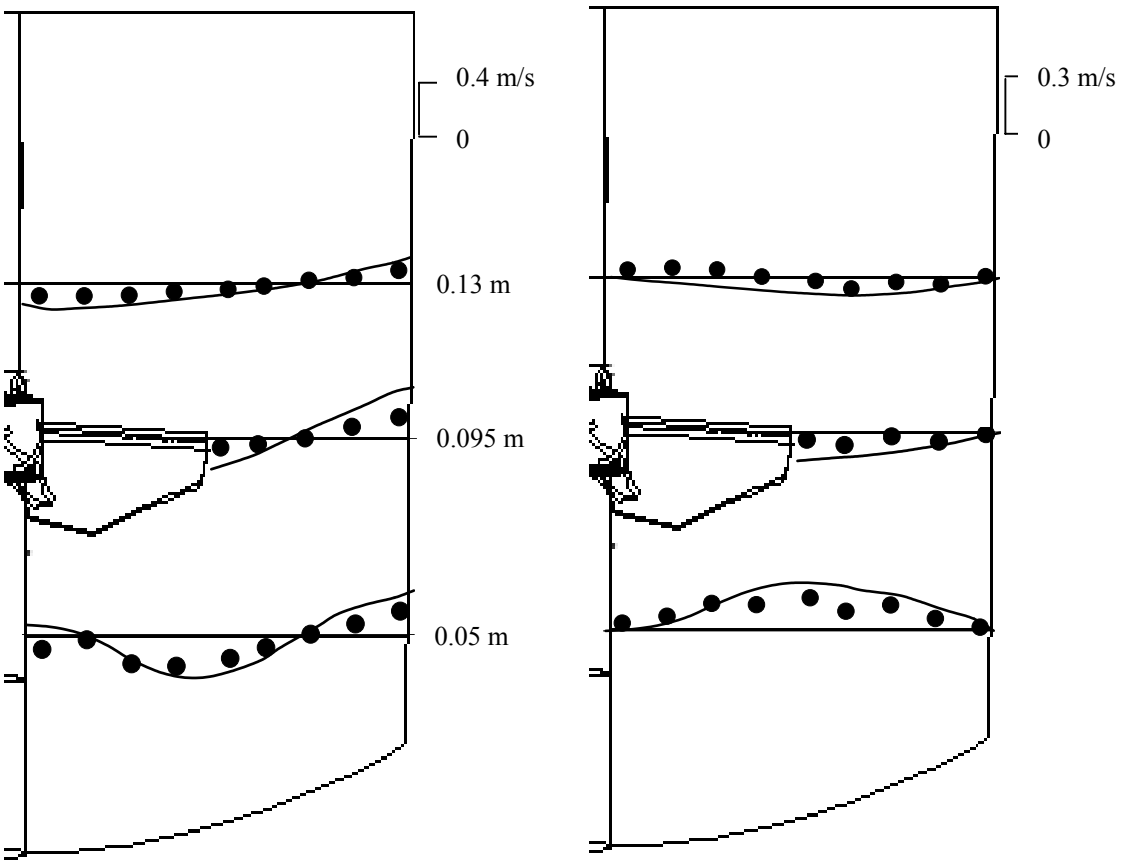

(a) Axial velocity (b) Radial velocity

Legends:

● Experimental data (Mavros *et al.*, 2000)
—— Predicted results

Figure 7.4: Comparison of Predicted Results and Experimental Data for Batch Operation, N= 180 rpm, Utip= 0.8954 m/s [continue on next page]

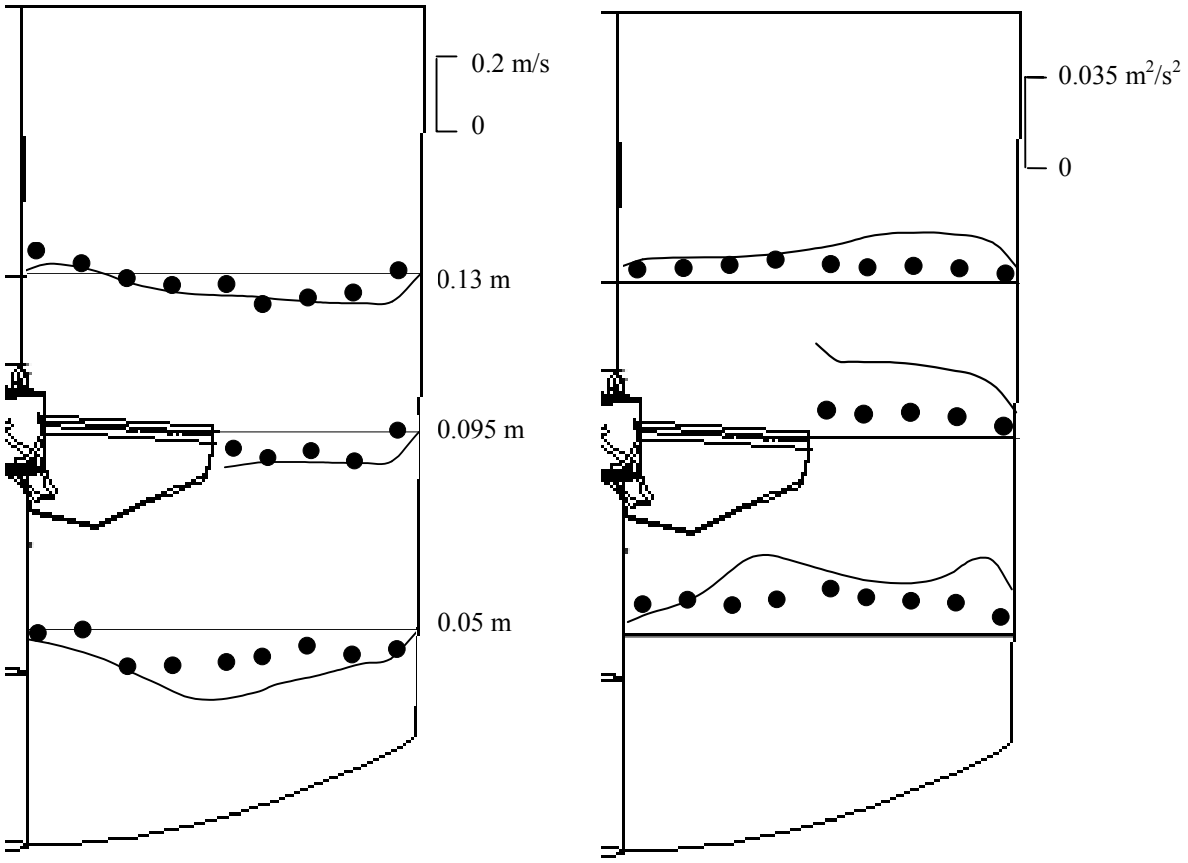

(c) Tangential velocity (d) Turbulent kinetic energy

Legends:

● Experimental data (Mavros *et al.*, 2000)
—— Predicted results

Figure 7.4: Comparison of Predicted Results and Experimental Data for Batch Operation, N= 180 rpm, Utip= 0.8954 m/s

between the predicted values of axial velocity and experimental data is satisfactory. The maximum axial velocity in the downward direction, at a height of 0.07 m from the bottom of the reactor, is about 0.45 times the impeller tip velocity (not shown in Figure 7.4a). The measured and predicted axial velocity field was used for calculating the flow (or pumping) number for the Mixel TT as:

$$N_Q = \frac{2\int \pi r U dr}{ND^3} \tag{7.2}$$

The limits of integration for the radial distance are from the surface of the shaft to the impeller radius. The predicted pumping number for Mixel TT (0.62) is in good agreement with the reported experimental value of 0.67 (Aubin *et al.*, 2001).

It can be seen (Figure 7.4b) that the comparison of the predicted and experimental radial mean velocities is also reasonably good. For a small region above the impeller, the predicted radial profiles show some deviation from the experimental data. The magnitude of such deviation is small. Agreement between predicted and experimental data for the tangential mean velocity is also reasonably good as that for the axial velocity. Tangential velocity profiles at the mid-baffle plane show some reverse circulation above the impeller, which was captured in the simulations (see Figure 7.4c).

The values of the turbulent kinetic energy are rather over-predicted (Figure 7.4d), especially in the region below the impeller. Reasons for these observed discrepancies are not obvious. The use of more complex models, like the Reynolds stress models, is not an answer to this problem, since it does not lead to any significant improvement over the standard k-ε model (see Jenne and Reuss, 1999). Recently, large eddy simulation (LES) models (see for example, Hartmann *et al.*, 2004) have used to simulate flow in stirred reactor. Although LES models have improved the prediction of the turbulent kinetic energy, but these models require significantly higher computational requirements. This restricts the use of LES models as a design tool for the reactor engineering applications. However, the observed discrepancies may not be a serious impediment to many reactor-engineering applications since some chemical engineering applications like blending are not sensitive to the turbulence levels and are

controlled by mean flow. For example, Ranade *et al.* (1991) has demonstrated that predicted mixing time in stirred reactors is not significantly affected by turbulent dispersion (order of magnitude change in the turbulent dispersion coefficient resulted in change of few percentages in predicted mixing time). Correct prediction of turbulence levels is important for applications controlled by turbulence quantities like dispersion of bubbles or micromixing. Fortunately, even many of such applications, the relevant processes depend on fractional power of turbulence energy dissipation rate (for example, prediction of Sauter mean diameter depends on $\varepsilon^{-0.4}$). Thus 30% over-prediction of energy dissipation rates leads to smaller (11 to 14%) error in Sauter mean diameter. Therefore, in the present work, we extended this computational model to understand the mixing process in a continuous-flow stirred reactor equipped with this (Mixel TT) impeller. Before we discuss the simulations of continuous-flow operation, it would be useful to examine the flow characteristics near the impeller blades of Mixel TT, in order to understand the role of special blade shape on the generated flow.

7.3.1.2Flow around blades of Mixel TT impeller

Similar to the down-flow pitched-blade turbine, the Mixel TT impeller generates high velocity jets moving downwards. An iso-surface of axial velocity around an impeller blade is shown in Figure 7.5a. It can be seen that the jet emanating from the front side is faster than that emanating from the backside of the blade. The jet flowing downwards from the backside of the blade appears to interact with the trailing vortex attached to the backside of the blade.

An iso-surface of turbulent kinetic energy is shown in Figure 7.5b. The leading edge of the blade generates the highest turbulence. However, the highest values of the turbulent kinetic energy are associated with the trailing vortex attached to the blade. The movement of the blade generates a high-pressure region ahead of the blade leading edge, and a low-pressure region behind the blade. Such a pressure difference leads to a trailing vortex behind impeller blades. Prediction of pressure field around impeller blades and of trailing vortex is especially crucial for extending the present approach for simulations of multiphase (gas-liquid) flows generated by impellers. The examination of the predicted results indicates that the pressure field seems to be simulated correctly.

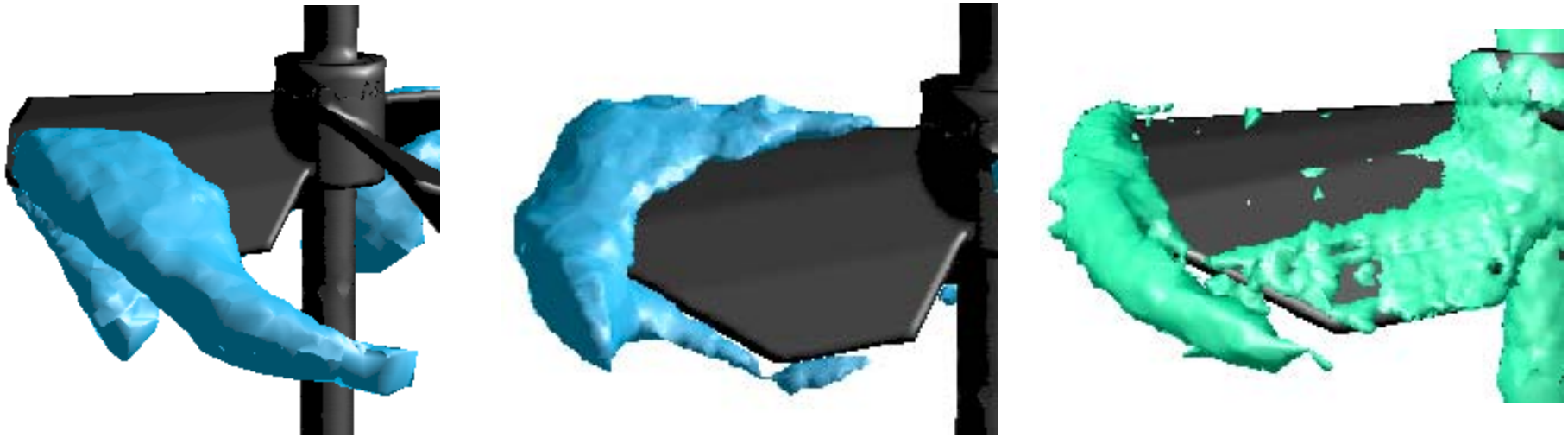

(a): Iso-surface of Axial Velocity Jet (iso-value = 0.3 m/s in downward direction)

(b): Iso-surface of Turbulent Kinetic Energy (iso-value = 0.015 m^2/s^2)

(c) Iso-surface of Z-vorticity, (iso-value = 25 s^{-1})

(Impeller is moving inwards through the paper)

Figure 7.5: Flow Field around Impeller Blades for Batch Operation, N= 360 rpm and U_{tip}= 1.7907 m/s

In order to examine the trailing vortex, the iso-surface of z-vorticity is shown in Figure 7.5c. The iso-surface shows the presence of a single vortex trailing behind the impeller blade. The center of the vortex appears to move away and downwards from the impeller.

The computational model was thus successful in capturing the major features of the flow generated by the Mixel TT impeller in the stirred reactor operating in batch mode. The comparison of simulated and reported experimental results shows reasonably good agreement. The model was then extended to simulate continuous operation with Mixel TT impeller.

7.3.2 Continuous operation

In a continuous-flow stirred reactor, apart from the size, shape, location and rotation speed of the impeller, the fluid dynamics are also a complex function of the inlet and outlet locations and of the liquid flow rate. Such complex fluid dynamics ultimately control the behaviour of the continuous-flow reactor and define whether it is closer to the ideal, single CSTR or far from it. Customarily, the ratio of residence time and mixing time is kept high (≥ 10) to avoid non-ideal flow behaviour in stirred reactors. The residence time (τ) is calculated from the ratio of the reactor volume (V_l) and the liquid flow rate (Q_l). The value of mixing time (t_m) is a function of impeller design and impeller rotational speed.

Mavros *et al.* (2000) studied the fluid dynamics of a continuous-flow stirred reactor equipped with a Mixel TT impeller for two different ratios of residence time and / mixing time. In both cases, the liquid flow rate was kept constant and equal to 2.01667×10^{-4} m^3/s. Two values of impeller speed were studied, to realize the two values of the ratio of residence time to mixing time (predicted from the correlation of Roustan and Pharamond, 1988) as 9.6 and 4.8 (impeller speed of 360 rpm and 180 rpm respectively). At the impeller speed of 360 rpm ($\tau/t_m=9.6$), the reactor is expected to behave almost like an ideal CSTR. At the lower impeller speed ($\tau/t_m=4.8$), non-ideal flow (non-ideal mixing) behaviour of the stirred reactor could be a distinct possibility.

In this work, we extend our computational model to study these two cases of continuous-flow operation.

7.3.2.1 Comparison with experimental data: For N= 360 rpm

In a continuous-flow operation, if the feed inlet is located in such a way that the high-velocity incoming jet passes through an opening between the impeller blades, the resulting flow field may be different from the one when the inlet is located in such a way that the high-velocity jet impinges on the blade. Therefore, as discussed in Section 7.2, three specific blade positions with respect to feed inlet were considered. In the first configuration, the feed tube was located above the last two sections of an impeller blade. In the second configuration, the feed tube was located above the first two sections of the impeller blade, whereas in the third configuration, the incoming feed was allowed to bypass the impeller through the clearance between two adjacent blades. The feed tube was located at a mid-baffle plane in all configurations considered. Comparison of the predicted velocity field and experimental data (at three different r-z planes: feed plane and 180° from feed plane) for all three configurations are shown in Figure 7.6.

The simulations captured the high-velocity jets emanating from the feed pipe and the impeller blades and the small reverse loop below the impeller. The location of the circulation "eye" is lowered and found to be closer to the bottom of the reactor compared to the batch operation. This is in agreement with the experimental observation of Mavros *et al.* (2000). The predicted flow field shows some variations within these three configurations, especially in the region below the impeller. For a quantitative examination of these differences, the predicted values of axial velocity for these three configurations at an axial location of 0.05 m from the reactor bottom are compared with the ensemble averaged results predicted for the batch reactor in Figure 7.7. It can be seen that there is a significant interaction between the impeller stream and the feed jet. As expected, the predicted axial velocity for configuration L3, in which the feed jet is located in the open space between the impeller blades, is highest. The difference between the predicted results for these three configurations decreases as one move away from the impeller. For detailed quantitative comparison with the

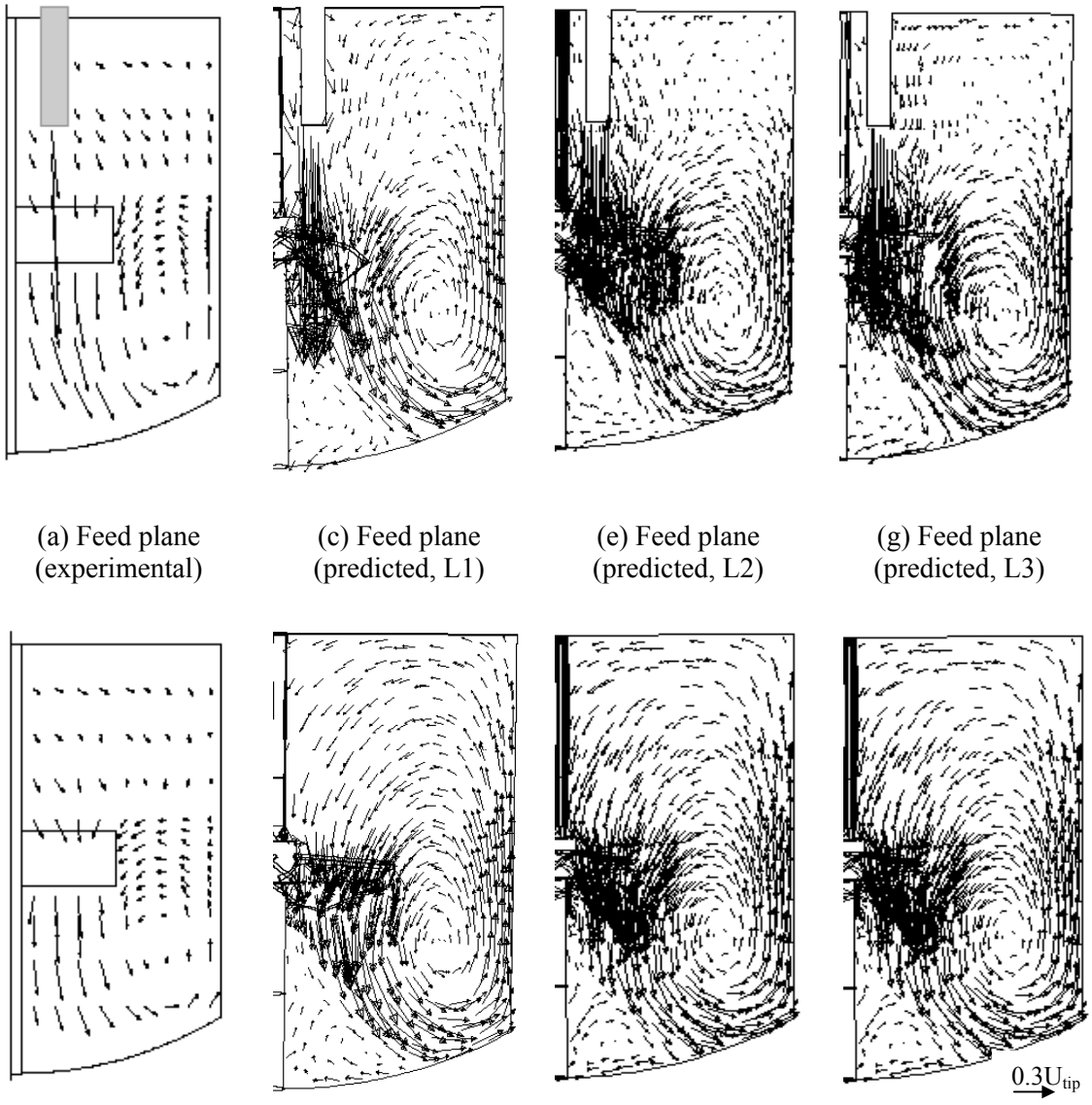

(a) Feed plane (experimental) | (c) Feed plane (predicted, L1) | (e) Feed plane (predicted, L2) | (g) Feed plane (predicted, L3)

(b) 180º from feed plane (experimental) | (d) 180º from feed plane (predicted, L1) | (h) 180º from feed plane (predicted, L2) | (i) 180º from feed plane (predicted, L3)

Figure 7.6: Mean Flow Field at Three r-z Planes for Continuous Operation for Three Specific Positions of Impeller Blades and Feed-tube, $Q_l = 2.01667 \times 10^{-4}$ m^3/s, N= 360 rpm and $U_{tip} = 1.7907$ m/s

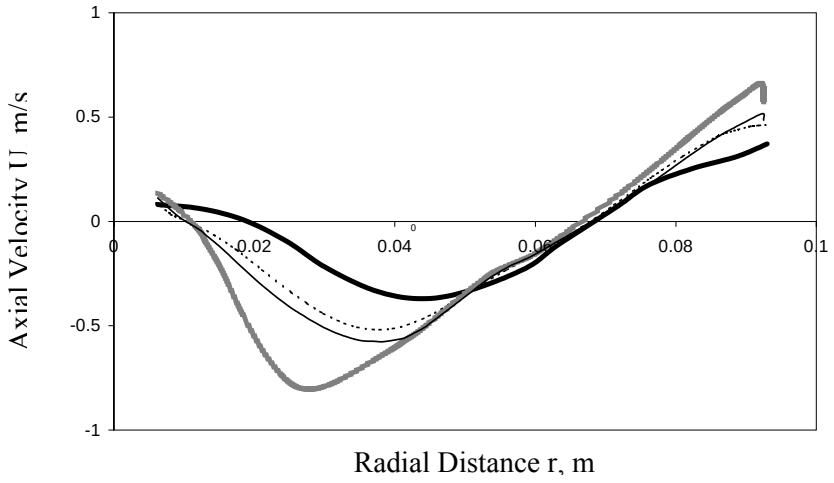

(a) Feed plane

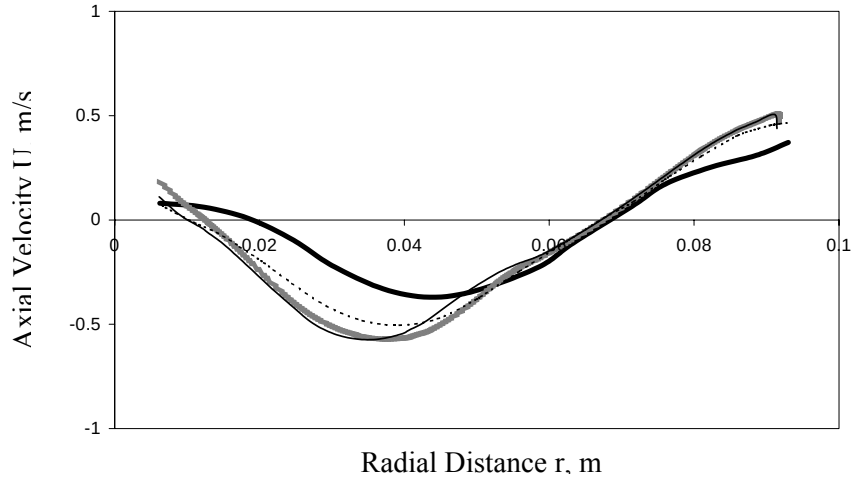

(b) 90° from feed plane

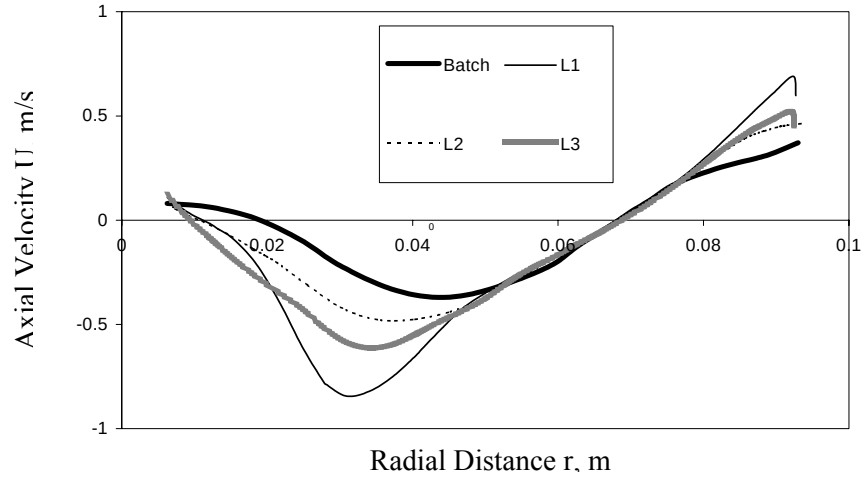

(c) 180° from feed plane

Figure 7.7: Comparison of Axial Velocity for Batch and Continuous Operation (for three specific positions of impeller blades and feed-tube), $Q_l = 2.01667 \times 10^{-4}$ m^3/s, N= 360 rpm, U_{tip}= 1.7907 m/s and z= 0.05 m

experimental data, additional simulations were carried out for three different positions of impeller blades relative to the baffles and the flow characteristics ware ensemble averaged.

The ensemble-averaged results are compared with the experimental data of Mavros *et al.* (2000) at three different axial locations in Figure 7.8. It can be seen that the comparison between the predicted axial velocity values and the experimental data is reasonably good. Higher values of axial velocities are predicted below the feed pipe and near the reactor wall. The incoming jet combines with the liquid being drawn by the impeller, and hence the axial velocities at the lower side of the impeller are considerably higher than in the batch case. It can be seen that the axial velocities close to the center of the reactor are relatively higher in the plane located at 180° from the feed plane. This indicates that part of the incoming liquid is added to the flow has been entrained in a tangential motion by the rotating impeller.

The comparison between the predicted radial velocity values and the experimental data is reasonably good. For the feed plane and for the plane at 180^{o} from the feed plane (Figure 7.8b), experimental data shows outward radial velocity just below the feed pipe. However, the predicted radial velocity profile does not show such outward velocity. For the plane at 180^{o} from the feed plane, radial velocity values at 0.05 m from the bottom are rather over-predicted. The comparison of predicted and experimental tangential velocities is shown in Figure 7.8c.It can be seen from Figure 7.8c that the comparison between the predicted results and experimental data is satisfactory.

The values of predicted turbulent kinetic energy are compared with the experimental data (Figure 7.8d). It can be seen that CFD model over predicted (Figure 7.8d) the turbulent kinetic energy especially in the region below the impeller. The predicted turbulence characteristics in the reactor may be sensitive to the turbulence level at the inlet pipe. To quantify such sensitivity, three simulations were carried out with three different turbulence intensity values at the inlet (0.1%, 10% and 20%). The simulated results are shown in Figure 7.9. It can be seen that the inlet boundary conditions do not significantly influence the prediction of turbulence field in the reactor (within the range

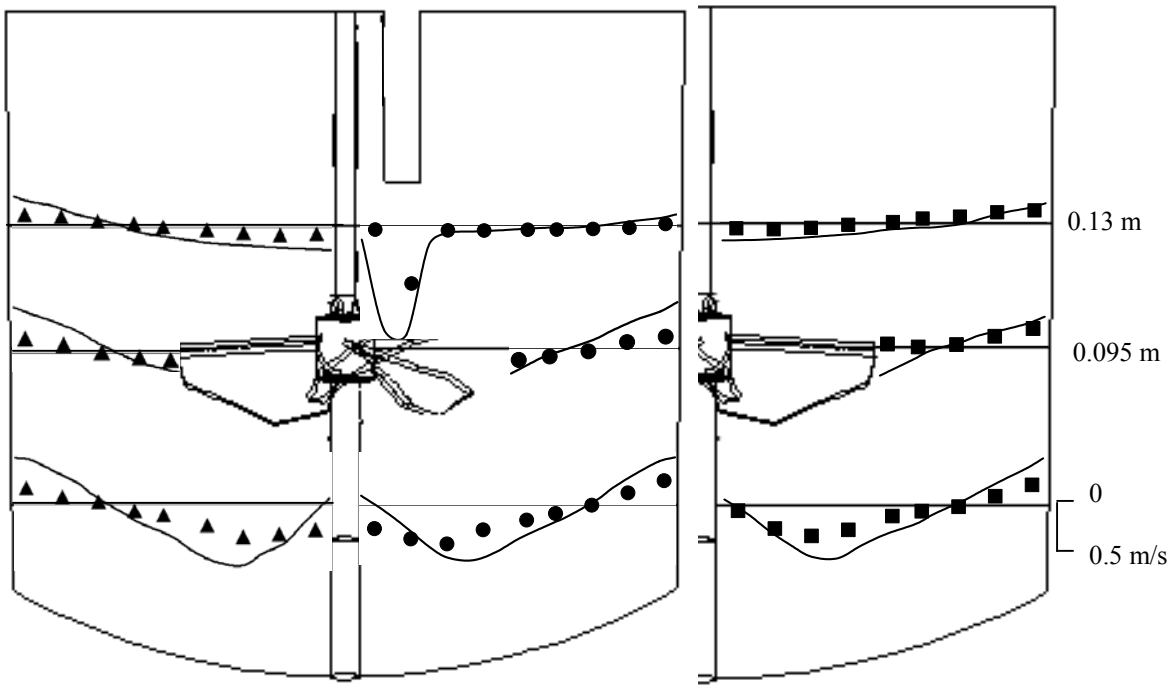

(a) Axial Velocity

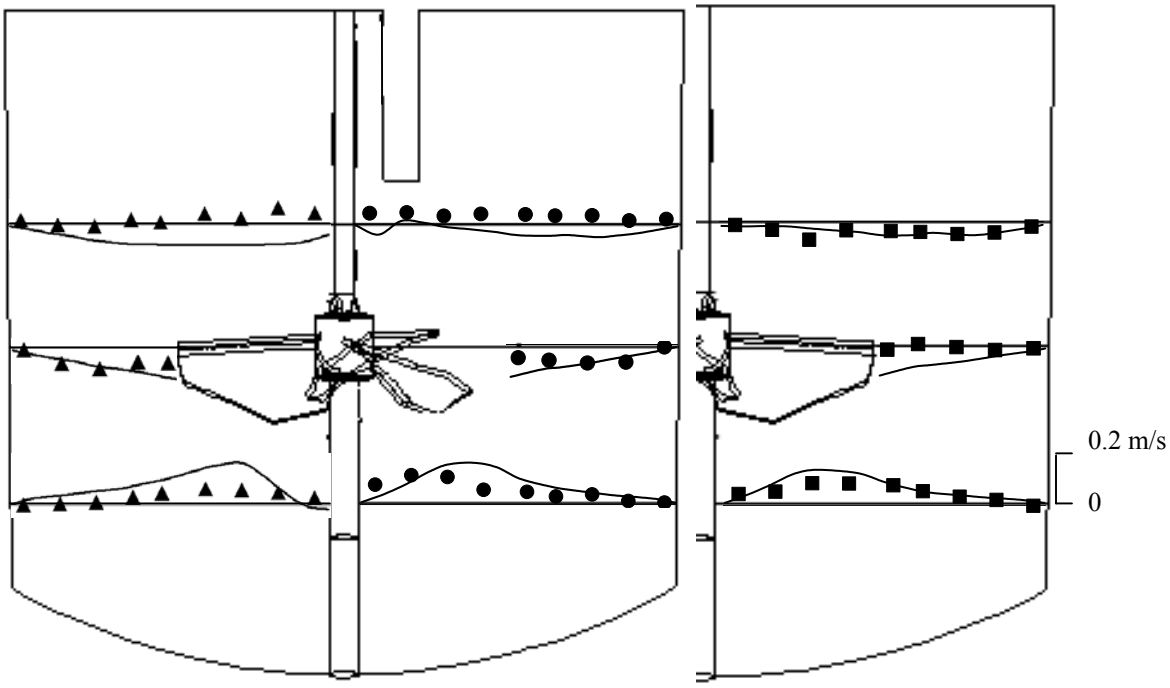

(b) Radial Velocity

Legends:			
	● Feed plane	■ 90° from feed plane
	▲ 180° from feed plane	—— Predicted results

Figure 7.8: Comparison of Predicted Results and Experimental Data for Continuous Operation, $Q_l = 2.01667\times10^{-4}$ m^3/s, N = 360 rpm and U_{tip}= 1.7907 m/s
(Symbols denote data of Mavros *et al.*, 2000) [continued on next page]

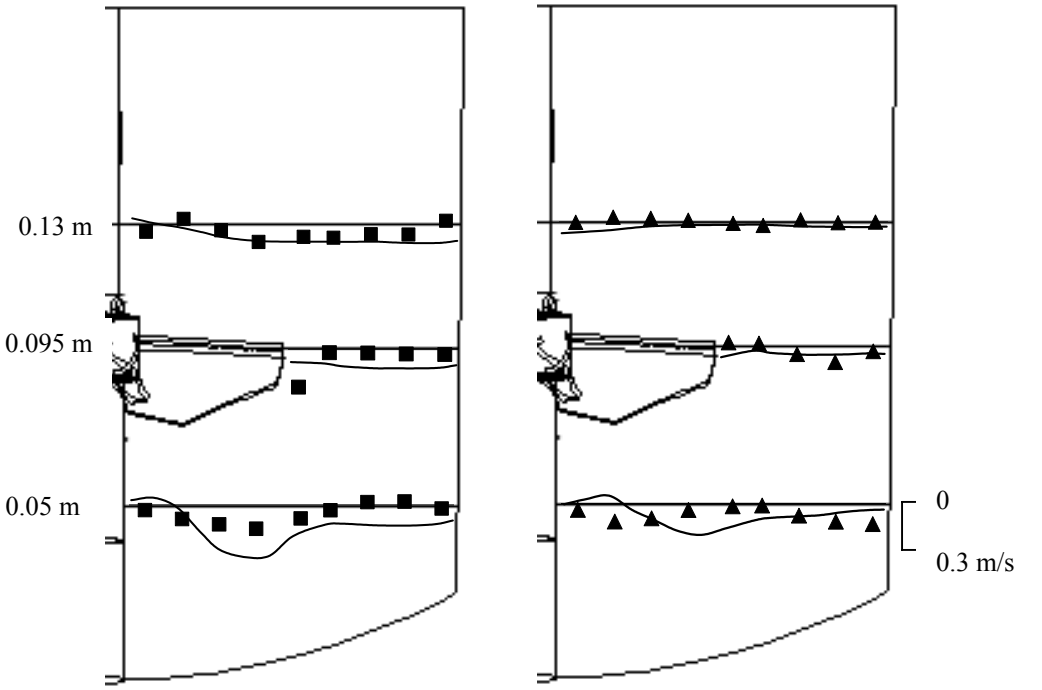

(c) Tangential Velocity

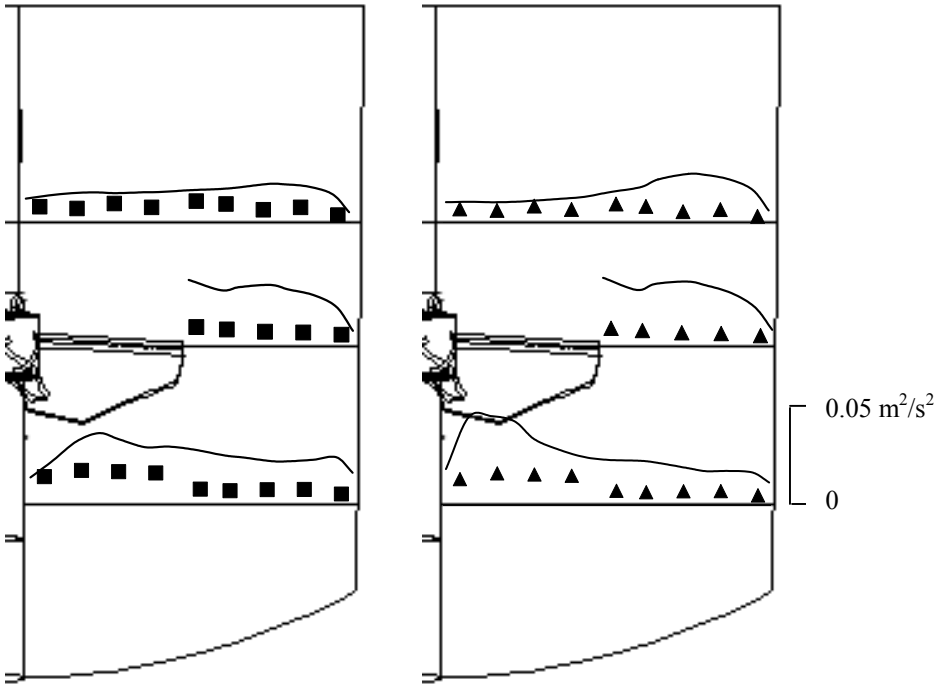

(d) Turbulent Kinetic Energy

Legends:		
	● Feed plane	■ 90° from feed plane
	▲ 180° from feed plane	—— Predicted results

Figure 7.8: Comparison of Predicted Results and Experimental Data for Continuous Operation, $Q_l = 2.01667\times10^{-4}$ m^3/s, N = 360 rpm and U_{tip}= 1.7907 m/s

(Symbols denote data of Mavros *et al.*, 2000)

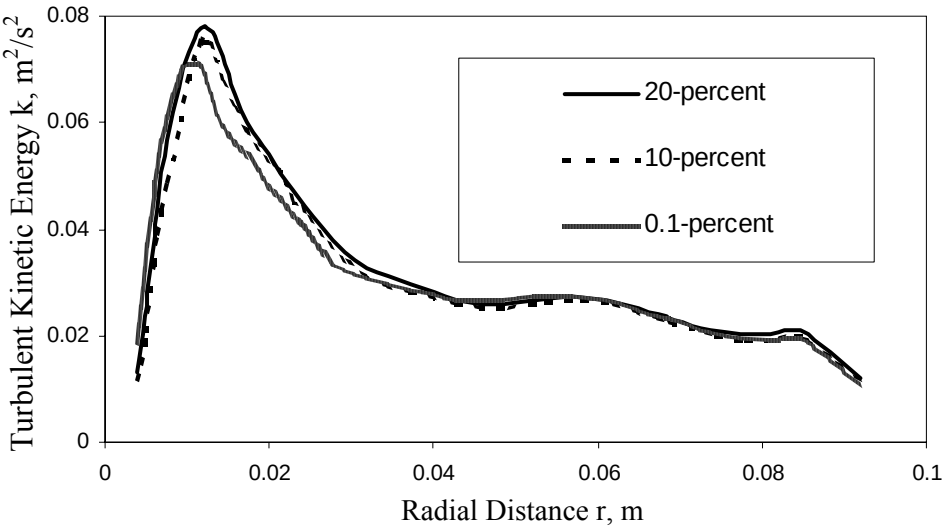

(a) Axial distance, z = 0.05 m

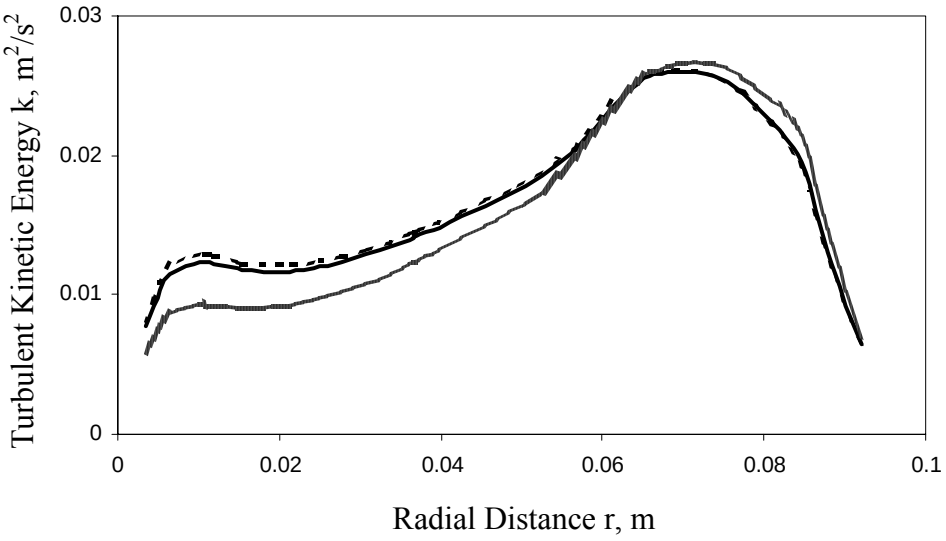

(b) Axial distance, z = 0.13 m

Figure 7.9: Effect of Turbulence of Incoming Fluid on the Turbulence Level in the Reactor for Continuous Operation, $Q_l = 2.01667\times10^{-4}$ m^3/s, N = 360 rpm and U_{tip}= 1.7907 m/s [180° from feed plane]

considered in the present work). Therefore, for all the subsequent simulations, the turbulence intensity of the incoming fluid was set to 10% of the mean velocity.

7.3.2.2 Comparison with experimental data: For N= 180 rpm

Simulations were also carried out at a lower impeller rotation speed of 180 rpm. This lower impeller speed leads to a decrease in impeller pumping, which will further enhance the influence of the incoming liquid feed on the flow field within the reactor. Comparison of the predicted velocity field and experimental data (at the feed plane, 90° and 180° from the feed plane) are shown in Figure 7.10. It can be seen from the simulated results that the eye of circulation has moved further towards the reactor bottom, which is in agreement with the experimental observations. The high-velocity feed interacts with the impeller stream and almost no reverse loop near the reactor bottom is observed for the lower impeller speed.

The quantitative comparison of the predicted results with the experimental data of Mavros *et al.* (2000) at three different axial locations is shown in Figure 7.11.The comparison between the predicted and experimental axial velocity values is shown in Figure 7.11a. The maximum axial velocity was observed below the feed tube (0.13 m from the bottom of the reactor). The axial velocity at the feed inlet was considerably higher than the circulating liquid. The strong incoming jet passes through the impeller region and appears on its lower side. High axial velocities were observed at the bottom of the reactor. This indicates possible short-circuiting of the inlet stream.

The comparison of the predicted radial velocity profiles and the experimental data is shown in Figure 7.11b. It can be seen that the agreement is reasonably good for the plane at 90^o from the feed plane. However, the agreement was not that good for the plane at 180^o from the feed plane. For the latter plane, the experimental data shows an outward radial velocity at a 0.05 m height from the bottom of the reactor. The computational model has not captured this. Experimental data of tangential velocities at planes located at 90^o and 180^o from the feed plane show very small tangential velocity values, compared to the predictions (Figure 7.11c). Similar to those predicted for a higher impeller rotational speed, the values of the predicted turbulent kinetic energy are

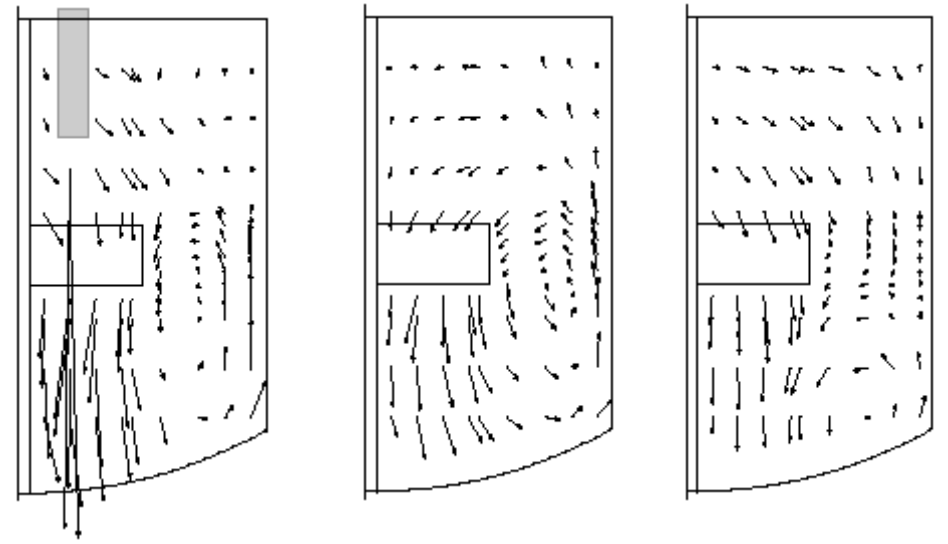

(a) feed plane (experimental)

(b) 90° form feed plane (experimental)

(c) 180° from feed plane (experimental)

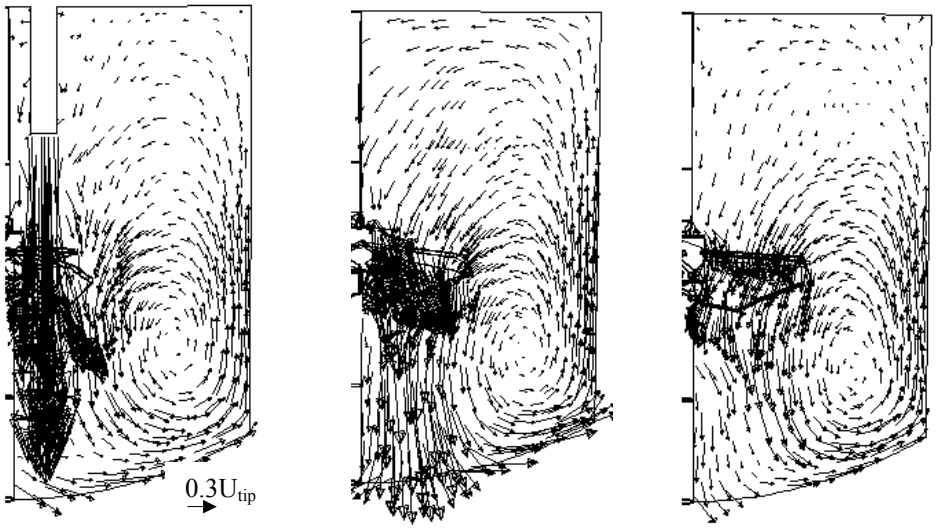

(d) Feed plane (predicted)

(e) 90° from feed plane (predicted)

(f) 180° from feed plane (predicted)

Figure 7.10: Mean Flow Field at Three r-z Planes for Continuous Operation, $Q_l = 2.01667 \times 10^{-4}$ m^3/s, N= 180 rpm and $U_{tip} = 0.8954$ m/s

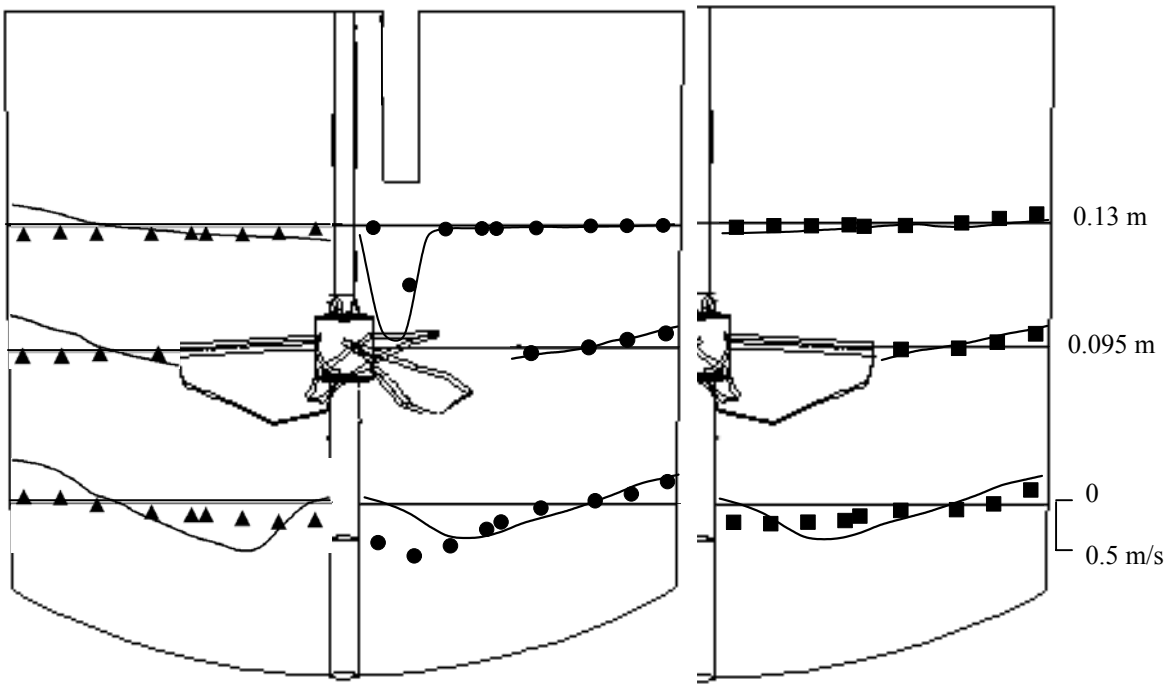

(a) Axial Velocity

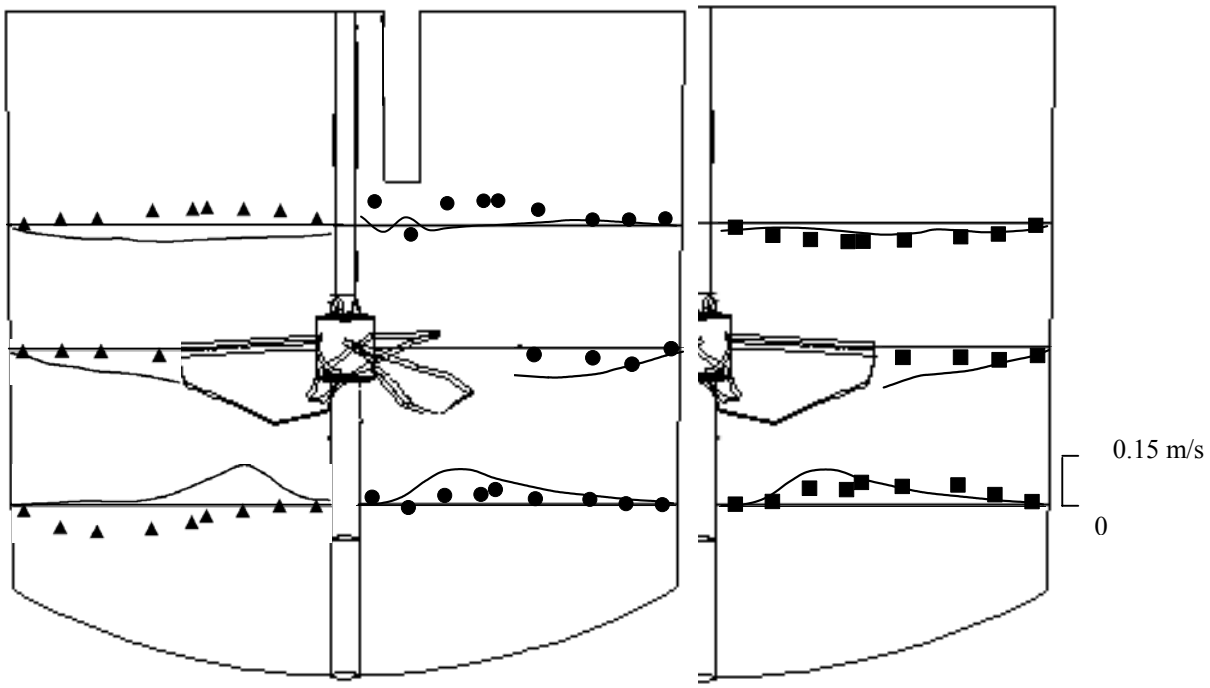

(b) Radial Velocity

Legends:

● Feed plane	■ 90° from feed plane
▲ 180° from feed plane	—— Predicted results

Figure 7.11: Comparison of Predicted Results and Experimental Data for Continuous Operation, $Q_l = 2.01667\times10^{-4}$ m^3/s, N = 180 rpm and U_{tip}= 0.8954 m/s

(Symbols denote data of Mavros *et al.*, 2000) [continued on next page]

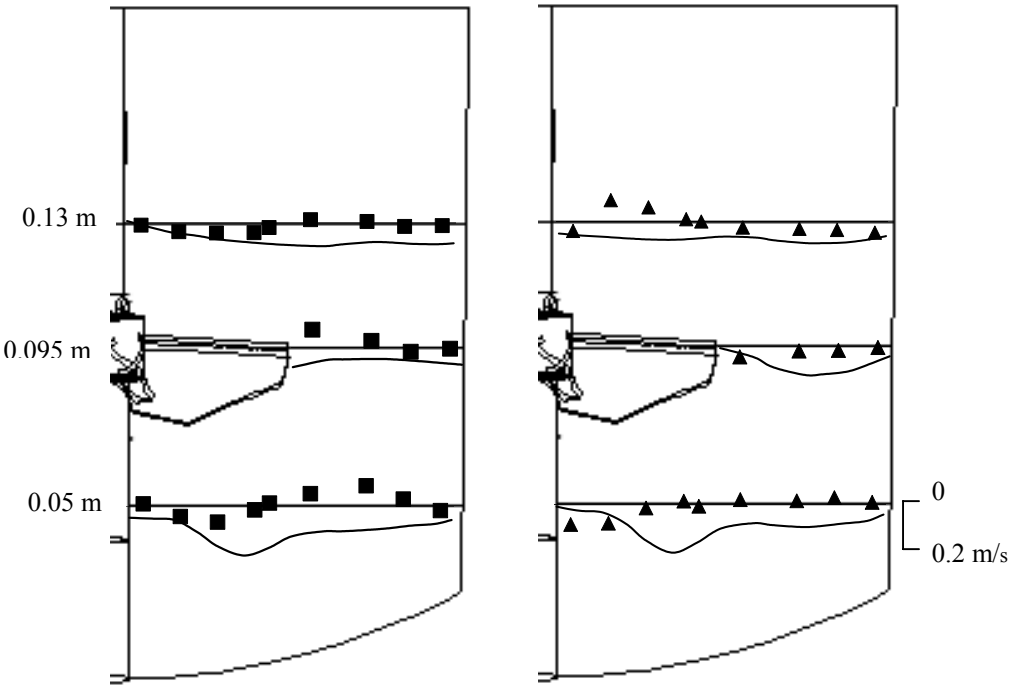

(c) Tangential Velocity

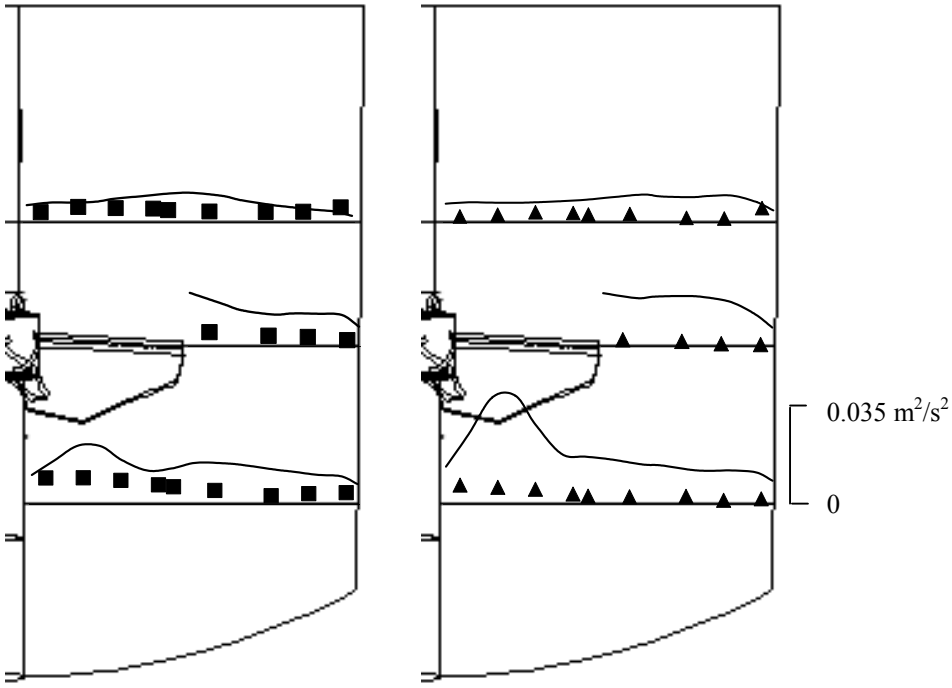

(d) Turbulent Kinetic Energy

Legends:		
	● Feed plane	■ 90° from feed plane
	▲ 180° from feed plane	—— Predicted results

Figure 7.11: Comparison of Predicted Results and Experimental Data for Continuous Operation, $Q_l = 2.01667\times10^{-4}$ m^3/s, N = 180 rpm and U_{tip}= 0.8954 m/s

(Symbols denote data of Mavros *et al.*, 2000)

higher than the experimental data (Figure 7.11d). Though the agreement of the predicted and experimental data for the continuous-flow operation for 180 rpm is not as good as for the batch operation and for the continuous-flow operation for 360 rpm, the simulations seem to capture the key flow characteristics. The computational model was therefore extended to simulate the mixing process and investigate the predictive possibility of the residence time distribution of the flowing-through liquid.

7.3.3 Mixing in continuous stirred reactor

Mavros *et al.* (2000) have studied the fluid dynamics of a continuous-flow stirred reactor equipped with a Mixel TT impeller at two different ratios of residence time to mixing time. In both the cases, the liquid flow rate was kept constant and equal to 2.01667×10^{-4} m^3/s. Two values of impeller speed were studied, in order to realize two values of the ratio of residence time to mixing time: 9.6 and 4.8 (at impeller speeds of 360 rpm and 180 rpm, respectively). Usually, continuous operation of a stirred reactor is considered as almost ideal when the ratio of residence time to mixing time is about 10. Considering this, ideal flow behaviour would be expected at the higher impeller speed (τ/t_m=9.6), while a non-ideal behaviour would be expected at the lower impeller speed (τ/t_m=4.8). Computational flow models developed in this work were used to evaluate these expectations.

7.3.3.1 N= 360 rpm

Simulation of mixing was carried out for an impeller rotation speed of 360 rpm and a liquid flow rate of 2.01667×10^{-4} m^3/s. Completely converged flow results were used for simulating mixing, assuming that the addition of the tracer does not influence the fluid dynamics in the stirred reactor. An instantaneous square pulse of tracer (at time t = 0) was introduced in the reactor through the inlet stream for 1 s (the mass fraction of the tracer at the inlet was set equal to 1). The species transport equations were solved for more than four times of residence time, to ensure the complete removal of tracer material from the reactor.

The evolution of the tracer concentration field within the reactor and the outlet concentration with respect to time were simulated and studied. The predicted snapshots of the tracer concentration field at various times are shown in Figure 7.12. It can be seen that the tracer follows the liquid circulation path and is pumped downwards by the impeller. It was interesting to note that even in the case of a high impeller speed, where the ratio of residence time to mixing time is about 10, a significant non-uniformity in tracer concentration exist within the reactor even higher than the mixing time, see for example, snapshot of tracer concentration field at 5 seconds. This indicates a deviation from the ideal CSTR reactor performance and shows a possibility of non-ideal mixing (or non-ideal flow behaviour) in the stirred reactor, even for the high ratio of residence time to mixing time.

To examine the non-ideality further, the history of tracer concentration at the outlet of the reactor was studied. Mixing simulations were carried out for all three specific positions of impeller blades and feed tube. The predicted exit age distributions were then compared with that of an ideal CSTR. It can be seen from Figure 7.13a and 7.13b that the exit age distribution is significantly different from that of the ideal CSTR for all three positions. For the L3 configuration, where the feed tube is positioned above the clearance between two impeller blades, a strong short-circuiting is observed even when the ratio of residence time to mixing time is about 10. The time of first appearance of the tracer at the outlet is about 1 s. From the overshoot in the tracer concentration observed at the outlet, it appears that the high velocity inlet jet may be interacting directly with the outlet leading to a considerable short-circuiting.

This is further confirmed by the lower slope of predicted residence time distribution curve compared to that of ideal CSTR. The combination of overshoot at the beginning and lower slope at later stage indicates that part of the incoming fluid bypasses stirred reactor and flows effectively through a small volume plug flow reactor and the remaining part of the incoming fluid flows through a stirred reactor with much larger effective residence time than that calculated from the total incoming flow (Figure 7.13b). The nature of predicted exit age distribution indicates that, it can be modeled as a combination of ideal stirred reactor and plug flow reactor operating in parallel. Preliminary analysis indicates that the effective residence time of the ideal CSTR part is about 68 s (this means only about 36% of the incoming liquid flows through a reactor

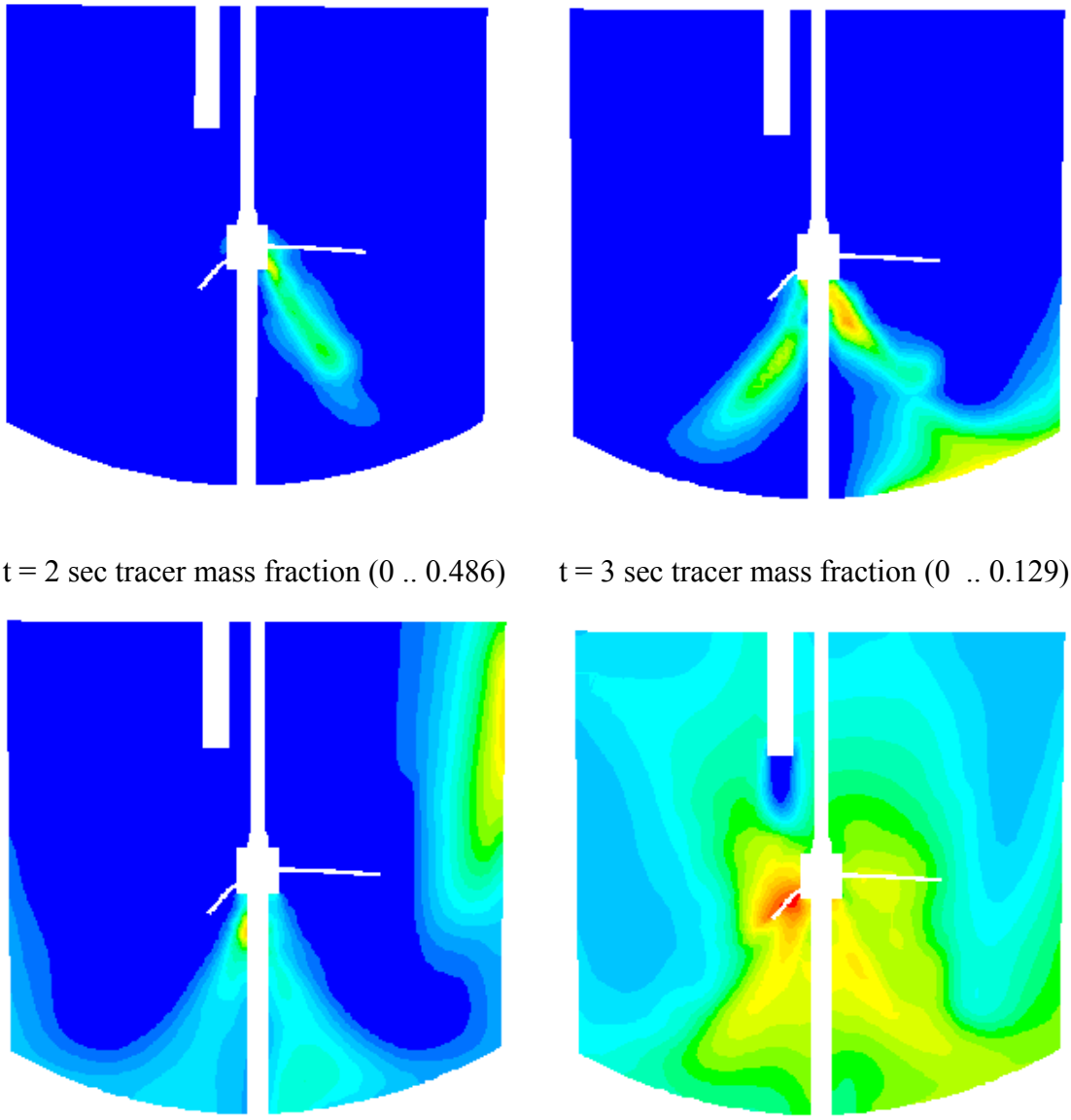

t = 2 sec tracer mass fraction (0 .. 0.486)

t = 3 sec tracer mass fraction (0 .. 0.129)

t = 5 sec tracer mass fraction (0 .. 0.0723)

t = 11 sec tracer mass fraction (0 ..0.0106)

Colour code: blue is minimum and red is maximum

Figure 7.12: Predicted Snapshots of Tracer Mass Fraction Field at Different Time for Continuous Operation, Q_l= 2.01667×10^{-4} m^3/s and N= 360 rpm

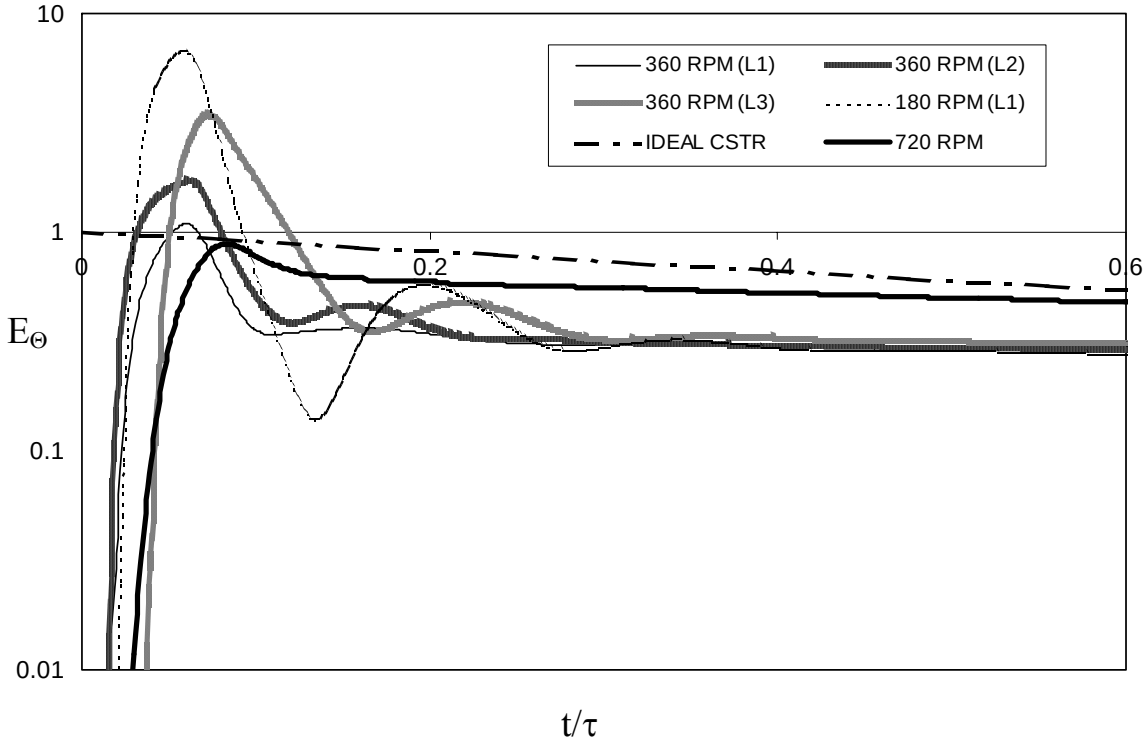

(a) Predicted tracer evolution curve

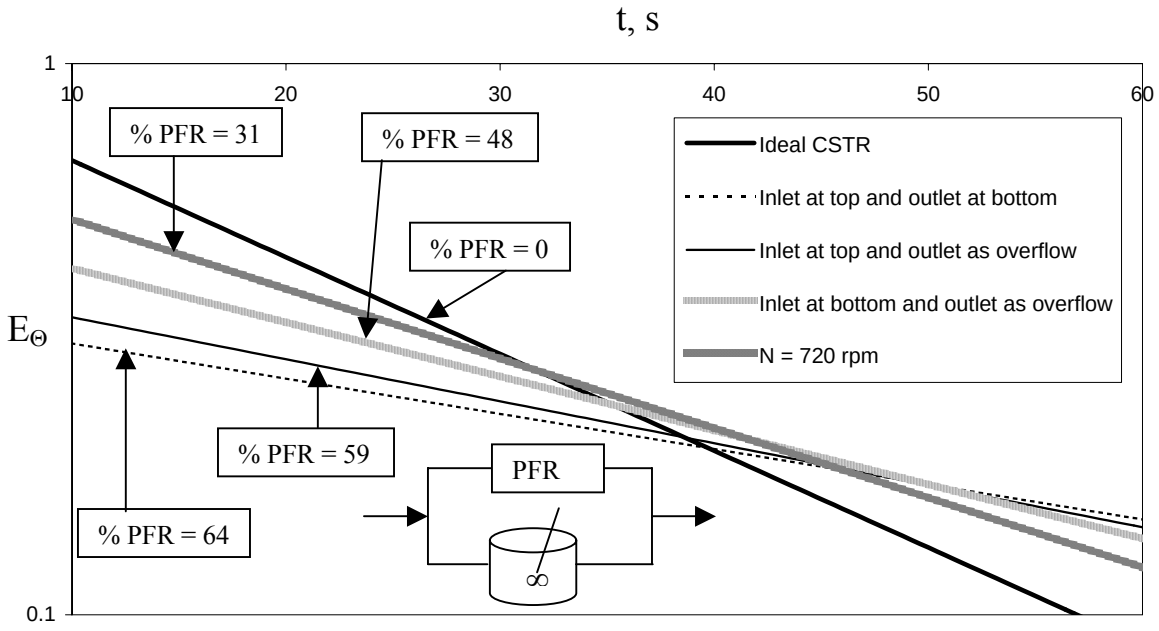

(b) Estimation of percentage short-circuiting feed

Figure 7.13: Comparison of Predicted Exit Age Distribution with Ideal CSTR

and about 64% of the incoming fluid short circuits to the outlet). To examine the influence of impeller speed, a case of continuous-flow operation at a lower impeller speed was simulated.

7.3.3.2 N= 180 rpm

The simulated exit age distribution for the lower impeller speed case is also shown in Figure 7.13 (for configuration L1). The predicted exit age distribution indicates a strong short-circuiting within the stirred reactor. The impeller pumping action is not sufficient to quickly mix the incoming liquid with the circulating liquid in the reactor. The incoming jet appears to be passing straight through the impeller region towards the outlet. Examination of the simulated velocity vectors (Figure 7.10) and axial velocity profiles (Figure 7.11a) at the bottom of the reactor also support these indications. Analysis of predicted RTD for lower impeller speed using the combination of ideal plug flow and idea CSTR indicates that about 72% of the incoming liquid short circuits to outlet.

Simulations of mixing indicate that, in addition to the relative importance of the impeller rotation speed and feed rate, the locations of the inlet and outlet also have a profound influence on the flow behaviour of continuous-flow stirred reactors. Even if the usual guidelines of keeping ratio of mixing time to residence time of more than 5 is followed, incorrect location of inlet and outlet nozzles may lead to severe short-circuiting as observed in the present case. Since the outlet location in the considered geometry was exactly below the impeller, significant part of the tracer short-circuits from the reactor. The early removal of tracer is clearly seen from the snapshots of tracer mass fraction at t= 3 seconds and t= 5 seconds (Figure 7.12). A different liquid outlet and inlet configuration would probably improve the performance of the stirred reactor.

7.3.4 Effect of inlet and outlet locations on the performance of reactor

To understand the interaction of incoming feed with impeller-generated flow, particle streak lines were simulated by releasing neutrally buoyant tracer particles from the inlet pipe. The simulated particle streak lines (for a flow time of 5 seconds) for different configurations are shown in Figure 7.14. It can be seen from Figure 7.14a that, when

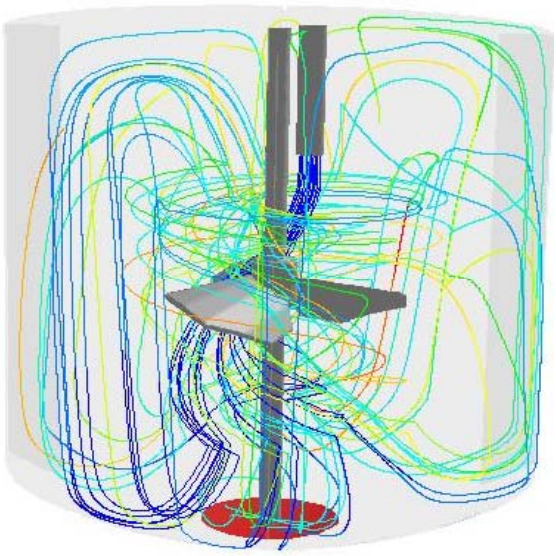

(a) Inlet at the top and outlet at the bottom, N = 360 rpm

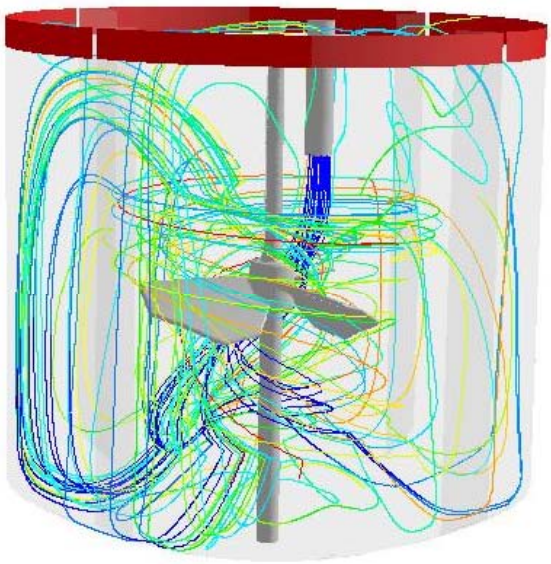

(b) Inlet at the top and outlet as overflow, N = 360 rpm

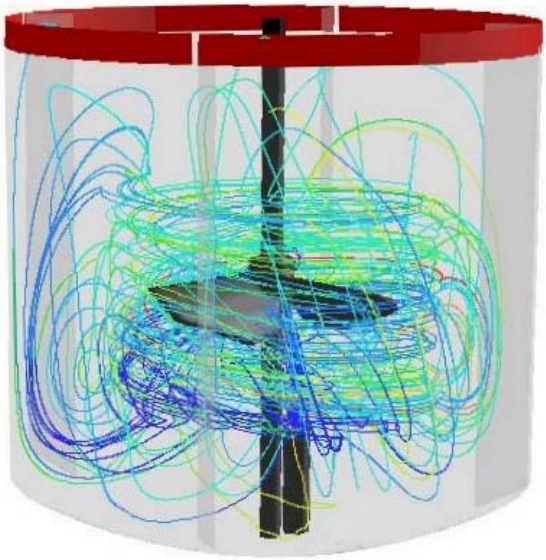

(c) Inlet at the bottom and outlet as overflow, N = 360 rpm

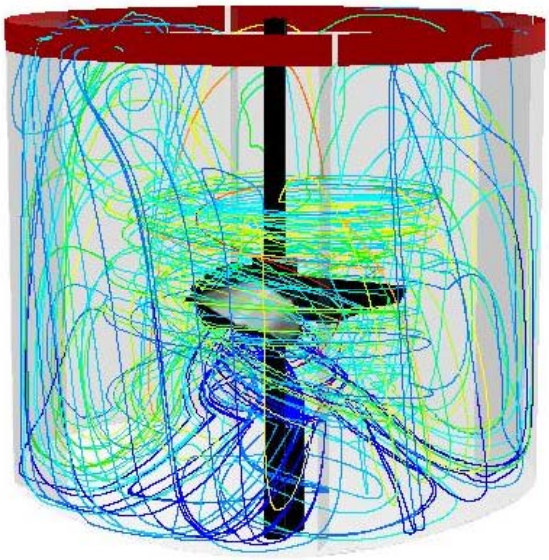

(d) Inlet at the bottom and outlet as overflow, N = 720 rpm

Figure 7.14: Streak Lines for Incoming Liquid Feed for Different Inlet/Outlet Configurations, $Q_l = 2.01667 \times 10^{-4}$ m^3/s

outlet is located below the feed pipe and impeller speed is not adequate, the part of incoming feed stream directly interacts with the outlet and leads short-circuiting in the reactor. The streaklines shows little effect of impeller action on the flow of incoming feed in the reactor. In order to reduce the direct interaction of incoming feed with the outlet location, the position of outlet of reactor was changed. The outlet was modelled as overflow from the reactor. The predicted exit age distribution (Figure 7.13b) shows some improvement over the case of outlet at the bottom. However, some short-circuiting in the reactor was still found to occur. It can be seen form Figure 7.14b that, the major fraction of the streak lines are grouped together and do not get homogeneously distributed in the whole reactor.

To evaluate different options to minimize the short-circuiting, a case where feed stream was introduced from the bottom was considered. The outlet was modelled as overflow. For such a configuration (Figure 7.14c), the feed stream is introduced in the reactor against the pumping action of the impeller. The predicted exit age distribution is shown in Figure 7.13b. It can be seen from Figure 7.13b that, this combination of inlet and outlet locations has further improved the mixing in the reactor. The predicted streak lines shown in Figure 7.14c indicate the interaction between inlet jet and impeller stream leading to better mixing. It may however be seen that the impeller generated flow is still not sufficient to disperse the injected feed homogeneously within the reactor. The particle streak lines are still not distributed all over the reactor. This suggested that possible increase in the impeller rotational speed might improve the extent of homogenization. The flow in stirred reactor was then simulated for an impeller rotational speed of 720 rpm (τ/t_m=19.2). The predicted exit age distribution for higher impeller rotational speed is shown in Figure 7.13. It can be seen from Figure 7.13 that, the predicted exit age distribution is now much closer to the ideal CSTR performance, as compared to the previous cases. The change in the location of inlet/outlet and increase in the impeller rotational speed was necessary to reduce the extent of by-passed fluid by more than half. Particle streak lines shown in Figure 7.14d also confirm that the incoming feed is distributed more or less in the whole reactor.

The idea of using quasi-steady state approach with multiple snapshots may be used to simulate the flow in an industrial continuous flow stirred tank reactor. The number of

snapshots needed to adequately represent the flow generated by an impeller and the interaction of the incoming liquid jet with the impeller would depend on the design of the impeller. After establishing the flow, detailed species transport equations with any one of the snapshots to obtain the residence time distribution at the outlet. Although, the mixing simulation with quasi-steady state approach does not accurately capture the interaction of the incoming jet with the rotating impeller, but the obtained results are sufficient for the 'a priory' suggestion for the evaluation of the different design configuration.

7.4 Summary and Conclusion

The flow generated by an axial flow impeller Mixel TT in a batch as well as continuous flow stirred reactor was simulated using multiple reference frame approach. The predicted results were compared with the reported experimental results for the batch as well as the continuous-flow mode of operation. The predicted results show reasonably good agreement with the reported experimental data. The predicted results show reasonably good agreement with the reported data for the batch mode of operation. Despite some discrepancies, the CFD model was able to capture the key features of the flow generated by the impeller. The computational model developed was used to study the characteristics of flow around the blades of the Mixel TT impeller. The simulated results show a single trailing vortex trailing behind the blades.

The model was then extended for simulating continuous-flow operation. The simulated flow field for the continuous operation also shows a reasonable agreement with the experimental data. The predicted results capture the key variations in the flow characteristics in angular direction (feed and other r-z planes). The experimental and predicted flow fields indicate the possibility of short-circuiting and non-ideal flow behaviour. The developed computational model was therefore further used to study the mixing process and the residence time distribution of the liquid in the continuous-flow operation of the stirred reactor. The predicted exit age distribution, the snapshots of tracer concentration and the streamlines of incoming feed explained the possible short-circuiting in the stirred reactor. Even for a high ratio of residence time to mixing time (τ/t_m= 9.6), the possibility of short-circuiting was observed.

The predicted results indicate that the inlet and outlet locations may be the cause for the observed short-circuiting for the present setup and the operating conditions. The computational model was then used to devise the new inlet/outlet configuration, which will improve the mixing quality in the reactor. It was observed that, the feed tube at the bottom of the reactor and overflow type outlet with impeller rotational speed of 720 rpm (τ/t_m=19.2) provides better mixing in the reactor for the present experimental setup and incoming liquid flow rate. The computational model shows promising results and seems to be a useful tool for designing and optimising the performance of a continuous stirred reactors.

Chapter 8

FLOW IN A TALL GAS-LIQUID STIRRED REACTOR

8.1 Introduction

Gas-liquid stirred reactors are widely used in chemical process industry to carry out gas-liquid reactions. In most of the industrial applications, tall reactors equipped with multiple impellers are increasingly used. The multiple impeller system provides better gas utilization, higher interfacial area and narrower residence time distribution in the flow system compared to a single impeller system. Also the multiple impeller systems are preferred in bioreactor, as they offer lower average shear as compared to single impeller system due to overall lower operational speed with nearly same power input and allow more degrees of freedom for controlling the gas dispersion as well as the bulk flow of liquid phase.

In multiple impeller gas-liquid stirred reactor, different gas flow regimes are realized in the reactor depending upon the reactor hardware and operating parameters such as impeller design, impeller spacing, rotational speed and the volumetric gas flow rate. These different flow regimes show different fluid dynamic conditions in the reactor and therefore, can have different rates of transport as well as mixing processes. It is therefore, essential to have better understanding of the influence of reactor hardware as well as operating parameters on the fluid dynamics, to manipulate and to have better control on the performance of the reactor.

Recently, Shewale and Pandit (2005) have experimentally studied the mixing process occurring in an aerated stirred reactor equipped with three down- pumping six blade pitched turbine operating in different gas flow regimes. They have found significant influence of the prevailing gas flow regimes on the time scale of the mixing process occurring in the reactor. They observed that the change in the flow regime significantly alters the rates of liquid phase mixing process. For extending their results to industrial systems, it is essential to develop computational models, which can quantitatively predict the influence of hardware and operating parameters on liquid phase mixing. In this work, such an attempt is made.

We have developed CFD models to understand fluid dynamics in different flow regimes and to understand the influence of the liquid flow patterns prevailing in the reactor on the mixing process. The developed computational model based on the

Eulerian-Eulerian approach was first used to simulate the gas-liquid flows in stirred reactor. The predicted gross characteristics of the fluid dynamics were compared with the experimental measurements of the Shewale and Pandit (2005). The particle trajectory simulations were then carried out to obtain the Lagrangian information (circulation time distribution) of the liquid phase. The obtained information on circulation time was then used to explain the implications of the liquid flow patterns on the mixing process. The computational model and the predicted results discussed in this work will be useful for providing better understanding of flow characteristics and mixing process occurring in tall aerated stirred reactor operating in different gas flow regimes.

8.2 Computational Model

8.2.1 Model Equations

8.2.1.1 Two-fluid model

For simulating gas-liquid flow in a stirred reactor, a two-fluid model based on the Eulerian - Eulerian approach was used in this work. The governing equations for each phase in Eulerian-Eulerian approach and for the standard k-ε turbulence model are given in chapter 5 and therefore not repeated here.

In the Eulerian-Eulerian approach, the correct modelling of the interphase momentum exchange terms controls the predictive capability of the computational model. The interphase momentum exchange term consists of four different interphase forces: the Basset force, the virtual mass force, the lift force and the interphase drag force. In most cases, the magnitude of the Basset force is much smaller than that of the interphase drag force. In the bulk region of the reactor, the velocity gradients are not large. Near the impeller, pressure gradients and interphase drag forces mainly dominate the motion of the bubbles. An order of magnitude analysis indicates that the magnitude of the lift force is much smaller than the interphase drag force. The numerical studies reported in previous chapter (Chapter 5) indicate that the effect of the virtual mass force is not significant in the bulk region of the stirred reactor. Considering these results, only the

inter-phase drag force was retained in the inter-phase momentum exchange terms in the present study.

The inter-phase drag force exerted on phase 2 in the *i* direction is given by:

$$F_{q_i} = F_{D2i} = -\frac{3\alpha_1\alpha_2\rho_1 C_D\left(\sum\left(\vec{U}_{2i}-\vec{U}_{1i}\right)^2\right)^{0.5}\left(\vec{U}_{2i}-\vec{U}_{1i}\right)}{4d_b} \tag{8.1}$$

In gas-liquid stirred reactors the interphase drag coefficient, C_D, is a complex function of the drag coefficient in a stagnant liquid, the gas holdup and prevailing turbulence. The influence of the free stream turbulence on the bubble drag coefficient is numerically studied in the Chapter 5. Following this, we have used the following correlation (Equation 8.2) for the calculation of the drag coefficient in turbulent flow:

$$\frac{C_D - C_{D0}}{C_{D0}} = K\left(\frac{d_b}{\lambda}\right)^3$$
$$C_{D0} = \max\left\{\left(\frac{2.667 * Eo}{Eo + 4.0}\right), \left(\frac{24}{\mathrm{Re}_b} * \left(1 + 0.15 * \mathrm{Re}_b^{0.687}\right)\right)\right\} \tag{8.2}$$

where, λ is the Kolmogorov length scale, d_b is the bubble diameter and K is an empirical constant, which was set to 6.5×10^{-6}. Equation (8.2) thus accounts for the increased drag coefficient due to prevailing liquid phase turbulence.

The gas-liquid flow in the stirred reactor was simulated using the computational snapshot approach. In this approach, the impeller blades are considered as fixed at one particular position (similar to taking a snapshot of the rotating impeller) with respect to the baffles. The formulation of snapshot approach for the simulation of two-phase flow is discussed in Chapter 4 and therefore it is not repeated here. The flow is simulated for a specific blade position with respect to the baffles. The results obtained with a specific snapshot position were not found to be significantly different from the ensemble average of a number of snapshots (see Ranade and van den Akker, 1994 for more details). The computational snapshot approach was implemented in the commercial CFD code FLUENT 4.5 (of Fluent Inc., USA) using user-defined subroutines.

8.2.1.2 Lagrangian particle trajectory simulations

The previously obtained Eulerian flow field of the continuous phase was used to simulate the particle trajectories. The force balance on a particle was written as:

$$\frac{dU_p}{dt} = F_D\left(U - U_p\right) + g\left(\rho_p - \rho\right)/\rho_p + F \tag{8.3}$$

where, U and U_p are the fluid and particle velocities respectively, ρ is the fluid density, ρ_p is the density of the particle. The first term on right hand side is the drag force per unit particle mass and is given by

$$F_D = \frac{18\mu}{\rho_p d_p^2}\frac{C_D \mathrm{Re}}{24} \tag{8.4}$$

Here, μ is the molecular viscosity of the fluid and d_p is the diameter of the particle. The particle Reynolds number, Re, is defined as:

$$\mathrm{Re}_p = \frac{\rho d_p \left|U_p - U\right|}{\mu} \tag{8.5}$$

The drag coefficient, C_D, is calculated using particle Reynolds number as:

$$C_D = a_1 + a_2/\mathrm{Re}_p + a_3/\mathrm{Re}_p^{\,2} \tag{8.6}$$

where the a_i values are constants and that apply over several ranges of Reynolds number (see Morsi and Alexander, 1972). In the present work, the particle Reynolds number varies between 1 and 1000. The values of a_i for this Reynolds number range are:

$1 < \mathrm{Re}_p < 10$: $a_1 = 1.222$, $a_2 = 29.1667$ and $a_3 = -3.8889$

$10 < \mathrm{Re}_p < 1000$: $a_1 = 0.6167$, $a_2 = 46.5$ and $a_3 = -111.67$

The last term in the right hand side of Equation 8.3 denotes the additional forces such as virtual mass force and pressure gradient force per unit mass of particle. However, the virtual mass force is important when $\rho > \rho_p$. For neutrally buoyant tracer particle the influence of the virtual mass force is negligible and hence not considered in the present study. An additional force arises due to the pressure gradient in the fluid and is written as:

$$F_x = \left(\frac{\rho}{\rho_p}\right) U_p \frac{\partial U}{\partial x} \tag{8.7}$$

It should be noted that the fluid velocities appearing in Equation 8.3 are instantaneous fluid velocities. In the present work, the fluid turbulence was modeled using the standard k-ε model and therefore, the instantaneous fluid velocities were not available directly. Two models, discrete random walk (DRW) model (Gosman and Ioannides, 1981) and continuous random walk (CRW) model (Thomson, 1987), are available for modeling the influence of the fluid turbulence on the motion of the particle. In DRW model, the random value of the fluctuating velocity component is kept constant over an interval of time given by the characteristic lifetime of eddies. Whereas, in CRW model, the fluctuating velocity components are obtained by solution of Langevin equation and therefore, provide more realistic description of the turbulent eddies at the expense of increased computational effort. The numerical study of Rammohan *et al.* (2003) has shown that the selection of the turbulence model does not have any significant influence on the predicted particle trajectory and the Lagrangian information. Since the CRW model is computationally more demanding, DRW model was used in the present work.

In the DRW model, the interaction of a particle with a succession of discrete fluid phase turbulent eddies is simulated. Each eddy is assumed to be characterized by Gaussian distributed random velocity fluctuation and a characteristic lifetime of an eddy τ_e. Assuming a Gaussian distribution function; the mean velocity was obtained as:

$$U = \vec{U} + \varsigma\sqrt{u'^2} \tag{8.8}$$

where, ζ is a normally distributed random number and $\sqrt{u'^2}$ is the local rms value of the velocity fluctuations and is obtained from the turbulent kinetic energy.

The characteristic lifetime of an eddy, τ_e, was considered as a random variation about the Lagrangian eddy time scale, T_L and are calculated as:

$$T_L \approx 0.15\frac{k}{\varepsilon} \qquad \text{and} \qquad \tau_e = -T_L \log(r) \tag{8.9}$$

where r is a uniform random number between 0 and 1. The particle is assumed to interact with the fluid phase eddy over this eddy lifetime. When the eddy lifetime is reached, a new value of the instantaneous velocity is obtained by applying new value of ζ.

Once the particle velocities are obtained from the force balance (Equation 8.3), the particle trajectories may be obtained by integrating

$$\frac{dx}{dt} = U_p \tag{8.10}$$

The integration was carried out using the Euler's method (see Fluent 4.4 User guide for more details).

8.2.2 Solution domain

In the present work, the experimental set-up used by Shewale and Pandit (2005) was considered. All the relevant dimensions like the impeller diameter, the reactor shape and diameter and so on were the same as the one used by Shewale and Pandit (2005). The system investigated consists of a stirred cylindrical reactor, with a flat bottom (diameter, T= 0.3 m, height, H= 0.9 m) with four baffles (width= T/10 = 0.03 m) equally spaced around the reactor periphery. The shaft (diameter d_s= 0.03 m) of the impeller was concentric with the reactor axis and extended till the bottom impeller. Three down- pumping pitched blade turbines, of diameter D = 0.1 m, were used for all simulations. The impeller off-bottom clearance for the bottom most impeller was (C1 = 0.15 m, measured from the mid-plane of impeller). The other two impellers were

separated with each other with an axial distance of 0.3 m from each other (C2 = C3= 0.3 m). The gas was sparged using ring sparger of having diameter, d_{sp}= 0.1 m and was located at 0.075 m from the bottom of reactor.

Considering the geometrical symmetry, half of the reactor was considered as a solution domain (see Figure 8.1). The baffles were considered at angles of 45^o and 135^o. The impeller was positioned in such a way that three blades were located at angles of 30^o, 90^o and 150^o (measured from center line of impeller blade). As discussed in Chapter 4, the computational snapshot approach divides the solution domain into an inner region, in which time derivative terms are approximated using spatial derivatives and an outer region, in which time derivative terms are neglected. The boundary between the inner and outer regions needs to be selected in such a way that the predicted results are not sensitive to its actual location. In the present work, for all the simulations, the boundary of the inner region was positioned at r = 0.088 m and 0.095 m ≤ z ≤ 0.82 m (where *z* is the axial distance from the bottom of the reactor).

In the present work, the sparger was modeled as a solid wall. The mass and momentum source of the gas phase was specified one cell above the sparger to simulate gas introduction into the reactor. Special boundary conditions are needed to simulate gas-liquid interface at the top through which bubbles escape the solution domain. Recently, Ranade (2002) has discussed different possible approaches to treat gas-liquid interface in detail. We have modeled the top surface of the dispersion as a velocity inlet. The outgoing (axial) velocity of gas bubbles was set equal to the terminal rise velocity of gas bubbles (estimated as 0.2 m/s for air bubbles). All the other velocity components for gas and liquid phase were set to zero). Implicit assumption here is that gas bubbles escape the dispersion with terminal rise velocity. Since the liquid velocity near the top gas-liquid interface is small and the overall volume fraction of gas is also small (< 10%), this assumption is reasonable. It should be noted that even after defining top surface as an inlet, gas volume fraction at the top surface is a free variable. The mass and momentum conservation equations for the gas phase were solved using FLUENT 4.5 (of Fluent Inc., USA) and the gas distribution within the reactor was predicted. The

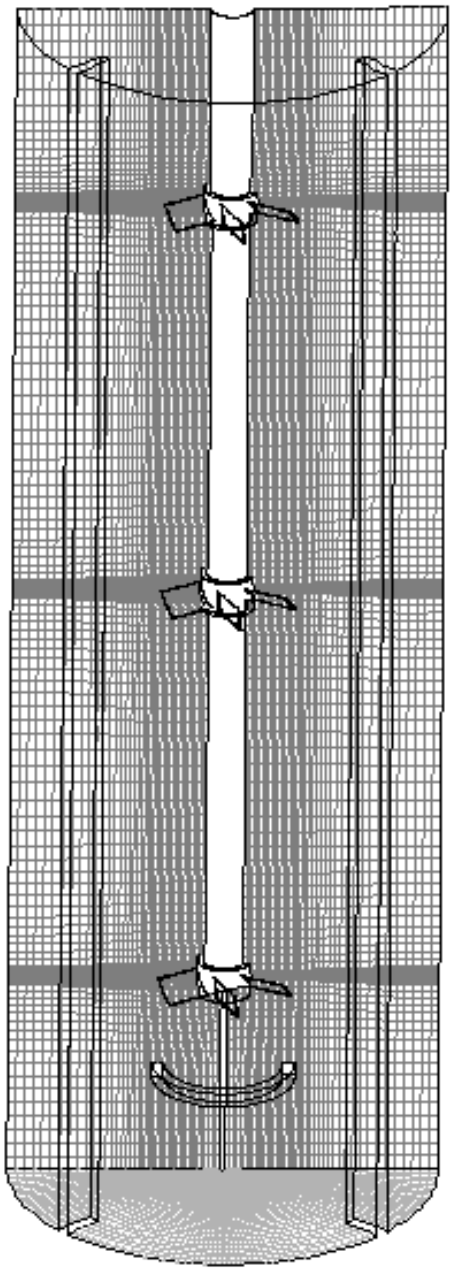

Grid Details	:
$r \times \theta \times z$	: $47 \times 94 \times 136$
Impeller blade	: $15 \times 2 \times 12$
Inner region	: $11 \leq k \leq 129$ $j \leq 36$

Figure 8.1: Computational Grid and Solution Domain

mass conservation was verified by comparing the integral gas mass flow rate across various horizontal planes with the input gas mass flow rate at the sparger.

In a gas-liquid stirred reactor, there is a wide distribution of bubble sizes. The prevailing bubble size distribution in a gas-liquid stirred reactor is controlled by several parameters like reactor configuration, impeller speed and gas flow rate. It is possible to develop a detailed multi-fluid computational model using population balance framework to account for bubble size distribution. However, the use of multi-fluid models based on the population balances increase the computational demands by manifolds. Unfortunately available experimental data of bubble size distribution in stirred reactor is not adequate to calculate the parameters appearing in the coalescence and break-up kernels. Considering these issues, in the present work, a single bubble size was specified (4 mm) over whole reactor domain for all the simulations. Fluid properties were set to those of water and air for the primary and secondary phases, respectively.

A commercial grid-generation tool, GAMBIT 2.0 (of Fluent Inc., USA) was used to model the geometry and to generate the body-fitted grids. It is very important to use an adequate number of computational cells while numerically solving the governing equations over the solution domain. The prediction of turbulence quantities is especially sensitive to the number of grid nodes and grid distribution within the solution domain. The previous work of Ranade *et al.* (2001a) as well as other published work (Ng *et al.*, 1998 and Wechsler *et al.*, 1999) gives adequate information on the influence of the grid on the predicted results. It was demonstrated that, in order to capture the details of the flow near impeller, it is necessary to use at least 200 grid nodes to resolve the blade surface. Based on the previous experience, the numerical simulations for the gas-liquid flows in stirred reactors were carried out for grid size of ($r \times \theta \times z$: $47 \times 94 \times 136$). In the present work, we have used ($r \times \theta \times z$: $15 \times 2 \times 12$) grid nodes to resolve the blade surface. The boundary of the inner region was positioned at $j \leq 36$ and $11 \leq k \leq 129$ (where j is the cell number in the radial direction from the shaft and k is the cell number in the axial direction from the bottom of the reactor). The computational grid used in the present work is shown in Figure 8.1.

Differencing of the advection terms has been carried out using the QUICK discretization scheme with the SUPERBEE limiter function (to avoid non-physical oscillations). Standard wall functions were used to specify wall boundary conditions. Different criteria like the reduction of the residuals, gas mass flow rate through various horizontal planes and variation of overall gas hold-up and energy dissipation rates were used to ensure adequate convergence. The validation of computational results with the reported experimental data is discussed in the following section.

8.3 Results and Discussion

8.3.1 Bulk flow characteristics

The gas-liquid flows generated by three down- pumping pitched blade turbines in a stirred reactor were simulated for a single volumetric gas flow rate (Q_g) of 1.06×10^{-3} m^3/s and for three impeller rotational speeds (N) equal to 100, 145 and 390 rpm respectively, corresponding to Fl= 0.638 & Fr= 0.028; Fl= 0.438 & Fr= 0.0597 and Fl= 0.163 & Fr= 0.430 respectively. Under these operating conditions, the fluid dynamics in the reactor represents, DFF, DDF and DDL flow regimes respectively (Shewale and Pandit, 2005). Where D represents for fully dispersed condition, L represents for loading condition and F represents for flooding condition. The DFF flow regime corresponds to upper impeller is in dispersed condition and middle and bottom impellers are in flooded condition. The other two flow regimes can also be explained using the same terminology.

The predicted liquid phase velocity vectors for all the three operating conditions are shown in Figure 8.2. It can be seen from Figure 8.2 that the computational model captured the significantly different flow fields for all the three conditions. For DFF (Fl= 0.638 & Fr= 0.028) flow regime, the predicted velocity field shows the presence of two- loop structure. It can be seen that the bottom loop present in the reactor was formed due to the upward rising sparged gas. This upward moving liquid circulation pattern was present till the middle impeller. However, the upper impeller generates a well known downward moving single circulation loop. Both these circulation loops interact with each other at middle impeller plane.

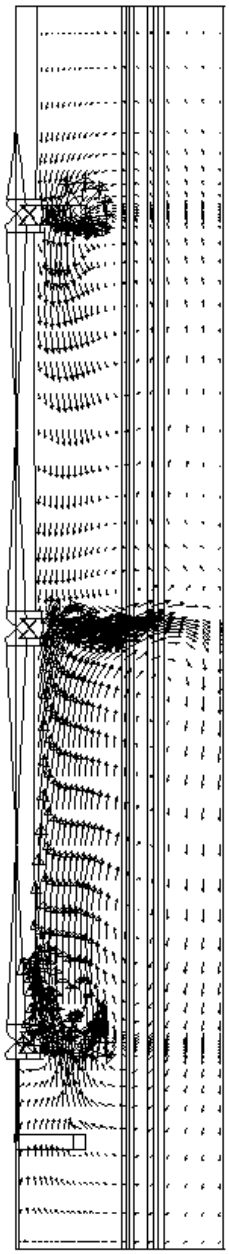

(a) DFF flow regime
(Fl = 0.678 & Fr = 0.028)

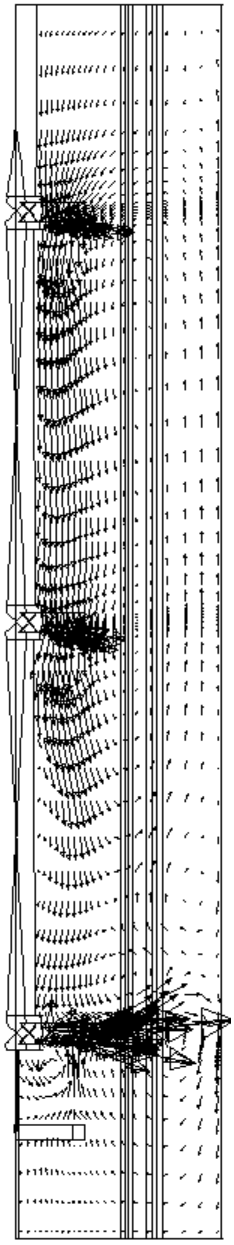

(b) DDF flow regime
(Fl = 0.438 & Fr = 0.0597)

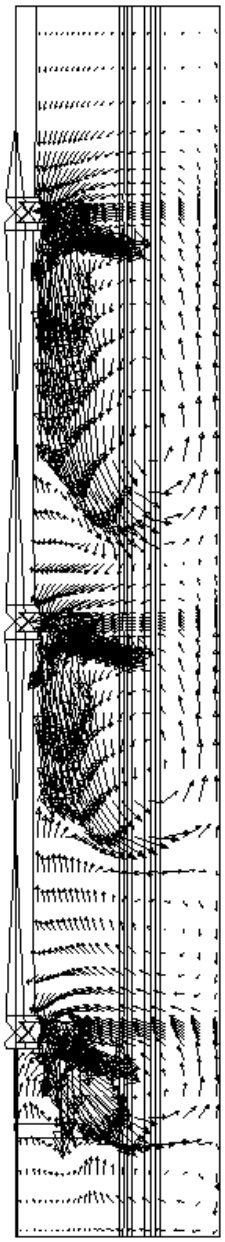

(c) DDL flow regime
(Fl = 0.163 & Fr = 0.430)

Figure 8.2: Predicted Mean Liquid Velocity Field at Mid-Baffle Plane for DFF, DDF and DDL Flow Regimes

The predicted liquid phase velocity field for DDF flow regime (Fl= 0.438 & Fr= 0.0597) is shown in Figure 8.2b. It can be seen from Figure 8.2b that the computational model have predicted the two-loop structure for DDF flow regime. However, the predicted two-loop structure for DDF flow regime was significantly different than the two-loop structure predicted for DFF flow regime. The predicted flow pattern shows the presence of a small circulation loop at the bottom of the reactor. This circulation loop was found to be generated due to the dominance of upward rising gas in the region below the bottom impeller and was present till the bottom impeller plane. Whereas, the flow generated by middle and upper impellers was found to interact with each other and form a single circulation loop. Along with these two primary circulation loops, the computational model has also captured a secondary circulation loop, present between the both circulation loops. Similarly, the predicted liquid phase velocity field for DDL flow regime (Fl= 0.163 & Fr= 0.430) is shown in Figure 8.2c. It can be seen that the computational model have predicted three separate circulation loops for each impeller. The predicted velocity field for DDL condition also captured two secondary circulation loops, one at the bottom of the reactor and another between the lower and middle impeller circulation loops. The complex interaction between the impeller- generated flow and gas- generated flow was responsible for the formation of these two secondary circulation loops in the reactor.

The gas hold-up distribution in the reactor is strongly affected by the gas and liquid properties, prevailing flow regime and reactor internals. In the present study, we have used the computational model to study the gas hold-up distribution in DFF, DDF and DDL flow regimes. The qualitative comparison of predicted gas hold-up distributions for all the three operating conditions [Fl= 0.638 & Fr= 0.028 (DFF); Fl= 0.438 & Fr= 0.0597 (DDF) and Fl= 0.163 & Fr= 0.430 (DDL)] with experimental snapshots is shown in Figure 8.3. It can be seen from Figure 8.3a that similar to experimental condition, the simulation has captured the inefficient dispersion of gas at bottom and middle impeller and dispersed condition of gas at upper impeller for DFF flow regime. The predicted contour plot clearly shows the upward and inward movement of the sparged gas while rising through the reactor till middle impeller. The contour plot shows that there is no effect of rotation of bottom impeller on the upward rising gas. This upward rising gas generates a single circulation loop in the bottom part of the

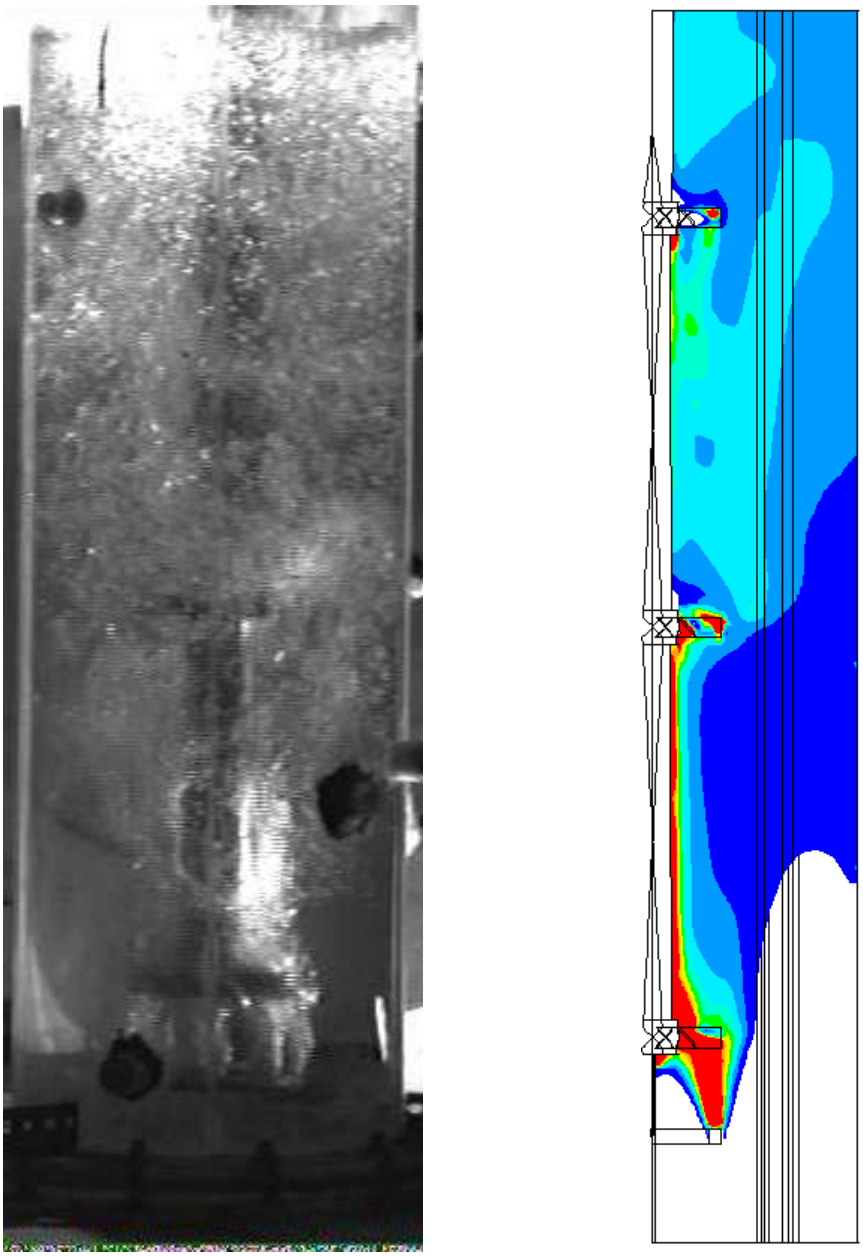

(i) Experimental snapshot (ii) Predicted gas holdup distribution

(10 uniform contours; minimum gas volume fraction, blue = 0.015 and maximum gas volume fraction, red ≥ 0.15)

(a) DFF flow regime, (Fl = 0.678 & Fr = 0.028)

Figure 8.3: Qualitative Comparison of Experimental Snapshot and Predicted Gas Holdup Distribution at Mid-Baffle Plane for DFF, DDF and DDL Flow Regimes

[continue on next page]

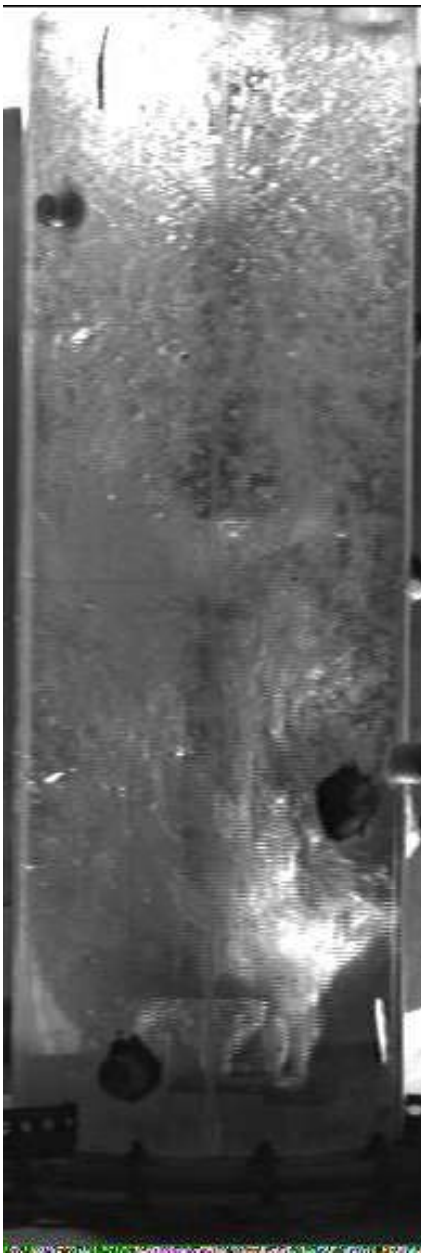

(i) Experimental snapshot

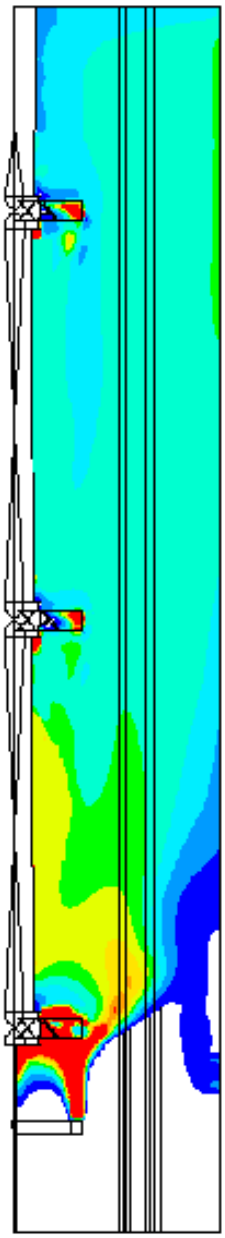

(ii) Predicted gas holdup distribution

(10 uniform contours; minimum gas volume fraction, blue = 0.015 and maximum gas volume fraction, red ≥ 0.15)

(b) DDF flow regime, (Fl = 0.438 & Fr = 0.0597)

Figure 8.3: Qualitative Comparison of Experimental Snapshot and Predicted Gas Holdup Distribution at Mid-Baffle Plane for DFF, DDF and DDL Flow Regimes

[continue on next page]

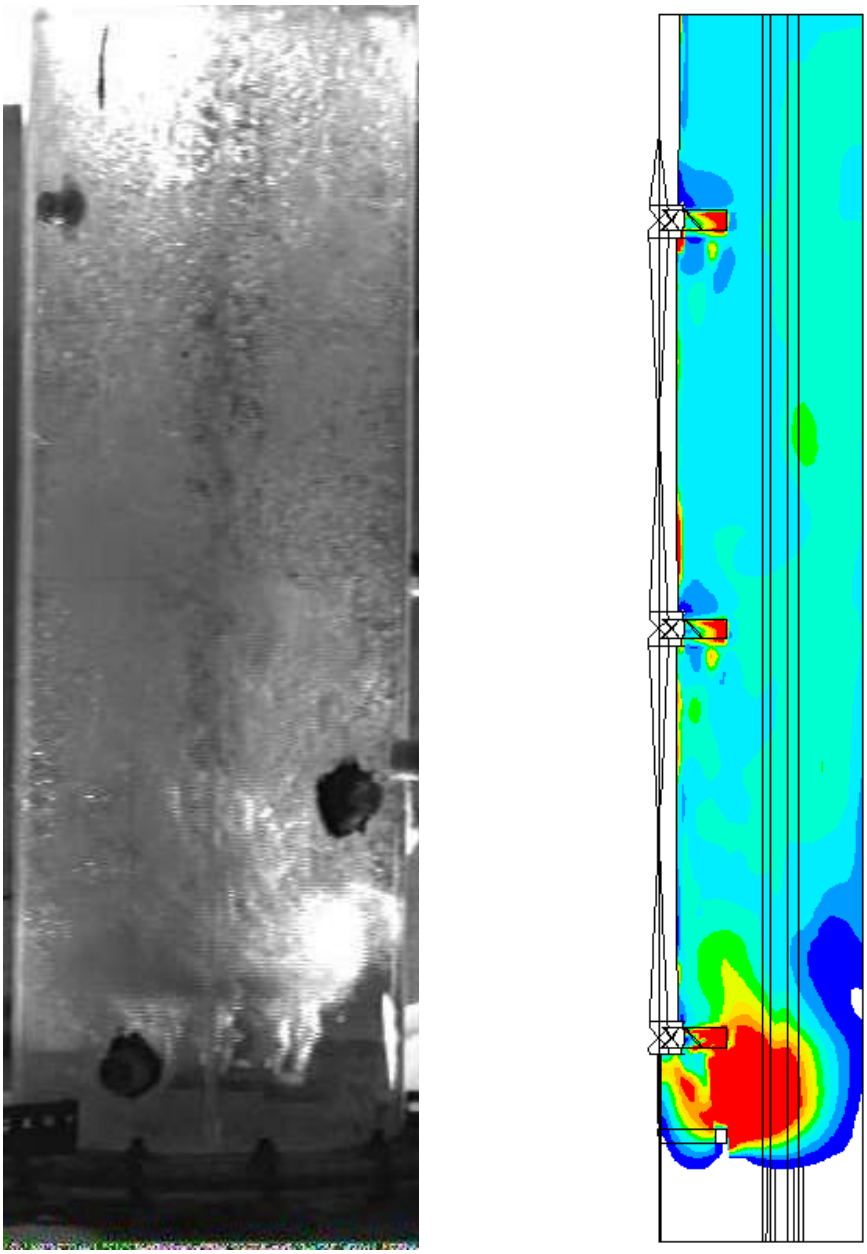

(i) Experimental snapshot (ii) Predicted gas holdup distribution

(10 uniform contours; minimum gas volume fraction, blue = 0.015 and maximum gas volume fraction, red ≥ 0.15)

(c) DDL flow regime, (Fl = 0.678 & Fr = 0.028)

Figure 8.3: Qualitative Comparison of Experimental Snapshot and Predicted Gas Holdup Distribution at Mid-Baffle Plane for DFF, DDF and DDL Flow Regimes

reactor and which was found to be present till middle impeller. The upward rising gas then gets dispersed in the circulation loop generated by an upper impeller.

The qualitative comparison of experimental snapshot of gas-liquid flow and predicted contour plot for the simulated gas hold-up distribution for DDF flow regime is shown in Figure 8.3b. It can be seen from Figure 8.3b that the simulation has captured the inefficient dispersion of gas by the bottom impeller and the complete dispersed conditions by the middle as well as upper impeller as observed in experiments. The impeller motion of the bottom impeller for DDF flow regime was found to be not sufficient to disperse the gas in the lower impeller region. Similarly, the simulated gas hold-up distribution for DDL flow regime and experimental snapshot of gas-liquid flow is shown in Figure 8.3c. It can be seen that for DDL flow regime, the predicted gas hold-up distribution shows the fully dispersed condition for upper and middle impeller and loading condition for the bottom impeller.

Predicted influence of gas flow rate on gross characteristics like power number and total gas hold up are also of interest. Power number was calculated from simulated results as:

$$N_p = \frac{2\int_V \alpha_l \rho_l \varepsilon dV}{\rho_l N^3 D_i^{\,5}} \tag{8.18}$$

where D_i is the impeller diameter and N is the impeller speed. The predicted as well as experimentally measured values of power number and total gas hold-up values are listed in Table 8.1. It can be seen that the computational model over-predicted the values of impeller power number and total gas hold-up.

Overall, it can be said that the computational model has simulated the three different flow regimes prevailing in a tall stirred reactor equipped with three down- pumping pitched blade turbines. The computational model has also captured the influence of the operating conditions/ flow regimes on the flow pattern developed in the reactor. Such significant change in the liquid flow pattern may result into different rates of transport and mixing process. Shewale and Pandit (2005) have observed different trends in the

Table 8.1: Gross Characteristics of a Tall Gas-Liquid Stirred Reactor (Experimental data from Shewale and Pandit, 2005)

Flow regime	Total gas holdup (%)		Power number, N_{Pg}		Average circulation time, t_c (predicted)	Mixing time, t_m (Experimental)	Percentage change	
	Predicted	Experimental	Predicted	Experimental			$t_c/t_{c,\,min}$	$t_m/t_{m,\,min}$
DFF (Fl = 0.6328 & Fr = 0.028)	2.99	2.47	2.64	2.2	13.851	59	1.493	1.553
DDF (Fl = 0.438 & Fr = 0.0597)	3.43	2.79	2.98	2.55	9.277	38	1	1
DDL (Fl = 0.163 & Fr = 0.430)	5.58	3.65	4.05	3.45	11.234	45	1.211	1.184

mixing time variation with change in the flow regime. The particle trajectory simulations, using Lagrangian approach were carried out to understand the influence of these flow patterns on the circulation time distribution.

8.3.2 Mixing in gas-liquid stirred reactor

Mixing time and circulation time are the two criteria used to characterize the liquid phase mixing in stirred reactors. Mixing time is the time required to achieve a certain degree of homogeneity (Ranade *et al.*, 1991). Whereas circulation time is the time necessary for a fluid element to complete a one circulation within the vessel (time difference between an event of fluid element exiting from the impeller swept volume and an event of its re-entry into impeller swept volume). The link between these two parameters is clear: lower the circulation time for particles to circulate in the reactor, the more efficient is the mixing. In common practice, mixing time is usually taken as some multiple of average circulation time (Joshi, Pandit and Sharma, 1982). In the present study, we have used the circulation time criteria to investigate the prevailing mixing process.

Recently, Khopkar *et al.* (2005) used the Eulerian gas-liquid flow field calculated using quasi-steady state approach, such as snapshot approach, for the calculation of circulation time distribution in a gas-liquid stirred reactor operating in two different gas flow regimes. They have compared the simulated circulation time distribution (based on 1000 circulations) with the CARPT measurements (more than 12,000 circulations). They found reasonably good agreement between the simulated results and the experimental data. The numerical approach presented by Khopkar *et al.* (2005) was used in the present study for the calculation of circulation time distribution.

Using the Eulerian flow field obtained as discussed in previous subsection, the particle trajectories were simulated. The particle trajectory simulations were carried out for three operating conditions [Fl = 0.638 & Fr = 0.028 (DFF)], [Fl = 0.438 & Fr = 0.0597 (DDF)] and [Fl = 0.163 & Fr = 0.43 (DDL)]. The size of neutrally buoyant particle may influence the predicted circulation time distribution. Rammohan *et al.* (2003) numerically studied the influence of particle size on the predicted values of the turbulent kinetic energy. They found that a neutrally buoyant particle of having size

0.25 mm adequately respond to the liquid phase turbulence. They observed that the ratio of estimated turbulent kinetic energy and to actual kinetic energy was found to be one for particle of having size ≤ 0.25 mm. Therefore in present study, a single neutrally buoyant particle (density equals with water) of diameter 0.25 mm was released in liquid for particle trajectory calculation. The particle was released in liquid at 10 different positions in the solution domain. These 10 particle release locations were selected randomly. The motion of particle in liquid phase was simulated using the Lagrangian framework. The simulated particle trajectories were used to calculate the circulation time distribution.

Before discussing the predicted results, it is essential to first identify the minimum number of circulations required to adequately represent the circulation time distribution in a gas-liquid stirred reactor. The particle trajectory simulations for DDF flow regime were therefore carried out to check the influence of the number circulations on the average circulation time. The predicted influence of the number of circulations on the average circulation time is shown in Figure 8.4. It can be seen from Figure 8.4 that minimum of 100 circulations were essential to reasonably predict the average circulation time. Above 100 circulations, the average circulation time varies only about ± 2% about the average circulation time calculated from 250 circulations. Therefore, in the present study 250 circulations of neutrally buoyant particles were thought to be adequate to explain the circulation time distribution in all the three flow regimes.

The simulated circulation time distributions for all the three operating conditions are shown in Figure 8.5. The simulated circulation time distribution was calculated based on 250 circulations of particle. It can be seen from Figure 8.5 that for DFF flow regime the simulated circulation time distribution show the presence of 82% of the total circulations with having circulation time lies between 4 s to 16 s. It looks that these 82% of circulations were from the particle following the lower circulation loop. The simulated distribution shows the presence of remaining 18% circulations having circulation time higher than 16 s. These circulations were because of the particle following the upper circulation loop and may lead to slower mixing in the reactor. Incidentally for the DFF flow regime almost no circulations (less than 1%) with having circulation time less than 4 s were found in the simulated circulation time distribution.

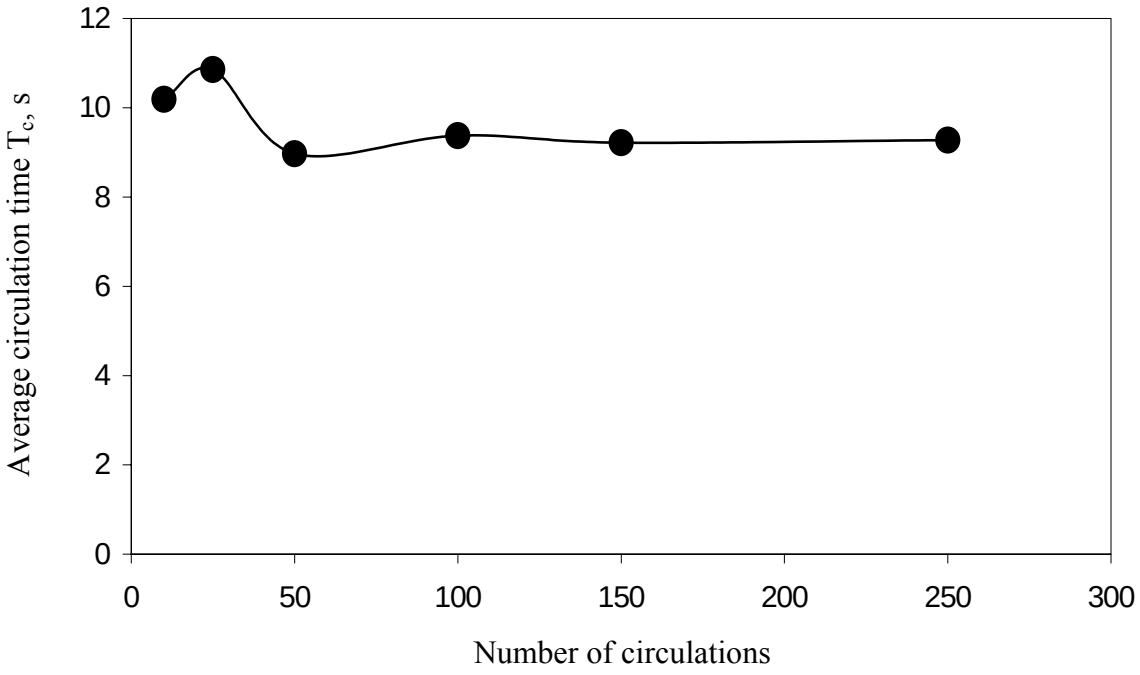

Figure 8.4: Influence of Number of Circulations on Average Circulation Time for DDF Flow Regime

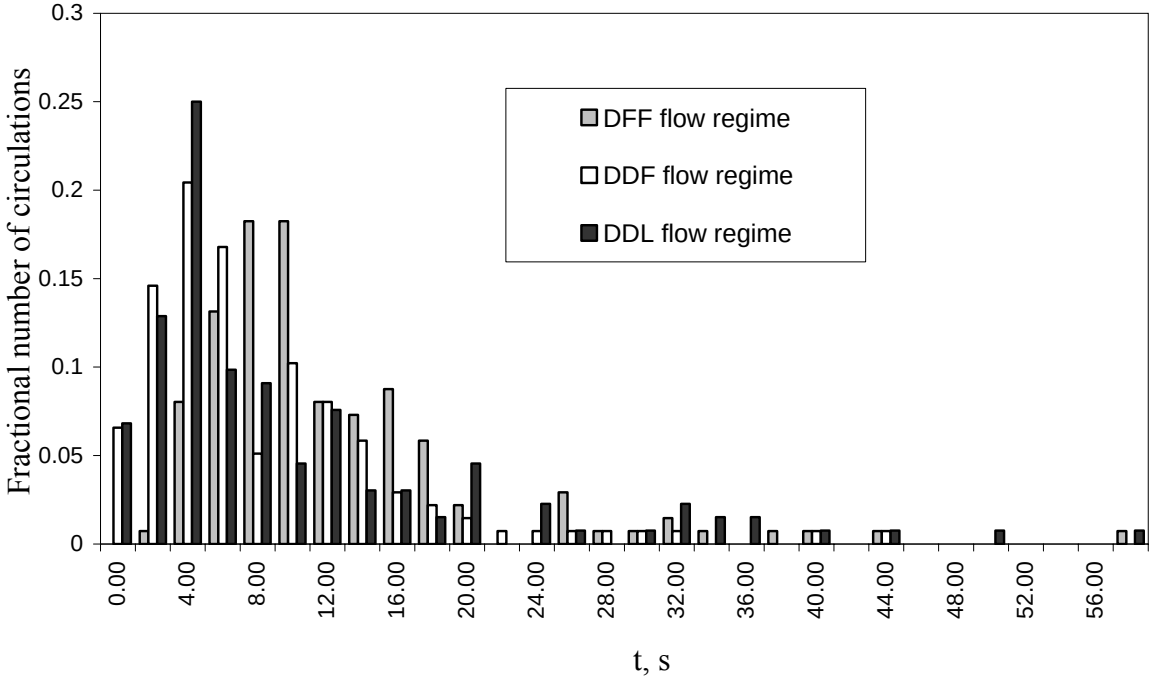

Figure 8.5: Predicted Circulation Time Distribution for DFF, DDF and DDL Flow Regimes

The simulated circulation time distribution for DDF flow regime is shown in Figure 8.5. It can be seen from Figure 8.5 that for DDF flow regime, almost 88% of the circulations with having circulation time less than 14 s were present in the simulated distribution. Out of these 88% circulations, almost 60% (in all 250 circulations) were found to have the circulation time less than 6 s. It looks like that these circulations were for the lower circulation loop, which ensures the faster mixing in the lower circulation loop region. The simulated circulation time distribution for DDF flow regime also show the presence of only 5% circulations with having circulation time more than 22 s. Therefore, it can be said that the fluid dynamics in DDF flow regime ensures a faster mixing in the reactor compare to the DFF flow regime. Similarly, the simulated circulation time distribution for DDL flow regime is shown in Figure 8.5. It can be seen from Figure 8.5 that similar to DDF flow regime 63% of the total circulation were found to have circulation time less than 8 s. These circulations were from the particle following the lower circulation loop. However, for DDL flow regime the simulated circulation time distribution shows the presence of 9% circulations with having circulation time more than 30 s. These circulations were because of the particle following the upper circulation loop and may lead to slower mixing in the reactor.

The predicted values of average circulation time and the experimental data are listed in Table 8.1. Whereas, Figure 8.6 shows the variation in the mixing time with changing flow regimes as reported by Shewale and Pandit (2005) and the time required for a fixed number of circulations as per the simulations in this work. It can be seen from Table 8.1 and Figure 8.6 that the predicted values of average circulation time has captured the trends similar to that observed in the experimental study of Shewale and Pandit (2005). The comparison of the increase in predicted average circulation time with respect to predicted minimum average circulation time (for DDF flow regime) was in excellent agreement with the observed rise in the mixing time as reported in the experimental data. Overall, it can be said that the circulation time distribution obtained using quasi steady state approach, such as snapshot approach, can indeed explain the implication of the local flow patterns on the mixing process.

The developed computational model not only captured the essential features of the gas-liquid flows operating in different flow regimes but also predicted the implication of

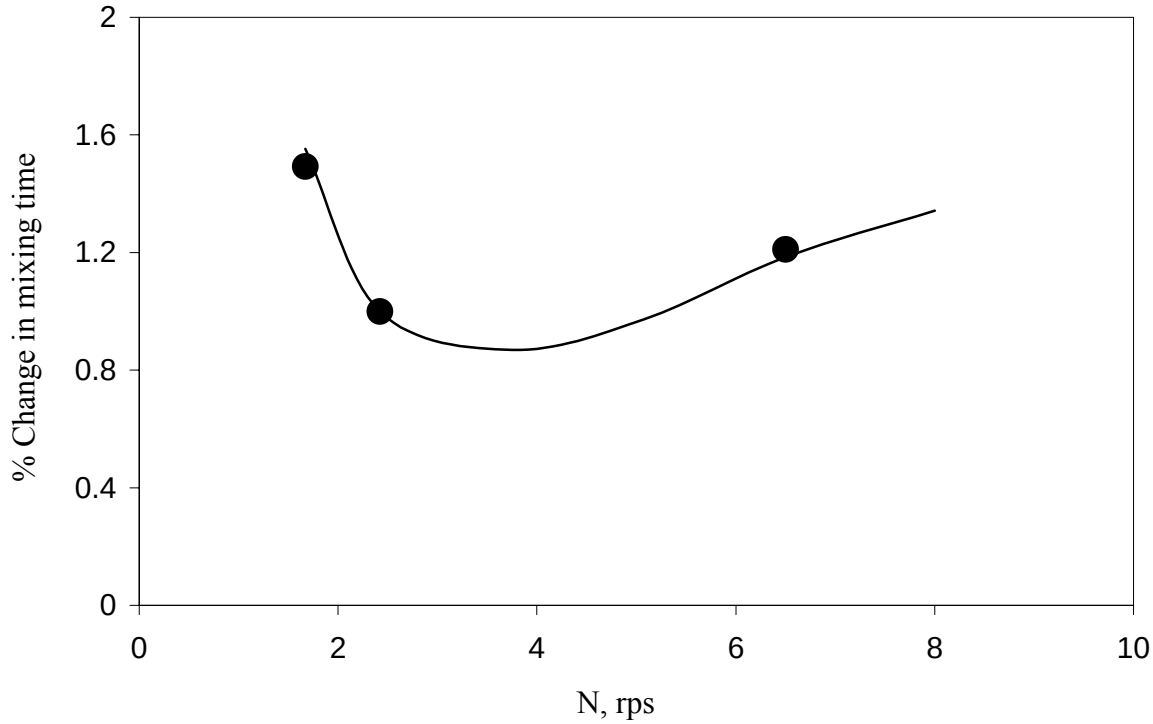

Legends: Experimental data (Shewale and Pandit, 2005)
Predicted results

Figure 8.6: Comparison of the Predicted Percentage Change in Mixing Time with Experimental data

the local flow patterns on the overall mixing process with reasonable accuracy. Such validated models will be useful to understand the implication of reactor hardware and scale of operation on the performance. The relative interaction between gas bubbles and impeller blades and mean liquid circulation time change dramatically with changes in the reactor hardware as well as reactor size. The computational model allows one to monitor these changes and allow prediction of their influence on the key transport processes. The model and the results presented here would provide useful basis to allow the extension of computational models to simulate industrial gas-liquid stirred reactors.

8.4 Summary and Conclusions

In this work, two-fluid model with the standard k-ε turbulence model was used to simulate the turbulent gas-liquid flows generated by the three down- pumping pitched blade turbine mounted on the same shaft for three operating conditions representing three distinct flow regimes. The computational model qualitatively captured the overall flow field generated by three down- pumping pitched blade turbines, including the liquid circulation loops and the dispersion quality of gas in reactor for all the three flow regimes. It was also found to simulate the variation in the power dissipation by impellers in the presence of the gas and the total gas hold-up reasonably well. The computational model was then used to study the circulation time distribution in the reactor. The predicted circulation time distribution was found to capture the influence of prevailing flow regimes on the mixing process. The predicted percentage change in the circulation time with prevailing flow regimes (DFF, DDF and DDL) showed good agreement with the experimental data.

The computational model shows promising results and seems to be able to predict the gas-liquid flow for any flow regime. The model and results presented in this work would be useful for extending the application of CFD based models for simulating large multiphase stirred reactors.

Chapter 9

CONCLUSIONS

"Don't measure yourself by what you have accomplished, but by what you should have accomplished with your ability".

John Wooden

The work presented in this thesis was carried out with an objective of developing experimental as well as computational tools for characterization of gas-liquid flows in stirred reactors. Experimental measurements were carried out to develop a non-intrusive tool for the identification of prevailing flow regimes and to extract the key time scales of aerated reactor. CFD models based on the Eulerian-Eulerian approach were developed to simulate the gas-liquid flows in stirred reactors operating in different flow regimes. The developed models were validated using available experimental data in the literature and also provided by our collaborators. The validated models were further used to study the flow around impeller blades, identify the similarities and differences between the flow generated by different types of impellers and address some of the reactor engineering issues.

In the first part of the thesis, wall pressure and torque fluctuation measurements were carried out to identify the prevailing flow regimes in the reactor. The gas-liquid flows generated by three different impellers were considered. Besides the identification of the prevailing flow regimes, the extraction of pumping efficiency information of impeller under aerated condition from the measured wall pressure fluctuations is also discussed. The key conclusions based on the first part of the thesis are listed in the following:

- The average values of the power consumption and the RMS values of the torque fluctuations clearly identified the flow regime transition for down- pumping pitched blade turbine. However for radial flow impellers, the accurate identification of regime transition using torque fluctuations was not possible.

- The power spectrum and the P statistics of the wall pressure fluctuations clearly identified the flow regimes prevailing in the reactor for all the three impellers (Rushton turbine, down- pumping pitched blade turbine and Smith turbine). Besides identification of the prevailing flow regime, the power spectrum of the pressure fluctuations can provide the information about cavity structure present behind the impeller blades and explain the interaction between the rotating impeller blades and stationary baffles.

- The P statistics of the wall pressure fluctuations can be used for the quantitative estimation of the drop in the pumping efficiency for the aerated conditions and

the relative contributions of gas-driven and impeller-driven liquid flows to the overall fluid dynamics in the stirred reactor.

In the second part of the thesis, the Eulerian-Eulerian simulations carried out to predict the pattern of gas holdup distribution for gas-liquid stirred reactors operating in different flow regimes are discussed. For understanding the possible influence of free stream turbulence and the presence of neighboring bubbles on the bubble drag coefficient, a two-dimensional sub-model was developed. The model predictions were used to evaluate and modify the available drag coefficient formulations. The modified bubble drag coefficient formulation was then incorporated in the CFD model and then successfully used to simulate the gas-liquid flows generated by different radial as well as axial flow impellers. The developed model was further used to understand the influence of the impeller blade shape and the impeller pumping direction on the fluid dynamics. The key conclusions based on the second part of the thesis are listed as following:

- An influence of turbulence on the bubble drag coefficient can be estimated by the correlation of Bakker and van den Akker (1994) and by the correlation of Brucato *et al.* (1998), with modified ($K= 6.5 \times 10^{-06}$) constant. For both of these correlations, volume averaged properties need to be used (turbulent viscosity in the first case and turbulent energy dissipation rate in the second case).

- The gas hold-up distribution in stirred reactors, predicted with the modified Brucato *et al.* (1998) correlation showed better agreement with the experimental data than other alternatives considered in this work.

- If the influence of turbulence on drag coefficient is appropriately accounted, the two-fluid model can reasonably simulate gas hold-up distribution for different flow regimes. However, the computational model based on the modified Brucato correlation over predicted the liquid velocities, turbulent kinetic energy near the impeller blades and total gas hold up values.

- The computational model was able to predict the influence of gas flow rate/ flow regimes on the gross impeller characteristics like pumping number and power number at least qualitatively.

- The model and the simulations were useful to shed some light on the complex flow characteristics near impeller blades. The model was able to capture the accumulation of gas behind the impeller blades and the influence of impeller blade shape and the pumping direction on the gas-liquid flows generated by different impellers.

- The model can be useful to provide the better understanding of the implication of the scale of operation with the performance of impeller/reactor for aerated operations.

In the third part of the thesis, the validated models were used to address the influence of the reactor hardware and the local flow patterns on the liquid phase mixing. The key conclusions based on the third part of the thesis are listed in the following.

- The quasi-steady state approach like multiple reference frame approach with multiple snapshots can simulate the flow in a continuous flow stirred reactor with reasonable accuracy and this approach is computationally very efficient.

- The mixing simulation with one snapshot is sufficient for 'a priory' prediction of the influence of the reactor hardware (inlet and outlet locations) on the performance of a continuous flow stirred reactor. However, fully transient simulation using sliding grid approach is essential for the correct simulation of the mixing process in continuously operated stirred reactor.

- The quasi-steady state approach, such as snapshot approach, reasonably predicted the circulation time distribution of liquid flow.

- The predicted circulation time distribution captured the implications of flow regimes on the overall mixing process.

RECOMMENDATIONS FOR FUTURE WORK

The simulations based on two-fluid model presented in this thesis have adequately predicted the gas-liquid flows in stirred reactor. However, these simulations lead to several open problems, which could form topics for further investigations. Some of these are listed below:

- The present study and the previously reported studies (see for example, Lane *et al.*, 2000 and 2005) have highlighted the importance of correct modelling of interphase forces. In the present study, the influence of interphase drag force and virtual mass force was studied. The predicted results show a small influence of the virtual mass on the predicted pattern of gas holdup distribution. However, the drag coefficient formulation significantly controls the prediction of gas holdup distribution. In the present study, a separate sub-model was developed to understand the influence of free stream turbulence and neighboring gas bubbles on the bubble drag coefficient. Although, the modified correlation predicted the gas-liquid flows reasonably, the validation of sub-model is necessary. However, no such experimental data is available in literature due to difficulties in experimentation. Well-designed experiments need to be undertaken for the estimation of bubble drag coefficient in turbulent flow. Similarly, the influence of lift force on the predicted gas holdup distribution need to be studied.

- In the present study, single bubble size (equal to average bubble diameter) for whole reactor, was used while simulating the gas-liquid flows. The correct prediction of the slip velocity not only depends on the interphase drag force but also on the bubble size. It is possible to develop the multi-fluid computational model for stirred reactors, capable of predicting the bubble size distribution over whole reactor. Unfortunately the available experimental data of bubble size distribution in stirred reactor is not adequate to calculate the parameters appearing in coalescence and break-up kernels of such models. Therefore, more experimental data on bubble size distribution is needed to validate the multi-fluid models.

- In gas-liquid stirred reactor, the gas bubbles shear away from the tip of the gas cavities present behind the impeller blades. The size of the bubbles emanating from the cavity tip is controlled by the size of the cavity, breakage of cavity and the turbulence level around the cavity. Unfortunately no direct experimental data for turbulent kinetic energy dissipation rate is available for validating the available cavity breakage models. In principal, simulation with volume of fluid (VOF) approach can simulate the formation of cavity and their shearing at the tip. More fundamental (experiments as well as numerical) studies are needed to develop and validate such models. The combination of VOF simulation and multi-fluid model may lead to more accurate simulation of bubble size distribution in stirred reactor.

- The simulated results in the present study show the over-predictions of the liquid phase velocity and turbulent kinetic energy in impeller discharge stream. This is probably due to in-accurate modelling of flow near impeller blades. In actual case, a gas pocket is present behind the impeller blades. In the present study, no attempt was made to model the formation of gas pocket behind the impeller blades. By modelling the formation of gas cavity behind the impeller blades may improve the predictions around the impeller blades. As said in previous point, simulations based on VOF approach can be used to understand the influence of the size of the gas pocket behind impeller blades on the impeller efficiency.

- In the present thesis, all the simulations were carried out on the laboratory and pilot scale reactors. The conclusions drawn on the impeller performance are therefore valid for the laboratory and pilot scale reactors. However, for large or industrial scale reactor, the ratio of characteristic length scales of impeller blades and the gas bubble are strikingly different as compared to small reactor. Therefore, the interaction of gas bubbles with the trailing vortices and the structure of the cavities might be significantly different for industrial scale as compared to small reactor. Though some indirect evidence of this is available, but no systematic study of influence of the scale on relative performance of the Scaba turbine is available. Therefore, there is a clear need to understand the influence of the scale, on the relative performance of the Scaba turbine. CFD

based model can be used to understand the influence of the scale of the operation on the impeller performance.

- In multiple-impeller system, different flow patterns prevail in reactor depending upon the reactor hardware and operating conditions. The change in fluid dynamics may result into the change in the rates of the transport and mixing processes occurring in the reactor. To obtain optimum performance of multiple-impeller system, the design guidelines for selection of better reactor hardware and operating conditions are essential. The detail experiments of hydrodynamic parameters are therefore needed.

NOTATIONS

Roman symbols

A_f : flow area, m^2

B : impeller blade height, m

C : impeller off-bottom clearance, m

C_1, C_2 : model parameters (Equation 5.5)

C_D : drag coefficient

C_{D0} : drag coefficient in stagnant water

C_{VM} : virtual mass coefficient

C_ω : model parameter (Equation 5.6)

D_{12} : turbulent diffusivity, m^2/s

d_b : bubble diameter, m

d_{in} : Inlet pipe diameter, m

d_p : diameter of particle, m

d_s : impeller shaft diameter, m

D_i : impeller diameter, m

d_{sp} : outer diameter of ring sparger, m

E_Θ : normalized RTD function

f : frequency, Hz

f_e : extra source of turbulent kinetic energy, kg/s^3-m

F_D : interphase drag force, N/m^3

F_q : interphase momentum exchange term

F_{VM} : virtual mass force, N/m^3

g : acceleration due to gravity, m/s^2

G : turbulence generation rate, kg-m/s^3

H : vessel height, m

I : turbulent intensity

k : turbulent kinetic energy, m^2/s^2

K : constant (Equation 5.13)

l : turbulent length scale, m

m : mass flow rate, kg/s

N : impeller rotational speed, rps

P : Power, watts

p : pressure, N/m^2

Q_l : volumetric flow rate, m^3/s

Q_g : volumetric gas flow rate, m^3/s

R_c : curvature of vessel bottom, m

R_{in} : hydraulic radius of feed pipe, m

r : radial coordinate, m

T : vessel diameter, m

T' : torque, N-m

t : time, s

t_c : circulation time, s

T_L : integral time scale of turbulence, s

t_m : mixing time, s

U : velocity, m/s

U_{slip} : slip velocity, m/s

U_{tip} : impeller tip speed, m/s

V : volume of vessel, m^3

W : impeller blade width, m

x : position vector, m

z : axial coordinate, m

Greek symbols

α : gas volume fraction

ε : turbulent kinetic energy dissipation rate, m^2/s^3

τ : shear stress, N/m^2

τ_p : particle relaxation time, s

ε : turbulent kinetic energy dissipation rate, m^2/s^3

λ : Kolmogorov length scale, m

ρ : density, kg/m^3

$\sigma_{\phi,l}$: model parameter (Equation 5.4)

σ : surface tension, dyne/cm

θ : tangential coordinate

μ : viscosity, kg/ms

ω : Z-vorticity, s^{-1}

ϕ : variable

Dimensionless numbers

Eo : Evotos number

Fl : gas flow number

Fr : Froude number

N_P : power number

N_Q : pumping number

Re : impeller Reynolds number

Re_b : bubble Reynolds number

Re_p : particle Reynolds number

Subscripts

1 : liquid

2 : gas

b : blade passage

CD : complete dispersion

F : flooding

g : gas

i : direction

l : liquid

p : particle

q : phase number

r : rotational speed

R : recirculation

t : turbulent

Superscript

- : time-averaged value

` : rms value

BIBLIOGRAPHY

Alves, S.S., Maia, C.I., Vasconcelos, J.M.T. and Serralheiro, A.J (2002), Bubble size in aerated stirred tank, *Chem. Eng. J.*, **89**, 109-117.

Aubin, J. (2001), Mixing capabilities of down- and up- pumping axial flow impellers in single-phase and gas-liquid systems: Experimental and CFD studies, *Ph.D. Thesis*, University of Sydney, Australia.

Aubin, J., Mavros, P., Bertrand, J., Fletcher, D. and Xuereb, C. (2001), Effect of axial agitator configuration (up-pumping, down-pumping, reverse rotation) on flow patterns generated in stirred vessels, *Chem. Eng. Res. Des.*, **79**, 845-856.

Aubin, J., Le Sauze, N., Bertrand, J., Fletcher, D. and Xureb, C. (2004), PIV measurements of flow in an aerated tank stirred by a down- and an up-pumping axial flow impeller, *Expt. Thermal and Fluid Sci.*, **28**(5), 447-456.

Bakker, A. and van den Akker, H.E.A. (1994), A computational model for the gas-liquid flow in stirred reactors, *Trans IChemE*, **72**, 594- 606.

Bakker, A. (1992), Hydrodynamics of stirred gas-liquid dispersion, *Ph.D. Thesis*, Delft University of Technology, The Netherlands.

Barigou, M. and Grevaes, A. (1991), A capillary suction probe for bubble size measurement, *Meas. Sci. Tech.*, **2**, 318-326.

Barigou, M. and Greaves, A. (1992), Bubble size distribution in a mechanically agitated gas-liquid contactor, *Chem. Eng. Sci.*, **47** (8), 2009-2025.

Baudou, C., Xuereb, C., & Bertrand, J. (1997a), 3-D hydrodynamics generated in a stirred vessel by a multiple-propeller system, *Can. J. Chem. Eng.*, **75**, 653-663.

Bertrand, J., Couderc, J.P. and Angelino, H. (1980), Power consumption, pumping capacity and turbulence intensity in baffle stirred tanks: Comparison between several turbines, *Chem. Eng. Sci.*, **35**, 2157-2163.

Bombac, A., Zun, I., Filipic, B. and Zumer, M. (1997), Gas-filled cavity structure and local void fraction distribution in aerated stirred vessel, *AIChE J*, **43** (11), 2921- 2931.

Boyer, C., Duqunne, A.M. and Wild, G. (2002), Measuring techniques in gas-liquid and gas-liquid-solid reactors, *Chem. Eng. Sci.*, **57**, 3185-3215.

Briens, L.A. and Briens, C.L. (2002), Cycle detection and characterization in chemical engineering, *AIChE J*, 2002, **48**(5), 970-980.

Brucato, A., Ciofalo, M., Grisafi, F. and Micale, G. (1998), Numerical prediction of flow fields in baffled stirred vessels: a comparison of alternative modelling approaches, *Chem. Eng. Sci.*, **53**, 3653-3684.

Brucato, A., Grisafi, F. and Montante, G. (1998), Particle drag coefficient in turbulent fluids, *Chem. Eng. Sci.*, **45**, 3295-3314.

Bruijn, W., Van't Riet, K and Smith, J.M. (1974), Power consumption with aerated Rushton turbines, *Trans IChemE,* **52**, 88.

Buwa, V.V. and Ranade, V.V. (2002), Dynamics of gas-liquid flow in rectangular bubble columns, *Chem. Eng. Sci*., **57**, 4715-4736.

Calderbank, P.H. (1958), Physical rate processes in industrial fermentation: part I, the interfacial area in gas-liquid contacting with mechanical agitation, *Trans IChemE,* **36**, 443.

Chapman, C.M., Nienow, A.W., Cook, M. and Middleton, J.C. (1983), Particle-gas-liquid mixing in stirred vessel, *Chem. Eng. Res. Des.*, **61**, 82-95.

Clift, R. and Gauvin, W.H. (1971), Motion of entrained particles in gas streams, *Can. J. Chem. Eng.*, **49**, 439-448.

Cooke, M., Middleton, J.C. and Bush, J.R. (1988), Mixing and mass transfer in filamentous fermentations, in *Proc. of 2nd Int. Conf. on Bioreactor Fluid Dynamics*, R King (ed), BHR Group, Cranfield, UK, 37-64.

Cui, Y.Q., van der Lans, R.G.J.M and Luben, K.Ch.A.M. (1996), Local power uptake in gas-liquid systems with single and multiple Rushton turbines, *Chem. Eng. Sci.*, **51,** 2631-2636.

Daw, C.S. and Halow, J.S. (1992), Modelling deterministic chaos in gas-fluidized beds, *AIChE Symp. Ser.*, **88** (289), 61.

Deen, N.G. (2001), An experimental and computational study of fluid dynamics in gas-liquid chemical reactors, *Ph.D. Thesis*, Aalborg University, Denmark.

Deen, N.G., Westerweel, J. and Hjertager, B.H. (2001), Upper limit of the gas fraction in PIV measurements in dispersed gas-liquid flows, *Proc. of 5th Int. Conf. On Gas-Liquid and Gas-Liquid-Solid Reactor Eng.*, Melbourne, Australia.

Deen, N.G., Solberg, T. and Hjertager, B. H. (2002), Flow generated by an aerated Rushton impeller, two-phase PIV experiments and numerical simulations, *Can. J. Chem. Eng.*, **80** (4), 1-15.

Deen, N.G.,van Sint Annaland, M. and Kuipers, J.A.M. (2004), Multi-scale modelling of dispersed gas-liquid two-phase flow, *Chem. Eng. Sci.*, **59**, 1853-1861.

Distelhoff, M.F. and Marquis, A.J. (2000), Scalar mixing in the vicinity of two disc turbines and two pitched blade impellers, *Chem. Eng. Sci.*, **55**, 1905-1920.

Drahos, J., Zahradnik, J, Puncochar, M., Fialova, M. and Bradka, F. (1991), Effect of operating conditions on the characteristics of pressure fluctuations in a bubble column, *Chem. Eng. Process.*, **29**, 107.

Dybbs, A. and Edwards, R.V. (1984), A new look at porous media fluid mechanics, Darcy to turbulent, In: J. Bear, and Y. Carapcioglu (Eds.), *Fundamentals of transport phenomena in porous media,* The Hague: Martinus Nijhoof, 199-251.

Escudié R. (2001), Structure Locale de l'Hydrodynamique Generée par une Turbine de Rushton, *Ph.D. Thesis*, INSA, Toulouse.

Feder, J. (1988), *Fractals*, Plenum Press, New York.

Fisher J., Broring S. and Lubbert A. (1991), Structure of the gas phase motion in aerated stirred tank reactors, *AIChE Symp. Series*, **88**, 98-113.

FLUENT 4.4 User's Guide (1997), Fluent Inc. USA, Centerra Resource Park, 10 Cavendish Court, Lebanon, NH ~ 03766, USA.

FLUENT 6.0 User's Guide (2002), Fluent Inc. USA, Centerra Resource Park, 10 Cavendish Court, Lebanon, NH ~ 03766, USA.

Franca, F., Acikgoz, M., Lahey, R.T. and Clausse, A. (1991), The use of fractal techniques for flow regime identification, *Int. J. Multiphase Flow*, **17**, 545.

Friberg, P.C. (1998), Three dimensional modelling of gas/liquid flow processes in bioreactors, *Ph.D. Thesis*, Telemark College, Norway.

Gosman, A.D. and Ioannides, E. (1981), Aspects of computer simulation of liquid fueled combustors, *19th Aerospace meeting, AIAA*, St. Louis, MO, Paper 81-03223.

Gosman, A.D., Lekakou, C., Politis, S., Issa, R.I. and Looney, M.K. (1992), Multi-dimensional modelling of turbulent two-phase flows in stirred vessels, *AIChEJ*, **38** (12), 1947-1956.

Guillard, F., Tragardh, C. and Fuchs. L. (2000), A study of turbulent mixing in a turbine agitated tank using a fluorescence technique, *Expt. Fluids*, **28**, 225-235.

Gunjal, P.R., Ranade, V.V. and Chaudhari, R.V. (2005), Computational study of a single-phase flow in packed beds of sphere, *AIChEJ,* **51**(2), 365-378.

Ho, B.P. and Leal, L.G. (1974), Inertial migration of rigid spheres in two-dimensional unidirectional flows, *J. Fluid Mech.*, **65** (2), 365-400.

Hughmark, G. (1980), Power requirements and interfacial area in gas-liquid turbine agitated systems, *Ind. Engg. Chem. Proc. Des. Dev.*, **19**, 641-646.

Hurst, H.E. (1951), Methods of using long-term storage in reservoirs, *ASCE*, **116**, 770.

Ishii, M. and Zuber, N. (1979), Drag coefficient and relative velocity in bubbly, droplet or particulate flows, *AIChE J.,* **25**, 843-855.

Jaworski, Z., Nienow, A.W., Koutsakos, E., Dyster, K. and Bujalski, W. (1991), An LDA study of turbulent flow in a baffled vessel agitated by a pitched blade turbine, *Trans IChemE*, **69**, 313-320.

Jenne, M. and Reuss, M., (1999), A critical assessment on the use of k-ε turbulence model for simulation of turbulent flow induced by a Rushton turbine in a baffled stirred tank reactor, *Chem. Eng. Sci.*, **54**, 3921-3941.

Joshi, J.B. and Ranade, V.V. (2003), Computational fluid dynamics for designing process equipment: Expectations, current status and path forward, *Ind. Eng. Chem. Res.*, **42**, 1115-1128.

Joshi, J.B., Pandit, A.B. and Sharma, M.M. (1982), Mechanically agitated gas-liquid reactors, *Chem. Eng. Sci.*, **37**, 813-844.

Kataoka, I., Besnard, D.C. and Serizawa, A. (1992), Basic equation of turbulence and modelling of interfacial terms in gas-liquid two phase flows, *Chem. Eng. Comm.*, **118**, 221.

Khopkar, A.R., Aubin, J., Xureb, C., Le Sauze, N., Bertrand, J and Ranade, V.V. (2003), Gas-liquid flow generated by a Pitched blade turbine: particle velocimetry measurements and CFD simulations, *Ind. Eng. Chem. Res.*, **42**, 5318-5332.

Khopkar, A.R., Aubin, J., Atoche, C.R., Xureb, C., Le Sauze, N., Bertrand, J and Ranade, V.V. (2004), Flow generated by radial flow impellers: PIV measurements and CFD simulations, *Int. J. Chem. React. Eng.*, **2**, A18.

Khopkar, A.R., Rammohan, A., Ranade, V.V. and Dudukovic, M.P. (2005), Gas-liquid flow generated by a Rushton turbine in stirred vessel: CARPT/CT measurements and CFD simulations, *Chem. Eng. Sci.*, **60**, 2215-2229.

Kovacs, T., Tragardh, C. and Fuchs, L. (2001), Flow and turbulence in the discharge of radial pumping turbines: influence of the turbine type, *Chem. Eng. Tech.*, **24**, 1035-1044.

Kuipers, J.A.M. and van Swaij, W.P.M. (1997), Application of computational fluid dynamics to chemical reaction engineering, *Rev. in Chem. Eng.*, **13**, 1.

Laakkonen, M., Moilanen, P., Alopaeus, V. and Aittamaa, J. (2004), Validation of population balance models for bubbles in agitated vessel using multi-block approach, *Proc. of 5th Int. Symp. on Mixing in Ind. Proc.*, Spain.

Lane, G. L., Schwarz, M. P. and Evans, G. M. (1999), CFD simulations of gas-liquid flow in a stirred tank, *Proc. of 3rd Int. Sym. on Mixing in Ind. Proc.*, Osaka, Japan, Sept., 21-28.

Lane, G. L., Schwarz, M. P. and Evans, G. M. (2000), Modelling of the interaction between gas and liquid in stirred vessels, *Proc. of 10th Euro. Conf. on Mixing*, Delft, The Netherlands, 197-204.

Lane, G. L., Schwarz, M. P. and Evans, G. M. (2005), Computational modelling of gas-liquid flow in mechanically stirred tanks, *Chem. Eng. Sci.*, **60**, 2203-2214.

Letzel, H.M., Schouten, J.C., Krishna, R. and van den Bleek, C.M. (1997), Characterization of regimes and regime transitions in bubble columns by chaotic analysis of pressure signals, *Chem. Eng. Sci.*, **52**, 4447-4459.

Lo, S. (2000), Application of population balance to CFD modelling of gas-liquid reactors, *Presented at Trends in Numerical and Physical Modelling of Multiphase Flows*.

Lu, W.M. and Ju, S.J. (1987), Local gas holdup, mean liquid velocity and turbulence in an aerated stirred tank using Hot film anemometry, *Chem. Eng. J.*, **35**, 9-17.

Lu, W. and Ju S. (1989), Cavity configuration, flooding and pumping capacity of disc type turbines in aerated stirred tanks, *Chem. Eng. Sci.*, **44**, 333-342.

Luo, J.Y., Gosman, A.D., Issa, R.I., Middleton, J.C. and Fitzgerald, M.K., (1993), Full flow field computation of mixing in baffled stirred vessels, *Trans. IChemE*, **71**, 342-344.

Luo, J.Y., Issa, R.I. and Gosman, A.D. (1994), Prediction of impeller induced flow in mixing vessels using multiple frames of reference, *IChemE Symp. Ser.*, **136**, 399-406.

Magelli, F., Fajner, D., Nocentini, M. and Pasquali, G. (1990), Solids distribution in vessels stirred with multiple impellers, *Chem. Eng. Sci.*, **45**, 615-625.

Marshall, E.M., Haidari, A. and Subbiah, S. (1996), Presented at *AIChE Annual Meeting*, Chicago, USA.

Mavros, P., Xuereb, C. & Bertrand, J. (1996), Determination of 3-D flow fields in agitated vessels by laser Doppler velocimetry: Effect of impeller type and liquid viscosity on liquid flow patterns, *Chem. Eng. Res. Des*., **74**, 658-668.

Mavros P., Naude I., Xuereb C. and Bertrand J. (1997), Laser Doppler Velocimetry in agitated vessels. Effect of continuous liquid stream on flow patterns, *Chem. Eng. Res. Des.*, **75**, 763-776.

Mavros, P., Barrue, H., Xureb, C., Fořt, I. and Bertrand, J (2000), Effect of axial-flow impeller and feed tube location on flow patterns in continuous flow stirred tank reactor, *Presented at 13th International Congress of Chemical and Process Engineering conference*, CHISA.

Mavros, P. (2001), Flow visualization in stirred vessels: a review of experimental techniques, *Chem. Eng. Res. Des.*, **79**, 113-127.

Mavros P., Xuereb C., Fořt I. and Bertrand J. (2002), Investigation by laser Doppler velocimetry of the effects of liquid flow rates and feed positions on the flow patterns induced in a stirred tank by an axial-flow impeller, *Chem. Eng. Sci*., **57**, 3939-3952.

Micale, G., Montante, G., Grisafi, F., Brucato, A. and Godfrey, J. (2000), CFD simulation of particle distribution in stirred vessels, *Trans. IChemE*, **78**, 435- 444.

Mishra, V.P. and Joshi, J.B. (1991), LDA measurements of gas-liquid flow in mechanically agitated reactors, *Proc. of 7th Euro. Conf. on Mixing,* Brugge, BHRA, 247-255.

Morsi, S.A., Alexander, A.J. (1972), An investigation of particle trajectories in two-phase flow system *J. Fluid Mech.,* **55** (2), 193-208.

Morud, K.E and Hjertager B.H. (1996), LDA measurements and CFD modelling of gas-liquid flow in stirred vessel, *Chem. Eng. Sci.*, **51**, 233-249.

Ng, K., Fentiman, N. J., Lee, K.C. and Yianneskis, M. (1998), Assessment of sliding mesh CFD predictions and LDA measurements of the flow in a tank stirred by a Rushton impeller, *Chem. Eng. Res. Des.*, **76**, 737-747.

Nienow, A.W., Wisdom, A.J. and Middleton, J.C. (1977), The effect of scale and geometry on flooding, recirculation and power in gassed stirred vessels, *Proc. of 2nd Euro. Conf. on Mixing*, Cambridge, Paper F1.

Nienow, A.W., Warmoeskerken, M.M.C.G., Smith, J.M. and Konno, M. (1985), On the flooding/loading transition and the complete dispersal condition in aerated vessels agitated by a Rushton turbine, *Proc. of 5th Euro. Conf. on Mixing*, Wurzburg, Paper 15.

Nienow, A.W. (1998), Hydrodynamics of stirred bioreactors, *Appl. Mech. Rev.*, **51** (1), 3-32.

Nienow, A.W. (1990), Gas dispersion performance in fermentor operation, *Chem. Eng. Prog.*, 61.

Oldshue, J.Y. (1984), *Fluid Mixing Technology*, McGraw Hill, New York.

Paglianti, A., Pintus, S. and Giona, M. (2000), Time-series analysis approach for the identification of flooding/loading transition in gas-liquid stirred tank reactors, *Chem. Eng. Sci.*, **55**, 5793-5802.

Perng, C.Y. and Murthy, J.Y. (1993), A moving-deforming mesh technique for simulation of flow in mixing tanks, *AIChE Symp. Ser.*, **89**(293), 37-41.

Peters, E.E. (1994), *Fractal market analysis: Applying chaos theory to investment economics*, Wiley, New York.

Pinelli, D., Montante, G. and Magelli, F. (2004), Dispersion coefficients and settling velocities of solids in slurry vessels stirred with different types of multiple impellers, *Chem. Eng. Sci.*, **59**, 3081-3089.

Prakash, O., Gupta, S.N. and Mishra, P. (1987), Newtonian and inelastic non-Newtonian flow across tube banks, *Ind. Eng. Chem. Res.*, **26**, 1365-1372.

Press, W.H., Teukolsky, S.A., Vellerling, W.T. and Flannery, B.P. (1987), *Numerical Recipes in FORTRAN*, Cambridge University Press.

Rammohan, A.R., Kemoun, A., Al-Dahhan, M.H. and Dudkovic, M.P. (2001a), A Lagrangian description of flows in stirred tanks via Computer Automated Radioactive Particle Tracking (CARPT), *Chem. Eng. Sci.*, **56**, 2629-2639.

Rammohan, A.R., Duducovic, M.P. and Ranade, V.V. (2003), Eulerian flow field estimation from particle trajectories: Numerical experiments for stirred type flows, *Ind. Eng. Chem. Res.*, **42**, 2589- 2601.

Ranade, V.V., Bourne, J.R. and Joshi, J.B. (1991), Fluid mechanics and mixing in agitated tanks, *Chem. Eng. Sci.*, **46**, 1883-1893.

Ranade, V.V. (1992), Numerical simulation of dispersed gas-liquid flows, *Sadhana*, **17**, 237-273.

Ranade, V.V. and H.E.A. van den Akker (1994), Modelling of flow in gas-liquid stirred vessels, *Chem. Eng. Sci.*, **49**, 5175-5192.

Ranade, V.V. (1995), Computational fluid dynamics for reactor engineering, *Rev. in Chem. Eng.*, **11**, 225.

Ranade, V.V. (1997), Modelling of turbulent flow in a bubble column reactor, *Chem. Eng. Res. Des.*, **75**, 14.

Ranade, V.V. and Deshpande V.R. (1999), Gas Liquid flow in stirred reactors: Trailing vortices and gas accumulation behind impeller blades, *Chem. Eng. Sci.*, **54**, 2305-2315.

Ranade, V.V. and Tayaliya, Y. (2000), Computational study of transfer and dissipation of impeller power, *Presented at ISHMT-15 conference*, Pune, India.

Ranade, V.V., Perrard, M., Le Sauze, N., Xureb, C. and Bertrand, J. (2001a), Trailing vortices of Rushton turbines, *Chem. Eng. Res. Des.*, **79A**, 3.

Ranade, V.V., Perrard, M., Xureb, C., Le Sauze, N. and Bertrand, J. (2001b), Influence of gas flow rate on the structure of trailing vortices of a Rushton turbine, *Chem. Eng. Res. Des.*, **79**, 957-964.

Ranade, V.V., Karve, H.R. and Shashi, S. (2001c), A computational study of gas accumulation and cavity formation behind impeller blades, *Presented at Int. Conf. On Multiphase Flows (ICMF)*, USA.

Ranade, V.V. (2002), *Computational Flow Modelling for Chemical Reactor Engineering*, Academic Press, New York.

Ranade, V.V., Krishnan, H. and Tayaliya, Y. (2002), CFD predictions of flow near impeller blades in baffled stirred vessels: assessment of computational snapshot approach, *Chem. Eng. Comm.*, **189**(7), 895-922.

Rewatkar, V.B. and Joshi, J.B. (1993), Role of sparger design on gas dispersion in mechanical agitated gas-liquid contactors, *Can. J. Chem. Eng.*, **71**, 278-291.

Roe, P.L. (1985), Some contributions to the modelling of discontinuous flows, in Lecture notes in applied mathematics, *Springer-Velarg, Berlin*, **22**, 163-193.

Rousar, I., Lubbert, A. and van den Akker, H.E.A. (1994), Modelling and measurements of gas-liquid dispersion in agitated tanks with single and multiple impellers, *IChemE Symp. Ser.*, **136**, 89-96.

Rouston, M. and Pharamond, J. C. (1988), Agitation et mélange, *Techniques de l'Ingenieur* A.10, A 5900.

Saito, F., Nienow, A.W., Chatwin, S. and Moore, I.P.T. (1992), Power, gas dispersion and homogenisation characteristics of Scaba SRGT and Rushton turbine impellers, *J. Chem. Eng. Japan*, **25**, 281-287.

Schafer, M., Wachter, P. and Durst, F. (2000), Experimental investigation of local bubble size distributions in stirred vessels using phase Doppler anemometry, *Proc. of 10th European Conference of Mixing*, Delft, The Netherlands, 205-212.

Schouten, J.C. and van den Bleek, C.M. (1998), Monitoring the quality of fluidization using the short-term predictability of pressure fluctuations, *AIChE J*, **44**, 48-60.

Sharma, R. N, Howk, R. A. and Lally, K.S. (1993), Flooding characteristics of impellers in stirred tanks, *AIChE Symp. Ser.*, **89** (293), 85.

Shewale, S.D. and Pandit, A.B. (2005), Studies in multiple impeller agitated gas-liquid contactors, *Chem. Eng. Sci.*, accepted for publication.

Smith, J.M. (1985,) *Dispersion of gases in liquids in Mixing of Liquids by Mechanical Agitation,* Ed. J.J. Ulbrecht and G.K. Patterson, Gordon and Breach, London.

Smith, J.M., Warmoeskerken, M.M.C.G. and Zeef, E. (1987), Flow conditions in vessel dispersing gases in liquids with multiple impellers, *Biotechnology Processes*, C.S. Ho and J.Y. Oldshue, eds., *AIChE*, 107-115.

Sommerfeld, M. (1990), Numerical simulation of the particle dispersion in turbulent flow: the importance of particle lift forces and particle/wall collision models, *ASME, Fluids Engineering Division (Publication) FED*, **91**, 11-18.

Suntahnkar, A.A. and Ranade, V.V. (1997), Dynamics of gas-liquid flow, *NCL Internal Report*.

Sutter, T.A., Morrison, G.L. and Tatterson, G.B. (1987), Sound spectra in an aerated agitated tank, *AIChE J*, **33** (4), 668-671.

Takahashi, K and Nienow, A.W. (1993), Bubble sizes, hold up and coalescence rates in aerated vessels agitated by Rushton turbine: Spacial variation, *J. Chem. Eng. Japan*, **26**, 536-542.

Takahashi, K. and Nienow, A.W. (1992), Vortex cavity shape and the associated path-line of discharged bubbles in an aerated vessel agitated by a Rushton turbine, *J. Chem. Eng. Japan*, **25**, 539.

Takens, F. (1981), *Lecture notes in Mathematics*, **898**, 366.

Tatterson, G.B. (1991), *Fluid Mixing and Gas Dispersion in Agitated Tanks*, McGraw Hill, London.

Thomson, D.J. (1987), Criteria for the selection of stochastic models of particle trajectories in turbulent flows, *J. Fluid Mech.*, **180**, 529-556.

Tsuchiya, K., Furumoto, A., Fan, L.S. and Zhang, J. (1997), Suspension viscosity and bubble rise velocity in liquid-solid fluidised beds, *Chem. Eng. Sci.*, **52**, 3053-3066.

Uhleherr, P.H.T. and Sinclair, C.G. (1970), The effect of free stream turbulence on the drag coefficient of spheres, *Proceedings Chemeca'*70, Vol.1, Butterworths, Melbourne, 1-13.

Van den Bleek, C.M. and Schouten, J.C. (1993), Deterministic chaos: a tool in fluidized bed design and operation, *Chem. Eng. J*, **53**, 75-87.

Van der Stappen, M.L.M., Schouten, J.C. and van den Bleek, C.M. (1993), Deterministic chaos analysis of the dynamical behavior of slugging and bubbling fluidized beds, *Fluidized Bed Combustion*, **1**, 129-140.

Van't Riet, K., Boom, J.M. and Smith, J.M. (1976), Power consumption, impeller coalescence and recirculation in aerated vessel, *Trans I Chem E.*, **54**, 124-131.

Vant't Riet, K. and Smith, J.M. (1973), The behavior of gas-liquid mixtures near Rushton turbines blades, *Chem. Eng. Sci.*, **28**, 1031-1037.

Veera, U.P., Patwardhan, A.W. and Joshi, J.B. (2001), Measurement of gas-holdup profiles in stirred tank reactors by Gamma ray attenuation technique, *Chem. Eng. Res. Des.*, **79**, 684-688.

Wachter, P., Steidl, W, Hofken, M. and Durst, F. (1996), Application of the ultrasound velocity measuring technique to stirred vessel flows, *Proc. Ist Int. Symp. Ultrasonic Doppler methods in fluid mechanics and fluid engineering*, Switzerland, 31-62.

Wang, M., Dorward, A., Vlaev, D. and Mann, R. (2000), Measurements of gas-liquid mixing in a stirred vessel using electrical resistance tomography (ERT), *Chem. Eng. J.*, **77**, 93-98.

Warmoeskerken, M.M.C.G. and Smith, J.M. (1982), Description of the power curves of turbine stirred gas-liquid dispersion, *Proc. of 4th Euro. Conf. on Mixing*, The Netherlands, Paper G1.

Warmoeskerken, M.M.C.G. and Smith, J.M. (1985), Flooding of disk turbines in gas-liquid dispersions: a new description of the phenomenon, *Chem. Eng. Sci.*, **40**, 2063.

Warmoeskerken. M.M.C.G. and Smith, J.M. (1989), The hollow blade agitator for dispersion and mass transfer, *Chem. Eng. Res. Des.*, **67**, 193-198.

Wechsler, K., Breuer, M. and Durst, F. (1999), Steady and unsteady computations of turbulent flows induced by a 4/45° pitched blade impeller, *J. of Fluids Eng.*, **121**, 318.

SYNOPSIS

Introduction

Stirred reactors are widely used in process industry to carry out large number of gas-liquid catalytic reactions (such as, hydrogenation, oxidation, alkylation, sulfonation). They offer maximum flexibility in operation and provide maximum number of degrees of freedom to manipulate the performance of the reactor. In stirred reactor, the overall reaction rate and the reactor performance (selectivity and conversion) are controlled by the fluid dynamics prevailing in the reactor. Despite the wide spread use of the stirred reactor, the fluid dynamics of these reactors, essentially for the gas-liquid system is not well understood. This lack of understanding and knowledge of basic fluid dynamics causes reliance on empirical information (Smith, 1985; Tatterson, 1991). The available empirical information is usually described in an overall/ global parametric form. This practice conceals detailed localised information, which may be crucial in the successful design of process equipment. The reliability of such empirical information and the efficient use of this information as a potential for the extrapolation beyond the range of parameters studied often remains questionable. It is therefore, essential to develop and apply new tools to enhance our understanding of fluid dynamics prevailing in the stirred reactors. Such understanding will be useful in devising cost effective and reliable scale-up of stirred reactors. The present study was therefore undertaken with an objective of developing a broad framework for understanding and modelling of the gas-liquid flows in stirred reactor equipped with different types of impellers.

Part I: Experimental Characterization of Gas-liquid Flows

Different flow regimes are prevailing in gas-liquid stirred reactor depending upon the impeller size, shape, rotational speed and gas flow rate. The fluid dynamic conditions as well as the rates of transport and mixing processes occurring in reactor significantly changes with the change in flow regimes. Significant research efforts have been spent on developing flow regime maps and the design correlations (see the excellent review of Nienow, 1998 and the references cited therein). However, the applicability of the developed flow regime maps to industrial systems and the question of whether the intended flow regime is realized in actual operation (with different reactor configurations and with different physical properties of gas and liquid) and whether this can be determined on-line are of great interest but are not well studied.

The wall pressure (using pressure transducer) and torque (using torque sensor) fluctuation measurements were carried out to identify the prevailing flow regimes and extract the information of relevant time scales of the prevailing fluid dynamics. The experiments were carried out in a cylindrical, flat-bottomed and fully baffled stirred vessel (of diameter, T = 0.7 m and liquid height, H = 0.7 m) employed with Rushton turbine, 6-blade down pumping pitched turbine and Smith turbine. The amplified signal from both the sensors was acquired using a laptop computer with 16-bit A/D PCMCIA converter card and data acquisition software 'dAtagate' (of nCode, UK). The fluctuations associated with the dynamic pressure field in the impeller discharge stream and instantaneous torque values were analyzed by using in-house code '**A**nalysis of **n**onlinear **T**ime **S**eries, **AnTS**'(Sunthankar and Ranade, 1997).

The torque sensor was used to measure the instantaneous value of torque for Rushton turbine, 6-blade down pumping pitched blade turbine and Smith turbine in gas–liquid stirred vessel. The average power reduction curve and the RMS values of torque fluctuations were analyzed. It was observed that the average power consumption curve and the RMS values of torque fluctuations help in identification of flow regimes in stirred vessel especially for down-pumping pitched blade turbine. In addition to the flow regime identification, the RMS value of the torque fluctuations provided the quantitative information of the wide torque fluctuations present in cavity formation regime for down-pumping pitched blade turbine. However, the analysis of torque fluctuations failed to provide the information of the cavity structure present behind the impeller blades. The knowledge of the cavity structure would have provided the detail flow regime map.

The pressure field around the impeller blades is linked with the cavity structure present behind the individual impeller blades. The identification of change in the pressure field can be related to the change in the cavity structure behind the impeller blades. The pressure transducer was then used to study the pressure fluctuations resulted in flow field due to the motion of gas cavities. The change in statistical properties of the pressure fluctuations was used to set up a criterion for the identification of flow regimes. The power spectrum, Hurst and P statistics analysis of the pressure fluctuations were carried out. The power spectrum of the pressure fluctuations not only

successfully captured the flow regimes present in the reactor but also obtained the information of cavity structure present behind the impeller blades. The Hurst and P statistics analysis estimated the mixing time scale of the reactor along with the identification of flow regimes. The mixing time measurements were carried out using conductivity measurement technique for the confirmation of mixing time information obtained from the P statistics analysis of wall pressure fluctuations. Thus the method developed in present study can become a useful tool for providing early warnings in the case of regime transition occurring due to sudden changes in process (operating) parameters or while intensifying the operation of the vessel.

Part II: Computational Modelling of Gas-Liquid Flows

The detail knowledge of the fluid dynamics is essential for correct quantification of the transport and mixing processes occurring in the reactor. The experimental techniques have provided the valuable information, but the efforts are mostly limited to single-phase flows. The presence of secondary phase makes the measurement difficult. In recent years, computational fluid dynamics (CFD) has emerged as the powerful tool for the understanding of the fluid dynamics in the reactors. However, its success in single-phase processes is significant while the presence of multiple phases makes the description of flow difficult (Ranade 2002). This requires the correct modelling of the momentum exchange between the phases and distribution of the secondary phase (such as bubble size distribution). The critical review of the literature show the lack of understanding for interphase forces as well as the bubble size distribution for gas-liquid stirred reactor. Therefore, in the present study an attempt was made to study the influence of interphase forces on the fluid dynamics and develop necessary sub-models for correct modelling of interphase forces. However, the bubble size was modeled by specifying single bubble size over whole reactor. Standard k-ε turbulence model was used to model the turbulence in reactor. The computational snapshot approach was used to simulate the impeller rotation in the reactor.

The experimental studies of Magelli and co-workers (1990, 2004) and Brucato et al. (1998) highlighted the influence of free stream turbulence on the settling velocity of the solid particles. They have shown the significant decrease in the settling velocity of

particles in the turbulent flow and propose the turbulent correction factor for calculation of drag coefficient in turbulent fluid. However, no such study is available in the literature explaining the influence of turbulence on the drag coefficient and hence the slip velocity of the gas bubbles. In the present study, a sub-model based on the CFD was developed to understand the influence of turbulence on the drag coefficient. A two-dimensional model case of flow through an array of cylindrical objects was considered for this purpose. Free slip wall boundary condition was used on the cylinder surface to define the object as gas bubbles. Appropriate source term for the turbulent kinetic energy (using user-defined function) was used to vary the prevailing levels of turbulence of flow. A modified correlation in lines with the correlation reported by Brucato et al. (1998) was developed on the basis of CFD simulations.

The developed sub-model was then incorporated in the computational model for simulating gas-liquid flows in stirred reactors. The computational model was first applied to predict the flow generated by a disc turbine operating in three distinct flow regimes. The model predictions were compared with the local gas holdup data reported by Bombac et al. (1997). The preliminary simulations show the significant effect of interphase drag force on the predicted pattern of gas holdup distribution. Different available correlations for interphase drag force, including the correlation developed in present study, were tested. The predicted results indicated the strong influence of the interphase drag force on the gas holdup distribution pattern. The computational model employed with the developed interphase drag force formulation predicted the gas holdup distribution pattern with reasonable accuracy for all three regimes. The influence of other interphase forces, such as virtual mass force and turbulent dispersion force was also studied in detail. The model predictions were then used to understand the influence of gas flow rate on the flow around impeller blades. The computational model has successfully captured the interaction of upward rising gas with trailing vortices and gas accumulation behind impeller blades adequately. The computational model first time predicted the change in the magnitude of gas accumulation with the change in flow regime. The model also enables ‘a priori’ prediction of drop in the impeller power dissipation and pumping efficiency in the presence of gas.

The computational model developed in this work was then used to study the flow generated by down pumping pitched blade and Scaba turbines. An attempt was made to

understand the flow around the impeller blades. The influence of the volumetric gas flow rate on the structure of trailing vortices and the gas accumulation was studied in detail. The model predictions were compared with the PIV measurements reported by Aubin et al. (2003) and Khopkar et al. (2003, 2004). The computational model was observed to capture the key features of the flow generated by down pumping pitched blade and Scaba turbine with reasonably good accuracy. Finally the validated computational model was used to simulate the flow generated by up pumping pitched turbine and paddle turbine. The model predictions were then used to compare the flow generated by all the studied impellers to understand the influence of size, shape and pumping mode on the flow generated by these impellers. An attempt was made to bring out the similarities and differences between the flow generated by these impellers. Such analysis will be useful to form a basis while selecting an impeller for a specific operation. The developed and validated computational models were then used to understand the reactor engineering design issues such as operational conditions, geometric configuration.

Part III: Application to Reactor Engineering

Reliable translation of batch-operated processes to continuous mode has a great importance in chemical industry. In continuously operated system, not only the operating conditions but also the hardware configuration such as impeller size, clearance and pumping direction, inlet and outlet nozzle locations control the performance of reactor. The flow and mixing simulations were carried out in a continuous stirred vessel equipped with '*Mixel TT*' impeller using a quasi-steady state approach to evaluate an influence of inlet and outlet nozzle locations on the performance. The operating conditions chosen in these simulations were such that one would expect almost ideal performance of reactor. However, the significant influence of inlet and outlet nozzle location and configurations was observed on predicted RTD curves. The study also demonstrated the potential of CFD based mixing simulations using a quasi-steady state approach to identify new inlet/outlet configuration for improving the mixing in the reactor.

Local flow patterns created by an impeller-generated flow and upward rising gas resulted into very complex flow field in gas-liquid stirred reactor. These local flow

patterns determine the rates of transport and mixing processes occurring in the reactor. The extension of the computational model to simulate the influence of these flow patterns on the mixing process is in progress. After the validation of the model predictions, the developed model can be used to simulate the operation of industrial gas-liquid stirred reactors.

References

Aubin, J., Le Sauze, N., Bertrand, J., Fletcher, D.F. and Xureb, C. (2004), PIV measurements of flow in an aerated tank stirred by a down- and an up- pumping axial flow impeller, *Experimental Thermal and Fluid Science*, **28**(5), 431-445.

Bombac, A., Zun, I., Filipic, B. and Zumer, M. (1997), Gas-filled cavity structure and local void fraction distribution in aerated stirred vessel, *AIChE J*, **43** (11), 2921- 2931.

Brucato, A., Grisafi, F. and Montante, G. (1998), Particle drag coefficient in turbulent fluids, *Chem. Engg. Sci.*, **45**, 3295-3314.

Khopkar, A.R., Aubin, J., Xureb, C., Le Sauze, N., Bertrand, J and Ranade, V.V. (2003), Gas-liquid flow generated by a Pitched blade turbine: Particle velocimetry measurements and CFD simulations, *Ind. Eng. Chem. Res.*, **42**, 5318-5332.

Khopkar, A.R., Aubin, J., C. Rubio-Atoche, Xuereb, C., Le Sauze, N., Bertrand, J. and Ranade, V. V. (2004), Flow generated by radial flow impellers: PIV measurements and CFD simulations, *I. J.C.R.E.*, Vol.**2**, A18.

Magelli, F., Fajner, D., Nocentini, M. and Pasquali, G. (1990), Solids distribution in vessels stirred with multiple impellers, *Chem. Engg. Sci.*, **45**, 615-625.

Pinelli, D., Montante, G. and Magelli, F. (2004), Dispersion coefficients and settling velocities of solids in slurry vessels stirred with different types of multiple impellers, *Chem. Eng. Sci.*, **59**, 3081-3089.

Ranade, V.V. (2002), *Computational Flow Modelling for Chemical Reactor Engineering*, Academic Press, New York.

Smith, J.M. (1985), Dispersion of gases in liquids in Mixing of Liquids by Mechanical Agitation, Ed. J.J. Ulbrecht and G.K. Patterson, Gordon and Breach, London.

Suntahnkar, A.A. and Ranade, V.V. (1997), Dynamics of gas-liquid flow, NCL Internal Report.

Tatterson, G.B. (1991), Fluid Mixing and Gas Dispersion in Agitated Tanks, McGraw Hill, London.